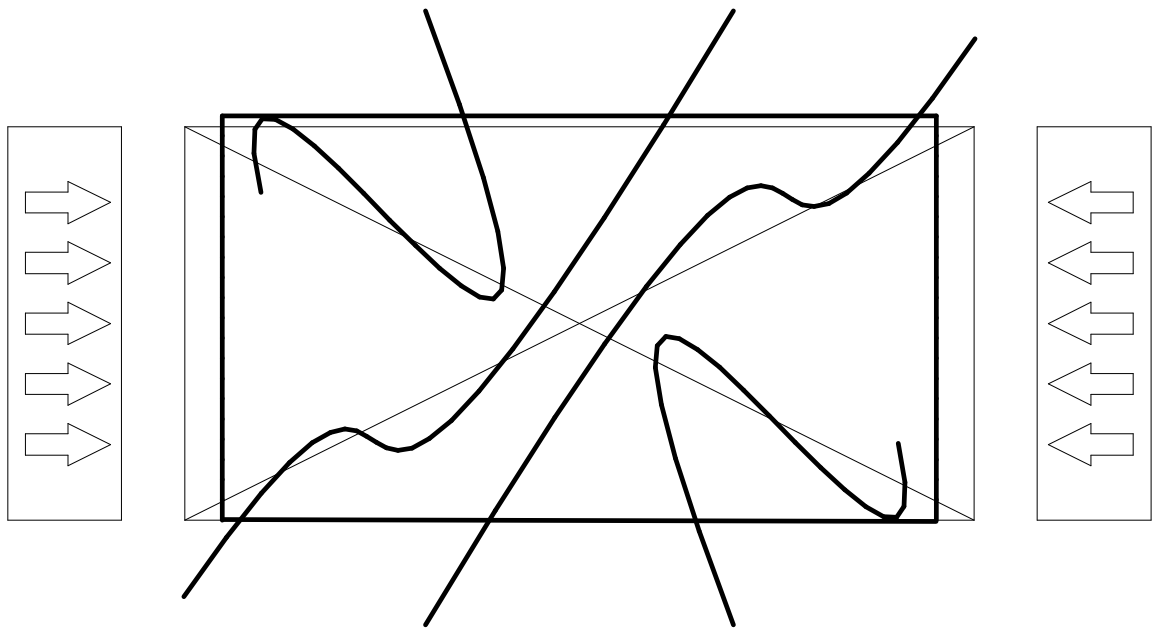


UNIVERSIDADE TÉCNICA DE LISBOA
INSTITUTO SUPERIOR TÉCNICO

**ROBUST VARIABLE DEGREE EQUILIBRIUM
ELEMENTS
(FORMULATION AND APPLICATION)**



Angus Charles Alexander Ramsay

Report on Post-Doctoral Research Year

May 1995

ROBUST VARIABLE DEGREE EQUILIBRIUM ELEMENTS

(FORMULATION AND APPLICATION)

Abstract

This report details a years post-doctoral research carried out by the author at the I.S.T. and funded through the *Human, Capital and Mobility Network*.

A formulation for robust variable degree equilibrium elements is presented in which the spurious kinematic modes are effectively and efficiently controlled at source by using the macro-element concept.

The performance of the macro-elements is evaluated through numerical example and is compared with that of traditional conforming displacement elements.

Recent developments in error estimation for displacement finite element solutions have utilised the properties available with the equilibrium element. With the availability of variable degree equilibrium elements this research has been further extended.

Acknowledgments

The feasibility of this current research became possible through collaboration between Dr E. A. W. Maunder of the University of Exeter, England and Professors J.A.T. de Freitas and J.P.B.M. de Almeida of I.S.T. and through the availability of funds from the *Human Capital and Mobility Network*. For this reason and to these people and this body the author is grateful.

The author would further like to express his gratitude to Professor J.P.B.M. de Almeida for his patient supervision of this project, and to Mr O.J.B.A. Pereira for his time and efforts in attempting, and often succeeding, to clarify the authors understanding of finite elements.

The author would also like to thank all the staff and students of the civil engineering department who have provided such a pleasant and friendly working environment. I would particularly like to express my thanks to Cornel Cismasiu and to Marco Piteri for their supportive friendship during this year.

I am also grateful to Dr Peter Petrov of the Institute of Electronics, Sofia, Bulgaria for his friendship during my first months in Portugal, to Professor Leonello Pogliani of the Department of Chemistry at the University of Calabria, Italy for his company and conversation during many an excursion both in Portugal and Spain, and to Anton Chichkov of the Instituto de Engenharia de Sistemas e Computadores for his friendship during my time in Lisbon.

Finally, I would like to express my thanks to the people of Portugal who, on average, have accepted a foreigner into their midst without complaint and even, on occasion, with enthusiasm.

List of Contents

CHAPTER 1: Introduction	1
CHAPTER 2: Formulation of Robust Variable Degree Equilibrium Elements	5
2.1 Introduction	5
2.2 Equations of Elasticity	5
2.3 Formulation for Primitive Equilibrium Elements	10
2.4 Implementation of a Triangular Primitive-Type Element	13
2.5 Polynomial Approximation Functions	15
2.6 Spurious Kinematic Modes	24
2.7 Assembly of Macro-Type Elements	27
2.8 Spurious Kinematic Modes in Macro-Elements	29
CHAPTER 3: Application of Robust Variable Degree Equilibrium Elements	33
3.1 Introduction	33
3.2 Confirmation of Program Integrity	33
3.3 Note on Degrees of Freedom	34
3.4 Note on Solution Bounds	35
3.5 Demonstration of Program Capability and Performance	37
3.5.1 Force Driven Problems (Zero Body Forces)	37
3.5.2 Force Driven Problems (Non-Zero Body Forces)	49
3.5.3 Displacement Driven Problems (Zero Initial Strains)	56
3.5.4 Displacement Driven Problems (Non-Zero Initial Strains)	60
CHAPTER 4: Displacement Elements Versus Equilibrium Elements	65
4.1 Introduction	65
4.2 Numerical Examples	67
4.3 Discussion of Results	79
CHAPTER 5: Error Estimation with Variable Degree Equilibrium Elements	81
5.1 Introduction	81
5.2 Example of the Ladevèze/Maunders Technique	82
5.3 Error Estimation	86
5.4 Numerical Examples	88
CHAPTER 6: Conclusions and Recommendations	99
APPENDICES	102
Appendix 1: Robust Equilibrium Elements: A Proposal	102
Appendix 2: Curious Convergence Characteristics	103
Appendix 3: Use of the Pseudo-Inverse: An Example	106
Appendix 4: User Guide to the Program	110
Appendix 5: Paper I	121
Appendix 6: Paper II	139
REFERENCES	170

Nomenclature

Scalars

E	Young's modulus
ν	Poisson's ratio
μ	coefficient of linear thermal expansion
ρ	material mass density
t	material thickness
p	degree of approximation temperature change

Vectors

b	vector of cartesian body forces
t	vector of edge boundary tractions
p	vector of cartesian boundary forces
u	vector of cartesian displacements
σ	vector of cartesian stress components
ϵ	vector of cartesian strain components

Matrices

T	stress/traction transformation matrix
R_1	rotation matrix for standard two-component vectors
R_2	rotation matrix for vectors of stresses and strains
∂	matrix of differential operators
k	material stiffness matrix
f	material flexibility matrix
S	stress interpolation matrix
V	edge displacement interpolation matrix
F	natural flexibility matrix

Coordinate systems

x,y	element cartesian
X,Y	global cartesian
S	element edge ordinate
ζ	element edge ordinate (non-dimensional)

Superscripts, subscripts and associated embellishments

^	for vectors is a coordinate system rotated away from global system
~	for estimated quantities for virtual quantities
c	for complimentary solutions
p	for particular solutions
o	for initial quantities e.g. initial strains
e	for error quantities

CHAPTER 1

Introduction

Equilibrium elements are a breed of finite element that provide statically admissible approximations to the exact solution. They are formulated by defining modes of statically admissible stress within an element and modes of displacement on element edges. Corresponding to these modes of edge displacement are modes of edge traction. In order for the edge tractions to equilibrate with the element stress field it is necessary for them (and therefore the corresponding edge displacements) to be of the same degree as the element stress field i.e. the degree of approximation should be the same for both element stress field and edge displacement.

For arbitrarily shaped elements this condition generally leads to hypo-static models and the traditional problems of spurious kinematic modes. For each spurious kinematic mode there is a corresponding mode of inadmissible traction. An example will serve to demonstrate this point.

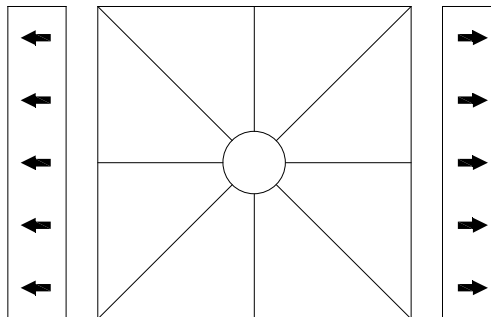


Figure 1.1 A finite element model

For the finite element model shown in figure 1.1 there are 8 elements and 24 edges. If we take the case of a constant degree of approximation then there are 3 statically admissible modes of stress per element and 2 modes of edge displacement per edge. Thus there are $24 \times 2 = 48$ equations of equilibrium of which only $48 - 3 = 45$ are independent (the three planar equations of structural equilibrium need to be satisfied). In terms of the unknowns in these equations there are $8 \times 3 = 24$ static variables to be determined. The model is, therefore, hypo-static to the tune of $45 - 24 = 21$ i.e. there are 21 spurious kinematic modes. Even for models where the number of static variables is equal to or greater than the number of independent equations of equilibrium (i.e. iso- or hyper-static models) linear dependencies between the equations can and do arise and again lead to spurious kinematic modes. This is a serious problem since in practice it

means that a solution for an arbitrarily defined mesh/load combination may not be feasible. Indeed, the combination shown in figure 1.1 is such an example where no solution is possible.

The use of equilibrium elements of arbitrary geometry and degree of approximation tend therefore to be confined to the realms of academia. In this context the work of Almeida and Freitas [1,2] is of note. For equilibrium elements to be of practical use they need to be *robust* [3]. This adjective is used to describe elements which are in themselves free from the effect of spurious kinematic modes. Such elements can be assembled with assurance that the model will also possess the same property. Assemblies of elements termed *macro-elements* for which the effect of spurious kinematic modes has either been eliminated entirely, or has been eliminated from the external edges of the macro are examples of robust equilibrium elements. The original concept of robust macro-elements dates back to Sander [4,5]. However, more recently the macro-element has enjoyed a revival through the work of Maunder [6,7]. One of the motivations behind this revival is due to the use of statically admissible solutions in error estimation for standard conventional displacement elements [7].

In this recent work quadrilateral macro-elements with degree of approximation up to quadratic have been studied [8]. The present research has been carried out with the aim of confirming the robust nature (a prediction by Maunder and Almeida) of macro-elements of variable degree of approximation and of demonstrating their capability in terms of practical analysis and error estimation. The proposal that was presented to the *Human, Capital and Mobility Network* as a basis for this work is shown in appendix 1. The report is laid out in the following manner.

In chapter 2 a formulation for general equilibrium elements is presented. This theory is used to develop a triangular primitive-element which will be the building block of the macro-elements. The triangular primitive-element suffers from spurious kinematic modes and the number and nature of these modes for a given degree of stress field are discussed. The triangular primitive-element is then assembled into macro-elements. Triangular and quadrilateral formats are considered in this report.

The triangular macro-element possesses the highly desirable property that for any degree of approximation considered, it is free from spurious kinematic modes. The quadrilateral macro-element, on the other hand, is effected by spurious kinematic modes and the number and nature of these modes is dependent on both the internal geometrical arrangement of the macro-elements and on the degree of approximation. Provided the spurious kinematic modes only involve displacements of edges internal to the macro-element then the element can be used safe in the knowledge that all modes of applied

boundary loading are admissible. However, the spurious kinematic mode, albeit internal to the macro-element, still exists and requires special treatment. The stiffness matrix for the macro is formed by assembling those of the primitive-elements and condensing out degrees of freedom associated with internal edges. This process requires the inversion of that part of the macro-element stiffness matrix which involves internal degrees of freedom. With the presence of spurious kinematic modes this part of the matrix is singular. In order to perform this inversion the pseudo-inverse is used. Although no proof is yet available for the number and nature of spurious kinematic modes occurring for an arbitrary internal geometric arrangement and degree of approximation, strong numerical evidence has led to a faith regarding the answer to this question. Based on this faith the number and nature of spurious kinematic modes can be predicted and treated accordingly.

In chapter 3 of this report, the capabilities of the equilibrium element are explored. Firstly, by way of introduction, the element is tested with statically and kinematically admissible stress fields corresponding to the degree of approximation which the element should be able to recover exactly. This test is essential in demonstrating that no errors have occurred in the coding. Next, force driven problems are considered. These problems include ones for which the loading is applied purely to the boundary of the model and those for which body force fields are applied. Displacement driven problems are then considered with both non-homogeneous boundary displacements and with applied thermal strain fields.

It is considered to be of some practical importance to compare the quality of the results generated with equilibrium elements with those of conventional displacement elements. Chapter 4 attempts to present such a comparison by applying the 8-noded serendipity displacement element and the linear quadrilateral macro-element to two of the problems considered in the previous chapter.

For particular classes of problems, equilibrium elements provide a bound on the exact strain energy that compliments that given by conforming displacement elements. This property has been used to advantage in the prediction of errors in conventional conforming finite element models. In particular, a method whereby the nodal forces from a conventional finite element analysis are transformed into boundary traction distributions which hold each element in equilibrium and are co-diffusive between elements has received some attention. These traction distributions are applied in an element-by-element manner to a corresponding equilibrium element thus achieving, at comparatively little expense, a dual solution to the problem. With such a solution the exact strain energy can be bounded and an upper bound on the global error for the displacement model obtained. To date this work has only been considered for 4-noded

displacement elements where the corresponding equilibrium element is the linear stress field quadrilateral macro-element. With the availability of variable degree equilibrium elements there is scope for applying the traction distributions to elements of higher degree. This idea is explored in chapter 5 of this report.

Finally, in chapter 6 conclusions are drawn and recommendations for future work are made.

CHAPTER 2

Robust Variable Degree Equilibrium Elements

2.1 Introduction

In the introduction to this report it was argued that because of the problem of spurious kinematic modes which appear in variable degree primitive-type equilibrium elements and propagate unpredictably to the structural level there is a need to develop what have been termed robust variable degree equilibrium elements. In this chapter the theoretical development of such elements for plane, linear-elastic problems will be presented. In developing this theory a number of criteria have been borne in mind. These are:

- that the elements be robust i.e. free from the effects of spurious kinematic modes,
- that they be of variable degree polynomial stress field, and
- that standard element configurations i.e. quadrilaterals and triangles be available.

The format of this chapter is as follows. Firstly, the basic elastic relations required in the development of the theory for the element will be stated. The theory of equilibrium elements will then be developed through virtual work principles. This theory will be used to develop a triangular primitive-type element - the basic element from which macro-elements will be assembled. A note on the causes of spurious kinematic modes will then be given for the triangular primitive. The primitive elements are then assembled into macro-elements of triangular and quadrilateral format and the way in which the spurious kinematic modes present in the primitive elements propagate to these macros and the way in which the effect of these modes is eliminated is discussed.

2.2 EQUATIONS OF ELASTICITY

The equations of plane linear-elasticity necessary for the development of the equilibrium element are stated in this section. Derivation of these equations may be found in any standard text - see for example [9].

2.2.1 EQUILIBRIUM OF FORCES

The equations of equilibrium within a domain are determined by considering the equilibrium of an infinitesimal domain as shown in figure 2.1. The three components of stress vary across this domain as shown and the shear stresses are defined so as to satisfy rotational equilibrium.

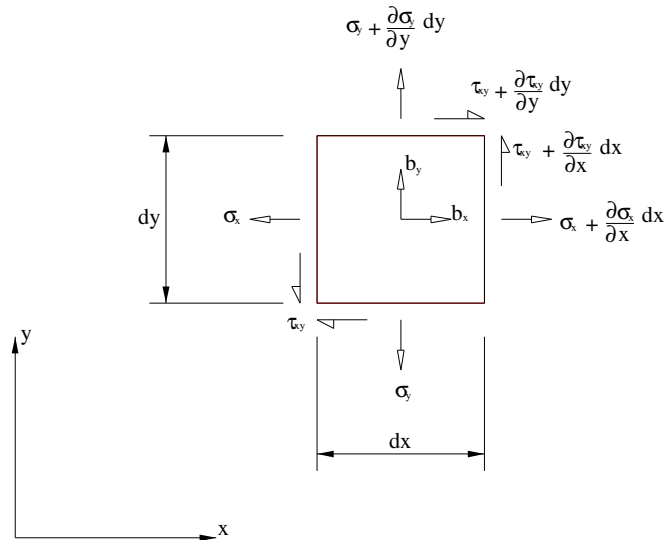


Figure 2.1 Equilibrium in the domain

Enforcing transitional equilibrium between the stresses and body forces leads to the following equations:

$$\partial^T \boldsymbol{\sigma} = -\mathbf{b} \quad (2.1)$$

where $\partial^T = \begin{bmatrix} \frac{\partial}{\partial x} & 0 & \frac{\partial}{\partial y} \\ 0 & \frac{\partial}{\partial y} & \frac{\partial}{\partial x} \end{bmatrix}$, $\boldsymbol{\sigma} = \begin{Bmatrix} \sigma_x \\ \sigma_y \\ \tau_{xy} \end{Bmatrix}$ and $\mathbf{b} = \begin{Bmatrix} b_x \\ b_y \end{Bmatrix}$.

Equilibrium on the boundary is achieved if the normal and tangential tractions, t_n and t_t respectively, are in equilibrium with the stresses emerging at the boundary. Figure 2.2 shows a portion of the boundary and the components of stress which act upon it.

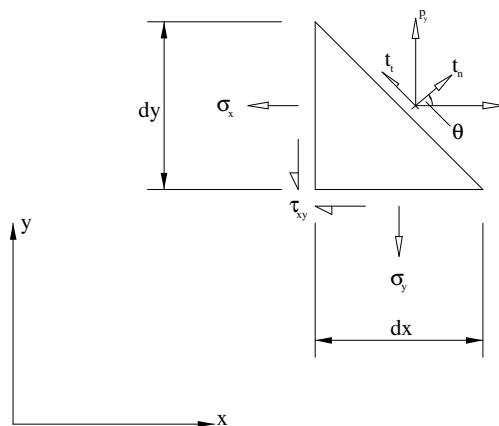


Figure 2.2 Equilibrium on the boundary

Equilibrium between the boundary tractions \mathbf{t} and the internal stresses $\boldsymbol{\sigma}$ is written as:

$$\mathbf{t} = \mathbf{T} \boldsymbol{\sigma} \quad (2.2a)$$

where $\mathbf{T} = \begin{bmatrix} \cos^2 \theta & \sin^2 \theta & 2 \sin \theta \cos \theta \\ -\sin \theta \cos \theta & \sin \theta \cos \theta & \cos^2 \theta - \sin^2 \theta \end{bmatrix}$ and $\mathbf{t} = \begin{Bmatrix} t_n \\ t_t \end{Bmatrix}$.

Alternatively boundary equilibrium can be expressed in terms of the boundary forces \mathbf{p} and the internal stresses $\boldsymbol{\sigma}$ and is written as:

$$\mathbf{p} = (\mathbf{T} \mathbf{n}) = \begin{bmatrix} \cos \theta & 0 & \sin \theta \\ 0 & \sin \theta & \cos \theta \end{bmatrix} \quad (2.2b)$$

where \mathbf{n} is the local normal to the surface and $\mathbf{p} = \begin{Bmatrix} P_x \\ P_y \end{Bmatrix}$.

2.22 STRAIN/DISPLACEMENT RELATIONS

The strains $\boldsymbol{\epsilon}$ are formed from the gradients of the displacements \mathbf{u} as shown in figure 2.3:

$$\boldsymbol{\epsilon} = \boldsymbol{\partial} \mathbf{u} \quad (2.3)$$

where the matrix $\boldsymbol{\partial}$ is the transpose of that given in equation (2.1), the strains $\boldsymbol{\epsilon} = [\epsilon_x, \epsilon_y, \gamma_{xy}]^T$ and the displacements $\mathbf{u} = [u, v]^T$.

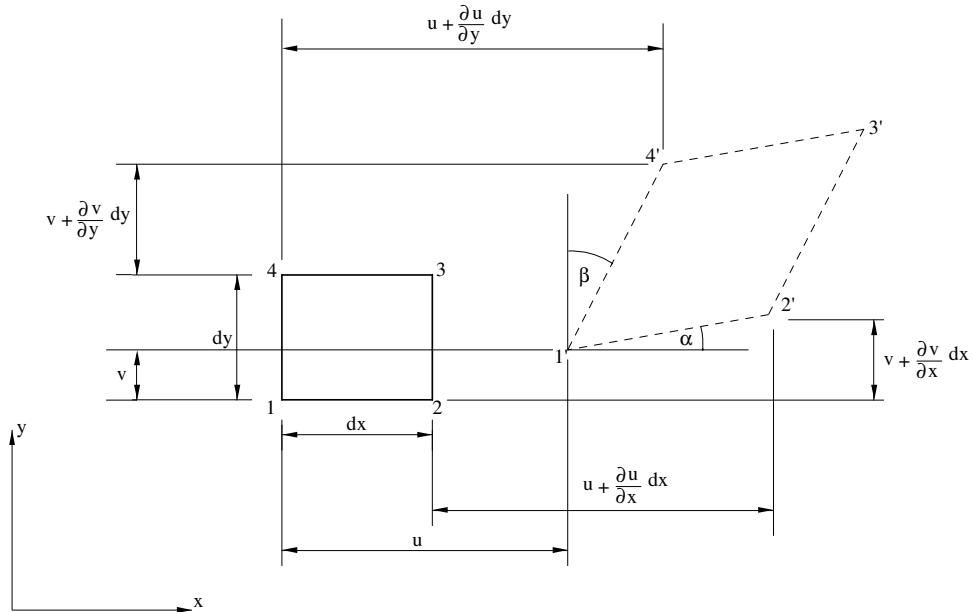


Figure 2.3 Strain/displacement derivation

2.23 Constitutive relations

The stresses $\boldsymbol{\sigma}$ are related to the strains $\boldsymbol{\varepsilon}$ through the constitutive relations for the material. These are written as:

$$\boldsymbol{\sigma} = \underset{(3 \times 3)}{\mathbf{k}} \boldsymbol{\varepsilon} \quad (2.4)$$

The nature of the coefficients of the material stiffness matrix \mathbf{k} depend on the particular constitutive relation that is chosen. In the case of plane linear-elasticity two possibilities exist namely the plane-stress and the plane-strain constitutive relations. The inverse of the material stiffness matrix is the material flexibility matrix \mathbf{f} and for the constitutive relationships considered the coefficients in the \mathbf{k} and \mathbf{f} matrices are:

For plane-stress:

$$\mathbf{k} = \frac{E}{1-\nu^2} \begin{bmatrix} 1 & \nu & 0 \\ \nu & 1 & 0 \\ 0 & 0 & \frac{1-\nu}{2} \end{bmatrix} \quad \mathbf{f} = \frac{1}{E} \begin{bmatrix} 1 & -\nu & 0 \\ -\nu & 1 & 0 \\ 0 & 0 & 2(\nu+1) \end{bmatrix} \quad (2.5a)$$

For plane-strain:

$$\mathbf{k} = \frac{E}{(1+\nu)(1-2\nu)} \begin{bmatrix} (1-\nu) & \nu & 0 \\ \nu & (1-\nu) & 0 \\ 0 & 0 & \frac{1}{2}-\nu \end{bmatrix} \quad \mathbf{f} = \frac{1+\nu}{E} \begin{bmatrix} (1-\nu) & -\nu & 0 \\ -\nu & (1-\nu) & 0 \\ 0 & 0 & 2 \end{bmatrix} \quad (2.5b)$$

where E is Young's modulus and ν is Poisson's ratio.

2.24 COMPATIBILITY OF STRAINS

Arbitrarily defined stress fields have corresponding elastic strains that are generally incompatible i.e. they have no corresponding displacement field. In order that the elastic strains be compatible then they must satisfy the following relation:

$$\left[\frac{\partial^2}{\partial y^2}, \frac{\partial^2}{\partial x^2}, -\frac{\partial^2}{\partial x \partial y} \right] = 0 \quad (2.6)$$

By writing equation (2.6) in terms of the stresses and substituting the homogeneous equations of equilibrium the harmonic equation is obtained:

$$\left(\frac{\partial^2}{\partial x^2} + \frac{\partial^2}{\partial y^2}\right)(\sigma_x + \sigma_y) = 0 \quad (2.7)$$

Stress fields satisfying the harmonic equation satisfy both equilibrium and compatibility.

2.25 COORDINATE TRANSFORMATIONS

The equations of coordinate transformation for displacement and stresses are now defined. Consider two Cartesian coordinate systems (x,y) and (\hat{x},\hat{y}) as shown in figure 2.4.

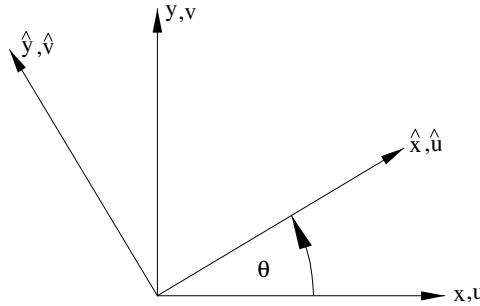


Figure 2.4 Rotation of Cartesian coordinates

The coordinate system (\hat{x}, \hat{y}) is rotated away from the system (x, y) through an angle θ . Displacement quantities transform according to the following relation:

$$\hat{\mathbf{u}} = \mathbf{R}_1 \mathbf{u} \quad (2.8)$$

(2×2)

where $\mathbf{R}_1 = \begin{bmatrix} \cos \theta & \sin \theta \\ -\sin \theta & \cos \theta \end{bmatrix}$ and $\hat{\mathbf{u}}$ are the displacements in the rotated (\hat{x}, \hat{y}) coordinate system.

Since the rotation matrix \mathbf{R}_1 is orthogonal, the inverse of equation (2.8) is simply $\mathbf{u} = \mathbf{R}_1^T \hat{\mathbf{u}}$.

Stresses transform in the following manner:

$$\hat{\boldsymbol{\sigma}} = \mathbf{R}_2 \boldsymbol{\sigma} \quad (2.9)$$

(3×3)

where $\mathbf{R}_2 = \begin{bmatrix} \cos^2 \theta & \sin^2 \theta & \sin 2\theta \\ \sin^2 \theta & \cos^2 \theta & -\sin 2\theta \\ -\frac{1}{2} \sin 2\theta & \frac{1}{2} \sin 2\theta & \cos 2\theta \end{bmatrix}$ and $\hat{\boldsymbol{\sigma}}$ are the stresses in the rotated (\hat{x}, \hat{y}) coordinate system.

Since the rotation matrix \mathbf{R}_2 is not orthogonal, the inverse of equation (2.9) is given as $\boldsymbol{\sigma} = \mathbf{R}_2^{-1} \hat{\boldsymbol{\sigma}}$.

2.3 FORMULATION FOR PRIMITIVE EQUILIBRIUM ELEMENTS

The governing equations for a primitive element are developed through the principles of virtual work. Other approaches may be used as discussed in [3,1] for example. The principle of virtual forces states that¹:

$$\int_{\Omega} \check{\boldsymbol{\sigma}}^T d\Omega = \int_{\Omega} \check{\mathbf{b}}^T \mathbf{u} d\Omega + \int_{\Gamma} \check{\mathbf{p}}^T \mathbf{u} d\Gamma \quad (2.10)$$

where all quantities are defined in the same coordinate system.

The virtual stress field $\check{\boldsymbol{\sigma}}$ is defined as the sum of two stress field i.e. $\check{\boldsymbol{\sigma}} = \check{\boldsymbol{\sigma}}_c + \check{\boldsymbol{\sigma}}_p$ such that the complimentary stress field $\check{\boldsymbol{\sigma}}_c$ satisfies the homogeneous form of the equilibrium equations and the particular solution $\check{\boldsymbol{\sigma}}_p$ is in equilibrium with the virtual body forces $\check{\mathbf{b}}$ i.e.:

$$\partial^T \check{\boldsymbol{\sigma}}_c = \mathbf{0} \quad (2.11a)$$

$$\partial^T \check{\boldsymbol{\sigma}}_p + \check{\mathbf{b}} = \mathbf{0} \quad (2.11b)$$

The virtual boundary forces $\check{\mathbf{p}}$ are defined as:

$$\check{\mathbf{p}} = (\partial^T \mathbf{n})(\check{\boldsymbol{\sigma}}_c + \check{\boldsymbol{\sigma}}_p) \quad (2.12b)$$

and thus the virtual quantities $\check{\boldsymbol{\sigma}}$, $\check{\mathbf{b}}$ and $\check{\mathbf{p}}$ form an equilibrium set. With equilibrium fulfilled the principle of virtual forces will lead to the equations of compatibility.

Equation (2.10) can now be written as:

¹All virtual quantities defined in this report are indicated with a $\check{\cdot}$ symbol.

$$\int_{\Omega} \bar{\sigma}_i^T \varepsilon \, d\Omega + \int_{\Omega} \bar{\sigma}_p^T \varepsilon \, d\Omega = - \int_{\Omega} (\partial^T \bar{\sigma}_p)^T \mathbf{u} \, d\Omega + \int_{\Gamma} \{(\partial^T \mathbf{n})(\bar{\sigma}_c + \bar{\sigma}_p)\}^T \mathbf{u} \, d\Gamma \quad (2.13)$$

The Gauss-Ostrogradski identity [10] enables the domain integrals involving the particular solution $\bar{\sigma}_p$ to be expressed as a single boundary integral:

$$\int_{\Omega} \bar{\sigma}_p^T \varepsilon \, d\Omega + \int_{\Omega} (\partial^T \bar{\sigma}_p)^T \mathbf{u} \, d\Omega = \int_{\Gamma} \{(\partial^T \mathbf{n})\bar{\sigma}_p\}^T \mathbf{u} \, d\Gamma \quad (2.14)$$

which, on substitution into equation (2.13) lead to:

$$\int_{\Omega} \bar{\sigma}_c^T \varepsilon \, d\Omega = \int_{\Gamma} \{(\partial^T \mathbf{n})\bar{\sigma}_c\}^T \mathbf{u} \, d\Gamma \quad (2.15)$$

Now let us define the strains so as to enforce the constitutive relations:

$$\varepsilon = \mathbf{f}(\sigma_c + \sigma_p) + \varepsilon_0 \quad (2.16)$$

where ε_0 are initial strains.

Substitution of equation (2.16) into equation (2.15) leads to:

$$\int_{\Omega} \bar{\sigma}_c^T \mathbf{f}\sigma_c \, d\Omega + \int_{\Omega} \bar{\sigma}_c^T \mathbf{f}\sigma_p \, d\Omega + \int_{\Omega} \bar{\sigma}_c^T \varepsilon_0 \, d\Omega = \int_{\Gamma} \{(\partial^T \mathbf{n})\bar{\sigma}_c\}^T \mathbf{u} \, d\Gamma \quad (2.17)$$

The complimentary stress field is now discretised as:

$$\sigma_c = \underset{(3 \times n)}{\mathbf{S}} \mathbf{s} \quad (2.18)$$

where the matrix \mathbf{S} contains α modes of statically admissible stress.

Substituting equations (2.18) into equations (2.17) yields:

$$\bar{s} \int_{\Omega} \mathbf{S}^T \mathbf{f}\mathbf{S} \, d\Omega \mathbf{s} + \bar{s} \int_{\Omega} \mathbf{S}^T \mathbf{f}\sigma_p \, d\Omega + \bar{s} \int_{\Omega} \mathbf{S}^T \varepsilon_0 \, d\Omega = \bar{s} \int_{\Gamma} \{(\partial^T \mathbf{n})\mathbf{S}\}^T \mathbf{u} \, d\Gamma \quad (2.19)$$

The displacements \mathbf{u} , at present defined in the same coordinate system as the stresses, are now replaced with displacements $\hat{\mathbf{u}}$ defined in a local edge coordinate system such

The displacements $\hat{\mathbf{u}}$ are discretised as:

$$\hat{\mathbf{u}} = \underset{(2 \times \beta)}{\mathbf{V}} \mathbf{v} \quad (2.21)$$

where the matrix \mathbf{V} contains β independent modes of edge displacement for the element.

Since these displacements only appear in the boundary integral they need not be defined within elements or be continuous between element edges.

$$\int_{\Omega} \mathbf{S}^T \mathbf{f} \mathbf{S} d\Omega \mathbf{s} + \int_{\Omega} \mathbf{S}^T \mathbf{f}_p d\Omega + \int_{\Omega} \mathbf{S}^T_o d\Omega = \int_{\Gamma} \{\mathbf{TS}\}^T \mathbf{V} d\Gamma \mathbf{v} \quad (2.22)$$

Equation (2.22) represents an integral form of compatibility.

The principle of virtual displacements is now used to enforce equilibrium between the tractions emerging at the boundary of an element due to the internal stress field $\boldsymbol{\sigma}$ and the applied tractions \mathbf{t} :

$$\check{\mathbf{v}} \int_{\Gamma} \mathbf{V}^T \mathbf{T} d\Gamma = \check{\mathbf{v}} \int_{\Gamma} \mathbf{V}^T \mathbf{t} d\Gamma \quad (2.23)$$

Compatibility between the virtual displacements is enforced and the resulting boundary equilibrium equations become:

$$\int_{\Gamma} \mathbf{V}^T \mathbf{TS} d\Gamma \mathbf{s} = \int_{\Gamma} \mathbf{V}^T \mathbf{t} d\Gamma - \int_{\Gamma} \mathbf{V}^T \mathbf{T}_p d\Gamma \quad (2.24)$$

Equations (2.22) and (2.24) form the governing equations for the primitive element and are written as:

$$\begin{bmatrix} -\mathbf{F} & \mathbf{D}^T \\ \mathbf{D} & \mathbf{0} \end{bmatrix} \begin{Bmatrix} \mathbf{s} \\ \mathbf{v} \end{Bmatrix} = \begin{Bmatrix} \mathbf{d} \\ \mathbf{g} \end{Bmatrix} \quad (2.25)$$

where the various symbols have the following meanings:

$$\underset{(\alpha \times \alpha)}{\mathbf{F}} = \int_{\Omega} \mathbf{S}^T \mathbf{f} \mathbf{S} d\Omega \quad \text{natural flexibility matrix} \quad (2.26a)$$

$$\underset{(\beta \times \alpha)}{\mathbf{D}} = \int_{\Gamma} \mathbf{V}^T \mathbf{TS} d\Gamma \quad \text{equations of edge equilibrium} \quad (2.26b)$$

$$\underset{(\beta \times 1)}{\mathbf{g}} = \int_{\Gamma} \mathbf{V}^T \mathbf{t} d\Gamma - \int_{\Gamma} \mathbf{V}^T \mathbf{T}_p d\Gamma \quad \text{applied edge tractions} \quad (2.26c)$$

$$\underset{(\alpha \times 1)}{\mathbf{d}} = \int_{\Omega} \mathbf{S}^T \mathbf{f}_p d\Omega + \int_{\Omega} \mathbf{S}^T_o d\Omega \quad \text{applied element deformations} \quad (2.26d)$$

Taking advantage of the positive-definite nature of the natural flexibility matrix \mathbf{F} enables the stress field amplitudes \mathbf{s} to be eliminated from equations (2.25) and leads to the following stiffness equations:

$$\mathbf{K}\mathbf{v} = \mathbf{q} \tag{2.27}$$

where $\mathbf{K} = \mathbf{D}\mathbf{F}^{-1}\mathbf{D}^T$ is the stiffness matrix for the primitive element and $\mathbf{q} = \mathbf{g} + \mathbf{D}\mathbf{F}^{-1}\mathbf{d}$.

The stress field amplitudes are recovered as:

$$\mathbf{s} = \mathbf{F}^{-1}(\mathbf{D}^T\mathbf{v} - \mathbf{d}) \tag{2.28}$$

Note that although the equations of edge equilibrium (2.24) allow an arbitrary definition of the applied tractions \mathbf{t} , for strong equilibrium they must conform (statically) with the element stress field. Kinematic boundary conditions are applied by prescribing components of the vector \mathbf{v} .

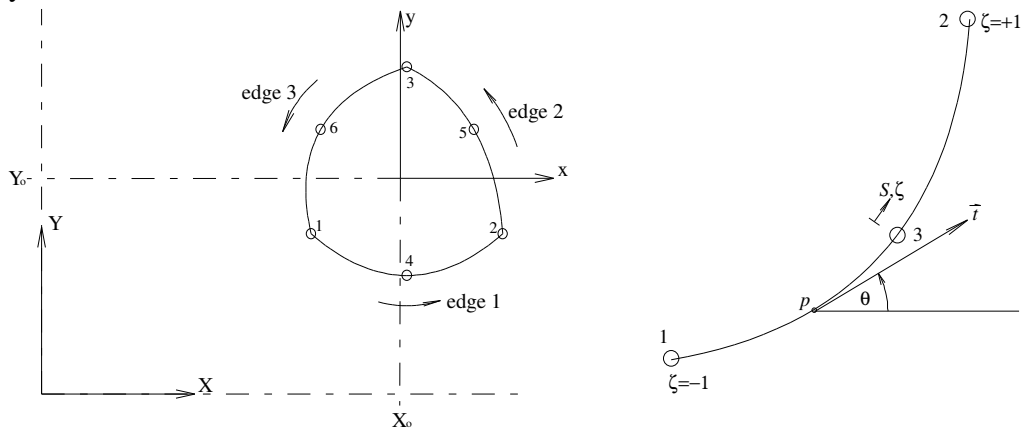
2.4 IMPLEMENTATION OF A TRIANGULAR PRIMITIVE-TYPE ELEMENT

Macro elements are formed as assemblies of triangular primitive elements. A triangular primitive element with curved edges will now be defined and is shown in figure 2.5(a).

The edges are numbered in an anti-clockwise direction as shown in the figure. Element Cartesian coordinates (x,y) are defined in terms of a global Cartesian coordinate system (X,Y) as:

$$\begin{aligned} x &= X - X_0 \\ y &= Y - Y_0 \end{aligned} \tag{2.29}$$

where X_0 and Y_0 are the co-ordinates of the origin of the element system in the global system.



(a) Element shape definition

(b) Edge shape definition

Figure 2.5 Shape definition of a primitive element

The origin of the element coordinate system is defined to lie at the mid-point of the mid-edge specifying nodes (nodes 4, 5 and 6):

$$\begin{aligned} X_o &= \frac{1}{3}(X_4 + X_5 + X_6) \\ Y_o &= \frac{1}{3}(Y_4 + Y_5 + Y_6) \end{aligned} \tag{2.30}$$

An element edge is defined as the parabola that goes through the three nodes defining the edge. The local node numbering for an edge is shown in figure 2.5(b). The shape of the element edges are defined parametrically with respect to a local edge ordinate ζ as:

$$\begin{aligned} x &= a_0 + a_1\zeta + a_2\zeta^2 \\ y &= b_0 + b_1\zeta + b_2\zeta^2 \end{aligned} \tag{2.31}$$

where the edge ordinate has its origin at the third specifying node and has values of -1 and +1 at nodes 1 and 2 respectively.

The a_i and b_i coefficients are determined by setting up and solving the following set of equations:

$$\begin{bmatrix} 1 & -1 & 1 \\ 1 & 1 & 1 \\ 1 & 0 & 0 \end{bmatrix} \begin{Bmatrix} a_0 \\ a_1 \\ a_2 \end{Bmatrix} = \begin{Bmatrix} x_1 \\ x_2 \\ x_3 \end{Bmatrix} \tag{2.32}$$

Equation (2.32) may be written as $\mathbf{M}\mathbf{a} = \mathbf{x}$ with solution \mathbf{a} being obtained by inverting the matrix \mathbf{M} which possesses an explicit inverse:

$$\mathbf{M}^{-1} = \begin{bmatrix} 0 & 0 & 1 \\ -0.5 & 0.5 & 0 \\ 0.5 & 0.5 & -1 \end{bmatrix} \quad (2.33)$$

and the coefficients \mathbf{a} and \mathbf{b} are obtained as $\mathbf{a} = \mathbf{M}^{-1}\mathbf{x}$ and $\mathbf{b} = \mathbf{M}^{-1}\mathbf{y}$ where $\mathbf{a} = [a_0, a_1, a_2]^T$, $\mathbf{b} = [b_0, b_1, b_2]^T$, $\mathbf{x} = [x_1, x_2, x_3]^T$ and $\mathbf{y} = [y_1, y_2, y_3]^T$ with x_i and y_i being the x and y coordinates of node i .

The angle θ at point p is given as:

$$\theta = \tan^{-1} \left(\frac{b_1 + 2b_2\zeta}{a_1 + 2a_2\zeta} \right) \quad (2.34)$$

Integration along an element edge is carried out in the local edge ordinate system through the following transformation:

$$\int_S dS = \int_{-1}^1 J d\zeta \quad (2.35)$$

where $\sqrt{\left(\frac{dx}{d\zeta}\right)^2 + \left(\frac{dy}{d\zeta}\right)^2}$ is the boundary Jacobian.

2.5 POLYNOMIAL APPROXIMATION

The modes of stress for the complimentary stress field σ_c are defined as columns of the matrix \mathbf{S} . Each column represents an independent mode of stress satisfying the homogeneous form of the equilibrium equations. Complete statically admissible polynomial stress fields are used and are written in the element coordinate system (x,y) . The number of independent statically admissible stress fields α for a particular degree of approximation p is given as:

$$\alpha = \sum_{i=0}^p 3 + i = \frac{1}{2}(p+1)(p+6) \quad (2.36)$$

Thus, for example, with $p=2$ the $\alpha = 12$ modes of stress would be:

$$\mathbf{S} = \begin{array}{c} \text{constant} \quad \text{linear} \quad \text{quadratic} \\ \left[\begin{array}{ccc|ccc|ccccc} 1 & 0 & 0 & x & y & 0 & 0 & x^2 & y^2 & 0 & 0 & 2xy \\ 0 & 1 & 0 & 0 & 0 & x & y & y^2 & 0 & x^2 & 2xy & 0 \\ 0 & 0 & 1 & -y & 0 & 0 & -x & -2xy & 0 & 0 & -x^2 & -y^2 \end{array} \right] \end{array} \quad (2.37)$$

The complete statically admissible stress fields for $0 \leq p \leq 10$ are given in table 2.1. In table 2.1(a) the statically and kinematically admissible stress fields for $p \leq 5$ are also given and these stress fields are plotted in figure 2.6.

The particular solution σ_p is assumed to be of the form:

$$\sigma_p = -\rho [a_x x, a_y y, 0]^T \quad (2.38)$$

where ρ is the material mass density and a_x and a_y are translational accelerations in the x and y directions respectively.

The body forces corresponding to this stress field are then:

$$\mathbf{b} = -\rho [a_x, a_y]^T \quad (2.39)$$

The modes of edge displacement $\hat{\mathbf{u}}$ are defined as columns of the matrix \mathbf{V} . Each column represents an independent mode of edge displacement. Complete polynomial displacements are used and are written in the edge coordinate system. The number of independent modes of edge displacement for a particular degree of polynomial p is given as:

$$\gamma = 2(p + 1) \quad (2.40)$$

In this report we shall restrict ourselves to considering primitive elements for which the degree of edge displacements is the same for all edges. Hence, the number of independent edge displacement variables for a triangular primitive element β is given as:

$$\beta = 3\gamma \quad (2.41)$$

Thus, for example, with $p=2$ the $\beta=18$ modes of edge displacement for the triangular primitive would be:

Degree	Statically admissible stress fields							Statically kinematically admissible stress fields						
	f_1	f_2	f_3	f_4	f_5	f_6	f_7	g_1	g_2	g_3	g_4	g_5	g_6	g_7
0	1	0	0	0	0	0	0	1	0	0	0	0	0	0
σ_x	0	1	0	0	0	0	0	0	1	0	0	0	0	0
σ_y	0	0	1	0	0	0	0	0	0	1	0	0	0	0
τ_{xy}	0	0	0	1	0	0	0	0	0	0	1	0	0	0
	f_1	f_2	f_3	f_4	f_5	f_6	f_7	g_1	g_2	g_3	g_4	g_5	g_6	g_7
1	x	y	0	0	0	0	0	x	y	0	0	0	0	0
σ_x	0	0	x	y	0	0	0	0	0	x	0	0	0	0
σ_y	0	0	0	0	x	y	0	0	0	0	x	0	0	y
τ_{xy}	-y	0	0	0	-x	0	0	-y	0	0	0	0	0	-x
	f_1	f_2	f_3	f_4	f_5	f_6	f_7	g_1	g_2	g_3	g_4	g_5	g_6	g_7
2	x^2	y^2	0	0	0	0	0	0	2xy	0	0	0	0	0
σ_x	x^2	y^2	0	0	0	0	0	0	2xy	0	0	0	0	0
σ_y	y^2	0	x^2	2xy	0	0	0	2xy	0	- x^2	0	0	0	0
τ_{xy}	-2xy	0	0	- x^2	-y ²	0	0	- x^2	-y ²	0	0	0	0	-2xy
	f_1	f_2	f_3	f_4	f_5	f_6	f_7	g_1	g_2	g_3	g_4	g_5	g_6	g_7
3	x^3	$3x^2y$	y^3	0	0	0	0	x^3	$3x^2y-2y^3$	y^3	0	0	0	0
σ_x	x^3	$3x^2y$	y^3	0	0	0	0	x^3	$3x^2y-2y^3$	y^3	0	0	0	0
σ_y	$3xy^2$	y^3	0	x^3	$3x^2y$	0	0	$3xy^2-2x^3$	y^3	- $3x^2y$	x^3	0	0	0
τ_{xy}	- $3x^2y$	- $3xy^2$	0	0	- x^3	-y ³	0	- $3x^2y$	- $3xy^2$	0	0	0	0	0
	f_1	f_2	f_3	f_4	f_5	f_6	f_7	g_1	g_2	g_3	g_4	g_5	g_6	g_7
4	0	y^4	0	- $4xy^3$	x^4	0	0	$2x^3y$	$2x^3y-4xy^3$	x^4-y^4	0	0	0	0
σ_x	0	y^4	0	- $4xy^3$	x^4	0	0	$2x^3y$	$2x^3y-4xy^3$	x^4-y^4	0	0	0	0
σ_y	x^4	0	- $4x^3y$	0	$6x^2y^2$	y^4	0	$2xy^3-4x^3y$	$2xy^3$	$6x^2y^2-2x^4$	y^4-x^4	0	0	0
τ_{xy}	0	0	x^4	y^4	- $4x^3y$	- $4xy^3$	0	$x^4-3x^2y^2$	$y^4-3x^2y^2$	- $4x^3y$	- $4xy^3$	0	0	0
	f_1	f_2	f_3	f_4	f_5	f_6	f_7	g_1	g_2	g_3	g_4	g_5	g_6	g_7
5	0	y^5	0	- $5xy^4$	x^5	0	0	x^5-5xy^4	$10x^3y^2-2y^5$	$10x^3y^2-10xy^4$	$5x^5y-y^5$	0	0	0
σ_x	0	y^5	0	- $5xy^4$	x^5	0	0	x^5-5xy^4	$10x^3y^2-2y^5$	$10x^3y^2-10xy^4$	$5x^5y-y^5$	0	0	0
σ_y	x^5	0	- $5x^4y$	0	$10x^3y^2$	y^5	0	$10x^3y^2-2x^5$	y^5-5x^4y	$5xy^4-x^5$	$10x^3y^2-10x^4y$	0	0	0
τ_{xy}	0	0	x^5	y^5	- $5x^4y$	- $5xy^4$	0	y^5-5x^4y	x^5-5xy^4	$2y^5-10x^2y^3$	$2x^5-10x^3y^3$	0	0	0

Table 2.1(a) Independent statically admissible polynomial stress fields ($0 \leq p \leq 5$)

Statically admissible stress fields

Degree	f_{σ_x}	f_{σ_y}	f_{σ_z}	$f_{\tau_{xy}}$	$f_{\tau_{yz}}$	$f_{\tau_{zx}}$	$f_{\tau_{xy}}$	$f_{\tau_{yz}}$	$f_{\tau_{zx}}$	f_{σ_x}	f_{σ_y}	f_{σ_z}	$f_{\tau_{xy}}$	$f_{\tau_{yz}}$	$f_{\tau_{zx}}$
	0	x^6	$15x^4y^2$	$20x^3y^3$	$3x^2y^4$	$6xy^5$	$15x^2y^4$	$20x^3y^3$	$3x^2y^4$	$6xy^5$	y^6				
6	x^6	$6x^4y$	$-6x^2y$	$20x^3y^3$	$3x^2y^4$	$6xy^5$	$15x^2y^4$	$20x^3y^3$	$3x^2y^4$	$6xy^5$	0	0			
	0	$-x^6$	$-13x^4y^2$	$-15x^3y^3$	$-4x^2y^4$	$-6xy^5$	$-15x^2y^4$	$-15x^3y^3$	$-4x^2y^4$	$-6xy^5$	0	0			
	f_{σ_x}	f_{σ_y}	f_{σ_z}	$f_{\tau_{xy}}$	$f_{\tau_{yz}}$	$f_{\tau_{zx}}$	$f_{\tau_{xy}}$	$f_{\tau_{yz}}$	$f_{\tau_{zx}}$	f_{σ_x}	f_{σ_y}	f_{σ_z}	$f_{\tau_{xy}}$	$f_{\tau_{yz}}$	$f_{\tau_{zx}}$
	0	x^7	x^5y	$3x^4y^2$	$3x^3y^3$	$5x^2y^4$	$5x^4y^3$	$3x^3y^4$	$3x^2y^5$	$21x^2y^5$	$7xy^6$	y^7			
7	x^7	$7x^5y$	$21x^3y^2$	$5x^2y^3$	$5x^3y^4$	$3x^2y^5$	$5x^4y^3$	$3x^3y^4$	$3x^2y^5$	$3x^2y^5$	0	0			
	0	$-x^7$	$-7x^5y$	$-3x^3y^2$	$-5x^2y^3$	$-5x^3y^4$	$-5x^4y^3$	$-3x^3y^4$	$-3x^2y^5$	$-7xy^6$	$-y^7$	0			
	f_{σ_x}	f_{σ_y}	f_{σ_z}	$f_{\tau_{xy}}$	$f_{\tau_{yz}}$	$f_{\tau_{zx}}$	$f_{\tau_{xy}}$	$f_{\tau_{yz}}$	$f_{\tau_{zx}}$	f_{σ_x}	f_{σ_y}	f_{σ_z}	$f_{\tau_{xy}}$	$f_{\tau_{yz}}$	$f_{\tau_{zx}}$
	0	x^8	$28x^6y^2$	$14x^5y^3$	$2x^4y^4$	$2x^3y^5$	$4x^4y^3$	$5x^3y^4$	$5x^2y^5$	$14x^4y^3$	$28x^2y^6$	$8xy^7$	y^8		
8	x^8	$8x^6y$	$28x^4y^2$	$14x^3y^3$	$5x^2y^4$	$2xy^5$	$4x^4y^3$	$5x^3y^4$	$2x^2y^5$	$2xy^5$	y^6	0			
	0	$-x^8$	$-8x^6y$	$-7x^4y^2$	$-4x^3y^3$	$-5x^2y^4$	$-5x^4y^3$	$-4x^3y^4$	$-4x^2y^5$	$-7x^2y^5$	$-8xy^7$	$-y^8$	0		
	f_{σ_x}	f_{σ_y}	f_{σ_z}	$f_{\tau_{xy}}$	$f_{\tau_{yz}}$	$f_{\tau_{zx}}$	$f_{\tau_{xy}}$	$f_{\tau_{yz}}$	$f_{\tau_{zx}}$	f_{σ_x}	f_{σ_y}	f_{σ_z}	$f_{\tau_{xy}}$	$f_{\tau_{yz}}$	$f_{\tau_{zx}}$
	0	x^9	$36x^7y^2$	$18x^6y^3$	$6x^5y^4$	$21x^4y^5$	$21x^5y^3$	$2x^4y^4$	$3x^3y^5$	$21x^4y^3$	$36x^2y^6$	$36x^2y^6$	$9xy^8$	y^9	
9	x^9	$9x^7y$	$36x^5y^2$	$18x^4y^3$	$6x^3y^4$	$21x^2y^5$	$21x^5y^3$	$2x^4y^4$	$3x^3y^5$	$6x^2y^5$	$3xy^6$	0	0		
	0	$-x^9$	$-9x^7y$	$-12x^5y^2$	$-14x^4y^3$	$-14x^3y^4$	$-3x^2y^5$	$-3x^4y^3$	$-3x^3y^4$	$-14x^2y^5$	$-12xy^6$	$-9xy^8$	0		
	f_{σ_x}	f_{σ_y}	f_{σ_z}	$f_{\tau_{xy}}$	$f_{\tau_{yz}}$	$f_{\tau_{zx}}$	$f_{\tau_{xy}}$	$f_{\tau_{yz}}$	$f_{\tau_{zx}}$	f_{σ_x}	f_{σ_y}	f_{σ_z}	$f_{\tau_{xy}}$	$f_{\tau_{yz}}$	$f_{\tau_{zx}}$
	0	x^{10}	$45x^8y^2$	$24x^7y^3$	$6x^6y^4$	$20x^5y^5$	$20x^8y^3$	$5x^6y^4$	$42x^5y^5$	$42x^5y^5$	$28x^3y^6$	$24x^3y^6$	$45x^3y^6$	$10xy^9$	y^{10}
10	x^{10}	$10x^8y$	$45x^6y^2$	$24x^5y^3$	$28x^4y^4$	$42x^3y^5$	$20x^7y^3$	$5x^6y^4$	$20x^5y^5$	$20x^5y^5$	$6x^2y^6$	$2xy^7$	0	0	
	0	$-x^{10}$	$-10x^8y$	$-9x^6y^2$	$-16x^5y^3$	$-35x^4y^4$	$-16x^7y^3$	$-6x^6y^4$	$-35x^6y^4$	$-35x^6y^4$	$-16xy^6$	$-9x^2y^6$	$-10xy^8$	$-y^{10}$	0

Table 2.1(b) Independent statically admissible polynomial stress fields ($6 \leq p \leq 10$)

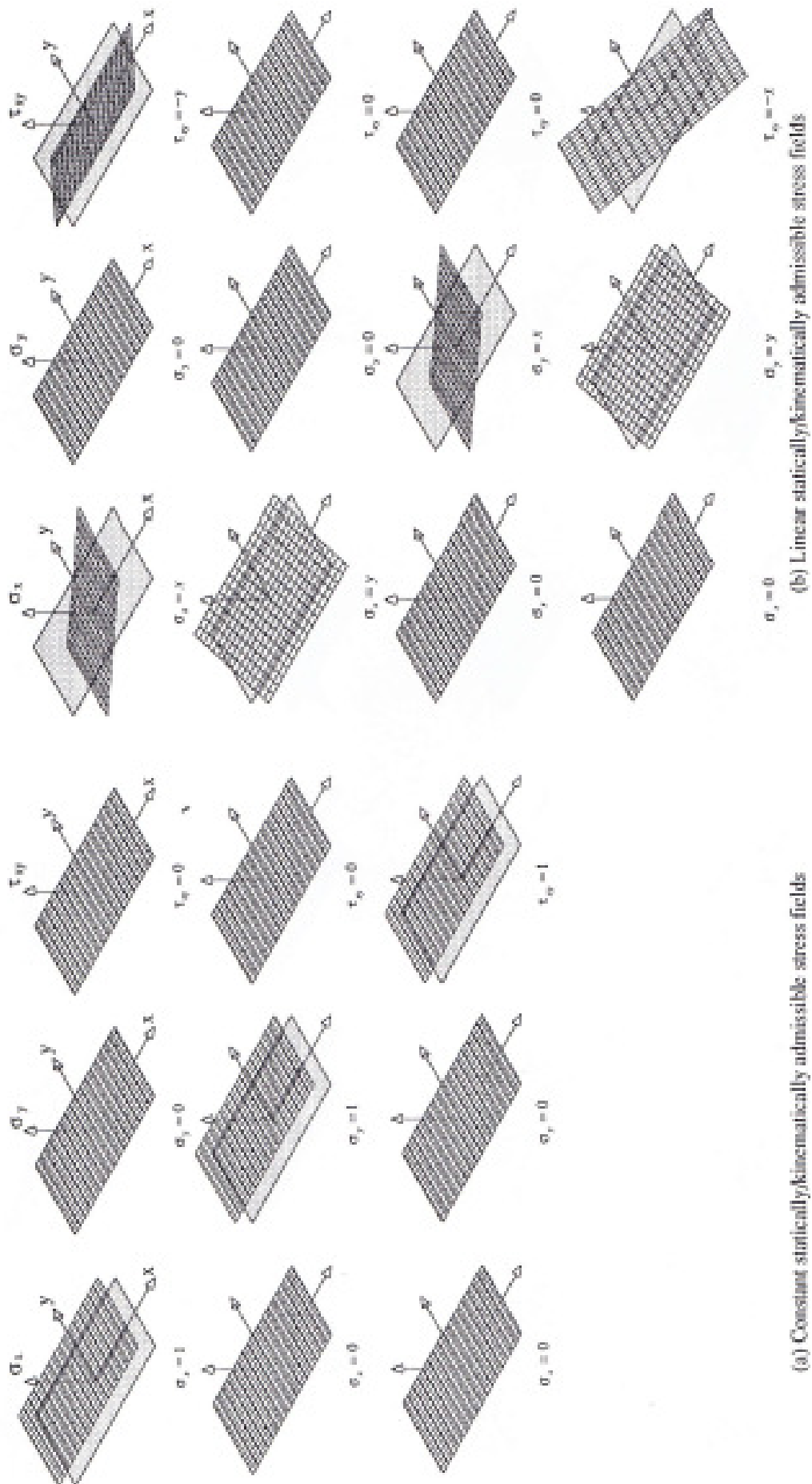


Figure 2.6(a) Constant and linear statically/kinematically admissible stress fields

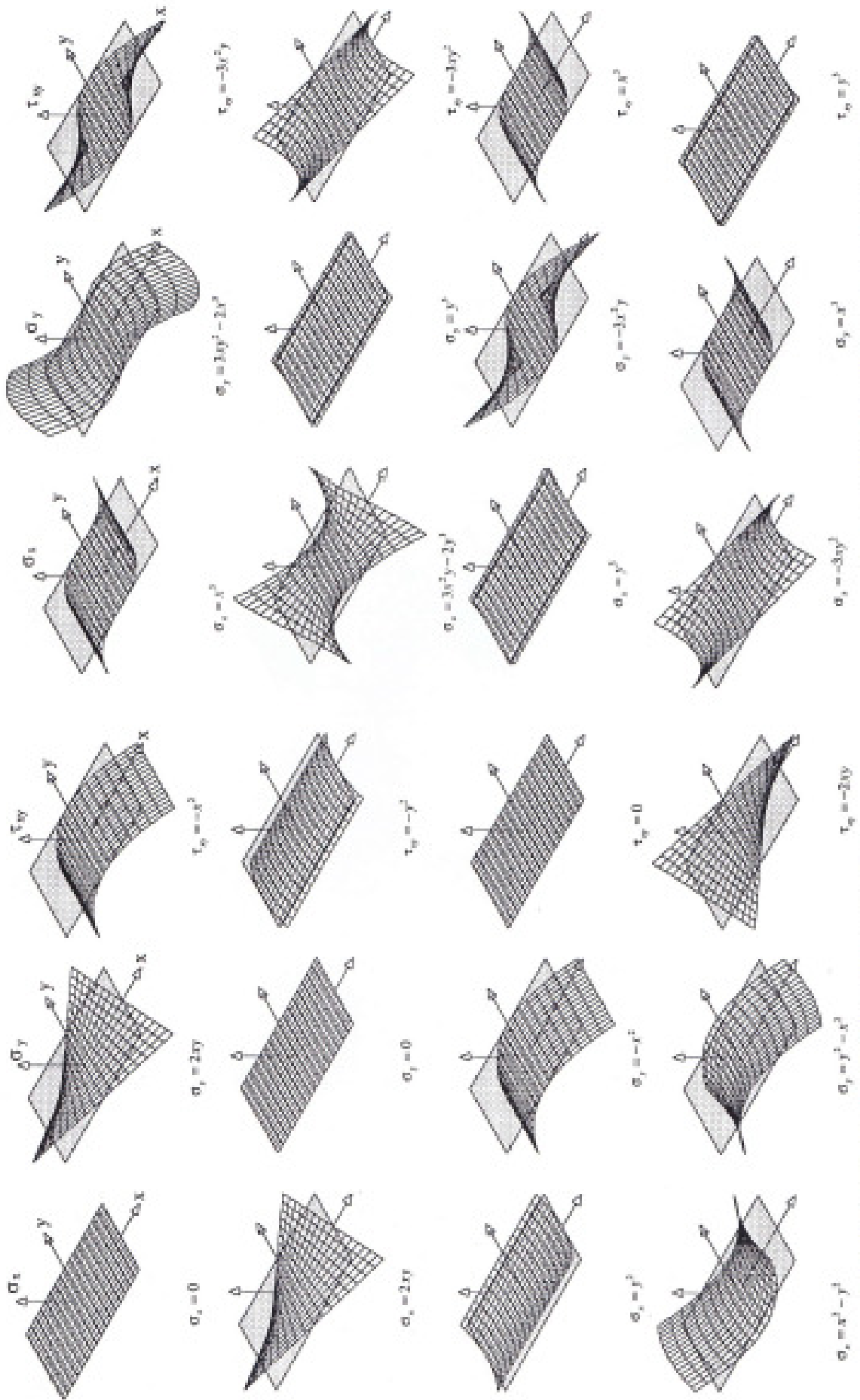
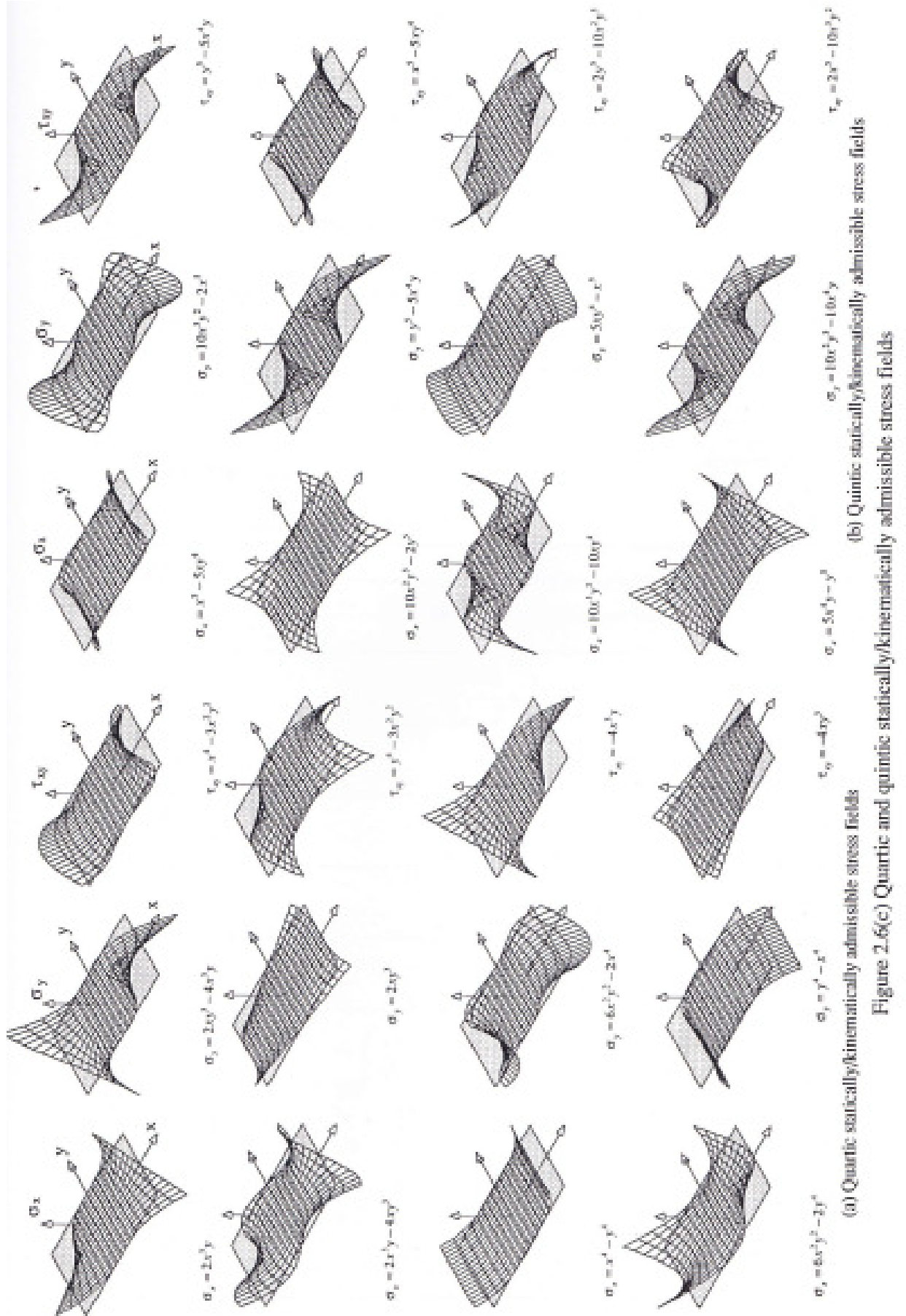


Figure 2.6(b) Quadratic and cubic statically/kinematically admissible stress fields



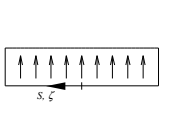
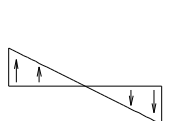
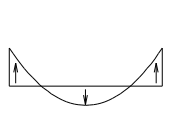
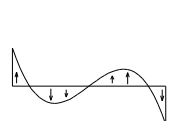
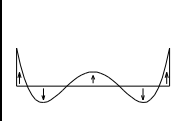
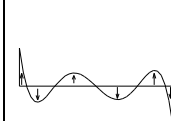
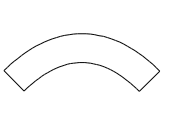
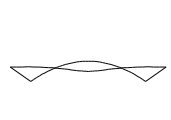
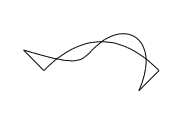
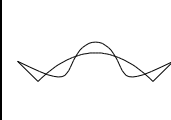
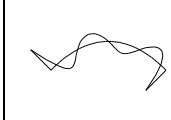
$$\mathbf{N} = \begin{bmatrix} \mathbf{N}_1 & \mathbf{0} & \mathbf{0} \\ \mathbf{0} & \mathbf{N}_2 & \mathbf{0} \\ \mathbf{0} & \mathbf{0} & \mathbf{N}_3 \end{bmatrix} \text{ where } \mathbf{N}_i = \begin{bmatrix} 1 & 0 & \zeta_i & 0 & -\frac{1}{2} + \frac{3}{2}\zeta_i^2 & 0 \\ 0 & 1 & 0 & \zeta_i & 0 & -\frac{1}{2} + \frac{3}{2}\zeta_i^2 \end{bmatrix} \quad (2.42)$$

and ζ_i is the local edge coordinate of edge i .

The complete edge displacements for $0 \leq p \leq 10$ are given in table 2.2 and for $p \leq 5$ have been plotted in figure 2.7. These modes of displacement were chosen such that $\int_s \mathbf{N}_{1,i} \mathbf{N}_{1,j} dS = 0$ when $i \neq j$ and to be unity at $\zeta = +1$.

Degree	Mode
0	1
1	ζ
2	$-\frac{1}{2} + \frac{3}{2}\zeta^2$
3	$-\frac{3}{2}\zeta + \frac{5}{2}\zeta^3$
4	$\frac{3}{8} - \frac{30}{8}\zeta^2 + \frac{35}{8}\zeta^4$
5	$\frac{15}{8}\zeta - \frac{70}{8}\zeta^3 + \frac{63}{8}\zeta^5$
6	$-\frac{5}{16} + \frac{105}{16}\zeta^2 - \frac{315}{16}\zeta^4 + \frac{231}{16}\zeta^6$
7	$\frac{35}{16}\zeta - \frac{315}{16}\zeta^3 + \frac{693}{16}\zeta^5 - \frac{429}{16}\zeta^7$
8	$\frac{32}{128} - \frac{315}{32}\zeta^2 + \frac{3465}{64}\zeta^4 - \frac{3003}{32}\zeta^6 + \frac{6435}{128}\zeta^8$
9	$-\frac{315}{128}\zeta + \frac{1155}{32}\zeta^3 - \frac{9009}{64}\zeta^5 + \frac{6435}{32}\zeta^7 - \frac{12155}{128}\zeta^9$
10	$-\frac{63}{256} + \frac{3465}{256}\zeta^2 - \frac{15015}{128}\zeta^4 + \frac{45045}{128}\zeta^6 - \frac{109395}{256}\zeta^8 + \frac{46189}{256}\zeta^{10}$

Table 2.2 Modes of edge displacement

p	0	1	2	3	4	5
S						
C						

(i) In this figure S and C denote straight and curved edges respectively

Figure 2.7 Edge displacement modes for $p \leq 5$

Finally, the initial strains $\boldsymbol{\epsilon}_0$ are defined as:

$$\boldsymbol{\epsilon}_0 = \mu \Delta T [1 \quad 1 \quad 0]^T \quad (2.43)$$

where μ is the coefficient of linear thermal expansion and ΔT the temperature of the body with respect to some (arbitrary) datum temperature.

For the elements considered in this report the degree of internal stress field will be the same as the degree of edge displacement and will be termed the *degree of approximation* for the element. For example, if $p=1$ the internal stress fields are linear and the element edge displacements are also linear.

Although integration over a triangular domain is perfectly feasible, numerical integration schemes for integrands of high degree are not widely available in the literature and where such schemes do exist there is more than a little discussion as to their correctness. For this reason it has been considered convenient to transfer such integrals to the boundary of an element and to then integrate numerically using a one-dimensional Gauss quadrature scheme. This is done in the following manner:

The natural flexibility matrix \mathbf{F} was defined in equation (2.26a) as:

$$\mathbf{F} = \int_{\Omega} \mathbf{S}^T \mathbf{f} \mathbf{S} d\Omega = t \int_{x \ y} \mathbf{S}^T \mathbf{f} \mathbf{S} dx dy \quad (2.44)$$

where t is the material thickness.

The divergence theorem state that:

$$\iint_{x \ y} \left(\frac{\partial \mathbf{A}}{\partial x} + \frac{\partial \mathbf{B}}{\partial y} \right) dx dy = \int_{\Gamma} (\mathbf{A} n_x + \mathbf{B} n_y) d\Gamma \quad (2.45)$$

where n_x and n_y are direction cosines.

Choosing $\mathbf{A} = \int_x \mathbf{S}^T \mathbf{f} \mathbf{S} dx$ and $\mathbf{B} = \mathbf{0}$ (an arbitrary but convenient choice) enables equation (2.44) to be written as:

$$\mathbf{F} = t \int_x \int_y \mathbf{S}^T \mathbf{f} \mathbf{S} dx dy = t \int_{\Gamma} \left\{ \int_x \mathbf{S}^T \mathbf{f} \mathbf{S} dx \right\} \mathbf{n}_x d\Gamma = t \int_{\Gamma} \mathbf{A} \mathbf{n}_x d\Gamma \quad (2.46)$$

The matrix \mathbf{A} being termed the *primitive* of \mathbf{F} .

2. 6 SPURIOUS KINEMATIC MODES

Spurious kinematic modes and their corresponding modes of inadmissible edge traction are now discussed. Equilibrium between generalised edge tractions \mathbf{g}_i for edge i and the element stresses characterised by the vector \mathbf{s}_j for element j is written as:

$$\mathbf{D}_{i,j} \mathbf{s}_j = \mathbf{g}_i \quad (2.47)$$

($\gamma \times \alpha$)

where $\mathbf{D}_{i,j} = \int_{\Gamma} \mathbf{V}_i^T \mathbf{T}_i \mathbf{S}_j d\Gamma$.

The contragredient transformation of equation (2.47) defines compatibility between the generalised edge displacements \mathbf{v}_i for edge i and the element deformations characterised by the vector $\boldsymbol{\delta}_j$:

$$\mathbf{D}_{i,j}^T \mathbf{v}_i = \boldsymbol{\delta}_j \quad (2.48)$$

($\alpha \times \gamma$)

The matrix \mathbf{D} for a model of m elements and n edges is constructed from a knowledge of the model topology:

$$\mathbf{D}_{(n\gamma \times m\alpha)} = \begin{bmatrix} \mathbf{D}_{1,1} & \mathbf{D}_{1,2} & \cdots & \mathbf{D}_{1,m} \\ \mathbf{D}_{2,1} & & & \\ \vdots & & \ddots & \\ \mathbf{D}_{n,1} & & & \mathbf{D}_{n,m} \end{bmatrix} \quad (2.49a)$$

where, depending on the model topology, some of the $\mathbf{D}_{i,j}$ may be zero.

For a single triangular primitive element j the matrix \mathbf{D} will be:

$$\mathbf{D}_{(\beta \times \alpha)} = \begin{bmatrix} \mathbf{D}_{1,j} \\ \mathbf{D}_{2,j} \\ \mathbf{D}_{3,j} \end{bmatrix} \quad (2.49b)$$

Although the columns of \mathbf{S}_j in equation (2.47) are independent, the columns of the product $\mathbf{T}_i \mathbf{S}_j$, which represent boundary tractions, will not be - for example the tractions on an edge parallel to the x -axis of the element coordinate system will be zero for the constant mode of stress $\sigma_x = \text{constant}$. The rank of the matrix $\mathbf{D}_{i,j}$ will, therefore, be less than $\min(m\alpha, n\gamma - \vartheta)$ where ϑ is the number of permissible rigid body motions.

If, on assembly, the rank deficiencies of the individual $\mathbf{D}_{i,j}$ matrices *do not* propagate then the matrix \mathbf{D} has rank $\rho(\mathbf{D}) = \min(m\alpha, n\gamma - \vartheta)$ and considering the relative magnitudes of the dimensions of the matrix \mathbf{D} there are three distinct possibilities:

With $m\alpha > n\gamma - \vartheta$ the model is *hyper-static* possessing $n_{\text{ssm}} = m\alpha - n\gamma + \vartheta$ self-stressing modes of stress \mathbf{s} which satisfy the homogeneous form of the equilibrium equations (2.47). Self-stressing modes reside in the null-space of the matrix \mathbf{D} . To each ssm corresponds a mode of inadmissible deformation $\boldsymbol{\delta}$.

With $m\alpha = n\gamma - \vartheta$ the model is *iso-static*.

With $m\alpha < n\gamma - \vartheta$ the model is *hypo-static* possessing $n_{\text{skm}} = n\gamma - \vartheta - m\alpha$ spurious kinematic modes of edge displacement \mathbf{v} which whilst not being rigid body modes satisfy the homogeneous form of the compatibility equations (2.48). Spurious kinematic modes reside in the null-space of the matrix \mathbf{D}^T . To each skm corresponds a mode of inadmissible traction \mathbf{g} .

This situation is summarised in table 2.3.

dimensions of \mathbf{D}	description	n_{ssm}	n_{skm}
$m\alpha > n\gamma - \vartheta$	hyper-static	$m\alpha - n\gamma + \vartheta$	0
$m\alpha = n\gamma - \vartheta$	iso-static	0	0
$m\alpha < n\gamma - \vartheta$	hypo-static	0	$n\gamma - \vartheta - m\alpha$

Table 2.3 Model characteristics with $\rho(\mathbf{D}) = \min(m\alpha, n\gamma - \vartheta)$

If, on the other hand, the rank deficiencies of the individual $\mathbf{D}_{i,j}$ matrices *do* propagate then the matrix \mathbf{D} has rank $\rho(\mathbf{D}) = \min(m\alpha, n\gamma - \vartheta) - s$ where s is the rank deficiency of \mathbf{D} . In this case both n_{ssm} and n_{skm} are increased by s irrespective of the relative magnitudes of the dimensions of \mathbf{D} as summarised in table 2.4.

dimensions of \mathbf{D}	description	n_{ssm}	n_{skm}
$m\alpha > n\gamma - \vartheta$	"hyper-static"	$m\alpha - n\gamma + \vartheta + s$	s
$m\alpha = n\gamma - \vartheta$	"iso-static"	s	s
$m\alpha < n\gamma - \vartheta$	hypo-static	s	$n\gamma - \vartheta - m\alpha + s$

Table 2.4 Model characteristics with $\rho(\mathbf{D}) = \min(m\alpha, n\gamma - \vartheta) - s$

Thus it is seen that if $s \neq 0$ then self-stressing modes and spurious kinematic modes can co-exist. An example demonstrating such a case and leading to a rather curious type of convergence behaviour is shown in appendix 2 of this report.

From the definition of the primitive element stiffness matrix in equation (2.27) it is evident that whilst self-stressing modes do not appear (the stress field amplitudes having been eliminated from the problem at this stage) spurious kinematic modes and their corresponding modes of inadmissible traction do appear with the rank of the stiffness matrix being identical to the rank of the matrix \mathbf{D} . Thus the number of spurious kinematic modes for the primitive element is:

$$n_{skm} = \beta - \vartheta - \rho(\mathbf{D}) = \beta - \vartheta - \min(\alpha, \beta - \vartheta) + s \quad (2.50)$$

For the triangular primitive element the number of skm's for degree of approximation in the range $0 \leq p \leq 5$ are given in table 2.5. The number of rigid body motions ϑ is 3 for the planar problem considered in this report.

p	β	α	s	n_{skm}	n_{ssm}
0	6	3	0	0	0
1	12	7	0	2	0
2	18	12	0	3	0
3	24	18	0	3	0
4	30	25	1	3	1
5	36	33	3	3	3

Table 2.5 Triangular primitive element characteristics

Since no analytical approach for determining s is available the values in table 2.5 have been determined numerically. For degrees of approximation $p > 5$ the number of skm's seems to remain constant at 3.

2.7 ASSEMBLY OF MACRO ELEMENTS

Macro elements are assemblies of triangular primitive elements for which the effect of the spurious kinematic modes has been eliminated from the external edges of the macro. Triangular and quadrilateral macros built up from three and four triangular primitives respectively as shown in figure 2.8 will be considered in this report.

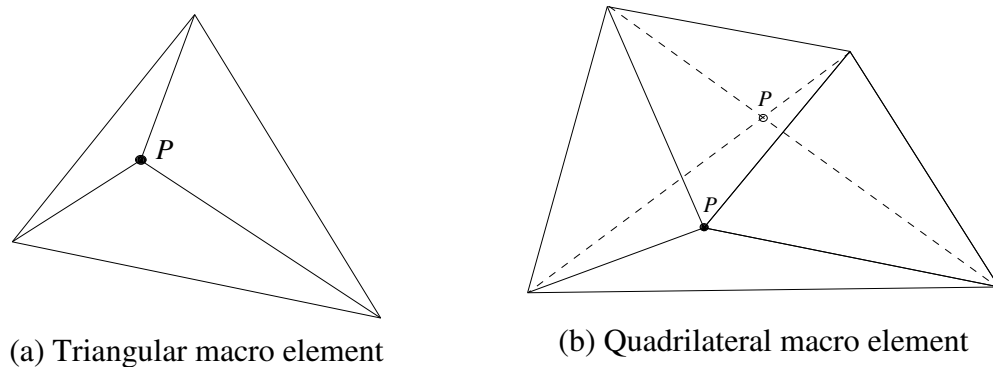


Figure 2.8 Two macro elements

Assembly of equilibrium elements is carried out in a manner similar to that used for displacement elements i.e. equilibrium of edge tractions and continuity of edge displacements is enforced at element interfaces. The assembled stiffness equations for the macro element are written as:

$$\begin{bmatrix} \mathbf{K}_{11} & \mathbf{K}_{12} \\ \mathbf{K}_{21} & \mathbf{K}_{22} \end{bmatrix} \begin{Bmatrix} \mathbf{v}_e \\ \mathbf{v}_i \end{Bmatrix} = \begin{Bmatrix} \mathbf{q}_e \\ \mathbf{q}_i \end{Bmatrix} \quad (2.51)$$

These equations have been partitioned into those involving modes of edge displacement of the internal edges \mathbf{v}_i and those involving modes of displacement of the external edges \mathbf{v}_e .

Condensing out the internal degrees of freedom leads to the following reduced set of equations in which only the external degrees of freedom remain as unknowns:

$$\mathbf{K}_m \mathbf{v}_e = \mathbf{q}_m \quad (2.52)$$

where $\mathbf{K}_m = \mathbf{K}_{11} - \mathbf{K}_{12} \mathbf{K}_{22}^{-1} \mathbf{K}_{21}$ is the stiffness matrix for the macro element and $\mathbf{q}_m = \mathbf{q}_e - \mathbf{K}_{12} \mathbf{K}_{22}^{-1} \mathbf{q}_i$.

The internal degrees of freedom are recovered after solving for the external degrees of freedom in the following manner:

$$\mathbf{v}_i = \mathbf{K}_{22}^{-1} (\mathbf{q}_i - \mathbf{K}_{21} \mathbf{v}_e) \quad (2.52)$$

If, as will be shown to be the case at least for the quadrilateral macro element, the spurious kinematic modes present in the primitives elements propagate, the matrix \mathbf{K}_{22} will be singular. In such cases the inverse of this matrix is replaced by its pseudo-inverse \mathbf{K}_{22}^* in the above assemble process. In order to construct \mathbf{K}_{22}^* *a priori* knowledge of the number and nature of spurious kinematic modes affecting the macro-element is required. Again, in the absence of any proof, numerical evidence is used and will be described in the following section.

A pseudo-inverse \mathbf{K}_{22}^* is obtained by performing singular value decomposition [11] on the matrix \mathbf{K}_{22} and leads to:

$$\mathbf{K}_{22} = \underset{(\Delta \times \Delta)}{\mathbf{U}} \underset{(\Delta \times \Delta)}{\mathbf{W}} \mathbf{V}^T \quad (2.54)$$

where $\Delta = \beta / 2$ and is the number of internal edge variables for the macro element.

The matrices \mathbf{U} and \mathbf{V} are each orthogonal and \mathbf{W} is a diagonal matrix in which the coefficients are the eigenvalues of the matrix $\mathbf{K}_{22}^T \mathbf{K}_{22}$. Equation (2.54) may be partitioned into:

$$\underset{(\Delta \times \Delta)}{\mathbf{U}} \mathbf{W} \mathbf{V}^T = [\underset{(\Delta \times \Delta)}{\mathbf{U}_1}, \underset{(\Delta \times \Delta - n_{skm})}{\mathbf{U}_2}] \begin{bmatrix} \underset{(\Delta \times \Delta - n_{skm})}{\mathbf{W}_1} & \mathbf{0} \\ \mathbf{0} & \mathbf{0} \end{bmatrix} \begin{bmatrix} \underset{(\Delta - n_{skm} \times \Delta)}{\mathbf{V}_1} \\ \mathbf{V}_2 \end{bmatrix}^T = \underset{(\Delta \times \Delta - n_{skm})}{\mathbf{U}_1} \underset{(\Delta - n_{skm} \times \Delta)}{\mathbf{W}_1} \underset{(\Delta - n_{skm} \times \Delta)}{\mathbf{V}_1}^T \quad (2.55)$$

A pseudo-inverse is now constructed as:

$$\mathbf{K}_{22}^* = \mathbf{V}_1 \mathbf{W}_1^{-1} \mathbf{U}_1^T \quad (2.56)$$

($\Delta \times \Delta$)

If the number of spurious kinematic modes is not known *a priori* then, provided the condition of the remaining equations is good, they can be detected by defining a (arbitrarily) small tolerance and checking the diagonal entries of the matrix \mathbf{W} against this tolerance. This, in effect, is the procedure adopted at the I.S.T. for obtaining solutions to meshes of primitive elements for which the spurious kinematic modes are not explicitly controlled. If, however, the remaining equations have poor condition then this procedure becomes prone to error since the distinction between dependent equations due to spurious kinematic modes and those due to ill-conditioning becomes 'fuzzy'.

2.8 SPURIOUS KINEMATIC MODES IN MACRO ELEMENTS

In this section numerical evidence regarding the number and nature of spurious kinematic modes in the macro elements is presented.

1) Triangular macro element

Numerical evidence confirms previous experience [12] that for this element there are no spurious kinematic modes irrespective of the position of the assembly point P and the degree of approximation p . With α and β now defined for the triangular macro the characteristic numbers are as shown in table 2.6.

p	β	α	s	n_{skm}	n_{ssm}
0	12	9	0	0	0
1	24	21	0	0	0
2	36	36	0	0	3
3	48	54	0	0	9
4	60	75	0	0	18
5	72	99	0	0	30

Table 2.6 Triangular macro element characteristics

For degree of approximation $p > 5$ the number of spurious kinematic modes appears to remain constant at zero.

2) Quadrilateral macro element

Numerical evidence confirms that for this element the number and nature of the spurious kinematic modes are dependent on both the position of the assembly point P and on the degree of approximation p [8]. The following findings are reported.

For the case of linear stress fields ($p=1$) there is always one spurious kinematic mode irrespective of the position of the assembly point. However, only when the assembly point lies at the intersection of the diagonals (the dashed line in figure 2.8) does the spurious kinematic mode become 'internal' to the macro i.e. only involving displacements of internal edges. Such modes are described as benign. For other positions of this point the spurious kinematic mode involves displacements of both internal and external edges and such modes are described as malignant. For degrees of approximation greater than linear ($p>1$) the situation changes. Now there is a single benign spurious kinematic mode when P lies at the intersection of the diagonals and no spurious kinematic modes for other positions of this point. The number and nature of spurious kinematic modes for the quadrilateral macro element are recorded in table 2.7.

			P at intersection of diagonals			P not at intersection of diagonals		
p	β	α	s	n_{skm}	n_{ssm}	s	n_{skm}	n_{ssm}
0	16	12	0	1	0	0	1	0
1	32	28	0	1	0	0	1	0
2	48	48	1	1	4	0	0	3
3	64	72	1	1	12	0	0	11
4	80	100	1	1	24	0	0	23
5	96	132	1	1	40	0	0	39

Table 2.7 Quadrilateral macro element characteristics

The shaded box in the table highlights the single case where the spurious kinematic mode is malignant. For degree of approximation $p>5$ the number of spurious kinematic modes remains constant at 1 for P at the intersection and 0 for all other positions.

Thus the prediction of Maunder and Almeida that for $p>2$ the number and nature of spurious kinematic modes remains the same as that for the case of $p=2$ is confirmed.

The nature of the spurious kinematic modes for the quadrilateral macro element is illustrated in figure 2.9 where a problem of uniform compression is analysed with a single quadrilateral macro. Four configurations of assembly point position and degree of approximation are considered as shown in the figure. For each of the four cases the true solution in stress is recovered. However, as figure 2.9 clearly demonstrates, the solution

in displacement is highly dependent on the position of the assembly point and on the degree of approximation. It should be noted with respect to the displacements that although equilibrium models generally give discontinuous edge displacements, for this particular case in which the exact solution is a constant stress field, any degree of approximation greater than constant ($p=0$) will result in edge displacements that are continuous unless affected by spurious kinematic modes.

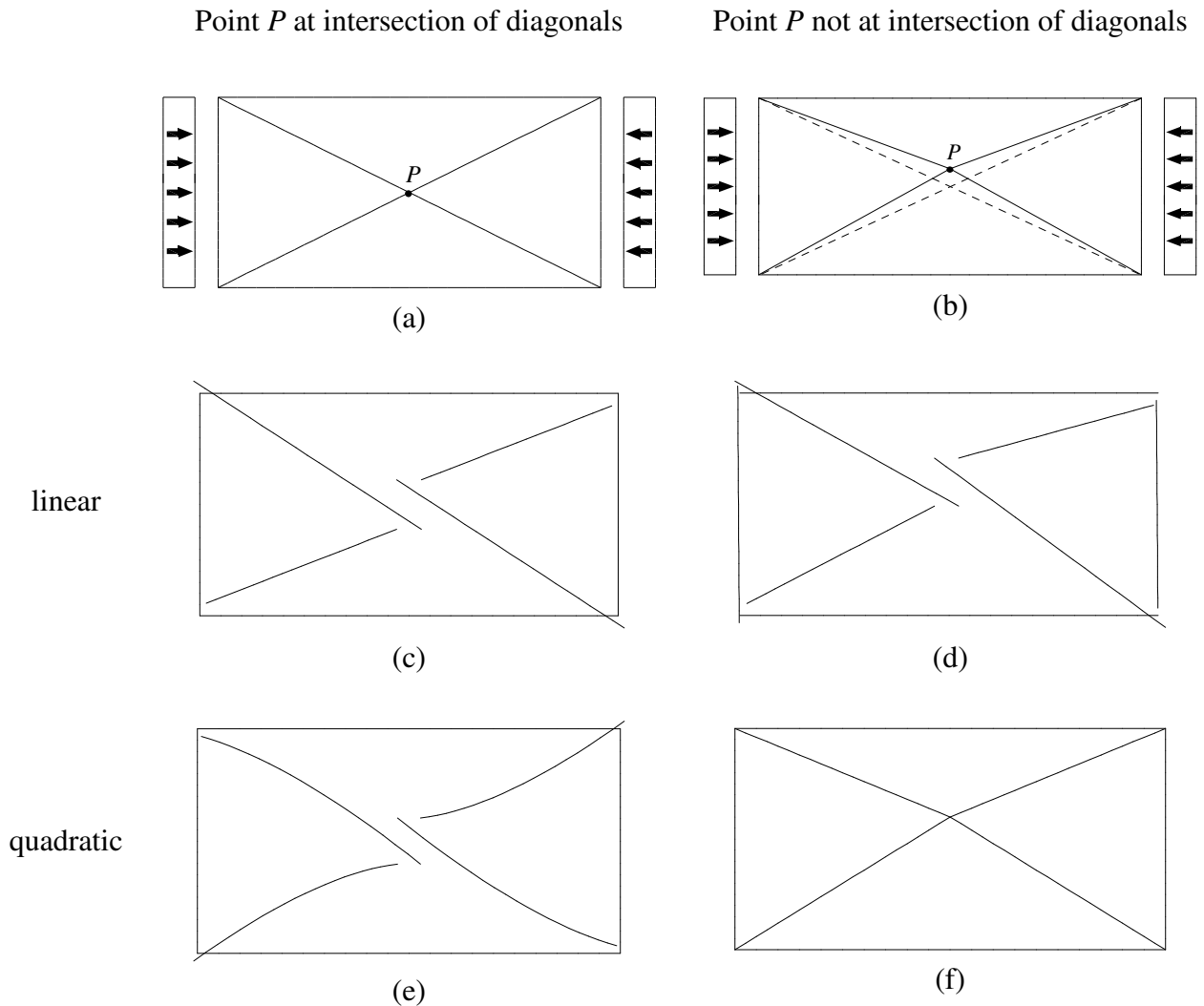


Figure 2.9 Displaced shapes for single macro-type element problem

Let us consider each case in turn.

1) P at intersection of diagonals and $p=1$: For this case the single spurious kinematic mode is benign and affects only internal edges of the macro. This is clearly seen in the displaced shape of figure 2.9(c) where, whilst the external edges show exact displacements, the displacements of internal edges are strongly affected by the presence of the spurious kinematic mode.

2) P not at intersection of diagonals and $p=1$: For this case the single spurious kinematic mode affects both internal and external edges of the macro. This is clearly demonstrated in figure 2.9(d). This spurious kinematic mode could propagate to neighbouring elements in a mesh of such macros and is therefore unacceptable.

3) P at intersection of diagonals and $p>1$: For this case the single spurious kinematic mode affects only the internal edges. This case is demonstrated for $p=2$ in figure 2.9(e).

4) P not at intersection of diagonals and $p>1$: For this case there is no spurious kinematic mode as shown in figure 2.9(f).

Thus, provided the assembly point P is placed at the intersection of the diagonals for the case of linear degree of approximation, the quadrilateral macro element can be used safe in the knowledge that any spurious kinematic modes present in the macro are internal to it and, therefore, meshes constructed of such elements will be free from the effects of spurious kinematic modes.

The figure shown on the title page of this report shows the deformed shape for a single rectangular macro element under uniform compression. A cubic degree of approximation is used with the assembly point at the intersection of the diagonals and the single benign spurious kinematic mode affecting only the internal edges is clearly visible. To clarify that the amplitude of the spurious kinematic mode is arbitrary, figure 2.10 illustrates different amplitudes for the figure given on the title page.

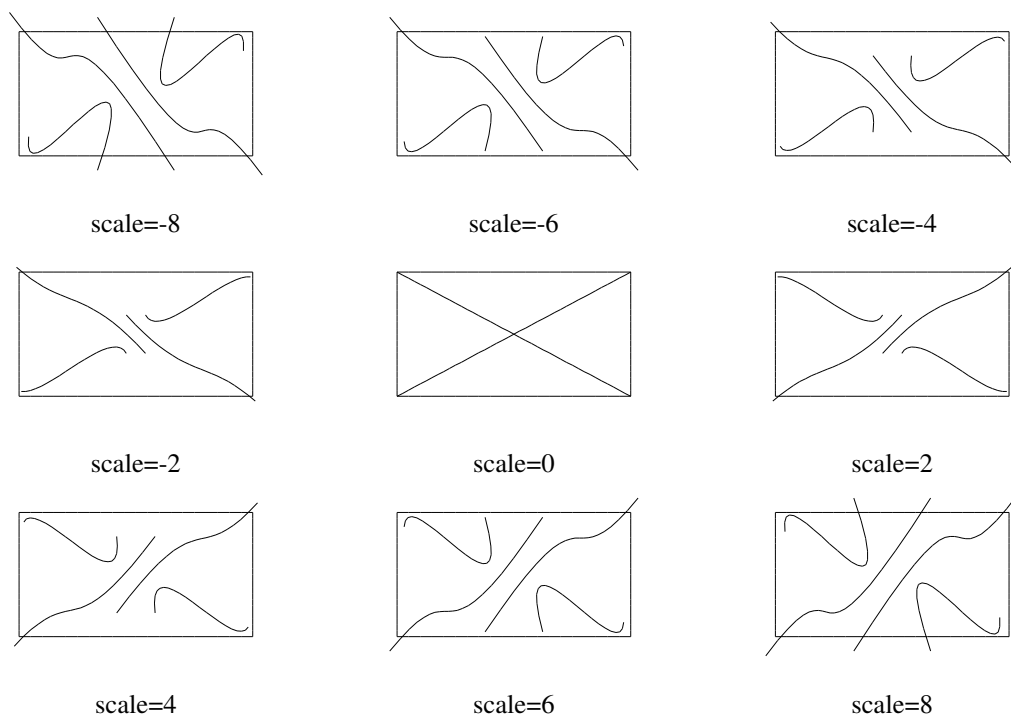


Figure 2.10 Effect of varying the amplitude of the spurious kinematic mode for $p=3$

CHAPTER 3

Application of Robust Variable Degree Equilibrium Elements

3.1 INTRODUCTION

In the previous chapter numerical evidence was presented confirming that both triangular and quadrilateral macro elements of high degree can be formulated in such a manner so as to eliminate the problems associated with spurious kinematic modes. Thus robust variable degree equilibrium elements are now available for practical analysis. It falls to this chapter to demonstrate how these elements perform. In order to do this a finite element program incorporating the two macro elements has been written. The program enables arbitrary meshes with degree of approximation in the range $0 \leq p \leq 10$ to be analysed. Details of the program are given as a user guide in appendix 4 of this report.

3.2 CONFIRMATION OF PROGRAM INTEGRITY

As with any new finite element program, it is essential to confirm that no errors have crept into the code. This is done by testing that the elements can model those stress fields that are contained within the formulation. In this instance this means that all statically and kinematically admissible stress fields up to and including degree $p=10$ can be modelled exactly. Thus, rather like a conventional patch test, single elements have been tested with applied static boundary conditions. The statically and kinematically admissible stress fields shown in table 2.1 have been used on the domain shown in figure 3.1.

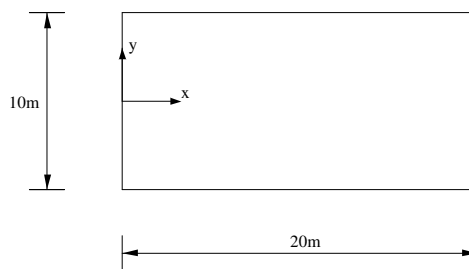


Figure 3.1 Rectangular domain for patch test

With the material and geometric properties $E = 210 \text{ N/m}^2$, $\nu = 0.3$ and $t = 0.1 \text{ m}$ the true strain energy has been evaluated. Symbolic algebra software has been used for this purpose and the true strain energy is given exactly as the ratio of two integers i.e. $U = \frac{\text{Numerator}}{\text{Denominator}}$.

The numerator and denominator for the various stress fields considered are given in table 3.1. The units are Nm.

Although only the results for degrees up to $p=5$ are shown, a similar procedure has been performed for all statically and kinematically admissible stress fields up to degree $p=10$ and the elements recover all stress fields exactly.

Stress field	Numerator	Denominator
g_1	1	21
g_2	1	21
g_3	13	105
g_4	155	21
g_5	25	63
g_6	400	63
g_7	355	21
g_8	788800	189
g_9	42925	189
g_{10}	98375	63
g_{11}	803725	189
g_{12}	138590000	49
g_{13}	6005625	49
g_{14}	61141875	49
g_{15}	22816875	49
g_{16}	511415000000	1323
g_{17}	2948515625	189
g_{18}	43947253125	49
g_{19}	68341684375	441
g_{20}	1194185052734375	3969
g_{21}	571468548828125	3969
g_{22}	811903929687500	14553
g_{23}	7574950677734375	14553

(i) The stress fields corresponding to the g_i parameters are given in table 2.1

Table 3.1 Exact strain energy as a ratio of two integers for the statically/kinematically admissible polynomial stress fields up to and including degree 5

3.3 NOTE ON DEGREES OF FREEDOM

The term *degrees of freedom* can have a number of meanings when discussing equilibrium elements:

- 1) The system of equations describing the primitive element {equation (2.16)} involves degrees of freedom associated with stress fields and edge displacements.
- 2) In obtaining a stiffness matrix for the primitive element {equation (2.18)} degrees of freedom associated with stress field amplitudes are condensed out leaving only degrees of freedom associated with edge displacements.
- 3) In the assembly of macro-elements the degrees of freedom associated with internal edges are condensed out leaving a system of equations written in terms of the degrees of freedom of the external edges {equation (2.46)}.
- 4) Finally, on assembly of macro-elements into a mesh of such elements, degrees of freedom associated with duplicated edges are condensed out leaving a set of structural equations with the number of degrees of freedom equal to the sum of the number of degrees of freedom associated with each edge.

In 1,2 and 3 above the condensation of degrees of freedom takes place at the primitive or macro-element level. These condensations can therefore be considered as part of the effort required in forming a stiffness matrix for the macro element. The effort required in solving a mesh of macro-elements will be approximately proportional to the square of the number of degrees of freedom in the structural equations.

For a mesh of macro-elements the following numbers of degrees of freedom are defined:

- n_{σ} - total number of stress degrees of freedom
- n_d - total number of displacement degrees of freedom
- n_d^r - reduced number of displacement degrees of freedom

3.4 NOTE ON SOLUTION BOUNDS

For linear-elastic problems in which the complimentary strain energy is equal to the strain energy (U), the total potential energy (Π) and the total complimentary potential energy (Π^*) are written as:

$$\Pi = U - W \tag{3.1a}$$

$$\Pi^* = U - W^* \tag{3.1b}$$

where $U = \frac{1}{2} \int_{\Omega} \sigma^T \epsilon d\Omega$ is the strain energy.

The work done by the applied forces W is given as:

$$W = \int_{\Gamma_t} \mathbf{t}^T \mathbf{u} \, d\Gamma_t + \int_{\Omega} \mathbf{b}^T \mathbf{u} \, d\Omega \quad (3.2a)$$

and the work done by the applied displacements W^* is given as:

$$W^* = \int_{\Omega} \boldsymbol{\sigma}^T \boldsymbol{\varepsilon}_0 \, d\Omega + \int_{\Gamma_u} \mathbf{t}^T \mathbf{u} \, d\Gamma_u \quad (3.2b)$$

where Γ_t represents the static boundary, Γ_u represents the kinematic boundary and $\Gamma = \Gamma_t \cup \Gamma_u$

The two total potential energy quantities are related in the following manner:

$$\Pi = -\Pi^* \quad (3.3)$$

The following bounds on the total potential energy and total complimentary potential energy of the conforming and equilibrium finite element models (${}^C\Pi$ and ${}^E\Pi$ respectively) hold:

$${}^C\Pi \geq \Pi \quad (3.4a)$$

$${}^E\Pi^* \geq \Pi^* \quad (3.4b)$$

Thus, for force driven problems $W^* = 0$ and:

$$U_h^C \leq U \leq U_h^E \quad (3.5a)$$

for displacement driven problems $W=0$ and:

$$U_h^E \leq U \leq U_h^C \quad (3.5b)$$

where U_h^C and U_h^E are the strain energies from conforming and equilibrating finite element models respectively.

For mixed problems $W^* \neq 0$ and $W \neq 0$ and no bounds can be placed on the strain energy. Proofs of the aforementioned statements may be found in [9] for example.

3.5 DEMONSTRATION OF PROGRAM CAPABILITY AND PERFORMANCE

Having demonstrated that the element can recover those stress fields which it should be able to, the capability and performance of the elements in a number of practical problems can now be explored. Problems that demonstrate some characteristic or other of the equilibrium element solution are chosen. Where possible problems with analytical solutions have been used but in general this has not been possible and in these cases a reference solution obtained with a refined finite element model is used. The section has been divided into four main parts depending on the nature of the applied loading:

3.5.1: Force driven problems with zero body forces

3.5.2: Force driven problems with non-zero body forces

3.5.3: Displacement driven problems with zero initial strains

3.5.4: Displacement driven problems with non-zero initial strains

In testing a variable degree element the philosophy of discretising the problem domain with the minimum number of elements sufficient to capture the geometry will be adopted. The complexity of the exact solution within the domain will, or will attempt to be recovered by escalation of the degree of approximation i.e. with p-type refinement. Two examples of h-type refinement will be given in chapter 4 where comparisons are made between equilibrium and conforming displacement elements. All problems considered in this chapter use a plane stress constitutive relationship.

3.5.1 FORCE DRIVEN PROBLEMS (ZERO BODY FORCES)

Three force driven problems are considered:

Problem 1 investigates the way in which a solution converges when the static boundary conditions are approximated. Such approximation occurs when the degree of approximation is lower than that required to equilibrate in a pointwise sense with the static boundary conditions. In this case the weak equilibrium of equation(2.24) is enforced on the static boundary. The problem chosen is one for which the true solution is of degree $p=10$.

Problem 2 demonstrates the way in which the solution varies with internal geometry of a macro-element. The number and nature of spurious kinematic modes in the quadrilateral macro-element is dependent on the position of the assembly point P and on the degree of approximation p (§2.8). In the case of a linear degree of approximation P must lie at the intersection of the diagonals in order to avoid the effects of spurious kinematic modes. Although for $p \geq 2$ the location of this point does not effect the usability of the element at least in terms of spurious kinematic modes, it should be

appreciated that the relative difference in the sizes of the triangular primitive-elements making up the quadrilateral macro increases with increasing taper and this can lead to ill-conditioning of the stiffness equations for high degrees of approximation. To avoid this the program defaults the position of the assembly point to the centroid¹ for $p \geq 2$. For $p \geq 2$ the effect of the position of the assembly point on the solution is demonstrated.

Problem 3 shows a problem which whilst having linear static boundary conditions has an internal stress field that is non-polynomial.

Problem 1: Statically and kinematically admissible stress field of degree 10

The first problem to be considered in this section is one for which the exact solution is polynomial of degree $p=10$. The problem domain is shown in figure 3.2.

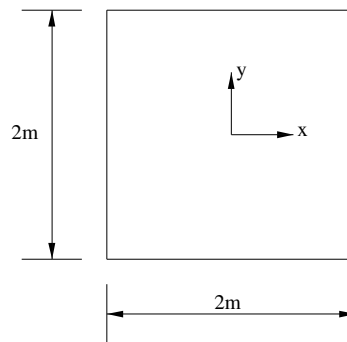


Figure 3.2 Problem 1

There are four such statically and kinematically admissible polynomial stress fields of degree $p=10$ of which the following one will be chosen:

$$\begin{aligned}
 \sigma_x &= x^{10} - 45x^8y^2 + 210x^6y^4 - 210x^4y^6 + 45x^2y^8 - y^{10} \\
 \sigma_y &= -x^{10} + 45x^8y^2 - 210x^6y^4 + 210x^4y^6 - 45x^2y^8 + y^{10} \\
 \tau_{xy} &= -10x^9y + 120x^7y^3 - 252x^5y^5 + 120x^3y^7 - 10xy^9
 \end{aligned}
 \tag{3.6}$$

The exact solution for this problem is shown in figure 3.3.

¹ The centroid is defined as the centre of mass of four unit masses placed at the vertices of the macro.

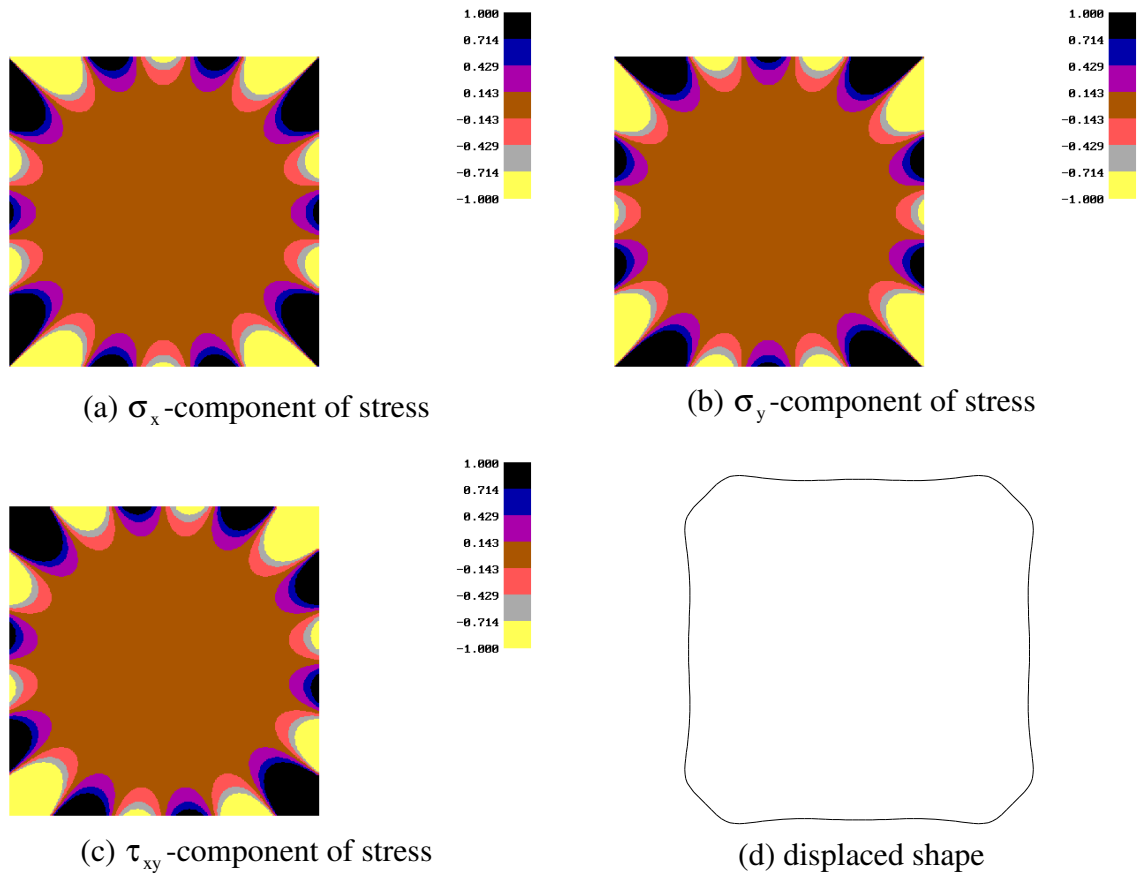


Figure 3.3 Exact solution for Problem 1.

For a Young's Modulus of $E = 10 \text{ N/m}^2$, a Poisson's ratio of $\nu = 0.3$ and a material thickness of $t = 1 \text{ m}$ the exact strain energy is:

$$U = \frac{33655808}{6839525} \approx 4.92078 \quad (3.7)$$

Using a single quadrilateral macro-type element the following finite element strain energy were recorded.

p	0	1	2	3	4	5	6	7	8	9	10
U_h	2.3695	7.7857	4.2764	10.2695	5.0698	5.8216	4.8623	4.9257	4.9206	4.9207	U

Table 3.2 Finite element strain energy for Problem 1

These values of strain energy have been plotted against the degree of approximation in figure 3.4.

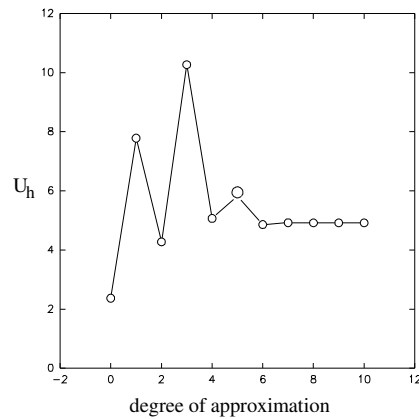
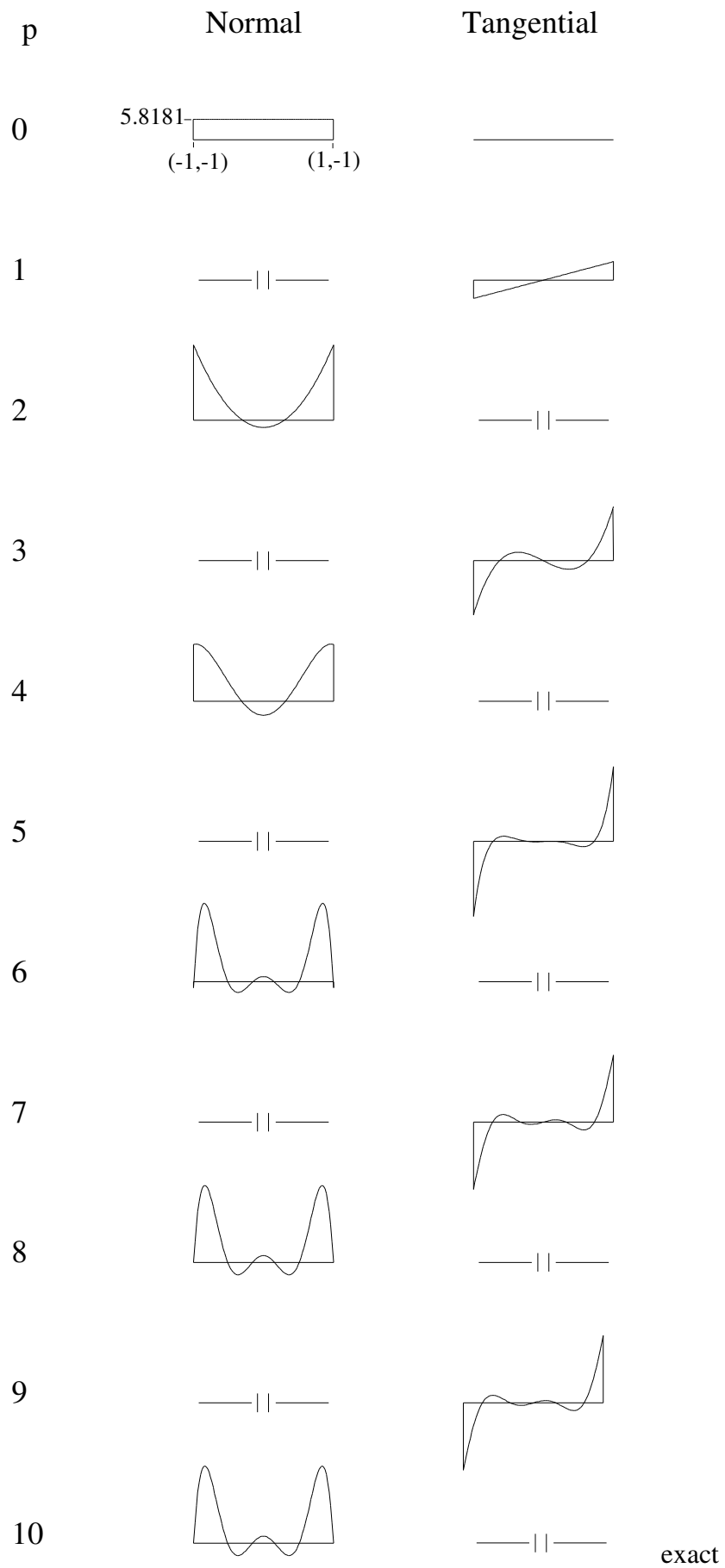


Figure 3.4 Convergence of finite element strain energy for Problem 1

The convergence shown in figure 3.4 is rather interesting in that it is oscillatory in nature. This behaviour requires some explanation. The static boundary conditions for this problem are polynomials of degree $p=10$. Thus only when the degree of approximation is of this degree can the boundary conditions be modelled exactly. For all lower degrees of approximation the exact boundary conditions are approximated weakly in the sense of equation (2.24). The exact solution for each approximate set of boundary conditions is not the same as the exact solution for the exact boundary conditions. The way in which the boundary conditions converge is shown in figure 3.5 where the normal and tangential stresses for edge $(-1,-1),(1,-1)$ have been drawn. The boundary stresses for the remaining edges can be deduced from the symmetry of the problem.

This problem demonstrates that for cases where the static boundary conditions are not enforced in a strong pointwise sense the bounded nature of the strain energy is lost.



exact

Figure 3.5 Boundary stress distributions for Problem 1

Problem 2: Tapered continuum with uniform endload

In this problem the variation of axial stress along the central axis of a tapered continuum under the action of uniform end tractions as shown in figure 3.6(a) is investigated. Results for two positions of the assembly point P will be compared. For the program developed during this research the default position for the assembly point for degrees of approximation greater than linear is the centroid i.e. $P = P_c$. For the linear case this point must be at the intersection of the diagonals i.e. $P = P_i$.

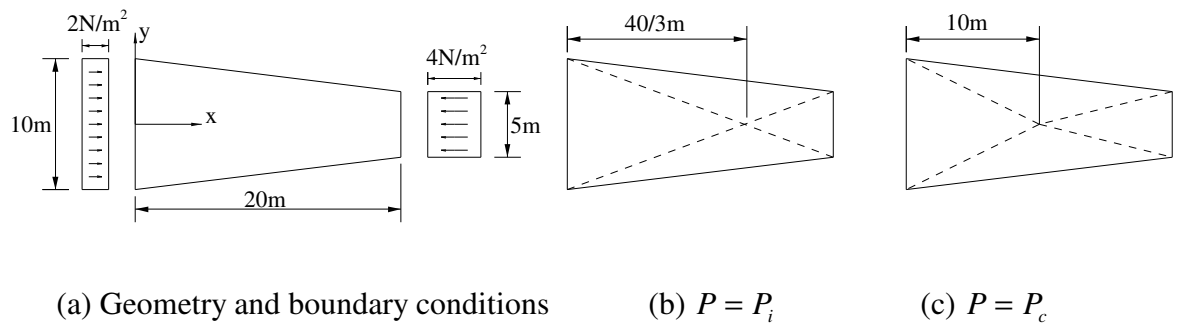


Figure 3.6 Problem 2

A Young's Modulus of $E = 1\text{N/m}^2$, a Poisson's ratio of $\nu = 0.3$ and a material thickness of $t = 1\text{m}$ will be used for this problem. A reference solution obtained by using four quadrilateral macro-type elements of degree $p=10$ is shown in figure 3.7. This reference solution was generated with P at the default position for all four elements.

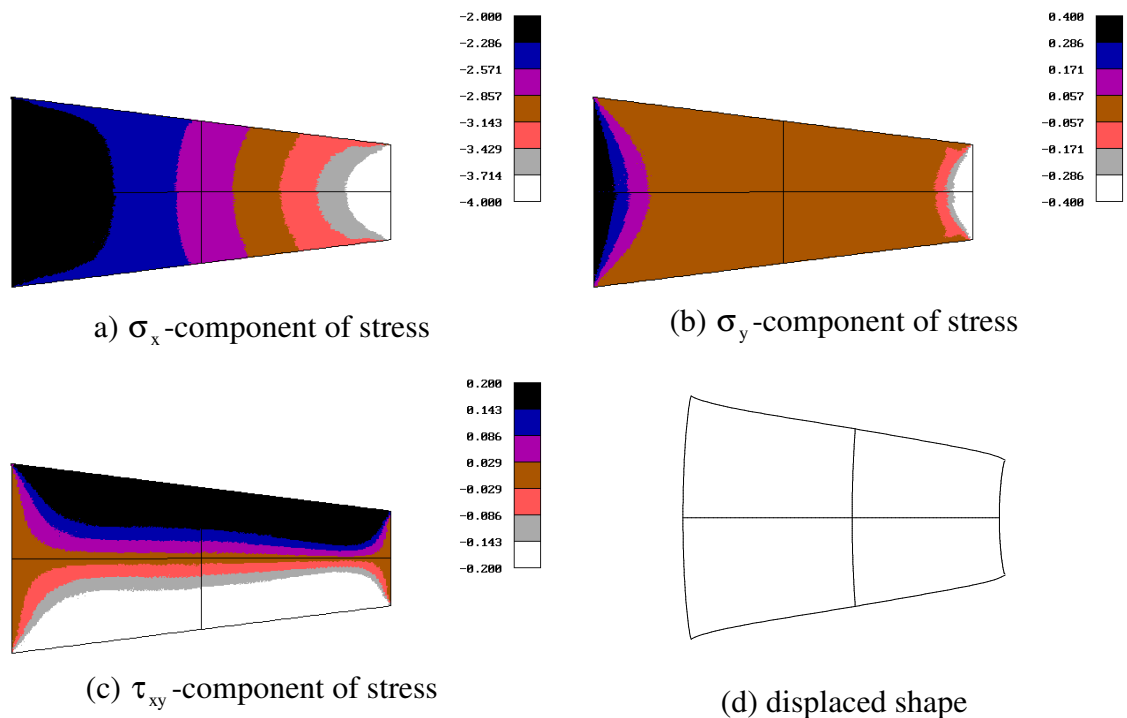


Figure 3.7 Reference solution for Problem 2 ($U_h=562.113$).

For $p=1$ the assembly point must be placed at the intersection of the diagonals (§2.8) and for this case the finite element strain energy is $U_h=576.700$.

The finite element strain energies are given in table 3.3 and have been plotted in figure 3.8.

p	2	3	4	5	6	7	8	9	10
P_i	564.133	562.604	562.308	562.223	562.174	562.149	562.134	562.125	562.108
P_c	564.967	562.877	562.384	562.241	562.183	562.155	562.138	562.128	562.121

Table 3.3 Finite element strain energy for Problem 2

Note that for $p=10$ and with P at intersection of diagonals the system of equations is ill-conditioned and the solution is therefore incorrect. Ill-conditioning is detected by comparing the results with equations that have been scaled with those that have not been scaled. If they are the same then ill-conditioning is not affecting the solution. With P at the centroid ill-conditioning does not occur when $p=10$.

It is interesting to observe that for $p \geq 2$ the strain energy obtained with $P = P_i$ is nearer to the exact value than that achieved with P at the centroid. This last statement can be made since it is known that for force driven problems the finite element strain energy for an equilibrium model is an upper bound (§3.4). The strain energies are plotted against degree of approximation in figure 3.8. It is seen that whilst the difference in the two values of strain energy is significant for low degrees of approximation (greater than linear) it decreases as the degree of approximation is increased and the exact solution is approached.

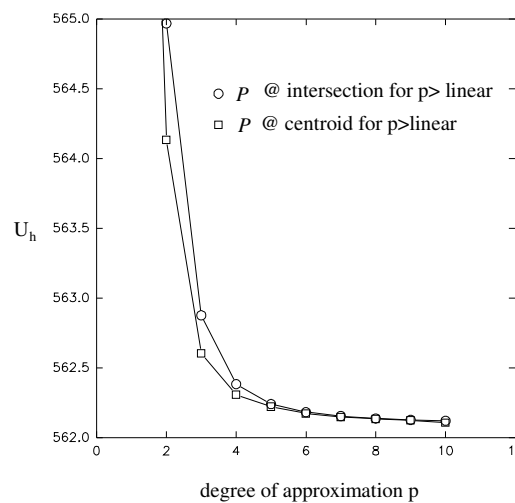


Figure 3.8 Convergence of finite element strain energy for Problem 2

The reason that the strain energy with P at the intersection of the diagonals is lower than that for P at the centroid has been explained in [8]. In this paper it is shown that the statical indeterminacy of the single quadrilateral macro-element is greater (by one) for the case where P lies at the intersection of the diagonals.

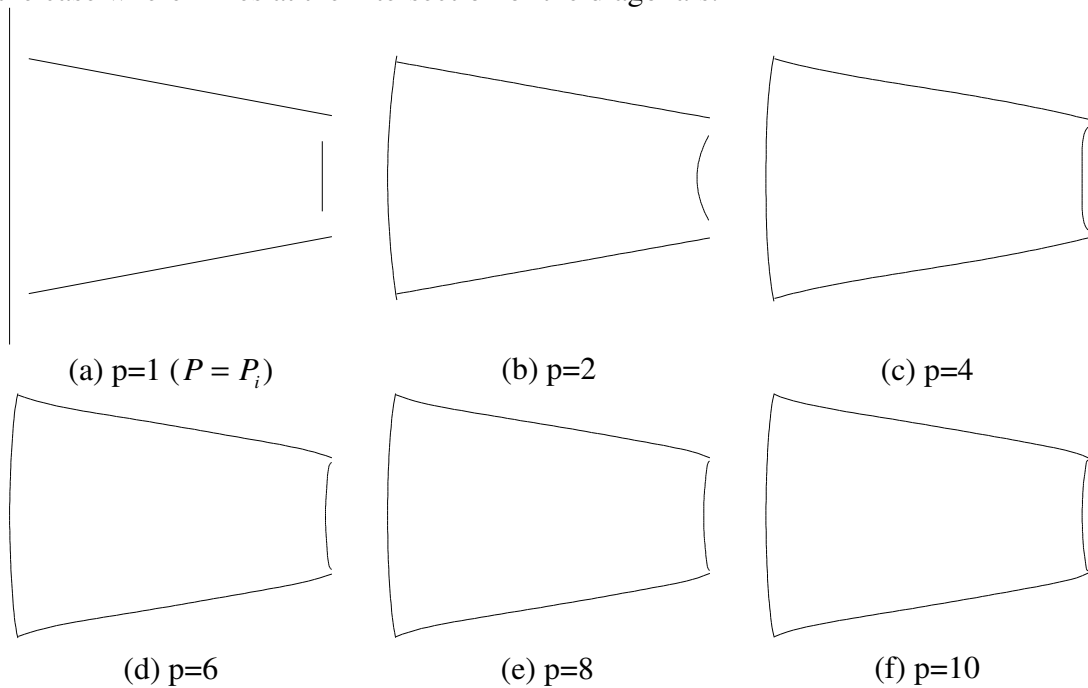


Figure 3.9 Convergence of deformed shape ($P = P_c$)

The convergence of the displaced shapes is shown in figure 3.9. This figure is for $P = P_c$ only. However, an idea of the difference in the displacements for the two positions of the assembly point can be obtained from figure 3.10 where displaced shapes for the two positions of the assembly point have been superimposed for a degree of approximation of $p=2$. It is seen that there are significant differences in the displacements on the edges $x=0$ and $x=20m$.

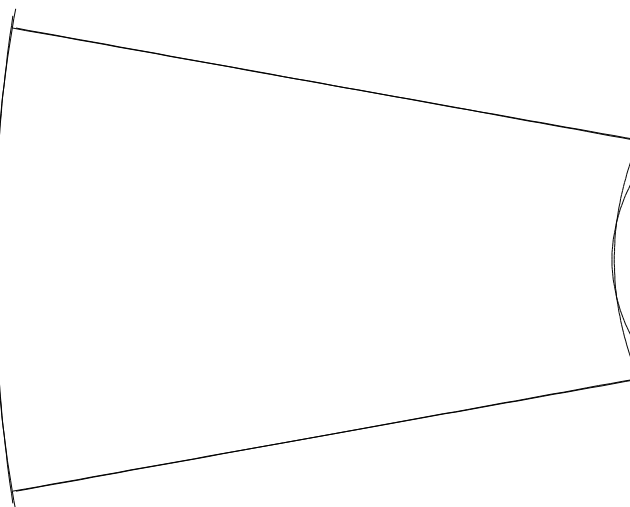


Figure 3.10 Superposition of displaced shapes for $P = P_c$ and $P = P_i$ with $p=2$

Finally, for this problem, the convergence of the axial stress (σ_x) along the centre-line of the model is shown in figure 3.13. It is seen from this figure that for low degrees of approximation significant discontinuities exist in this stress at the assembly point and that there is still an observable if small discontinuity for $p=10$. The reference solution is drawn in the $p=1$ figure for comparison purposes. For the $p=2$ figure the distributions for both assembly point positions are given and it is seen that the improvement in strain energy noted with P at the intersection of the diagonals is reflected in the distribution of axial stress for which the discontinuity at this point is smaller than that occurring with P at the centroid.

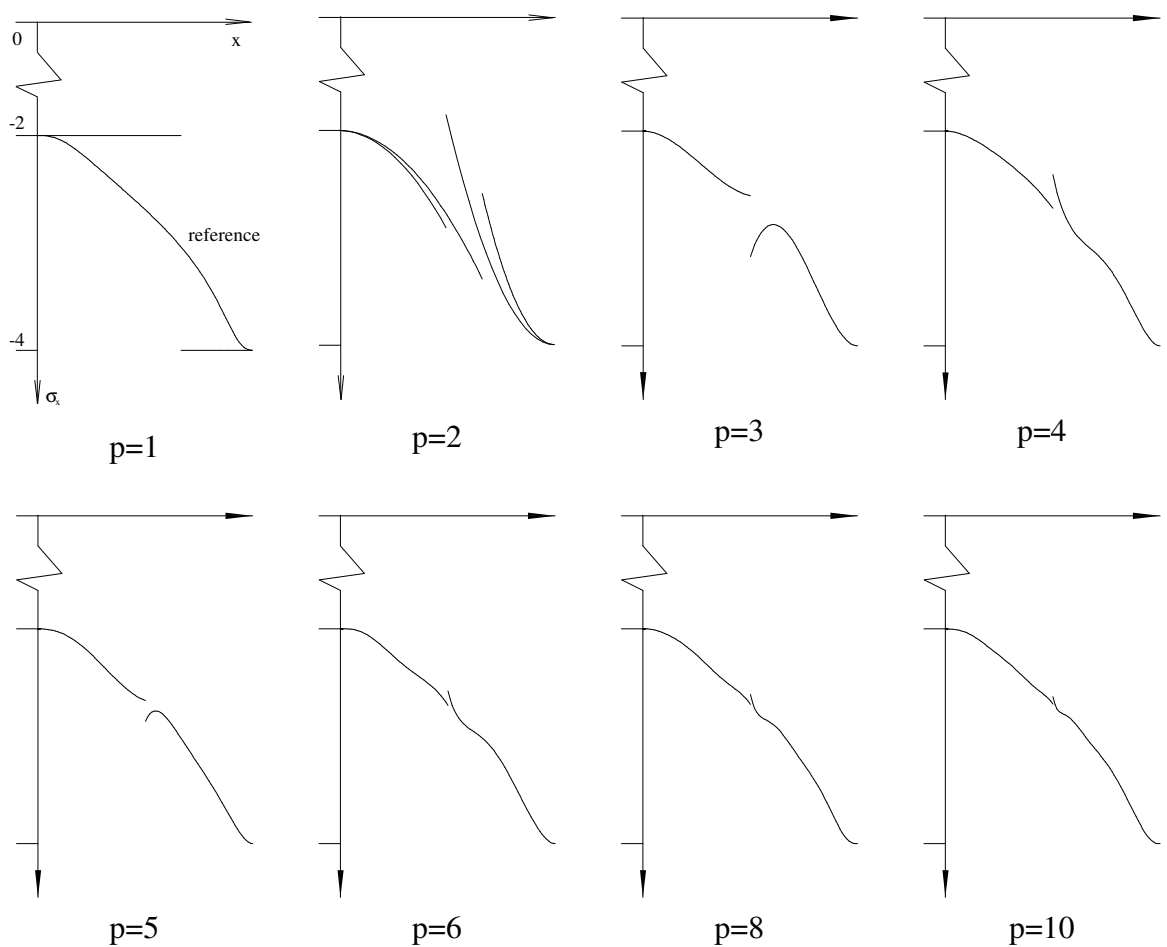


Figure 3.11 Convergence of axial stress along centre-line for Problem 2 ($P = P_c$)

Problem 3: Rectangular continuum with linear boundary tractions

This problem is an interesting one because whilst the boundary tractions are linear, the internal stress field is non-polynomial but smooth. This problem has been studied in [13] and is denoted as BMT5 in this thesis. The static boundary conditions are determined from the following stress field:

$$\begin{aligned}\sigma_x &= x^2 \\ \sigma_y &= y^2 \\ \tau_{xy} &= -2xy\end{aligned}\tag{3.8}$$

which whilst being statically admissible is incompatible.

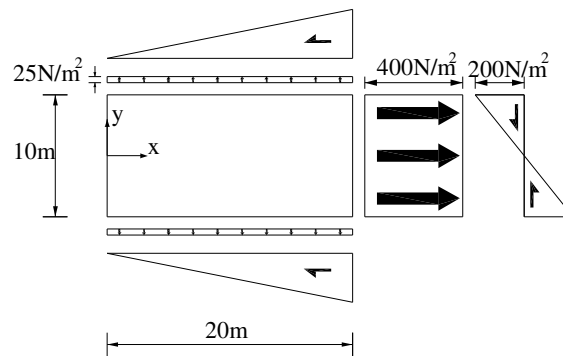


Figure 3.14 Problem 3

The stresses and displacements for a reference solution obtained using a four element mesh and a degree of approximation $p=10$ are shown in figure 3.13.

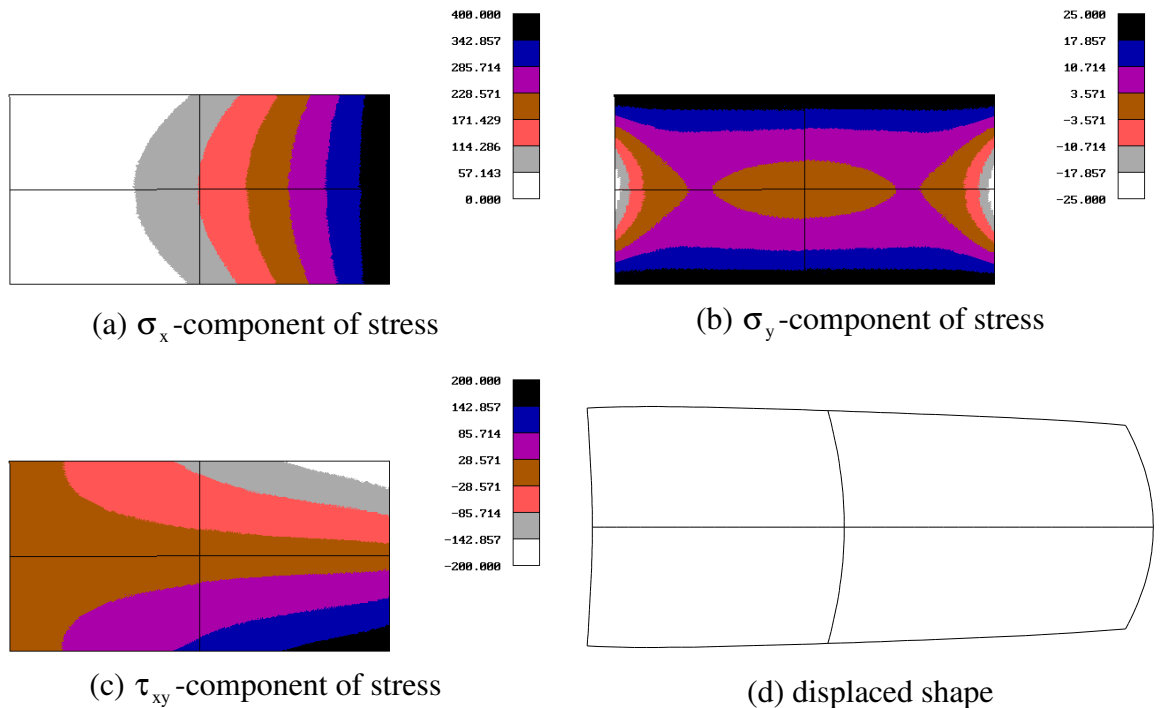


Figure 3.13 Reference solution for Problem 2 ($U_h = 2041.602289$).

The finite element strain energies are given in table 3.4 and have been plotted in figure 3.14.

p	1	2	3	4	5	6	7	8	9	10
U_h	2168.650	2042.541	2041.802	2041.634	2041.611	2041.604	2041.60272	2041.60237	2041.60230	2041.60229

Table 3.4 Finite element strain energy for Problem 3

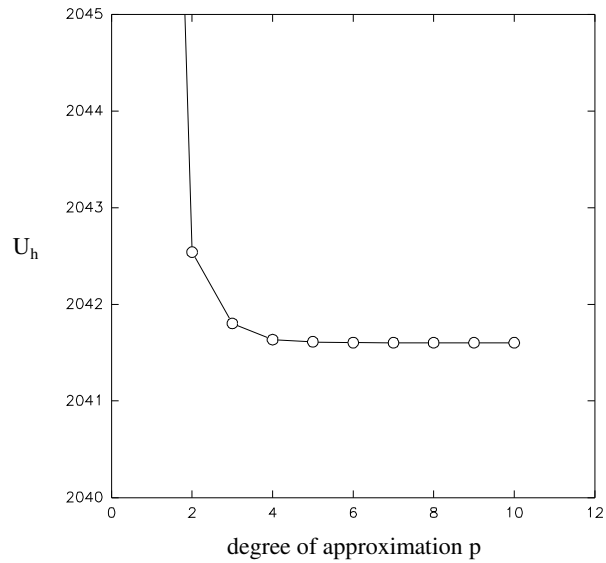


Figure 3.14 Convergence of finite element strain energy for Problem 3

The convergence of the displaced shapes is shown in figure 3.15. The rapid convergence of the solution observable in the strain energy of figure 3.14 is reflected in the displaced shapes where it is seen that for $p=4$ the discontinuities of the edges are too small to be seen at the scale with which the shapes are plotted.

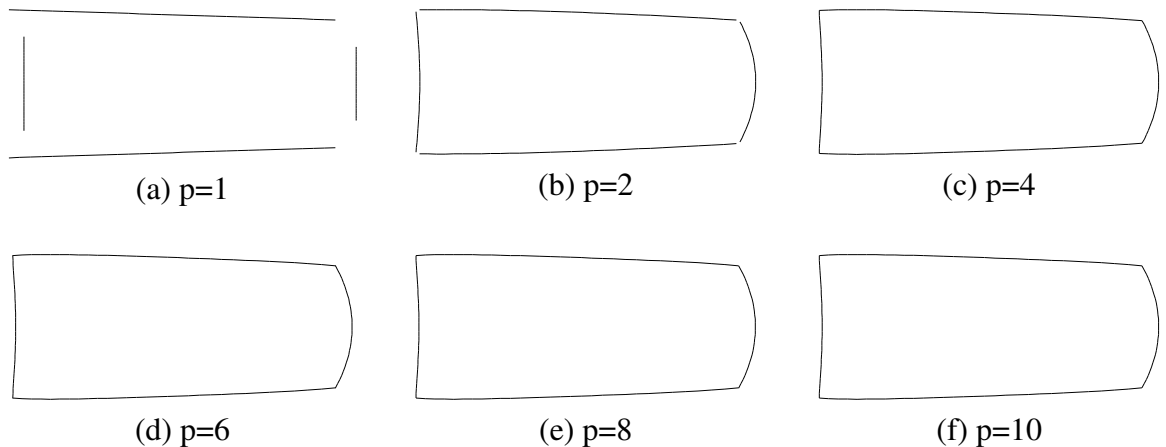


Figure 3.15 Convergence of deformed shape

The convergence of the σ_y -component of the stress along the line $y=0$ is shown in figure 3.16. The figure for $p=1$ shows the reference solution for comparative purposes. The rapid convergence already noted is also seen in the stress distributions.

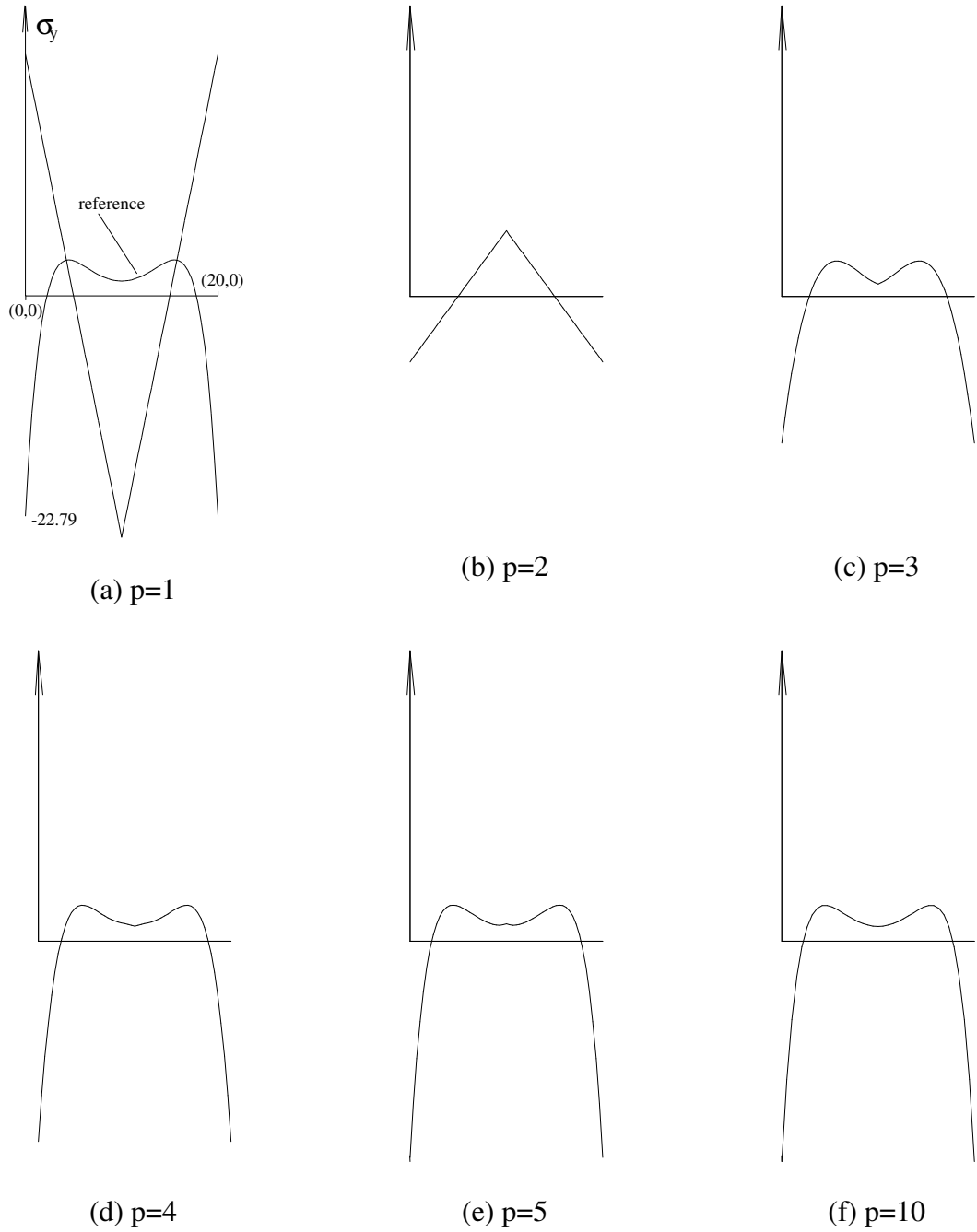


Figure 3.16 Convergence of σ_y along line $y=0$

3.5.2 FORCE DRIVEN PROBLEMS (NON-ZERO BODY FORCES)

Three force driven problems with non-zero body forces are considered:

Problem 4 is a problem for which the true stress field is linear. It is included here for the purpose of program verification.

Problem 5 investigates a rectangular beam built-in at both ends and loaded with a uniform body force. Whilst the gross behaviour for the beam can be captured adequately with relatively low degree of approximation, the detailed behaviour at the corners involves singularities in stress which can not be accurately predicted with elements for which smooth polynomial approximation functions are used. The way in which these singularities are approximated is investigated.

Problem 6 is included to demonstrate the practical usability of the macro-elements (both quadrilateral and triangular) and of the program developed during this research in modelling part of a cathedral.

Problem 4: Linear stress field resulting from uniform acceleration.

Figure 3.17 shows a rectangular continuum subject to uniform body force field. The continuum is maintained in equilibrium through the application of a uniform traction on the lower edge.

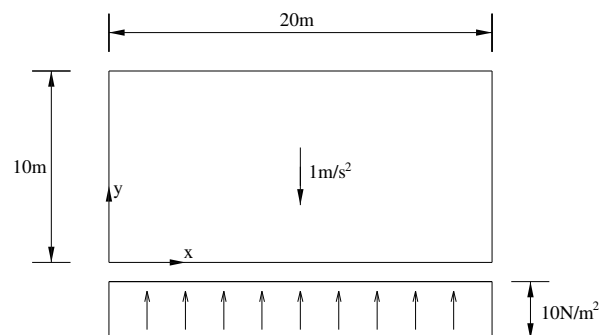


Figure 3.17 Problem 4

The exact stress field for this problem is:

$$\begin{aligned}\sigma_x &= 0 \\ \sigma_y &= y - 10 \\ \tau_{xy} &= 0\end{aligned}\tag{3.9}$$

For a Young's Modulus of $E = 210\text{N/m}^2$, a Poisson's ratio of $\nu = 0.3$, a material density of $\rho = 1\text{kg/m}^3$ and a material thickness of $t = 0.1\text{m}$ the exact strain energy for this problem is:

$$U = \frac{100}{63} \approx 1.5873 \tag{3.10}$$

A single quadrilateral macro-element with degree of approximation $p=1$ can recover the exact solution to this problem.

Problem 5: Built-in beam loaded with self-weight

This problem involves a rectangular beam built in at each end and loaded with a uniform body force as shown in figure 3.18.

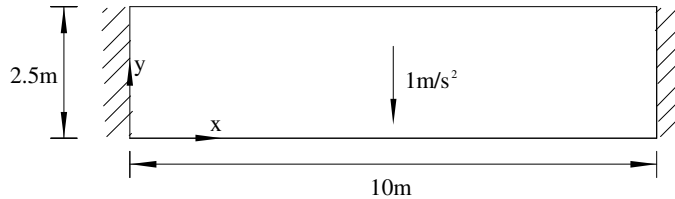


Figure 3.18 Problem 5

A Young's Modulus of $E = 10\text{N/m}^2$, a Poisson's ratio of $\nu = 0.3$, a material density of $\rho = 1\text{kg/m}^3$ and a material thickness of $t = 10\text{m}$ will be used for this problem. A reference solution obtained using four quadrilateral macro-elements of degree $p=10$ is shown in figure 3.19.

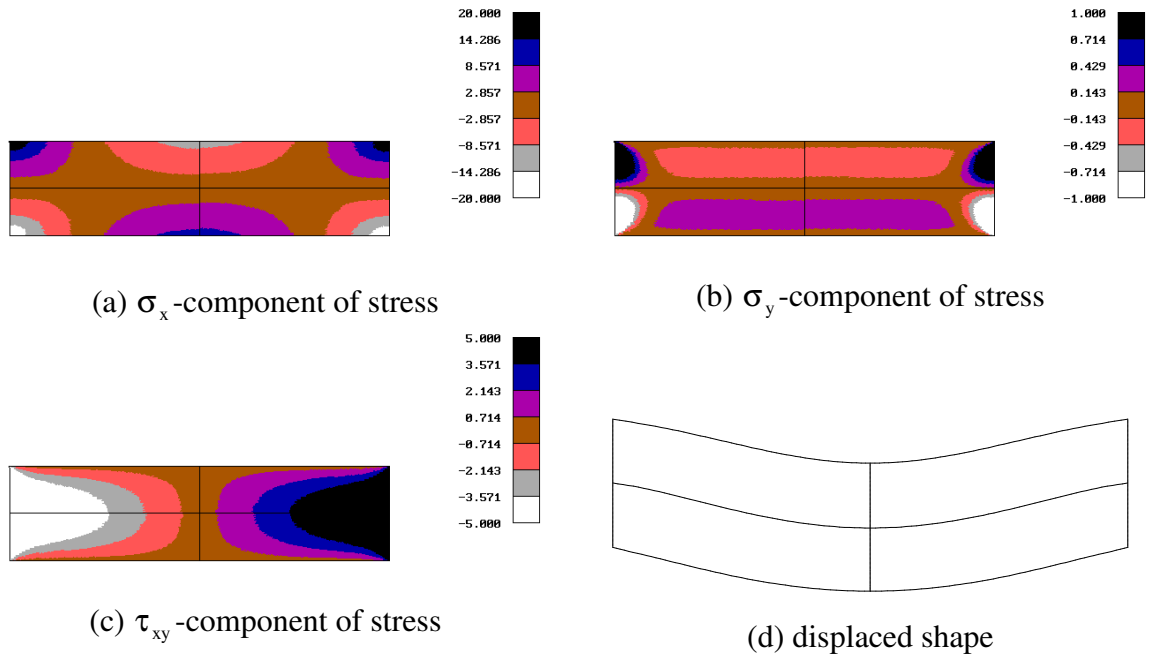


Figure 3.19 Reference solution for Problem 5 ($U_h=642.075$).

The finite element strain energies are shown in table 3.5 and have been plotted against degree of approximation in figure 3.20.

p	1	2	3	4	5	6	7	8	9	10
U_h	1211.588	662.801	652.495	646.918	644.709	643.795	643.232	642.840	642.590	642.421

Table 3.5 Finite element strain energies for Problem 5

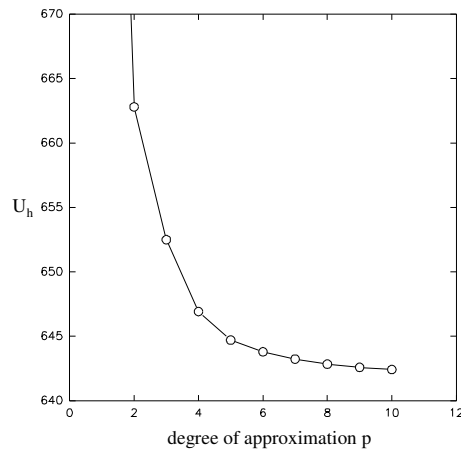


Figure 3.20 Convergence of finite element strain energy for Problem 5

The convergence of the displaced shapes shown in figure 3.21 would tend to indicate that the degree of approximation necessary to capture the gross elastic behaviour is $p=4$.

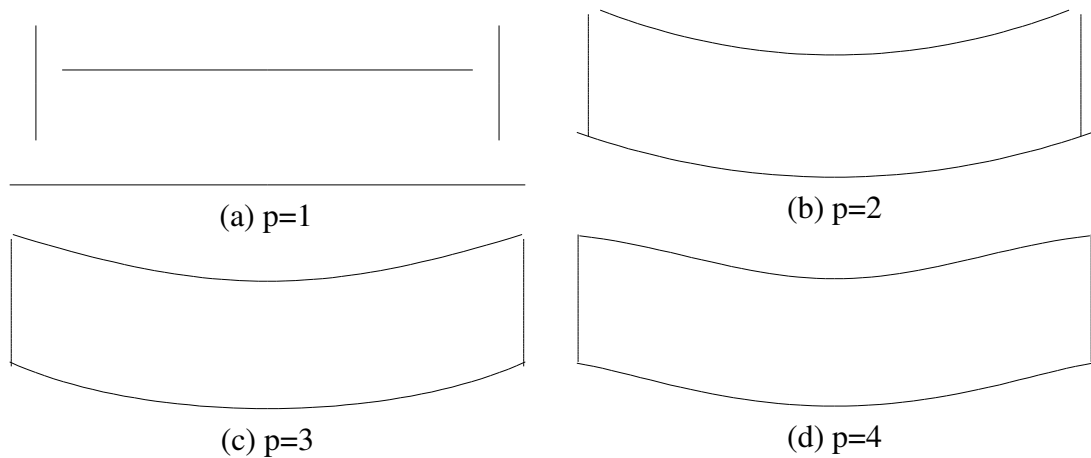


Figure 3.21 Convergence of displaced shape

The quality of the displacements for $p=4$ is demonstrated in figure 3.22 where this displaced shape is superimposed on the reference solution.

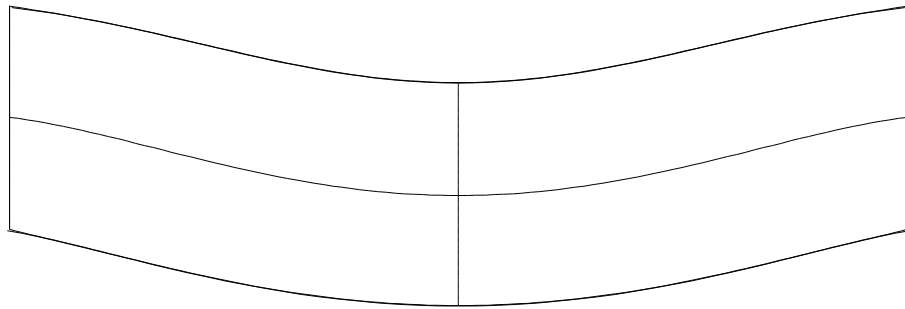


Figure 3.22 Reference solution superimposed on solution for Mesh 1, $p=4$.

Even though the gross elastic behaviour is good, discontinuities still remain at the corners where the singularities in stress occur. Figure 3.23 shows a close up view of the upper right hand corner of figure 3.22 and the discontinuities that remain are clearly visible.

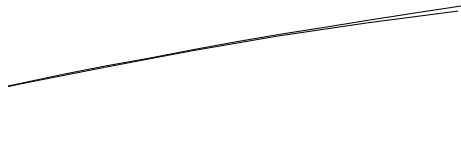
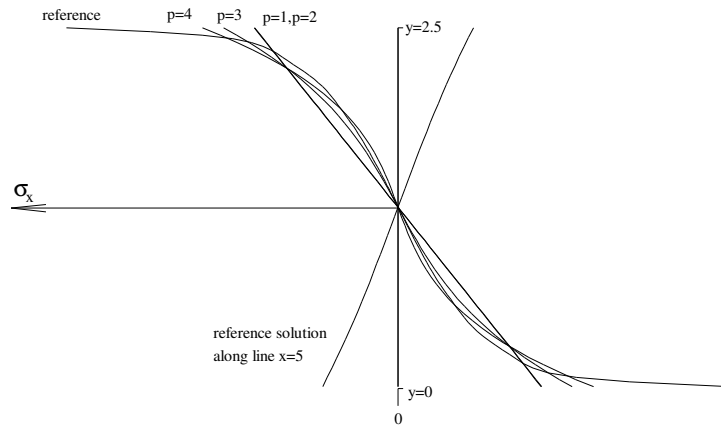


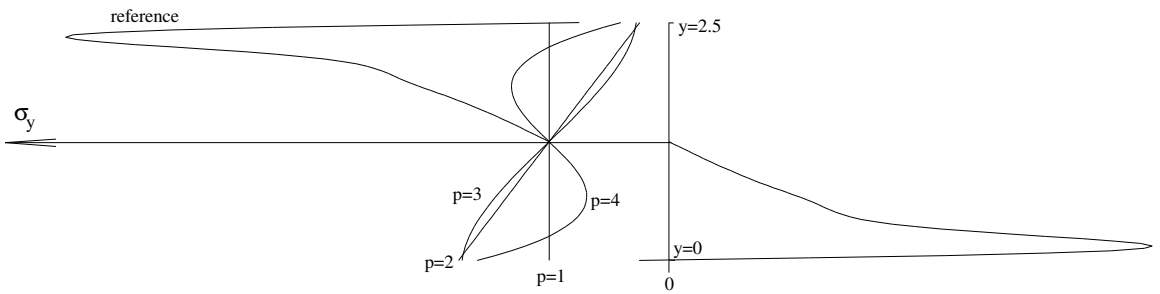
Figure 3.23 Zoom of upper right hand corner of figure 3.22 showing lack of continuity

The convergence of the stresses on the edge $x=0$ are shown in figure 3.24. The poor approximation of the high stress gradients near to the corners is clearly visible. In figure 3.24(a) the reference solution along the line $x=5m$ is also given. The stress along this line, being removed from the local effects of the singularities, should vary approximately linearly and this is seen to be the case. This example demonstrates the extreme care that needs to be exercised when interpreting finite element results. Whilst it has been seen that the gross elastic behaviour for this problem is recovered with relatively low degree of approximation ($p=4$, say) the distributions of stress along the ends of the beam are extremely poor and should be treated with the utmost caution.



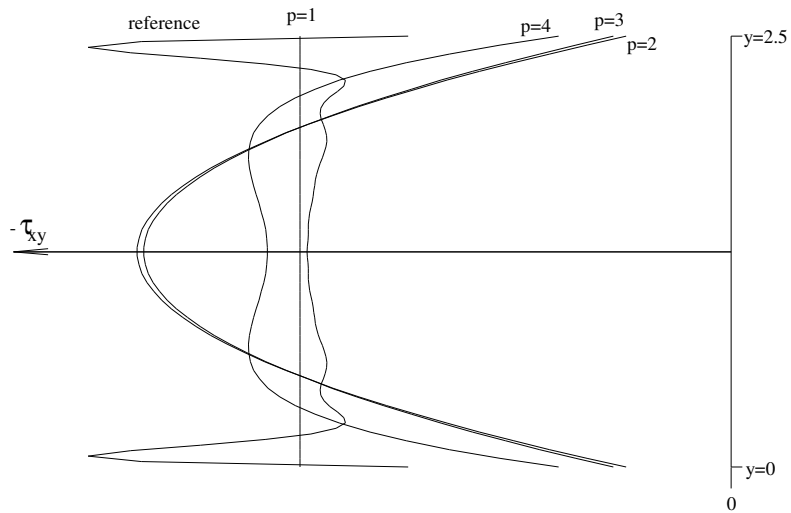
($\sigma_x = -20$ @ $x=0, y=0$ for $p=1$ and $p=2$)

(a) σ_x -component of stress



$\sigma_y = 1.25$ @ $x=0$ for $p=1$)

(b) σ_y -component of stress



($\tau_{xy} = -5$ @ $x=0$ for $p=1$)

(c) τ_{xy} -component of stress

Figure 3.24 Convergence of stresses on edge $x=0$

Problem 6: Western Nave of Exeter Cathedral

This analysis forms part of continuing research being conducted by Dr E.A.W. Maunder of the School of Engineering at the University of Exeter on the western nave of Exeter Cathedral and uses a finite element mesh which was prepared for analysis using standard displacement elements [14]. The three dimensionality of the actual nave is taken account of by varying the thickness of the elements throughout the mesh and the loading involves body forces due to gravitational acceleration and a roof load of 108KN as shown in figure 3.25. This problem serves as an example of the feasibility of using equilibrium elements in practical problems.

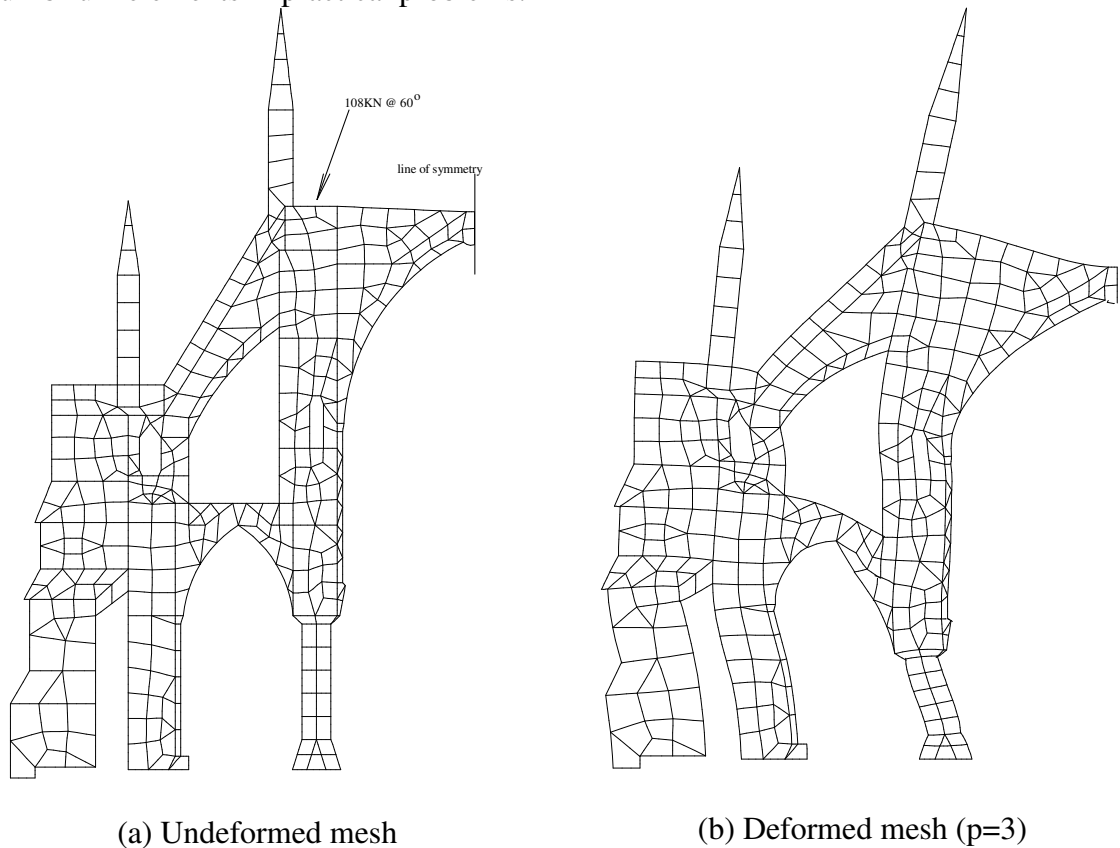


Figure 3.25 Undeformed and deformed meshes.

Finite element analyses were performed for degree $0 \leq p \leq 3$ and the strain energies are shown in table 3.6.

p	0	1	2	3
U_h	3897.43	2640.61	2618.00	2619.43
n_d^r	4470	8940	13410	17880

Table 3.6 Finite element strain energies for Problem 5

With respect to the strain energies shown in table 3.6 it is noted that for p=3 the strain energy is greater than that for p=2. This should not be and although clearly due to numerical instability a fuller explanation is still sought.

In this analysis which involves a masonry structure, it is the position and value of the maximum tensile stresses which are considered important. The convergence of the stress contours of the maximum principal stress are shown in figure 3.26.

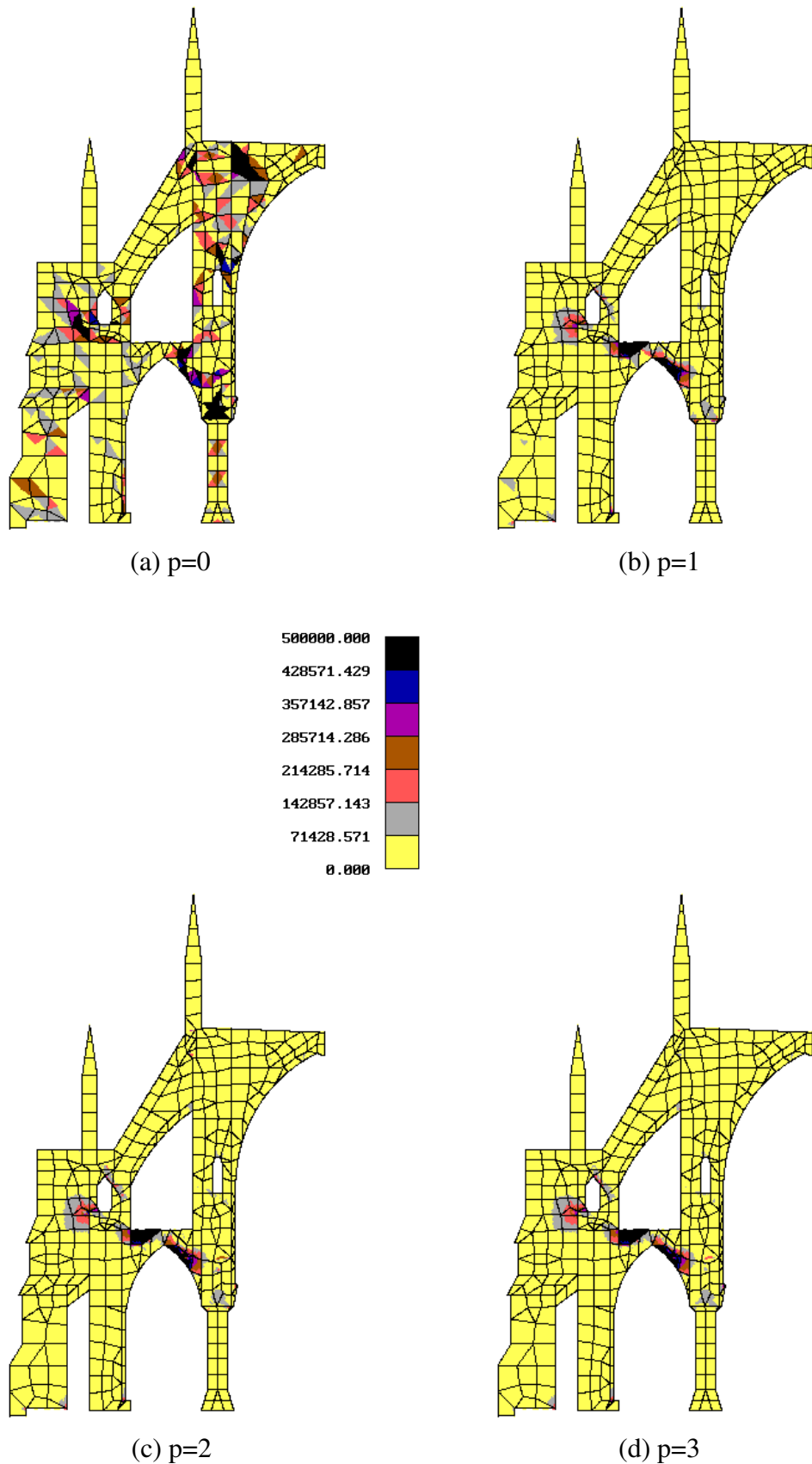


Figure 3.26 Contours of maximum principal stress

3.5.3 DISPLACEMENT DRIVEN PROBLEMS (ZERO-INITIAL STRAINS)

A single problem is shown simply in order to demonstrate that equilibrium elements perform satisfactorily for displacement driven problems.

Problem 7: Rectangular continuum with linear tangential edge displacements.

A rectangular continuum is loaded with a linear displacement distribution on two opposite edges as shown in figure 3.27.

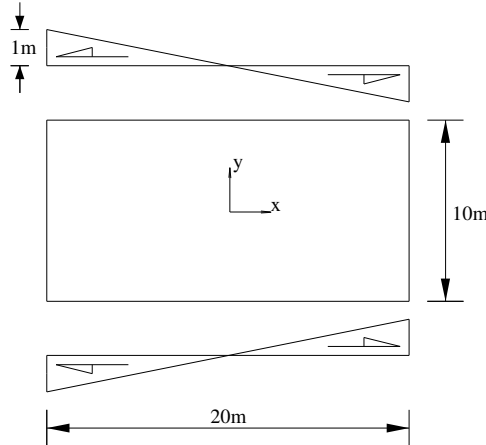


Figure 3.27 Problem 7

A Young's Modulus of $E = 210\text{N/m}^2$, a Poisson's ratio of $\nu = 0.3$ and a material thickness of $t = 0.1\text{m}$ will be used for this problem. A reference solution obtained using four quadrilateral macro elements of degree $p=10$ is shown in figure 3.28.

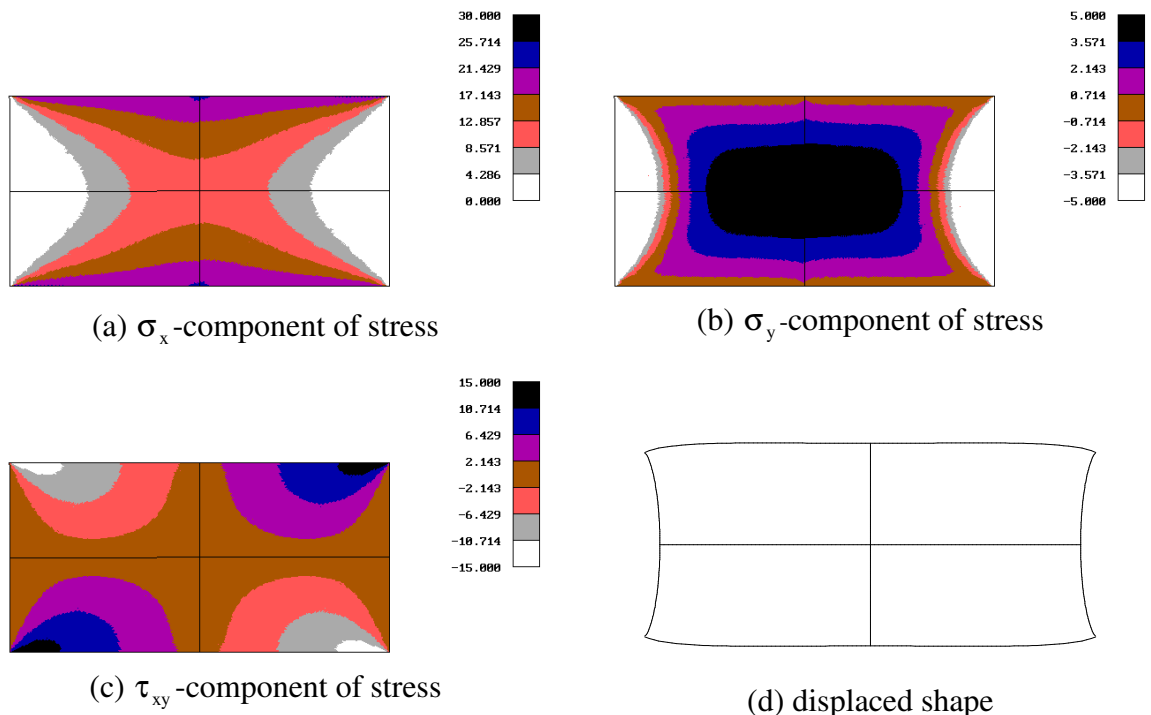


Figure 3.28 Reference solution for Problem 7 ($U_h=9.8844$)

The finite element strain energies are given in table 3.7 and have been plotted in figure 3.29.

p	1	2	3	4	5	6	7	8	9	10
U_h	7.5932	9.0334	9.6389	9.7494	9.8115	9.8435	9.8586	9.8675	9.8726	9.8758

Table 3.7 Finite element strain energy for Problem 7

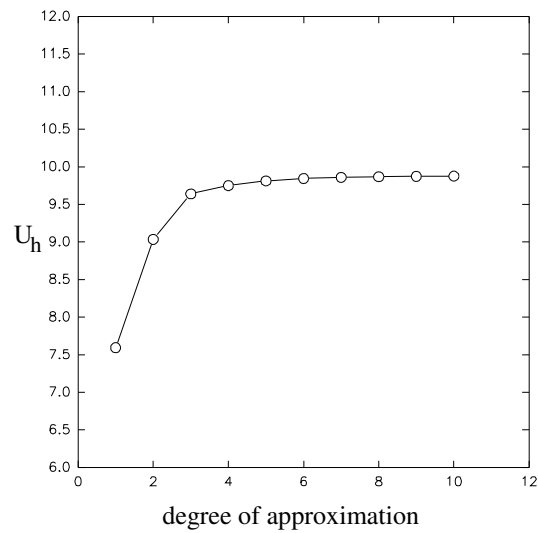


Figure 3.29 Convergence of finite element strain energy for Problem 7

Note that for displacement driven problems convergence of the strain energy occurs from below the true value (§3.4). This problem has high stress gradients in the vicinity of the corners of the model. This can be seen in the stress distributions shown in figure 3.28 and can also be observed by comparing the rate of convergence of the strain energy with that for problems 3 and 5; the rate of convergence for this problem appearing to lie somewhere between those for problems 3 and 5. The convergence of the displaced shapes is shown in figure 3.30 and it seen that the discontinuities in displacement remain visible even for a degree of approximation of $p=10$. The convergence of the σ_x - component of stress along line $x=0$ is shown in figure 3.31. This line is removed from the corners and thus shows a fairly rapid convergence to the reference solution.

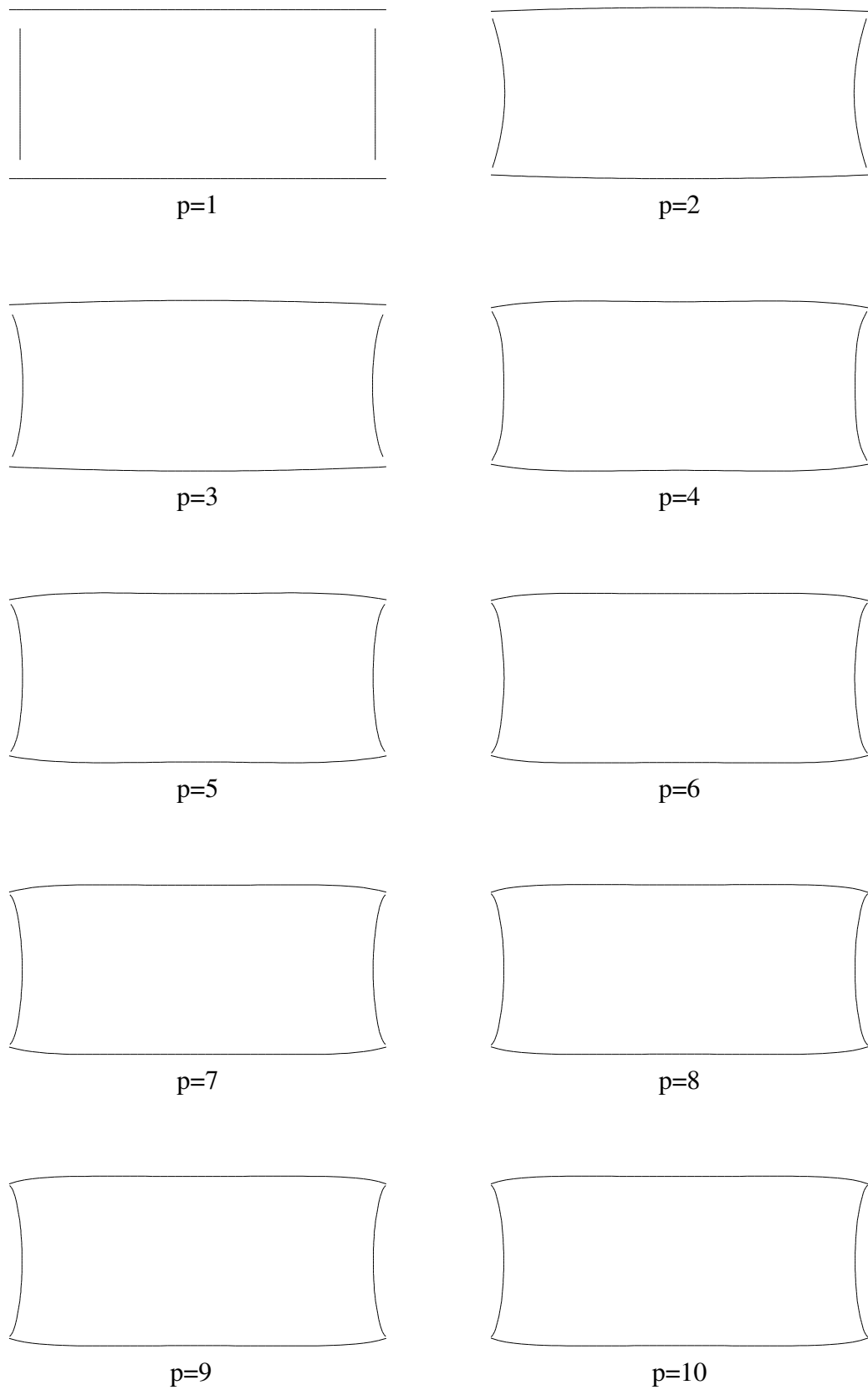


Figure 3.30 Convergence of displaced shapes for Problem 7

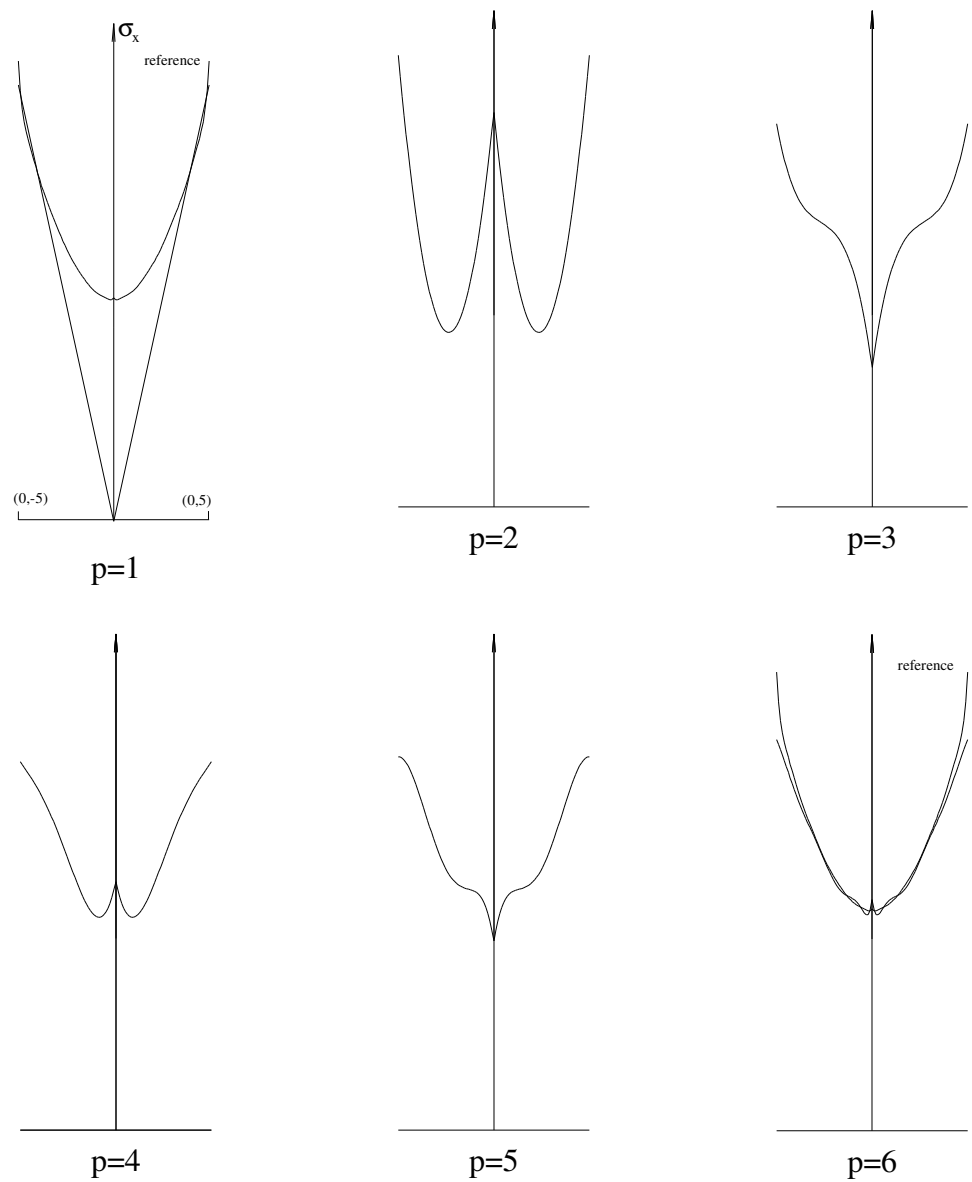


Figure 3.31 Convergence of distribution of σ_x along line $x=0$.

3.5.4 DISPLACEMENT DRIVEN PROBLEMS (NON-ZERO INITIAL STRAINS)

Two displacement driven problems with non-zero initial strains are considered:

Problem 8 is a simple problem for which the exact solution is a constant stress field and is included for purposes of program verification.

Problem 9 involves a piecewise constant temperature distribution over a fully restrained square continuum. Apart from the cathedral problem for all other problems a single element has been sufficient to capture the geometry, material and loading accurately. This problem is one in which a mesh of nine elements is required.

Problem 8: Constant bi-axial state of stresses due to uniform temperature increase.

The geometry and loading (a thermal loading resulting from a unit temperature increase) are shown in figure 3.32. The boundaries of the membrane are fully restrained. The material and geometric properties are: $E = 210 \text{ N/m}^2$, $\nu = 0.3$, $t = 0.1 \text{ m}$ and $\mu = 1.0/^\circ\text{K}$.

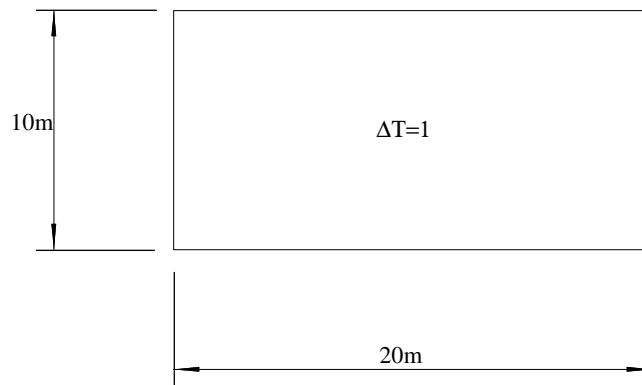


Figure 3.32 Problem 8

The exact stress field for this problem is:

$$\begin{aligned}\sigma_x &= -300 \\ \sigma_y &= -300 \\ \tau_{xy} &= 0\end{aligned}\tag{3.11}$$

and the true strain energy is $U = 3000 \text{ Nm}$.

A single quadrilateral macro-type element of degree $p=0$ should be able to recover the true solution and this has been shown to be the case.

Problem 9: Square membrane with stepwise constant thermal loading.

This problem involves a fully restrained square membrane of uniform material and geometric properties subjected to stepwise constant thermal loading and is shown in figure 3.33.

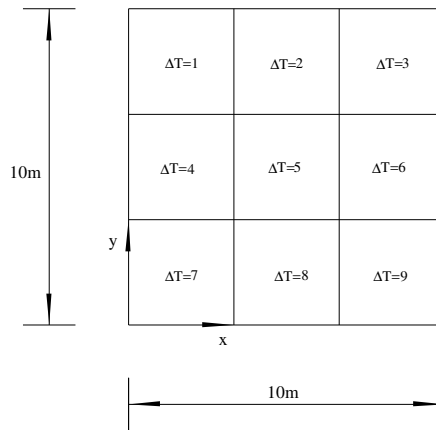


Figure 3.33 Problem 9

The mesh chosen for this problem will be the simplest required to model the geometry and loading of the problem i.e. nine square macro-type elements (one each for the different thermally loaded patches shown in figure 3.33). A Young's Modulus of $E = 1\text{N/m}^2$, a Poisson's ratio of $\nu = 0.3$, a material thickness of $t = 1\text{m}$ and a coefficient of linear thermal expansion $\mu = 1.0/^\circ K$ are used for this problem. A reference solution obtained using the same nine element mesh but with a degree of approximation $p=10$ is shown in figure 3.34.

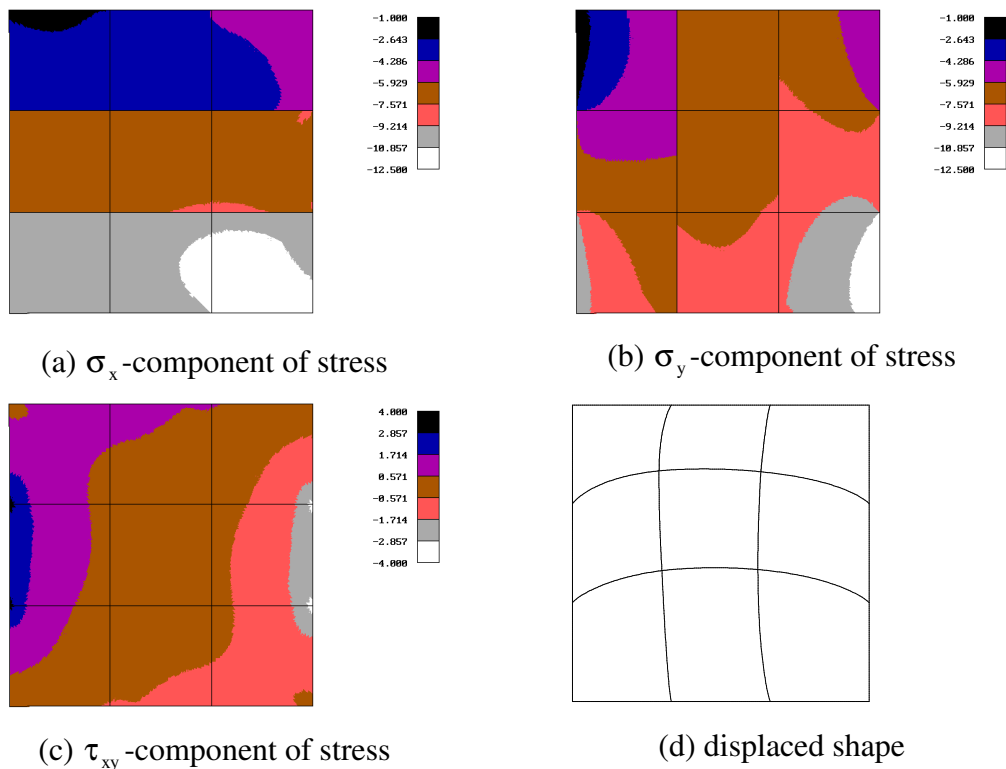


Figure 3.34 Reference solution for Problem 9 ($U_h = 4108.025$)

The finite element strain energies for this problem are recorded in table 3.8 where it is seen that by the degree $p=2$, convergence to a reasonable solution appears to have taken place.

The convergence indicated by the results shown in table 3.8 is confirmed by investigating the stress distributions and displaced shapes shown in figures 3.35 and 3.36 respectively. These figures show very clearly that for degree $p=2$ the model has effectively converged.

p	0	1	2	3	4	5
U_h	4055.406	4103.205	4107.110	4107.727	4107.895	4107.963

Table 3.8 Finite element strain energy for Problem 9

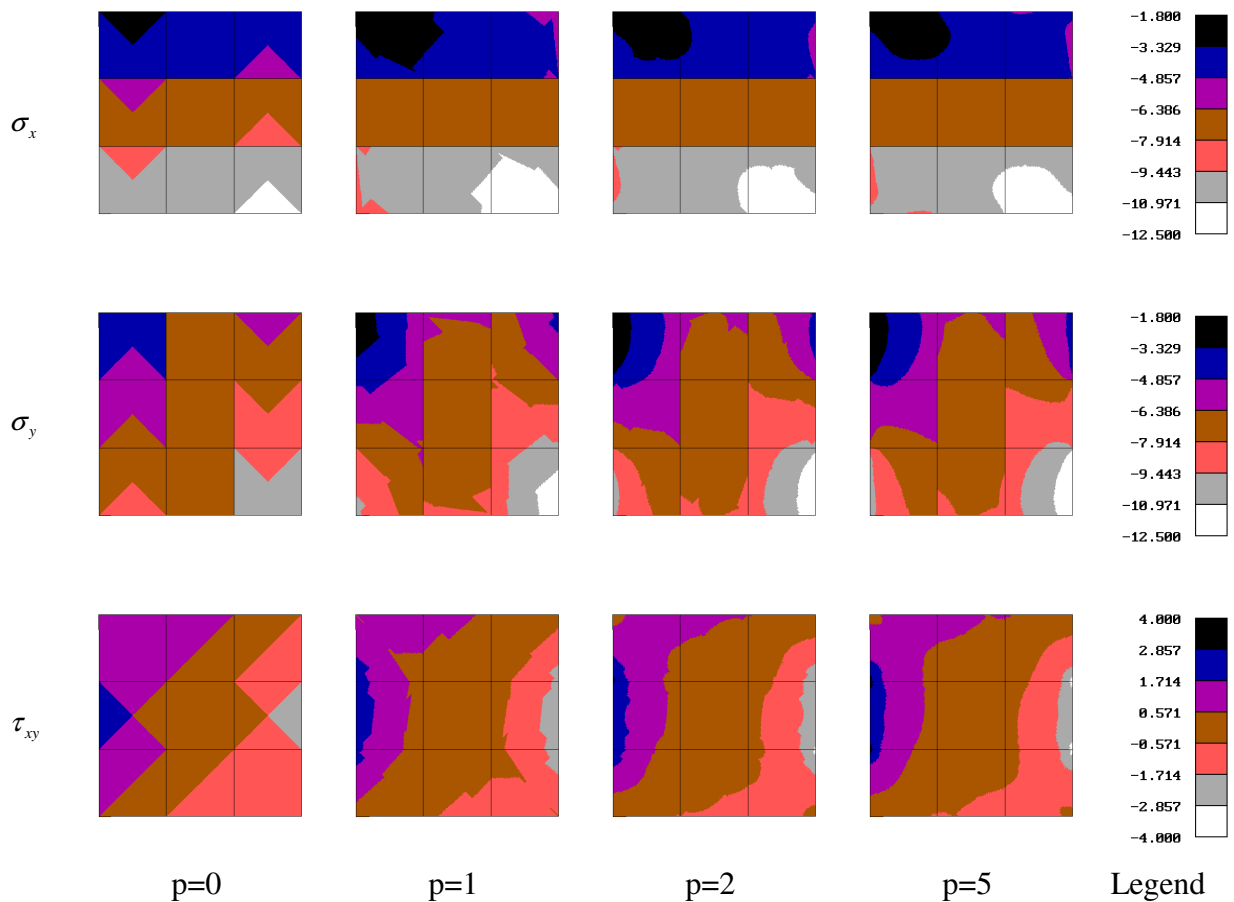


Figure 3.35 Convergence of stresses for Problem 9

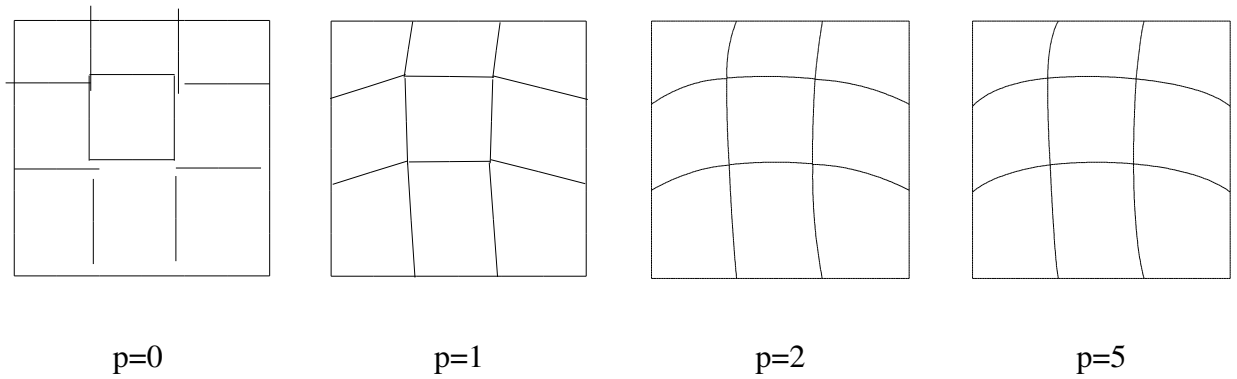


Figure 3.36 Convergence of displaced shapes for Problem 9

Figure 3.37 shows the normal and shear stress for this problem. The stresses are plotted on a developed boundary of the model. The coordinates of each corner of the model are given in parenthesis on the abscissa of each figure and the distribution of stress shown between each pair of coordinates is that corresponding to the boundary indicated by that pair of coordinates. The scale used is the same for both the normal and the shear stress.

As further proof that the reference solution for this problem is reasonable, the problem has been analysed with a nine by nine element mesh and the results are shown in figure 3.37. A degree of approximation of $p=5$ was used giving a strain energy of $U_h=4108.014$.

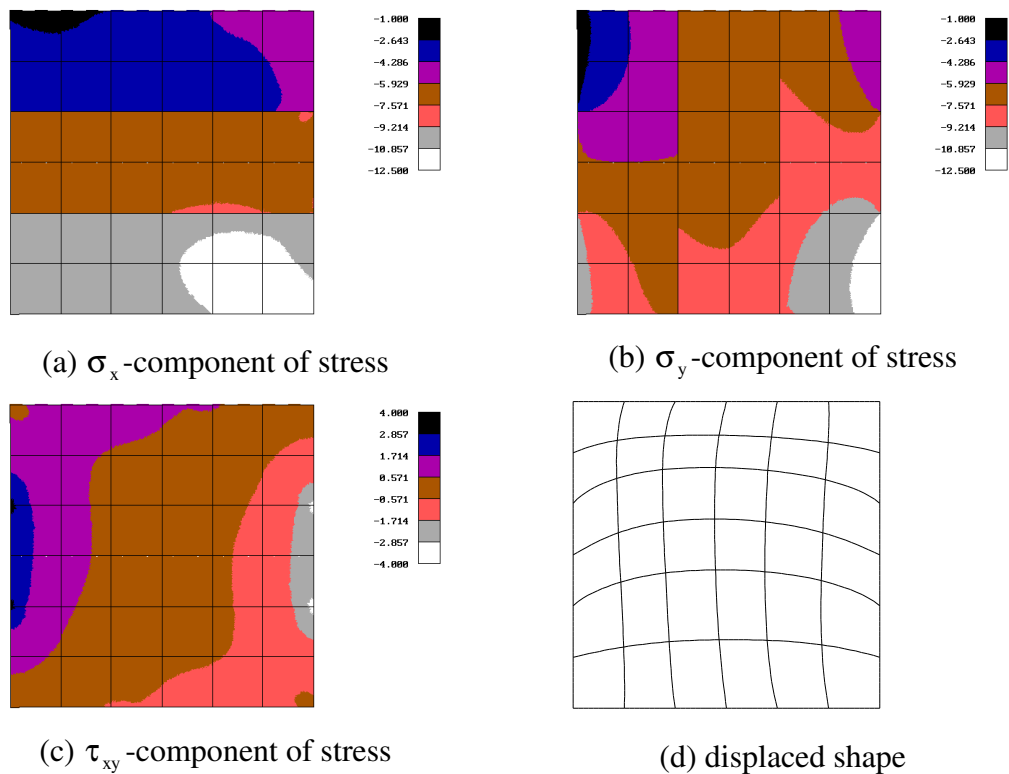


Figure 3.37 Confirmation of reference solution for Problem 9 ($p=5$)

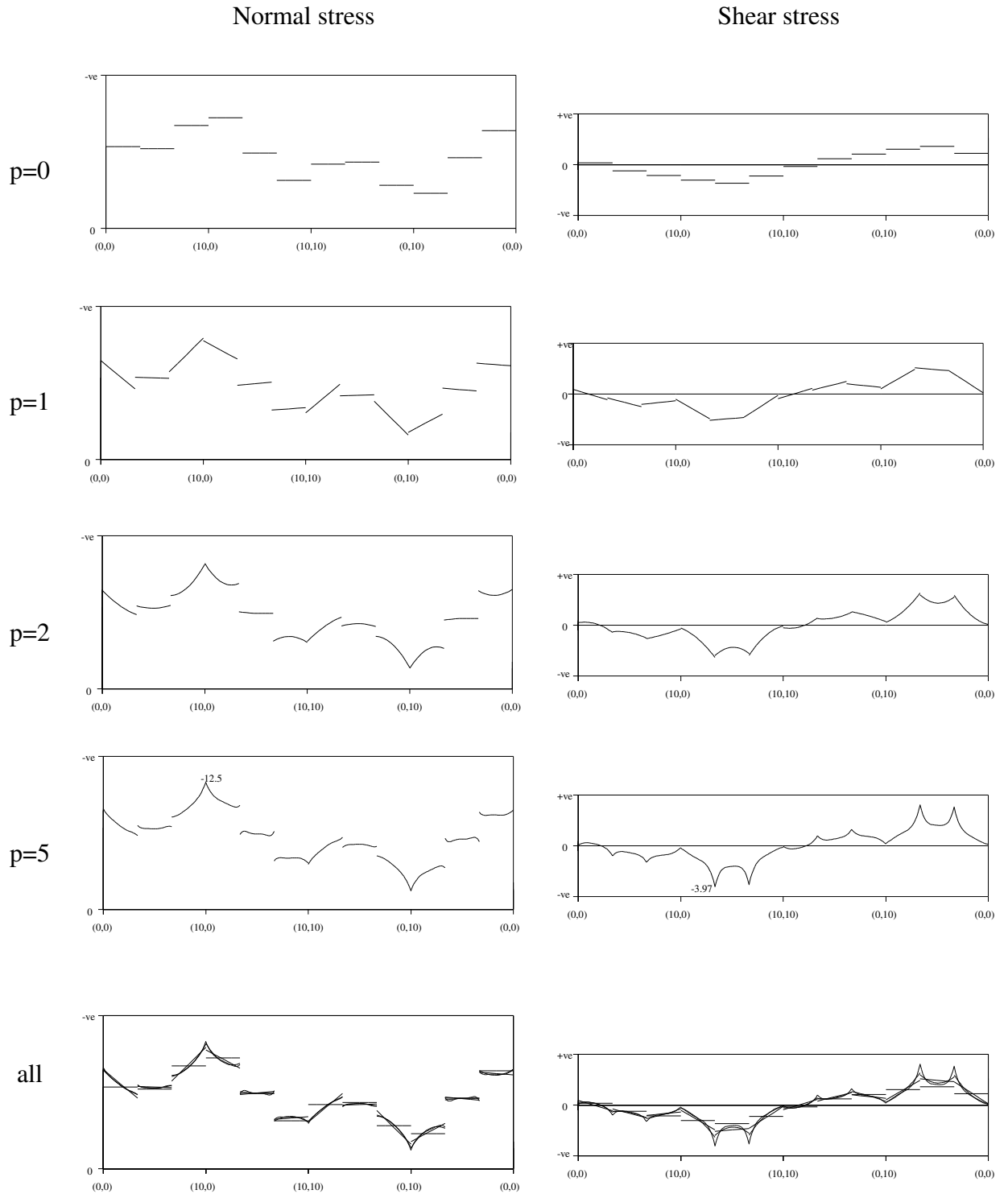


Figure 3.37 Convergence of boundary stresses for Problem 9

CHAPTER 4

Displacement Elements Versus Equilibrium Elements

4.1 INTRODUCTION

The previous chapter has demonstrated how the variable degree equilibrium element performs for a number of practical problems. P-type refinement was used almost exclusively and it was seen that convergence to solutions which might be considered of practical engineering utility were generally achieved within the range of degree of approximation available and with just sufficient elements necessary to capture the geometric complexity of the problem. For those problems containing singularities the smooth polynomial approximating functions were unable to recover the true behaviour in the vicinity of the singularity. Though this is to be expected it was seen that the solution obtained away from the points of singularity appeared to satisfactory.

Whilst the subject of equilibrium elements provides academics with an interesting and fruitful field of research, it must be appreciated that such elements are simply an alternative to the existing displacement element. Although the characteristics of solutions obtained with equilibrium elements may be usefully exploited in certain instances - see chapter 5 for such an example - their performance relative to 'corresponding' displacement elements will determine if they can provide a viable alternative to the existing displacement elements which have tended, and still do tend to dominate the commercial finite element market.

The only fair comparison between displacement and equilibrium elements (or any elements) might be, as suggested by Almeida, to challenge two optimised adaptive finite element codes to a race to the true solution for a set of given problems. The one which consistently reaches the true solution first being declared the winner. Unfortunately, since such codes do not at present exist, this approach is not possible.

In order to provide some sort of comparison between equilibrium and displacement elements, the author has chosen to compare the 8-noded displacement element (arguably the most widely used displacement element) with the linear equilibrium macro element. As justification for this comparison it could be pointed out that both elements contain complete linear stress fields and, for the single element, have equal numbers of degrees of freedom - 16 nodal displacement dofs for the 8-noded displacement element versus 16 edge displacement dofs for the linear equilibrium element. This justification might be

considered a little tenuous for two reasons. Firstly, the linear equilibrium element is considerably more complicated than the 8-noded displacement element i.e. it is built up from four linear triangular primitives. Secondly, the correspondence between the numbers of degrees of freedom which exists for the single element is lost as soon as a mesh of elements is considered. It is also noted that whilst similar numbers of dofs represent similar solution times for the structural equations, the effort required to generate the stiffness matrix for a linear equilibrium element is considerably greater than that required for the 8-noded displacement element.

Accepting these limitations, this chapter compares the performance of linear equilibrium elements with 8-noded displacement elements for two of the problems considered in chapter 3 of this report. The first problem (problem 3 of chapter 3) is a force driven problem whilst the second problem (problem 7 of chapter 3) is displacement driven. The results are compared on the basis of convergence of stress, displacement and global strain energy as a mesh is refined. In addition to the linear equilibrium element and the 8-noded displacement element some results will also be presented for the quadratic equilibrium element and the 4-noded displacement element. These results can be used for comparison. For the 8-noded displacement element two sets of results are presented corresponding to full (exact) and reduced integration of the element stiffness matrix. Reduced integration is a common ploy used with displacement elements for compensating (in some fashion) for the 'over-stiff' nature of such elements. For the 8-noded element reduced integration leads to a spurious kinematic mode (the so-called hour glass mode) at the element level. Because of this results for the single 8-noded element with reduced integration are not reported. For meshes of elements the element level spurious kinematic modes do not propagate and the results obtained are often better than those achieved with full integration.

The two problems studied in this chapter are shown in figure 4.1. Further details can be found in chapter 3.

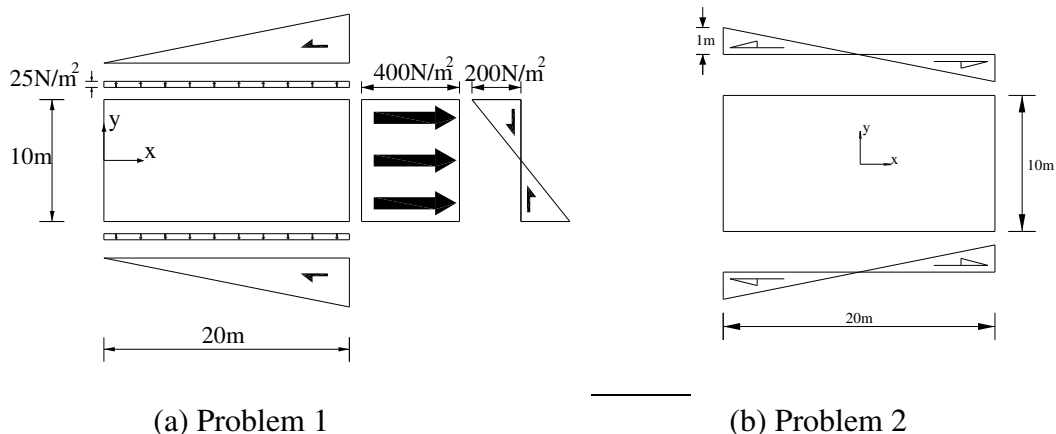


Figure 4.1 The two problems

Four meshes will be considered as shown in figure 4.2.

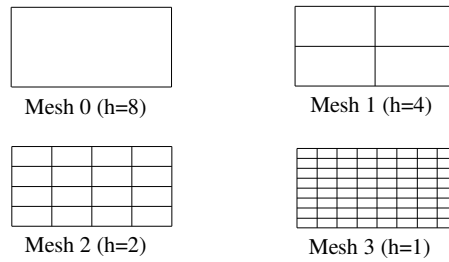


Figure 4.2 Meshes for problems considered in chapter 4

4.2 NUMERICAL EXAMPLES

Results for the two problems will be presented in this section and will be discussed in section 4.3.

4.2.1 Problem 1

The strain energies for problem 1 are tabulated in table 4.1 and the logarithm of the error in strain energy has been plotted against the logarithm of the characteristic length of a typical element in the mesh in figure 4.3. The true strain energy is taken as $U = 2041.602291\text{Nm}$. This value is a converged value using both p- and h-type refinement equilibrium models.

Element	Mesh 1	Mesh 2	Mesh 3	Mesh 4
4-node	851.327	1702.598	1953.359	2019.156
8-node (full integration)	1987.002	2036.765	2041.174	2041.570
8-node (reduced integration)	/	2038.905	2041.429	2041.591
equilibrium p=1	2168.650	2050.422	2042.310	2041.655
equilibrium p=2	2042.541	2041.809	2041.615	2041.602

Table 4.1 Finite element strain energies for problem 1

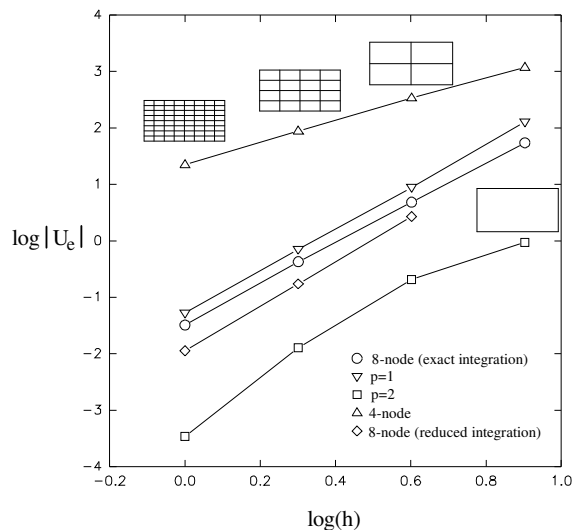


Figure 4.3 Convergence of strain energy for problem 1

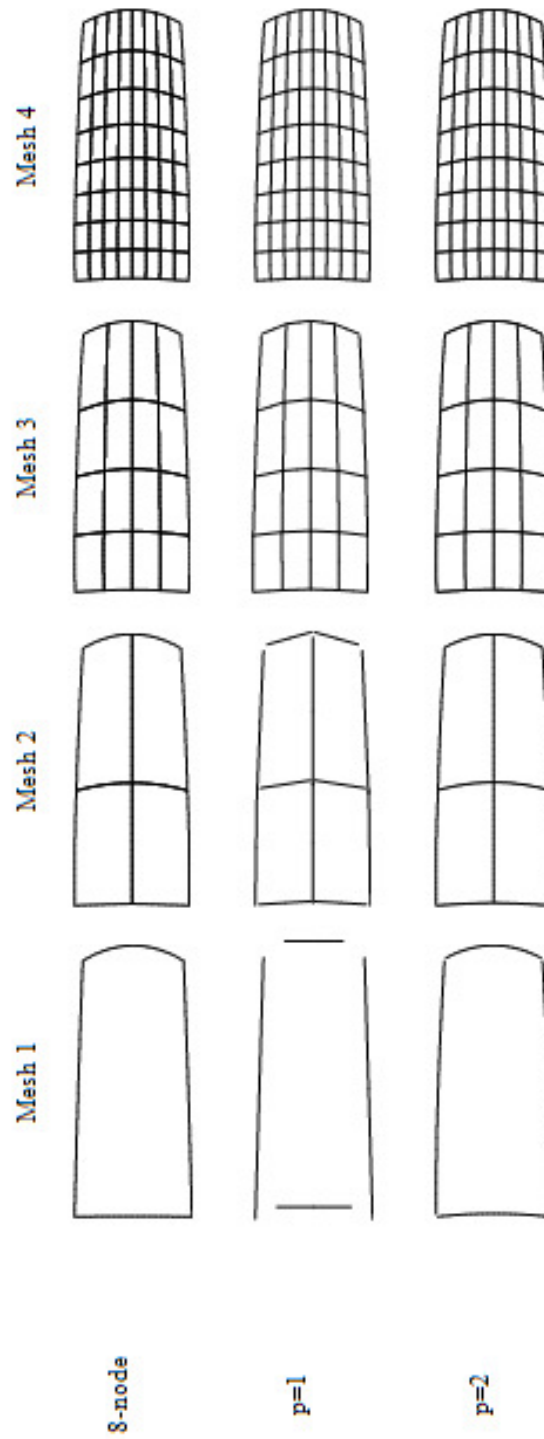


Figure 4.4 Convergence of displaced shapes for problem 1

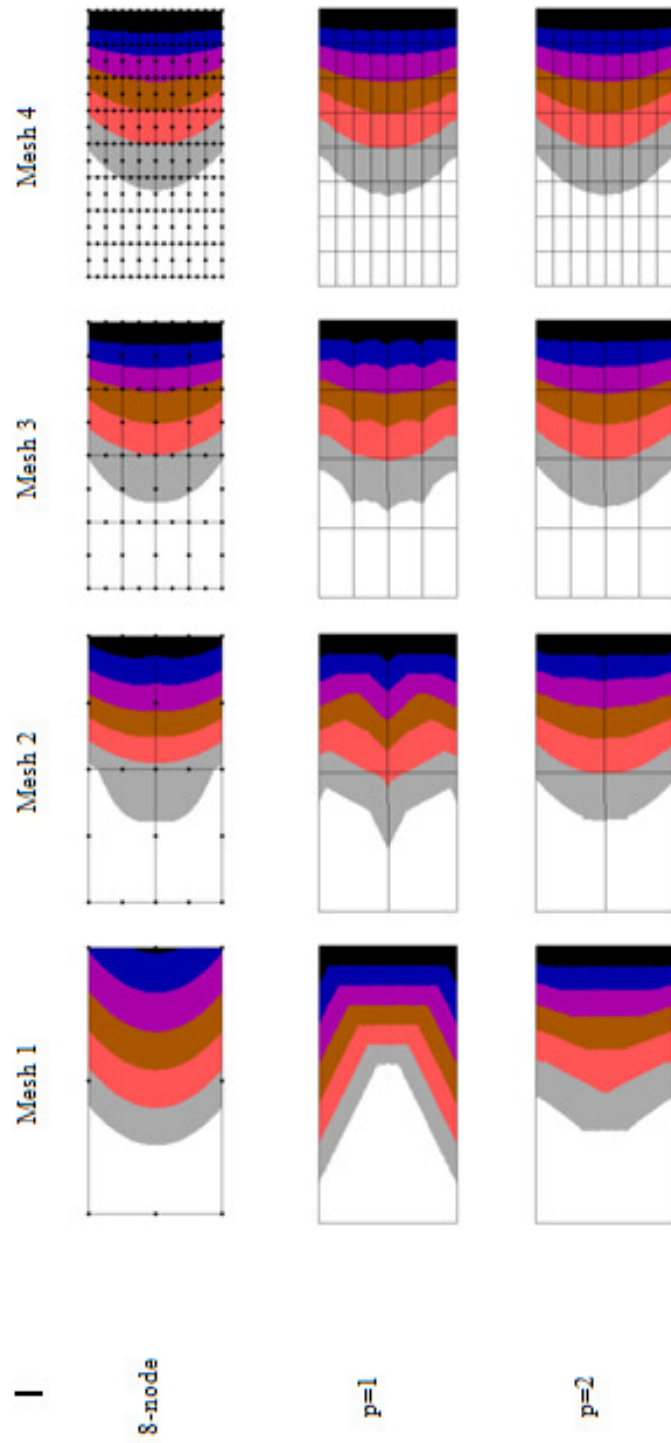


Figure 4.5 Convergence of σ_x -component of stress for problem 1

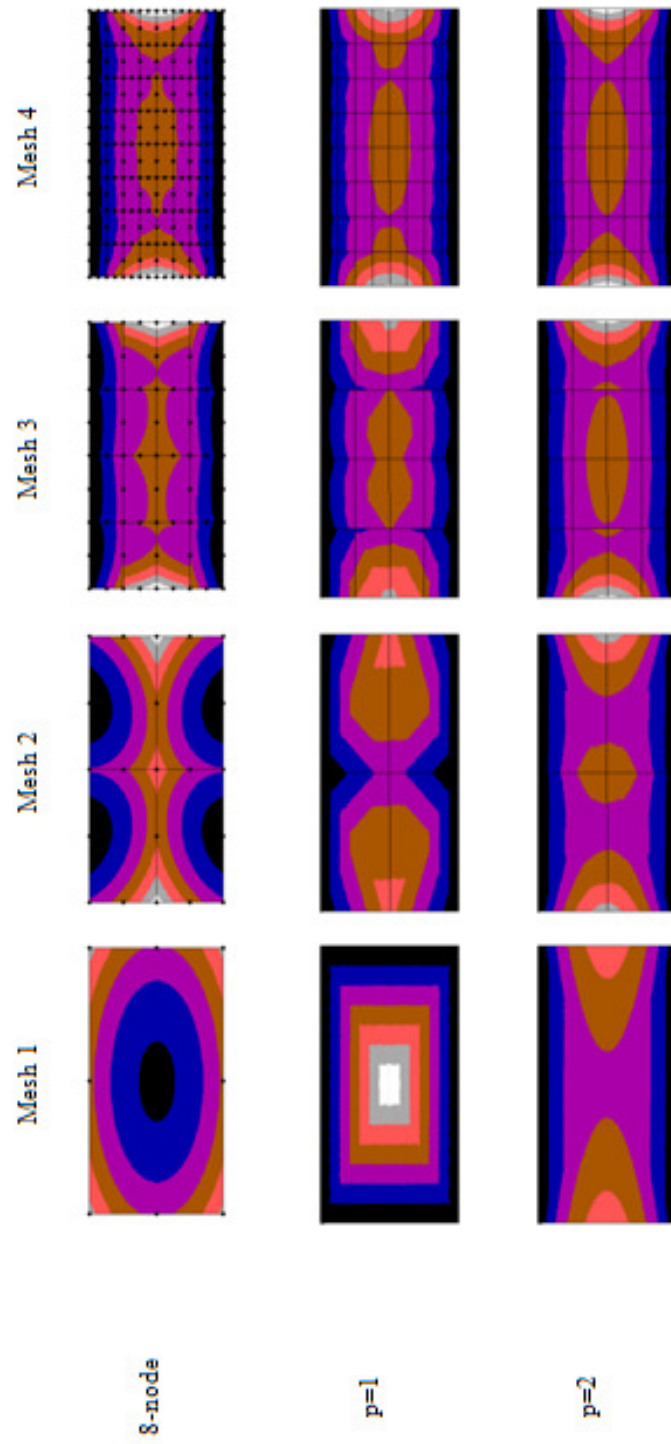


Figure 4.6 Convergence of σ_y -component of stress for problem 1

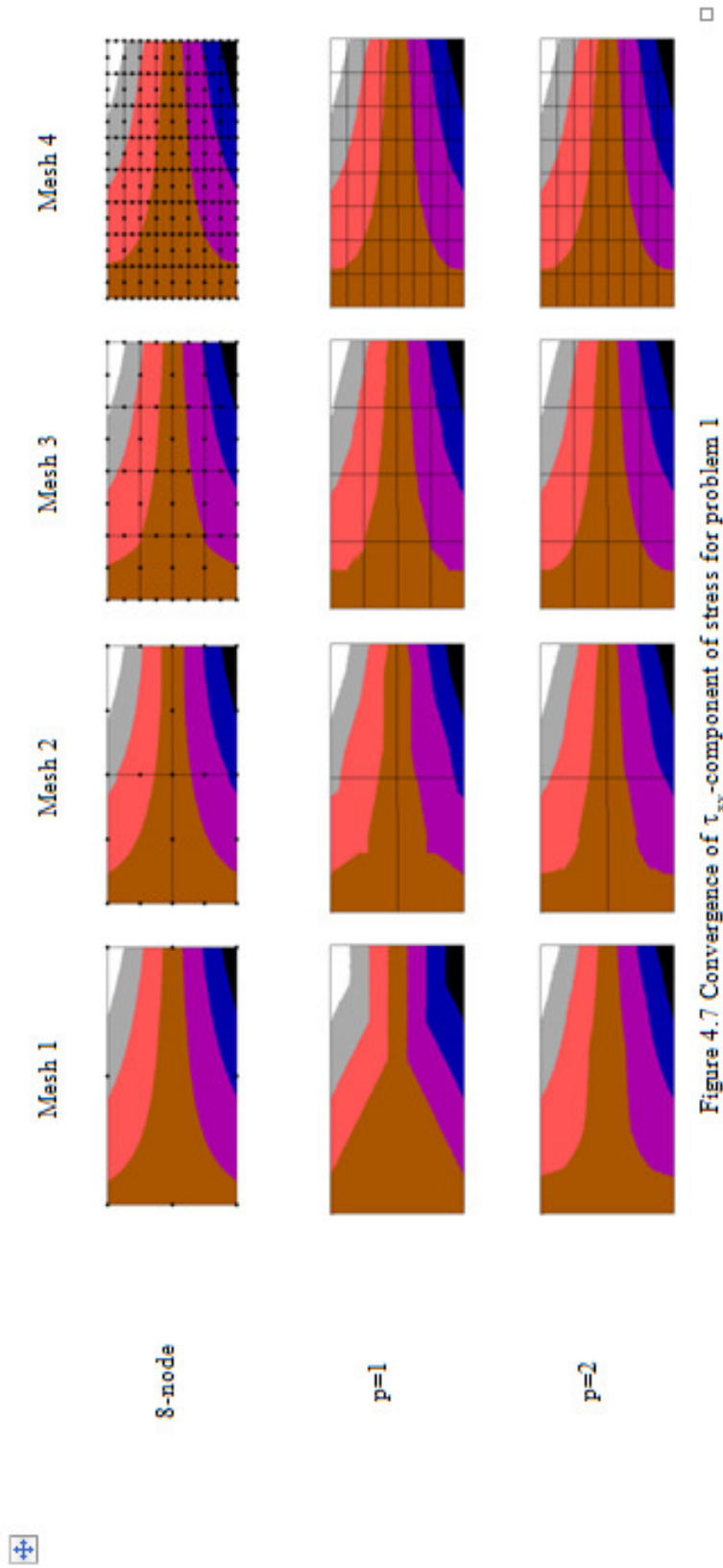


Figure 4.7 Convergence of τ_{xy} -component of stress for problem 1

□

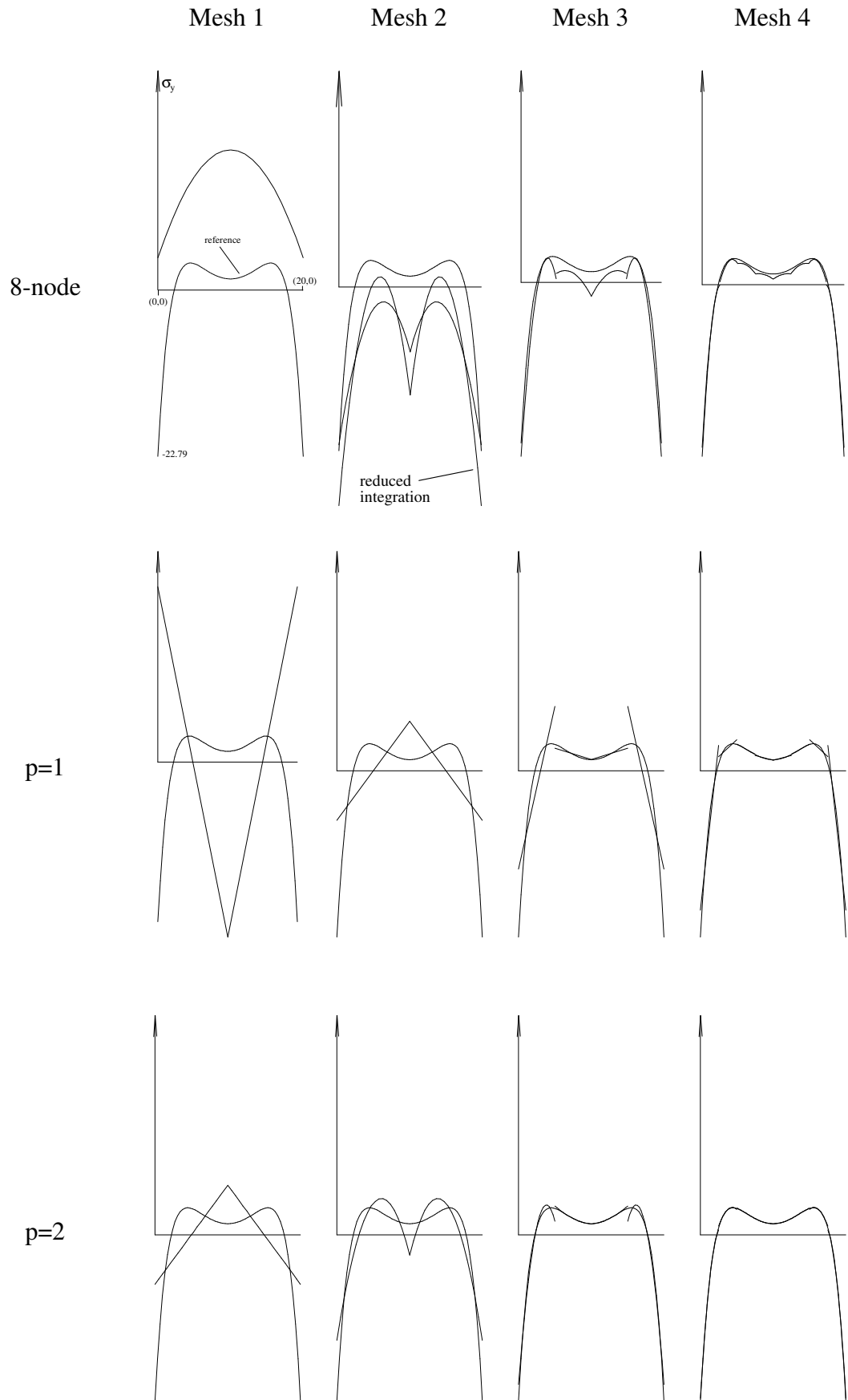


Figure 4.8 Convergence of σ_y along line $y=0$ for problem 1

The convergence of the displaced shapes and the stress fields are shown in figures 4.4 - 4.7 and the convergence of the σ_y -component of the stress along the line $y=0$ is shown in figure 4.8.

4.2.2 Problem 2

The strain energies for problem 2 are tabulated in table 4.2 and have been plotted against the characteristic length of a typical element in the mesh in figure 4.9. Two figures are shown. The first showing the complete convergence and the second showing a close-up view of the convergence for the more refined meshes.

Element	Mesh 1	Mesh 2	Mesh 3	Mesh 4
4-node	21.0000	14.2658	11.8197	10.5833
8-node (full integration)	11.8297	11.0371	10.1937	9.9437
8-node (reduced integration)	/	10.2333	10.0143	9.9012
equilibrium p=1	7.5932	8.5704	9.5861	9.8183
equilibrium p=2	9.0334	9.6374	9.8354	9.8768

Table 4.2 Finite element strain energies for problem 2

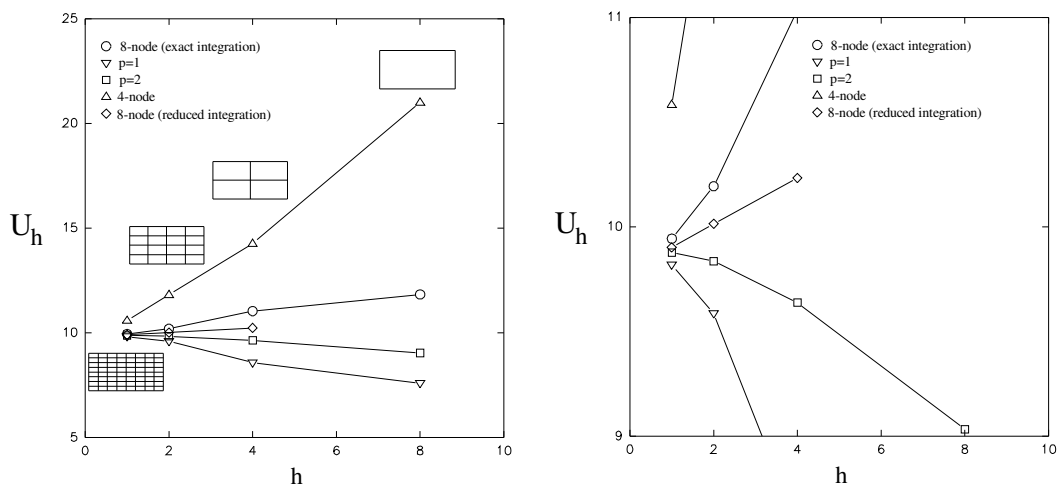


Figure 4.9 Convergence of strain energy for problem 2

The convergence of the displaced shapes and the stress fields are shown in figures 4.10 - 4.13 and the convergence of the σ_x -component of stress along line $x=0$ is shown in figure 4.14.

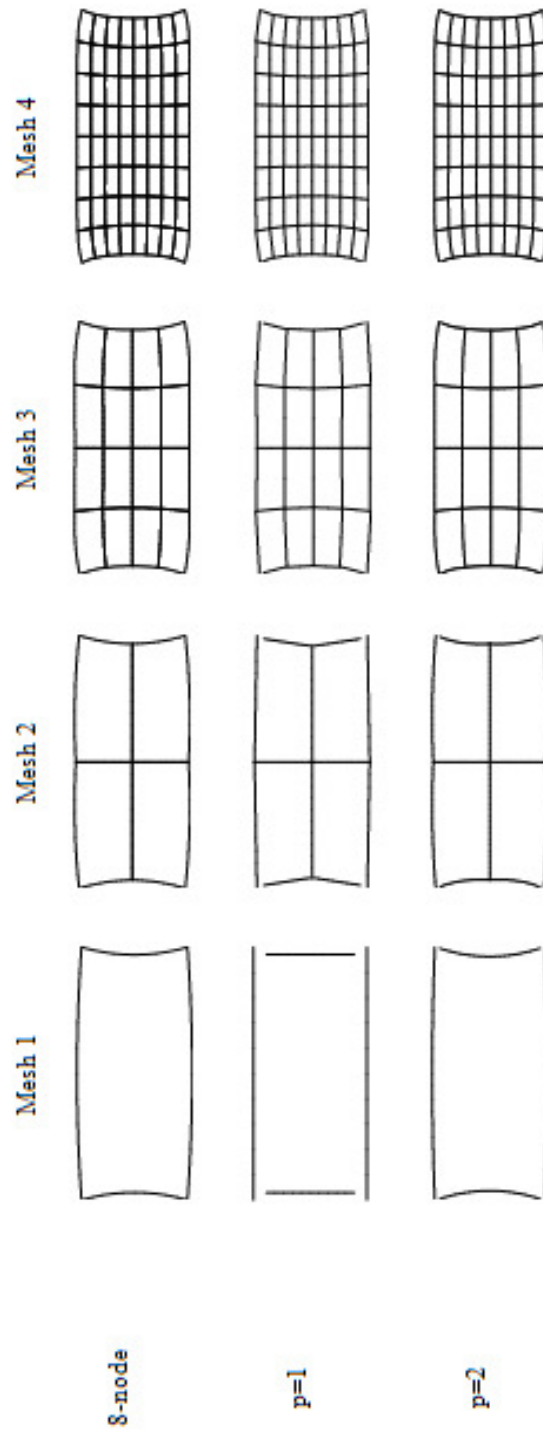
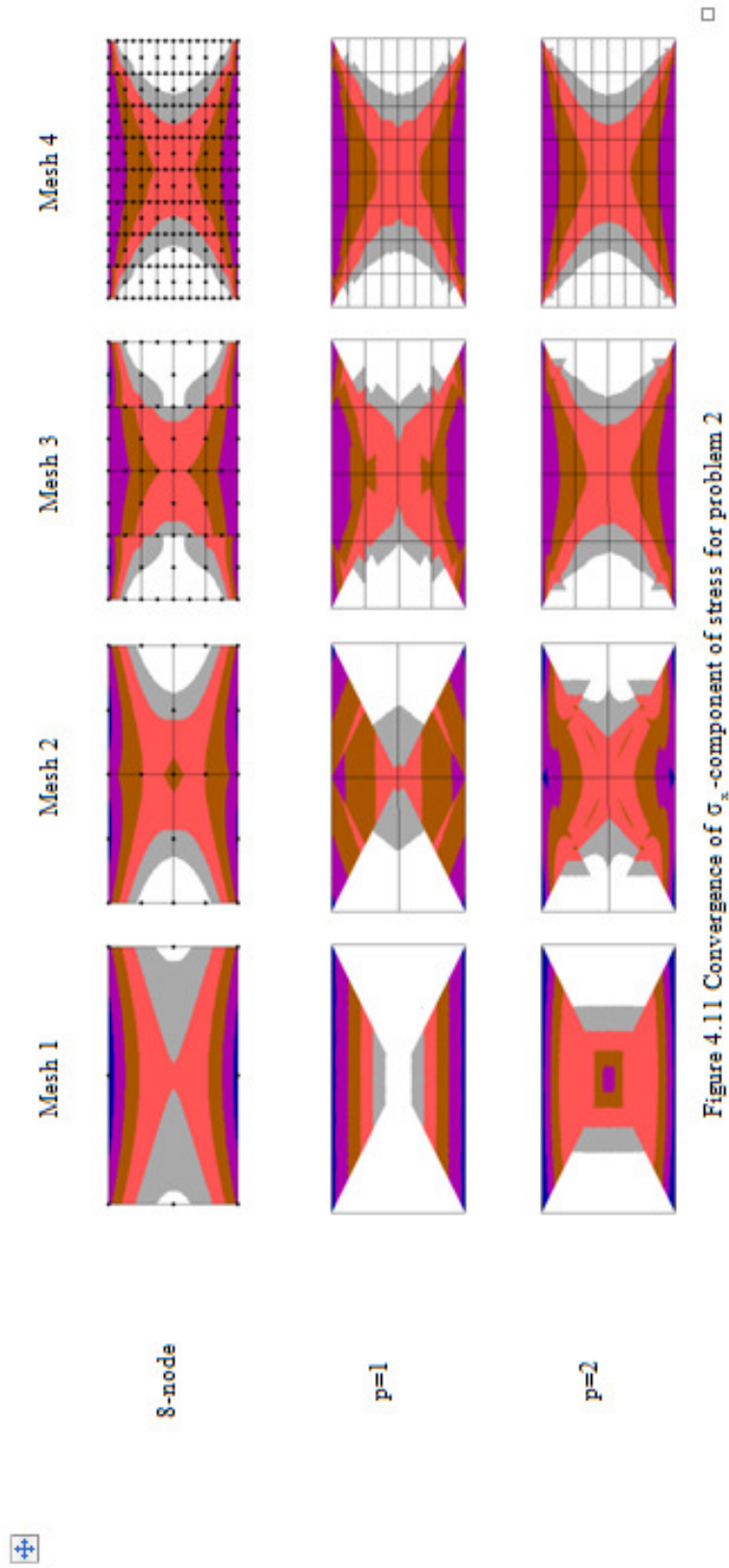


Figure 4.10 Convergence of displaced shapes for problem 2



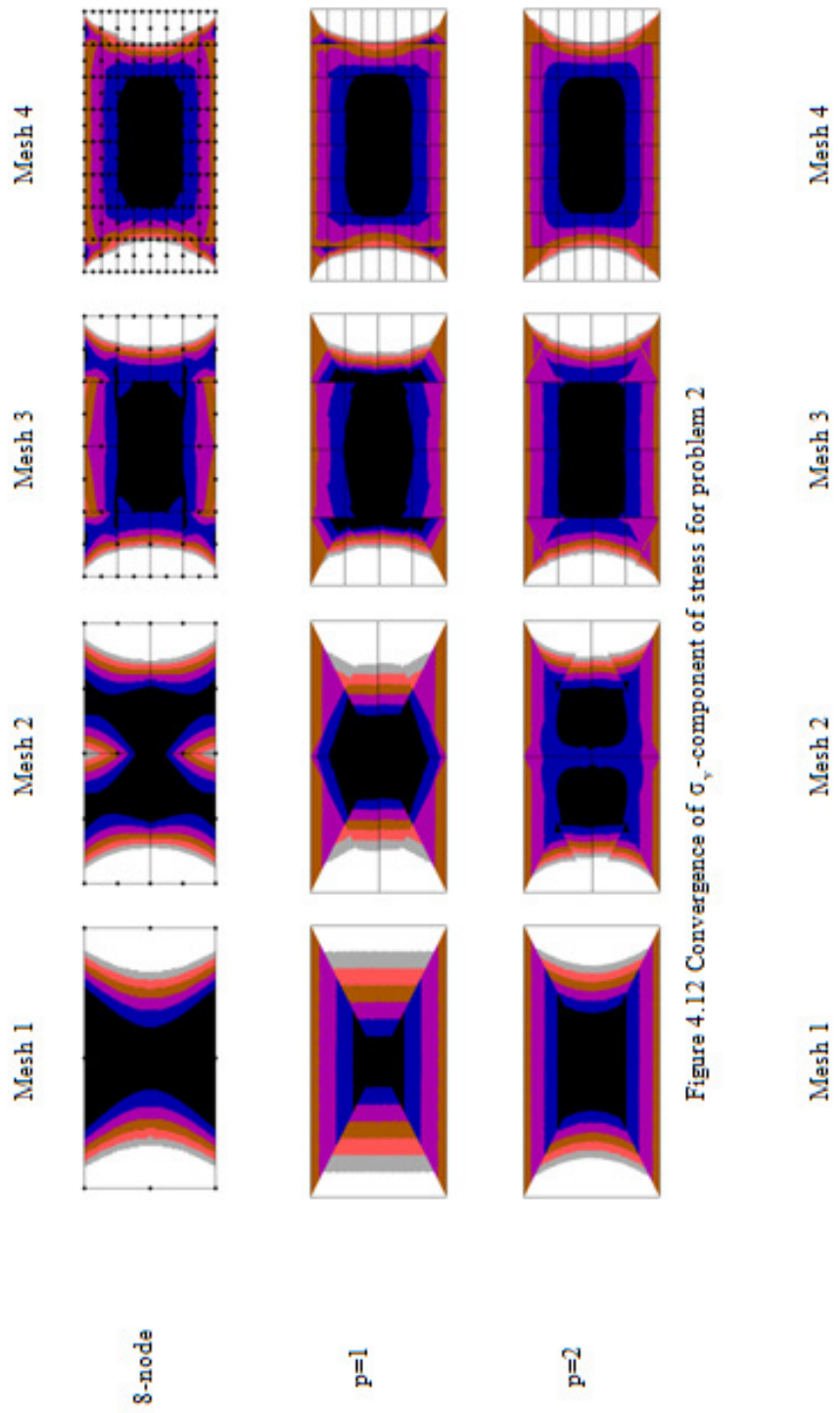


Figure 4.12 Convergence of σ_y -component of stress for problem 2

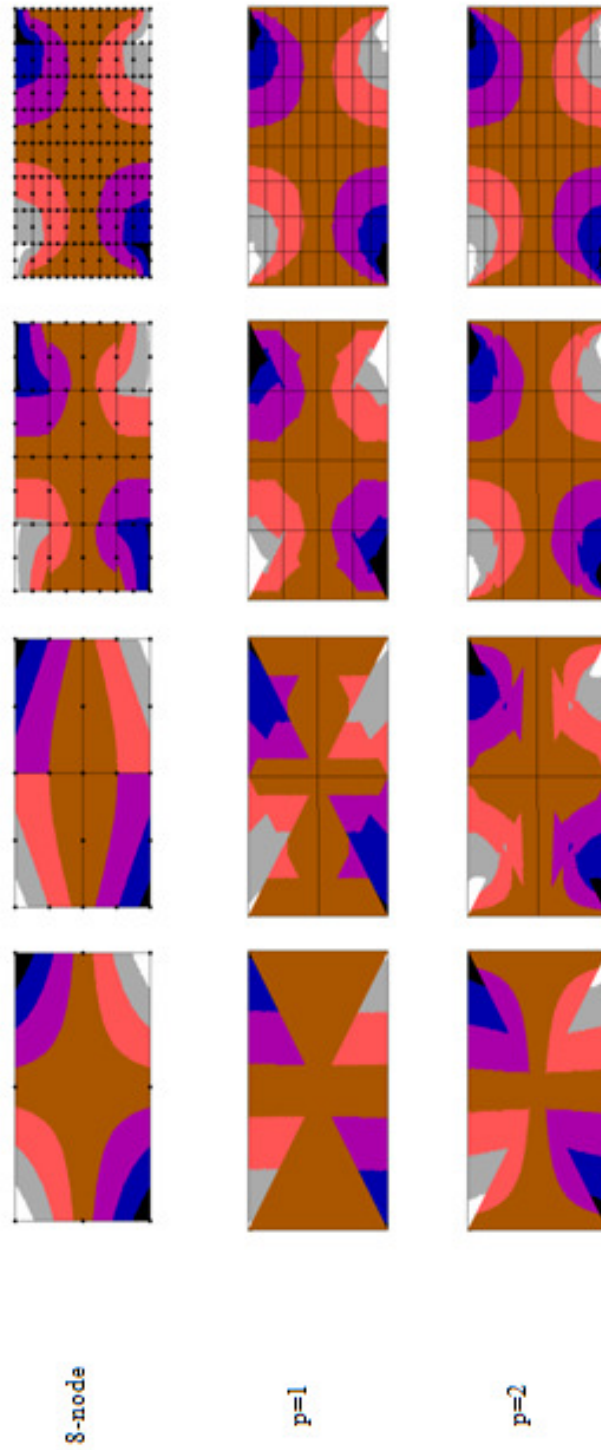


Figure 4.13 Convergence of τ_{xy} -component of stress for problem 2

□

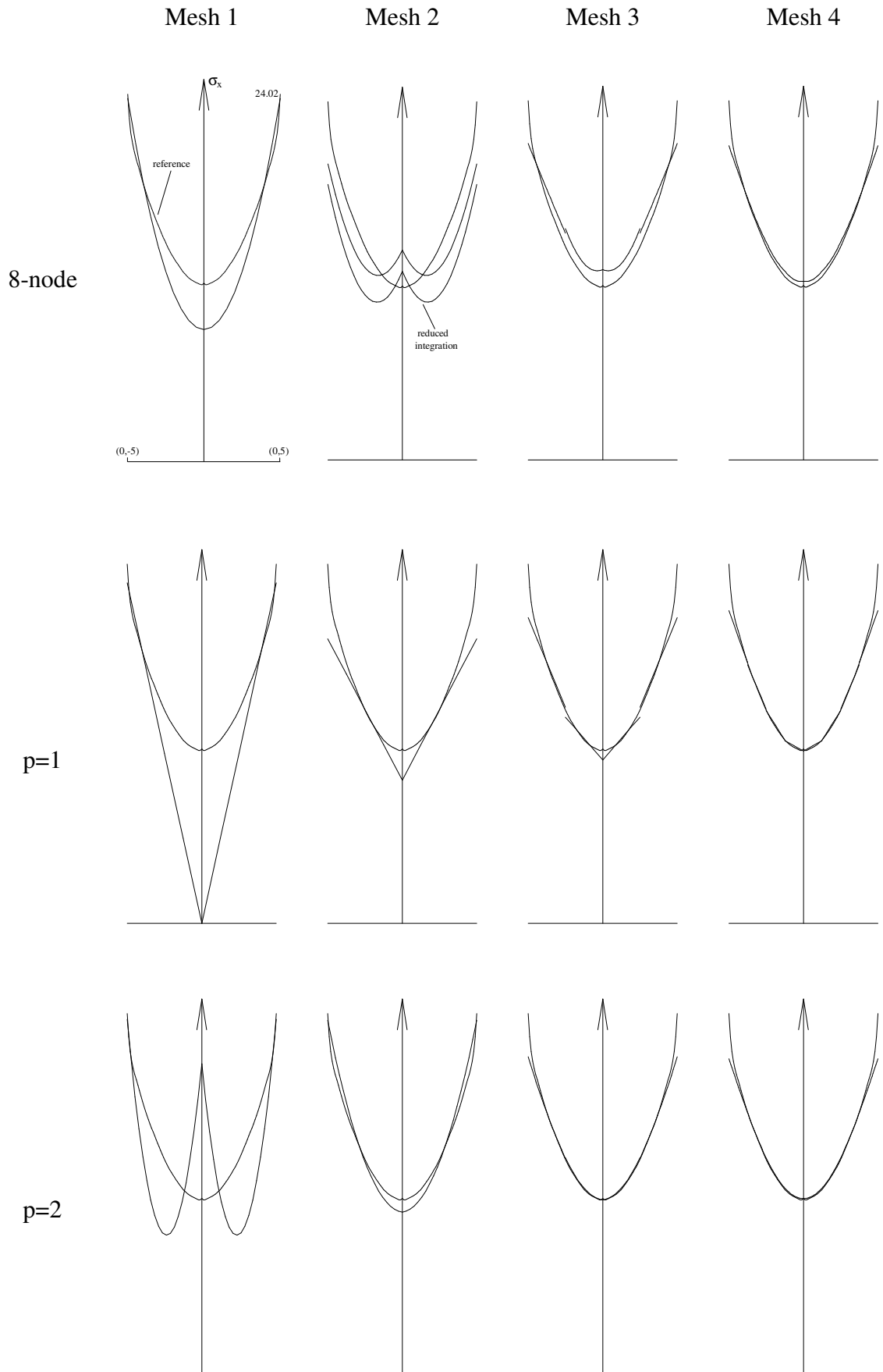


Figure 4.14 Convergence of σ_x along line $x=0$ for problem 2

4.3 DISCUSSION OF RESULTS

Although it is appreciated that the results presented in this chapter are somewhat limited, it is felt that a number of useful observations may be made.

For problem 1 where a good estimate of the true solution is available and the strain energy of the exact error was therefore calculable, it is seen that the 8-noded element performs better than the linear equilibrium element but less well than the quadratic equilibrium element. This picture of behaviour is reinforced in the evolution of stress distribution with h-type refinement where it is seen that the 8-noded element gives smoother and more realistic predictions of the true distribution of stress. Whilst it has not been possible to determine a sufficiently accurate prediction of the exact solution to problem 2, similar statements may be made regarding the smoothness of the stress fields. An explanation for the improved smoothness of the stress fields obtained using the 8-noded element over those of the linear equilibrium element is that the 8-noded element whilst containing complete linear stress fields within its formulation also contains an number of quadratic terms which help to reduce discontinuities.

With regard to the displacements it is seen that for both problems the equilibrium elements provides realistic yet discontinuous solutions. The edgewise linear displacements provided by the linear equilibrium element are, however, considerably less palatable than the continuous ones achieved using the 8-noded displacement element.

The reason that reduced integration is often used with the 8-noded element is clearly demonstrated for problem 1 where it is seen that the strain energy is significantly closer to the exact solution especially for the coarser meshes.

In terms of the computational effort required to generate and solve systems of equations for the two elements being compared, the following may be noted. The linear equilibrium element requires considerably more computational effort to generate the stiffness matrix for an individual element. Although it would require optimised codes to provide an accurate figure, the author is prepared to bet that the factor involved will be at least an order of magnitude. As already noted, whilst the numbers of degrees of freedom occurring in the structural stiffness matrix are the same for single elements, with uniform mesh refinement this number grows faster for the linear equilibrium element than for the 8-noded element. For the 8-noded element the number of dofs for a uniform mesh of $n \times n$ elements is $2(3n^2 + 4n + 1)$ whilst for the linear equilibrium element the number of dofs is $4(2n^2 + 2n)$. The factor by which the number of degrees of freedom for the linear equilibrium element grows over and above that of the 8-noded element is $4n/(3n+1)$ which has a limiting value of $4/3$ as n tends to infinity. The time

taken to solve the structural equations is approximately proportional to the square of the number of degrees of freedom. Thus, in the limit as n tends to infinity, the time factor required to solve the structural equations for the linear equilibrium element over and above that required for the 8-noded element will always be less than $16/9$.

In summary then it is seen that the 8-noded displacement element appears to provide superior results at a cheaper computational price than those achieved by the linear equilibrium element.

CHAPTER 5

Error Estimation with Variable Degree Equilibrium Elements

5.1 INTRODUCTION

In the previous two chapters it has been demonstrated how the variable degree equilibrium element can be used to obtain statically admissible solutions for a given problem. In conjunction with a confirming displacement element, equilibrium elements enable dual analysis to be performed which can lead to bounds on the value of the exact strain energy. The ability to bound the exact solution in this manner is a useful property since in the absence of the exact solution it enables an upper bound on the error energy to be determined. The main drawback with dual analysis, however, is that for each mesh examined two complete finite element analyses are required and this may be considered as expensive.

An alternative approach in which equilibrating element tractions are determined from the displacement finite element solution was first proposed by Ladevèze [15]. With such equilibrating element tractions it becomes possible to obtain statically admissible solutions in an efficient element-by-element manner.

Although attractive this method has certain potential problems of which the most significant is that the equilibrating element tractions are not uniquely determined from the displacement model nor are they generally the ones that would be obtained from a full re-analysis with equilibrium elements. A physical interpretation of the Ladevèze method reported by Maunder [16] illustrates this very clearly. In this interpretation it is shown that the tractions obtained are dependent on the choice of the position of the so-called pole point used in decomposition of the nodal forces. Thus, whilst in a full dual analysis the statically admissible solution will be the best available in a global energy sense, statically admissible solutions obtained in an element-by-element manner as proposed by Ladevèze will generally not lead to this optimum solution. In other words, the solution obtained whilst being a valid statically admissible solution to the problem is generally further away from the exact solution than that obtained by full re-analysis.

The consequence of this is that whilst strict upper bounds on the error energy are always achieved, the bounds may be too wide to provide effective error estimation. Error estimators based on statically admissible estimated stress fields derived in the aforementioned manner have been tested in [17]. In this research the statically

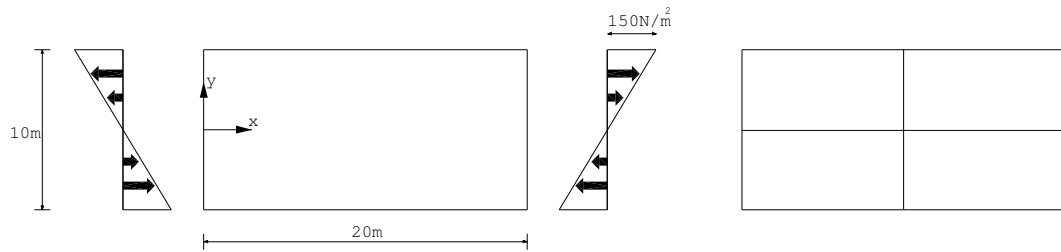
admissible stress fields were obtained using an equilibrium element of just sufficient degree of approximation so as to be able to equilibrate the equilibrating element tractions achieved by the Ladevèze technique. Thus, for example, equilibrium elements with linear degree of approximation were used to obtain statically admissible solutions for four-noded displacement elements. However, there is no reason why equilibrium elements with higher degree of approximation could not be used. Although such an approach is likely to lead to a reduction in the upper bound of the error energy as achieved from low degree equilibrium elements, it remains to be seen if this reduction is of any significance in terms of the effectivity of an error estimator. This question will now be investigated.

5.2 EXAMPLE OF THE LADEVÈZE/MAUNDER TECHNIQUE

The Ladevèze/Maunder technique can be used to obtain equilibrating element tractions which are then applied to an equilibrium element to obtain statically admissible stress fields:

- 1) Perform a (displacement) finite element analysis to obtain element nodal forces. Model nodes are in equilibrium under the action of element nodal forces and applied consistent nodal forces and reactions. (unique for given displacement element)
- 2) Redistribution of the nodal forces to the element edge extremities using the Ladevèze-Maunder technique such that element equilibrium is maintained and co-diffusivity of the redistributed forces between elements and on the static boundary is achieved. (dependent on choice of position of pole point)
- 3) Transform the edge extremity forces into equilibrating edge tractions. (unique although self-balancing traction modes may be added)
- 4) Determine statically admissible stress fields equilibrating with the edge traction distributions independently for each element. (unique for given equilibrium element)

Having outlined the basic steps involved in the Ladevèze/Maunder technique a numerical example will now be given. Consider the problem shown in figure 5.1.



(a) Geometry and boundary conditions

(b) Mesh

Figure 5.1 Constant moment problem

The exact stress field for this problem is:

$$\begin{aligned}\sigma_x &= 30y \\ \sigma_y &= 0 \\ \tau_{xy} &= 0\end{aligned}\tag{5.1}$$

and for a Young's Modulus of $E = 210\text{N/m}^2$, a Poisson's Ratio of $\nu = 0.3$ and a material thickness of $t = 0.1\text{m}$, the strain energy is:

$$U = \frac{2500}{7} \approx 357.14\text{Nm}\tag{5.2}$$

The applied nodal forces and element nodal forces recovered from a conventional displacement analysis of the mesh shown in figure 5.1(b) and using 4-noded elements are shown in figure 5.2. So as to be able to show both element and nodal equilibrium in a single diagram, the elements have been shrunk. Only the forces acting on one element have been dimensioned. The remaining values can be determined from the symmetry of the problem.

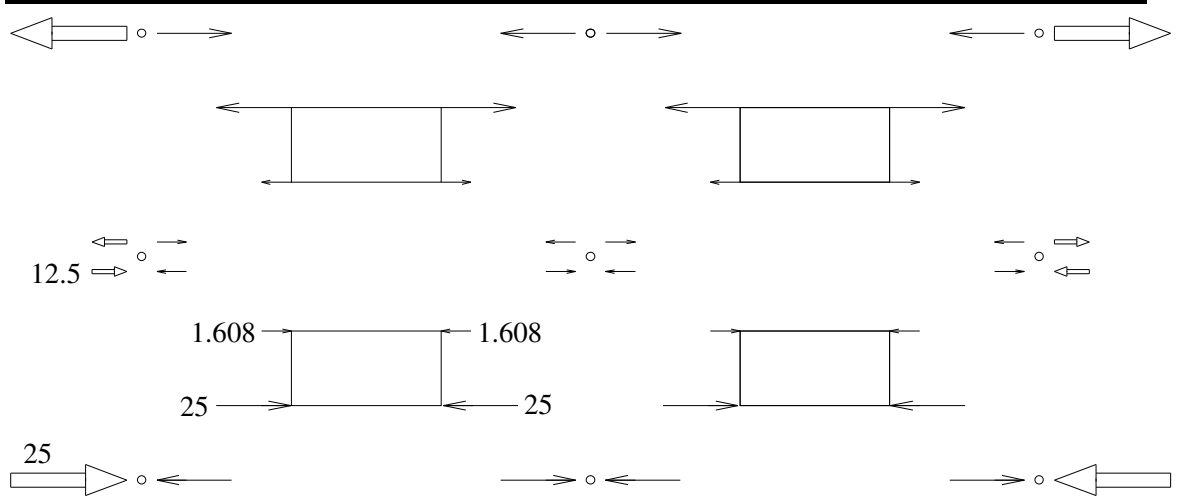


Figure 5.2 Element and nodal equilibrium ($U_h=253.41130$)

Applying the Ladevèze/Maunders technique to the finite element results shown in figure 5.2 leads to the edge extremity forces shown in figure 5.3. Note that for all examples given in this chapter the position of the decomposition or pole point is as recommended in [16].

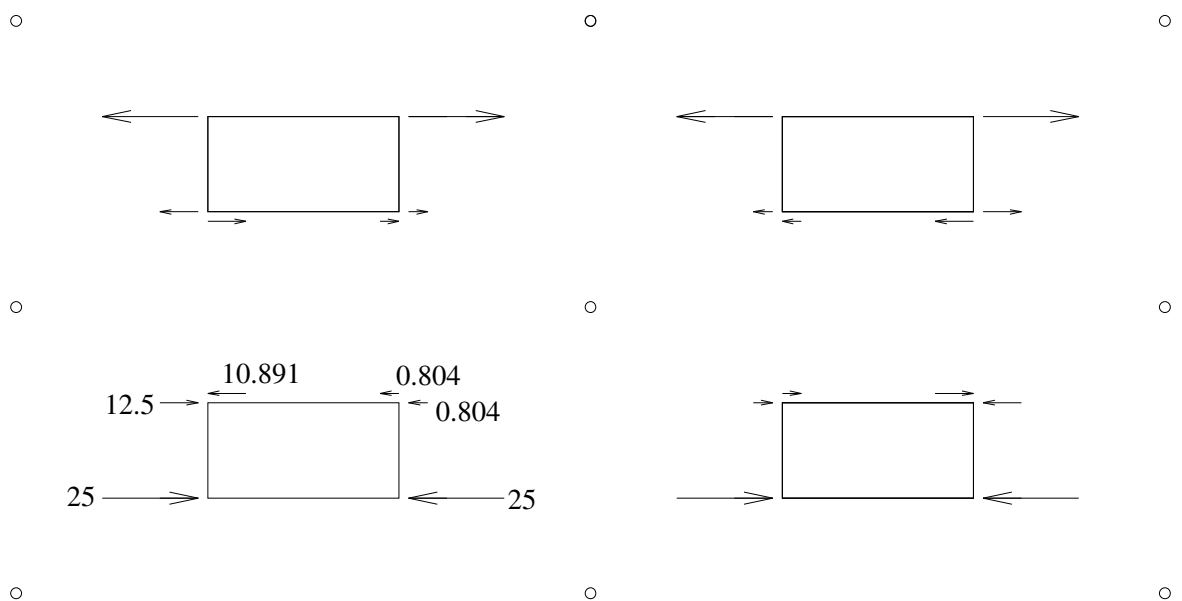


Figure 5.3 Element equilibrium with edge extremity forces

The element edge tractions are determined from the edge extremity forces and are shown in figure 5.4.

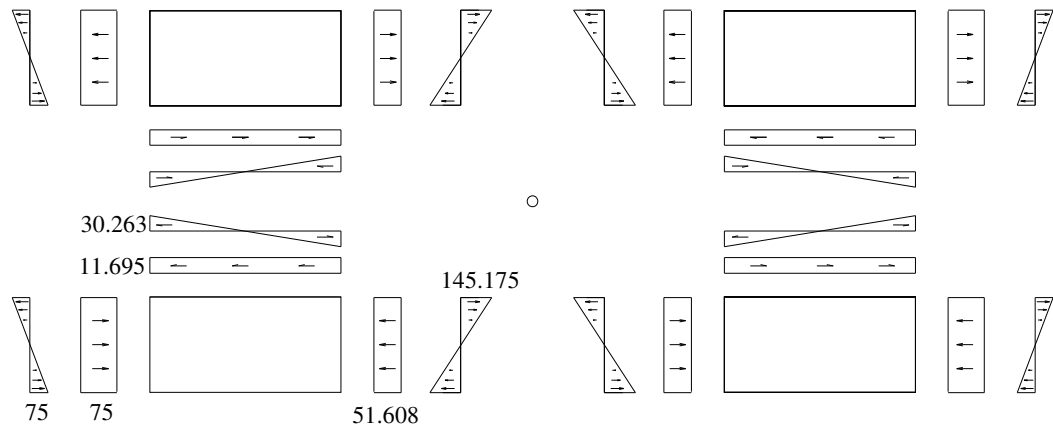


Figure 5.4 Element equilibrium with boundary tractions after L/M decomposition

The final stage is to apply the element edge tractions to an equilibrium element individually for each element. This has been done using the linear macro element and the results are shown in figure 5.5.

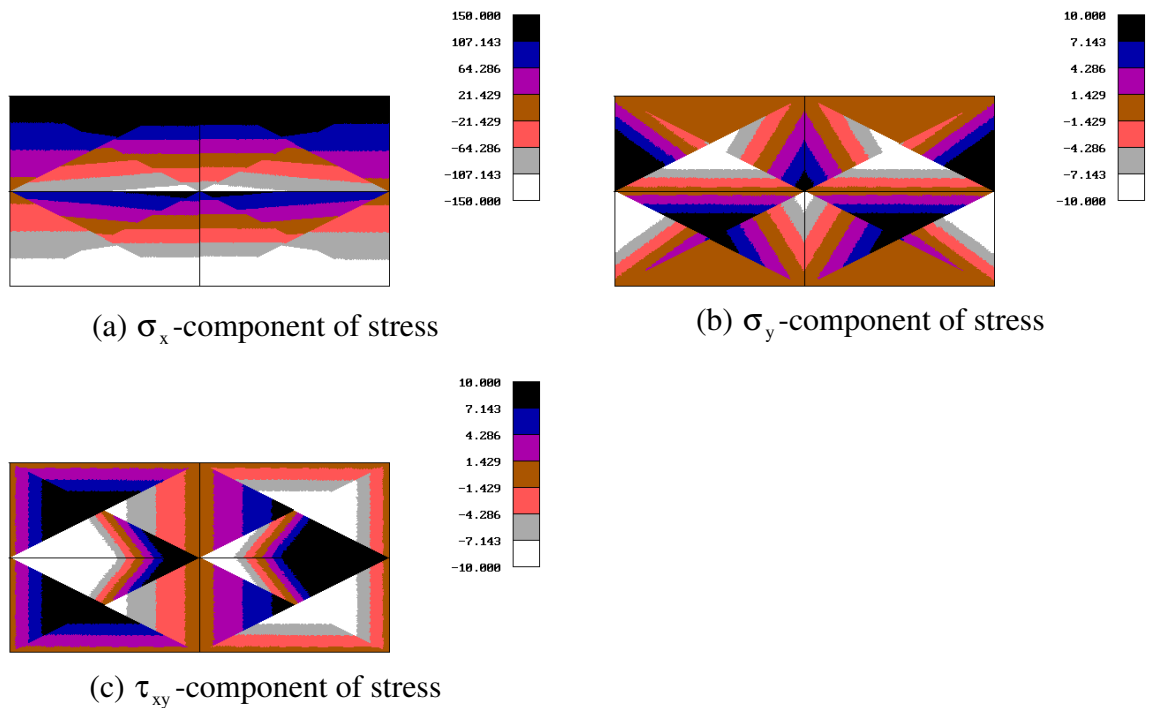


Figure 5.5 Linear statically admissible stress fields corresponding to boundary tractions of figure 5.4 ($\tilde{U}=480.43618$)

5.3 ERROR ESTIMATION

A brief synopsis of error estimation is now presented. The philosophy adopted in this presentation follows that of [18]. The case where the estimated stress field has the property of being statically admissible, the strain energy of the estimated error can be defined directly as the difference between the strain energies of the statically admissible estimated stress field and that of the conforming displacement finite element stress field. Further details of this philosophy and some numerical results for a number of other error estimators are shown in appendix 5.

The **exact error** in the finite element stress field $\boldsymbol{\sigma}_e$ is determined as the difference between the exact stress field $\boldsymbol{\sigma}$ and the finite element stress field $\boldsymbol{\sigma}_h$:

$$\boldsymbol{\sigma}_e = \boldsymbol{\sigma} - \boldsymbol{\sigma}_h \quad (5.1)$$

The strain energies corresponding to the exact and the finite element stress fields are:

$$U = \frac{1}{2} \int_{\Omega} \boldsymbol{\sigma}^T \boldsymbol{\epsilon} \, d\Omega \quad (5.2a)$$

$$U_h = \frac{1}{2} \int_{\Omega} \boldsymbol{\sigma}_h^T \boldsymbol{\epsilon}_h \, d\Omega \quad (5.2b)$$

and the strain energy of the exact error is:

$$U_e = \frac{1}{2} \int_{\Omega} \boldsymbol{\sigma}_e^T \boldsymbol{\epsilon}_e \, d\Omega = U + U_h - \int_{\Omega} \boldsymbol{\sigma}_h^T \boldsymbol{\epsilon}_h \, d\Omega \quad (5.3)$$

For force driven problems (homogeneous kinematic boundary conditions):

$$\int_{\Omega} \boldsymbol{\sigma}_h^T \boldsymbol{\epsilon}_h \, d\Omega = \int_{\Gamma} \boldsymbol{t}^T \boldsymbol{u}_h \, d\Gamma = 2U_h \quad (5.4)$$

hence:

$$U_e = U + U_h - 2U_h = U - U_h \quad (5.5)$$

The **estimated error**¹ in the finite element stress field $\tilde{\boldsymbol{\sigma}}_e$ is determined as the difference between an estimated stress field $\tilde{\boldsymbol{\sigma}}$ and the finite element stress field $\boldsymbol{\sigma}_h$.

$$\tilde{\boldsymbol{\sigma}}_e = \tilde{\boldsymbol{\sigma}} - \boldsymbol{\sigma}_h \quad (5.6)$$

The strain energy corresponding to the estimated stress field is:

$$\tilde{U} = \frac{1}{2} \int_{\Omega} \tilde{\boldsymbol{\sigma}}^T \tilde{\boldsymbol{\epsilon}} \, d\Omega \quad (5.7)$$

¹All estimated quantities are indicated with a tilde.

and the strain energy of the estimated error is:

$$\tilde{U}_e = \frac{1}{2} \int_{\Omega} \boldsymbol{\sigma}_e^T \tilde{\boldsymbol{\epsilon}}_e \, d\Omega = \tilde{U} + U_h - \int_{\Omega} \boldsymbol{\sigma}_e^T \boldsymbol{\epsilon}_h \, d\Omega \quad (5.8)$$

For force driven problems (homogeneous kinematic boundary conditions) and statically admissible estimated stress fields:

$$\int_{\Omega} \boldsymbol{\sigma}_e^T \boldsymbol{\epsilon}_h \, d\Omega = \int_{\Gamma} \boldsymbol{t}^T \mathbf{u}_h \, d\Gamma = \int_{\Gamma} \boldsymbol{t}^T \mathbf{u}_h \, d\Gamma = 2U_h \quad (5.9)$$

hence:

$$\tilde{U}_e = \tilde{U} + U_h - 2U_h = \tilde{U} - U_h \quad (5.10)$$

For statically admissible estimated stress fields the exact strain energy is bounded as given in equation(3.5a) i.e. $U_h \leq U \leq \tilde{U}$. Substituting equations 5.5 and 5.10 into this inequality leads to the following inequality:

$$0 \leq U_e \leq \tilde{U}_e \quad (5.11)$$

which shows that for statically admissible estimated stress fields the strain energy of the estimated error provides an upper bound on the strain energy of the exact error.

The effectivity of the estimated stress field is quantified in terms of the effectivity ratio β which is the ratio of the strain energy of the estimated error and the strain energy of the exact error:

$$\beta = \frac{\tilde{U}_e}{U_e} \quad (5.12)$$

For statically admissible estimated stress fields $\beta \geq 1$. For effective error estimation β should be close to unity and should tend to unity as the mesh is refined. It should be noted that the effectivity *ratio* β as defined here differs from the definition of the effectivity *index* θ generally used in current literature on error estimators. The relationship between these two quantities is given as $\theta = \sqrt{\beta}$. The strain energy quantities described above are evaluated at the individual element level. By summing all these quantities over all the elements of a model, values are obtained for the error in the model. It is these global values of strain energies and effectivity ratios that will be used in this chapter.

For the constant moment problem the following values are reported:

$$\begin{aligned}U &= 2500 / 7 \approx 357.14285 \\U_h &= 253.41130 \\ \tilde{U} &= 480.43618 \\U_e &= U - U_h = 103.73155 \\ \tilde{U}_e &= \tilde{U} - U_h = 227.02488 \\ \beta &= 2.1885\end{aligned}\tag{5.13}$$

5.4 NUMERICAL EXAMPLES

The Ladevèze/Maunders technique will now be used to obtain equilibrating element tractions for two planar problems. Statically admissible stress fields will then be determined from these tractions using the variable degree equilibrium element developed in this text.

5.4.1 PROBLEM 1: Parabolic shear problem

The problem shown in figure 5.6 involves a rectangular membrane loaded with static boundary conditions consistent with the quadratic statically admissible stress field typically associated with a simply supported beam under the action of a transverse shear force.

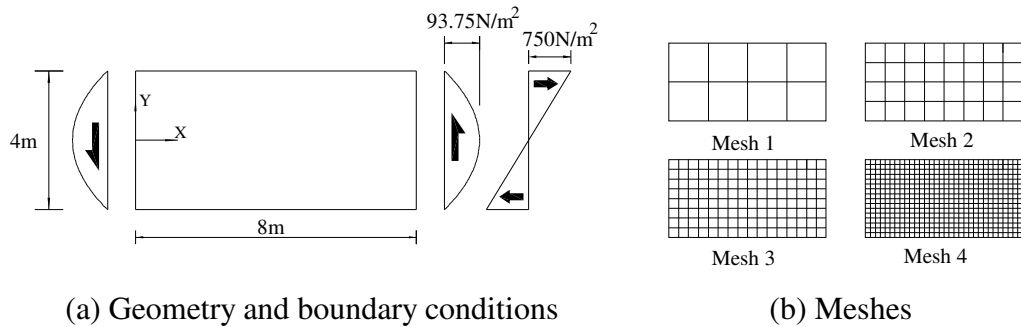


Figure 5.6 Problem 1

The exact stress field for this problem is:

$$\begin{aligned} \sigma_x &= 46.875xy \\ \sigma_y &= 0 \\ \tau_{xy} &= 93.75 - 23.4375y^2 \end{aligned} \tag{5.14}$$

For a Young's Modulus of $E = 3 \times 10^7 \text{ N/m}^2$, a Poisson's Ratio of $\nu = 0.3$ and a material thickness of $t = 1 \text{ m}$, the strain energy for the problem is:

$$U = \frac{239}{6000} \approx 0.03983 \text{ Nm} \tag{5.15}$$

This problem was taken from [17]. In this reference the Ladevèze/Maunder technique is used to determine equilibrating element tractions and a statically admissible stress field is recovered using a macro element with a linear degree of approximation. As such it provides results with which those generated in the present report can be checked. This problem has been further studied in [13,19] where the effectivity ratios of a number of other error estimators were presented.

5.4.2 PROBLEM 2: Problem 3 of chapter 3

This problem is defined in chapters 3 of this report but is shown again for convenience in figure 5.7.

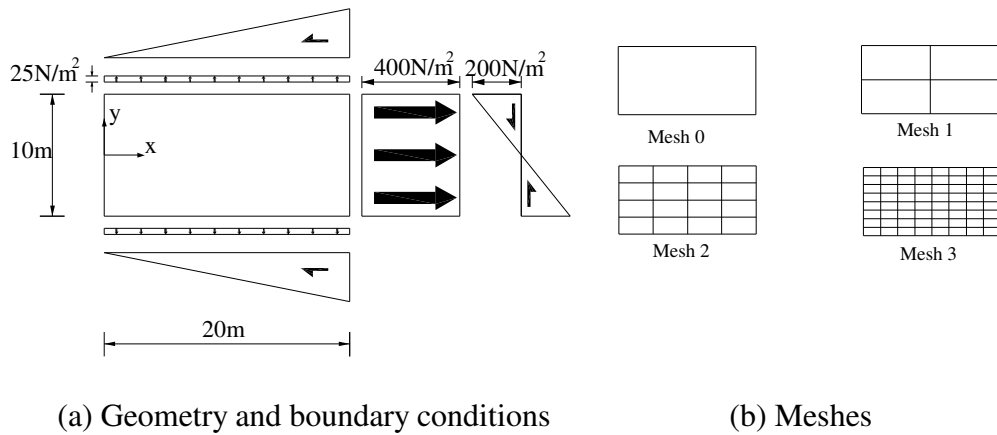


Figure 5.7 Problem 2

The static boundary conditions are defined by the following stress field which does not correspond to the exact solution within the domain.

$$\begin{aligned}
 \sigma_x &= x^2 \\
 \sigma_y &= y^2 \\
 \tau_{xy} &= -2xy
 \end{aligned}
 \tag{5.16}$$

For a Young's Modulus of $E = 210 \text{ N/m}^2$, a Poisson's Ratio of $\nu = 0.3$ and a material thickness of $t = 0.1 \text{ m}$, the converged finite element strain energy for the problem is:

$$U \approx 2041.602291 \text{ Nm}
 \tag{5.17}$$

Results for the two problems in terms of strain energies and effectivity ratios are tabulated in tables 5.1 and 5.2 respectively. The results for three values of p i.e. $1 \leq p \leq 3$ are reported. The values quoted under the headings \tilde{U}_{opt} and β_{opt} are optimum values obtained using full re-analysis with an equilibrium model.

p	Mesh	1	2	3	4
1	\tilde{U}	0.04336165	0.04153918	0.04041479	0.04000123
2		0.04265188	0.04099546	0.04019131	0.03993075
3		0.04258826	0.04095979	0.04017831	0.03992689
(i)	U_h	0.03487469	0.03847183	0.03948344	0.03974459
(i)	dof	30	90	306	1122
1	\tilde{U}_{opt}	0.03985243	0.03983452	0.03983340	0.03983333
2		exact	exact	exact	exact
3		exact	exact	exact	exact
1	β	1.71	2.25	2.66	2.89
2		1.56	1.85	2.02	2.09
3		1.55	1.82	1.98	2.05
1	β_{opt}	1.0038	1.0008	1.0001	1.0000
2		unity	unity	unity	unity
3		unity	unity	unity	unity

(i) refers to 4-noded displacement element model

Table 5.1 Results for problem 1

p	Mesh	1	2	3
1	\tilde{U}	2115.9247	2075.1713	2053.1304
2		2064.4385	2053.0407	2045.6574
3		2059.6215	2050.6501	2044.8232
(i)	U_h	1702.5974	1953.3584	2019.1561
(i)	dof	18	50	162
1	\tilde{U}_{opt}	2050.4228	2042.3103	2041.6552
2		2041.8093	2041.6150	2041.6026
3		2041.6240	2041.6027	2041.6022
1	β	1.219	1.380	1.513
2		1.067	1.129	1.180
3		1.053	1.102	1.143
1	β_{opt}	1.026	1.008	1.002
2		1.000	1.000	1.000
3		1.000	1.000	1.000

(i) refers to 4-noded displacement element model

Table 5.2 Results for problem 2

The way in which the effectivity ratios converge as the meshes are refined is shown in figure 5.8. For the purposes of comparison the effectivity ratio for another error estimator is also shown (β_2^b). This error estimator is one in which the estimated stress field is continuous and boundary admissible and is discussed in detail in [13,19] (a pre-review version of reference 19 is shown in appendix 5 of this report).

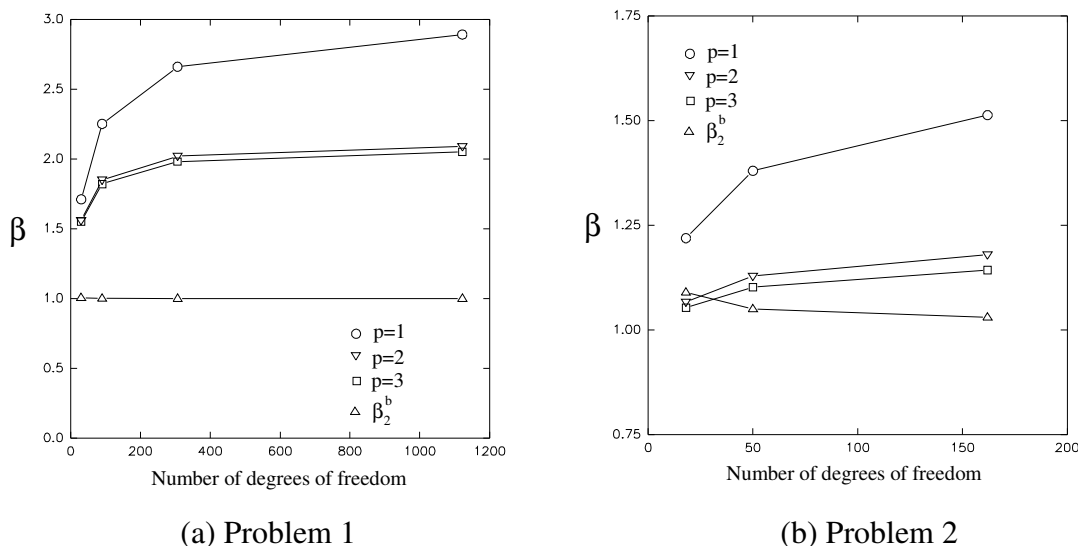
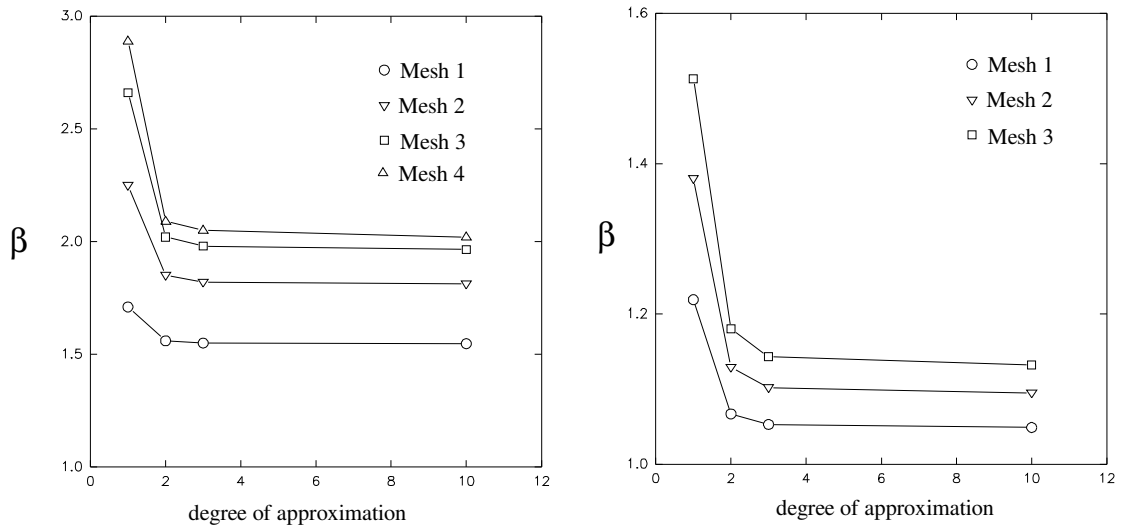


Figure 5.8 Convergence of effectivity ratios with degrees of freedom

Problem 1 is identical to that studied in [17] and the results for $p=1$ agree with those reported in this reference. It is seen that the effectivity ratios are greater than unity and therefore conform with the anticipated behaviour. Unfortunately, however, the effectivity ratios are considerably greater than unity and do not converge to unity as the mesh is refined i.e. the error estimator is not asymptotically exact. Thus although giving a strict upper bound on the error energy the error estimator is not good at predicting the error in a model.

The use of higher degrees of approximation to obtain the statically admissible estimated stress field has a beneficial effect as shown in the results. Whilst the upper bound nature of the error energy is retained such p -type refinement has the effect of pulling the strain energy of the estimated error nearer to the true value. This effect is most pronounced for a refinement from $p=1$ to $p=2$ and becomes less pronounced as p increases. This last point is demonstrated in figure 5.9 which shows the convergence of the effectivity ratio with degree of approximation.



(a) Problem 1 (b) Problem 2
 Figure 5.9 Convergence of effectivity ratio with degrees of approximation

The effect of such p-type refinement on the estimated stress field is shown in figures 5.10 and 5.11 which show the stress fields for mesh 1 of problems 1 and 2 respectively. In these figures the finite element stress field is compared with the estimated stress field for $p=1,2$ and 10 and the exact stress field. The effect of p-type refinement is seen in the way in which the estimated stress field *within* a given element becomes smoother. In this figure the estimated stress fields although obtained in a piecewise manner have been plotted together on the same mesh.

Although p-type refinement is beneficial in improving the effectivity of the error estimator the problem remains that the effectivity ratio is still relatively large and does not converge to unity. The reason for this is that the rate of convergence of the strain energy of the estimated stress field (\tilde{U}) is less than that for the strain energy of the finite element stress field (U_h). The following explanation may prove helpful.

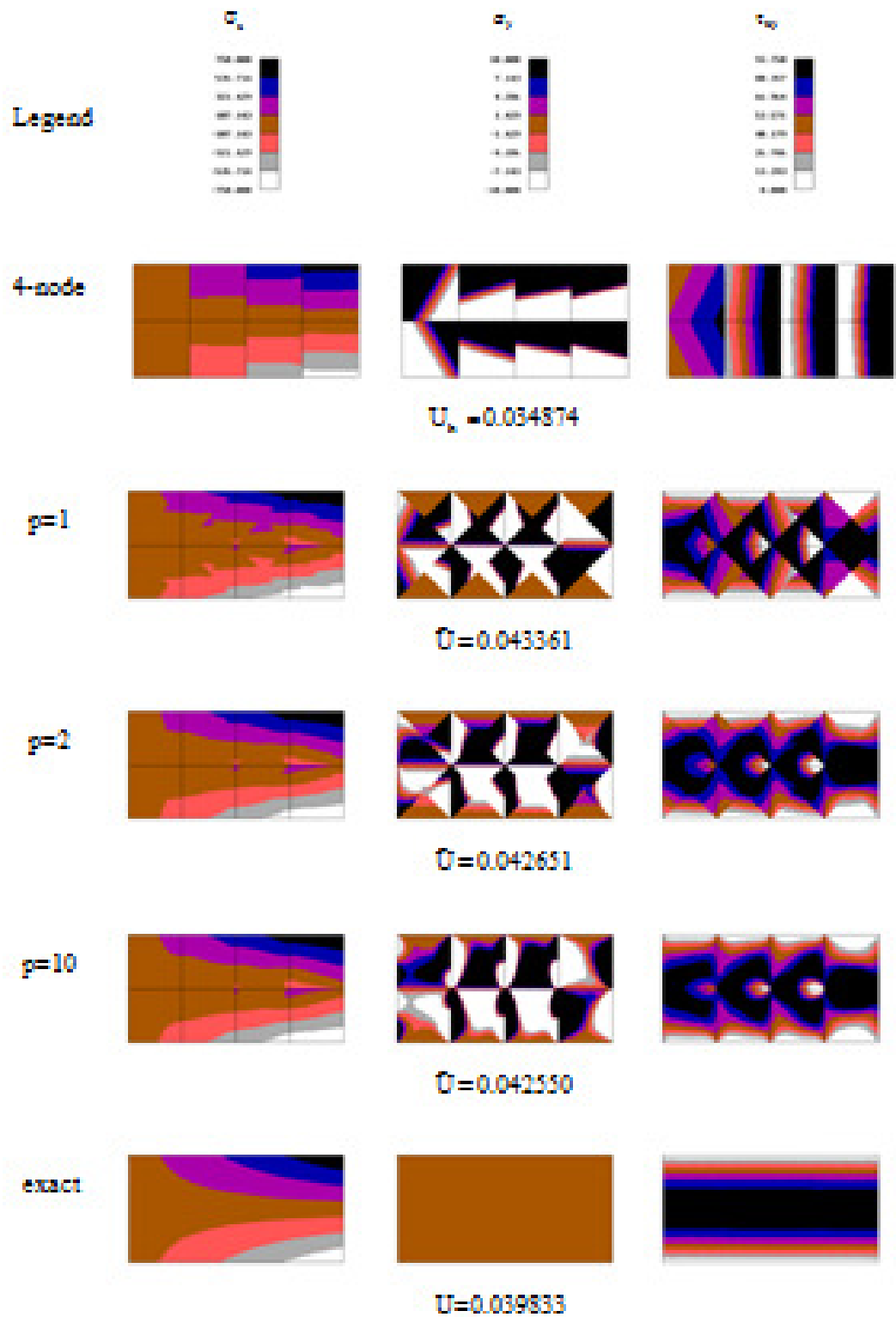


Figure 5.10 Stress fields for Problem 1 - Mesh 1

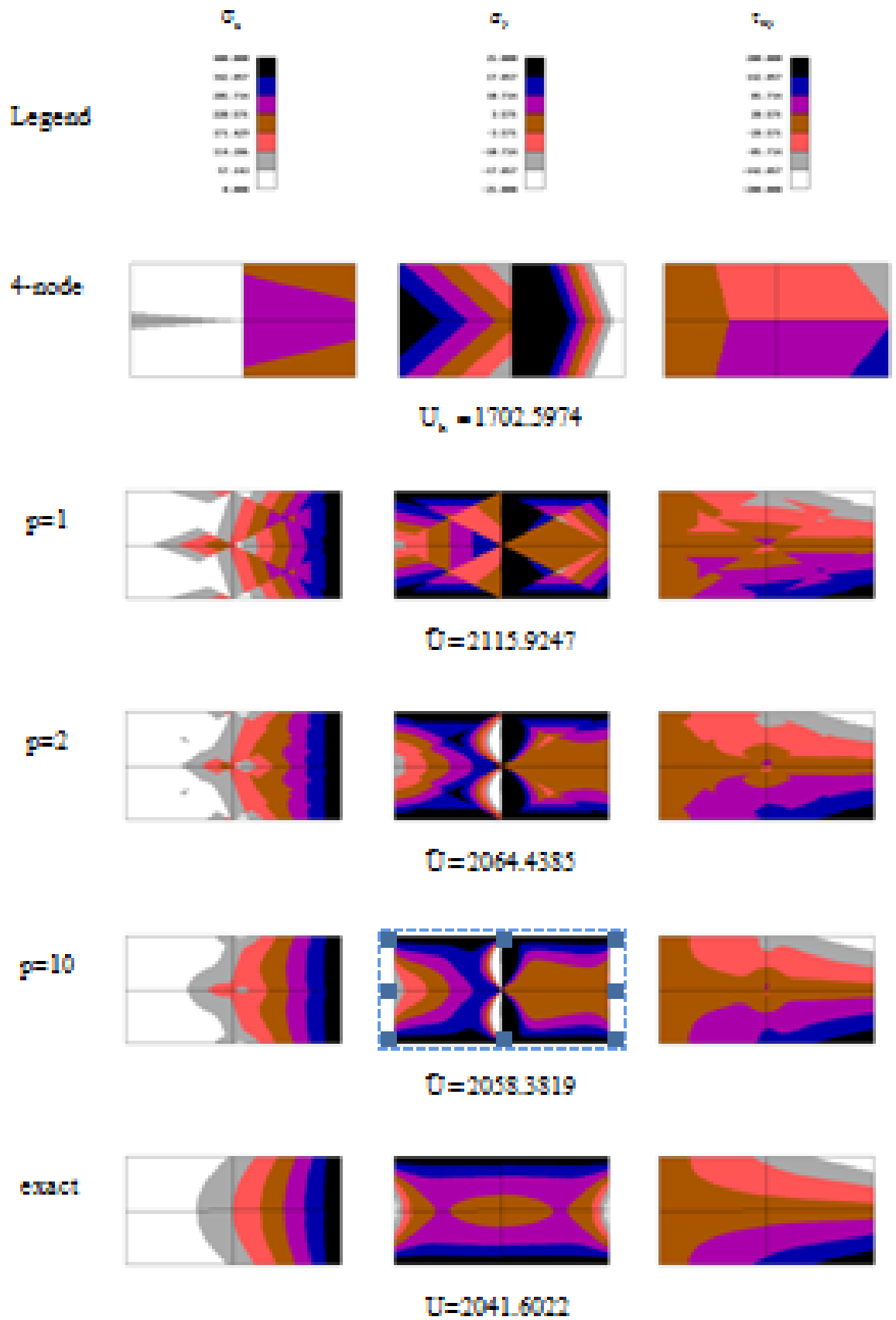


Figure 5.10 Stress fields for Problem 2 - Mesh 1

□

Let us assume asymptotic convergence for \tilde{U} and U_h :

$$U_h = U - \frac{1}{h^r} \quad (5.18a)$$

$$\tilde{U} = C + \frac{1}{h^{\tilde{r}}} \quad (5.18b)$$

where U is the exact strain energy and C is a constant the value of which is hopefully close to U . The characteristic dimension of an element is defined as h and the indices r and \tilde{r} give the rate of convergence of U_h and \tilde{U} respectively.

The effectivity ratio is then:

$$\beta = \frac{\tilde{U}_e}{U_e} = \frac{\tilde{U} - U_h}{U - U_h} = \frac{(C - U) + (h^{-\tilde{r}} + h^{-r})}{h^{-r}} \quad (5.19)$$

Assuming that \tilde{U} does converge to the exact value i.e. that $C=U$ then:

$$\beta = \frac{(h^{-\tilde{r}} + h^{-r})}{h^{-r}} = 1 + \frac{h^{-\tilde{r}}}{h^{-r}} \quad (5.20)$$

Thus with respect to the relative magnitudes of the rates of convergence of U_h and \tilde{U} (r and \tilde{r} respectively) we have the following possibilities:

$$\tilde{r} = r \quad \beta = 2 \quad (5.21a)$$

$$\tilde{r} < r \quad \beta \rightarrow \infty \text{ (divergence)} \quad (5.21b)$$

$$\tilde{r} > r \quad \beta \rightarrow 1 \text{ (convergence)} \quad (5.21c)$$

Thus it is seen that asymptotic convergence of the effectivity ratio will only occur when $\tilde{r} > r$ i.e. when the rate of convergence of \tilde{U} is greater than that of U_h . Such convergence could be called superconvergence. For the error estimator under discussion it is clear that $\tilde{r} < r$ and this is demonstrated in figure 5.12 where the logarithm of the absolute error in the strain energy is plotted against the logarithm of h . The slope of the graphs gives the rate of convergence and it is seen that the rate of convergence of the displacement model is greater than that for the statically admissible solution recovered in an elementwise fashion.

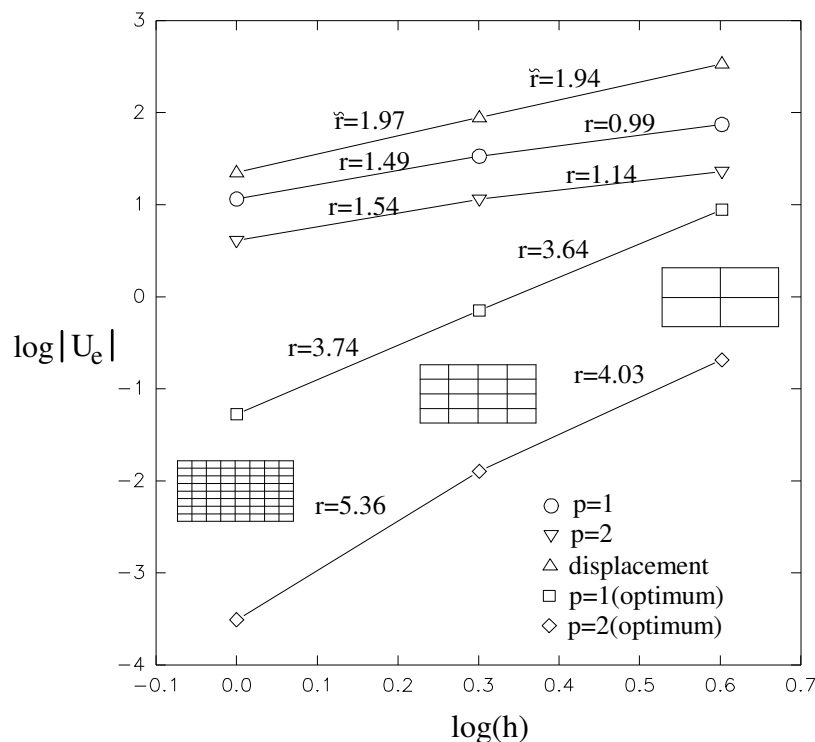


Figure 5.12 Convergence of error in strain energy for problem 2

Figure 5.13 shows the way in which the estimated stress fields converge with h-type refinement for problem 2. The stress fields shown are the ones recovered with a degree of approximation of $p=10$ and therefore are relatively smooth inside the elements. However, it is seen that the inter-element discontinuities converge very slowly. This is particularly evident for the σ_y -component of the stress along the vertical mesh lines $x=\text{constant}$. There exist two variables in the Ladevèze/Maunders technique which can be 'tuned'. These variables are the choice of pole point position and the addition of self-balancing traction modes. Whilst discussions have taken place regarding the possibilities of selecting these variables such as to minimise the global energy little work appears to have been done in actually proposing and implementing schemes whereby this can be achieved. The true minimum will obviously only be achieved through the solution of a global set of equations - something to be avoided if one wishes to retain the cheapness of computation associated with the elementwise calculations here used. Some criteria need to be proposed and tested for determining the magnitudes of these tuneable variables which only involve local calculation. One such criteria could be to select the magnitudes of the tuneable variables so as to minimise the discontinuities in stress at nodes. This seems to be a possibly fruitful area of further research that could be explored.

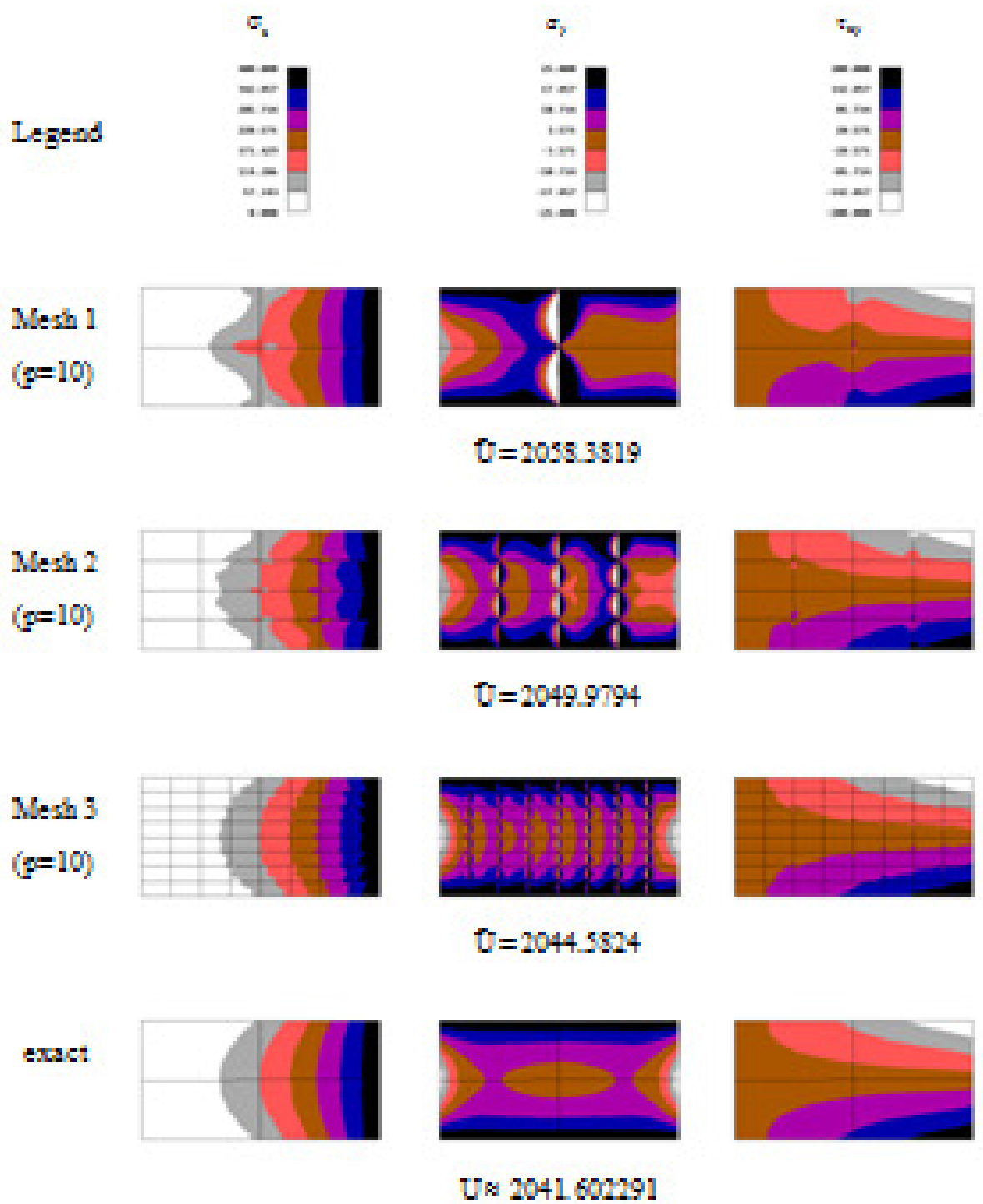


Figure 5.13 Stress fields for Problem 2 - p=10

CHAPTER 6

Conclusions and Recommendations

The traditional problem with general primitive-type equilibrium elements is that of the unpredictable propagation of spurious kinematic modes which leads to the intolerable possibility of unobtainable solutions for arbitrary mesh/load combinations. An example of such a case was given in the introduction to this report. Through the use of the macro element concept in which spurious kinematic modes are effectively controlled at the element level, the problem of propagation of spurious kinematic modes is solved.

In recent years the equilibrium element has enjoyed something of a renaissance firstly with the work of Maunder who has extended the original concept of the macro element and widened the potential uses of such elements to error estimation, and Almeida who has considered the analysis of elasto/plastic media using equilibrium elements of arbitrary geometry and degree of approximation. The generality of the definition of the elements in this latter work leads to meshes of elements for which spurious kinematic modes are generally present and solutions are obtained (where the applied loads are admissible) through the use of solution routines capable of 'solving' singular systems of equations.

This present work was motivated by a desire on the behalf of the author to attempt to combine the robust (skm free) properties of the macro element with the generality of definition of stress field in the work of Almeida. The result of this work is therefore a successful extension of the work of Maunder and Almeida and has led to the formulation and implementation of the robust variable degree macro element described in this report. This work has also been prepared for publication as a paper and the pre-review version of this paper is shown in appendix 6.

The research reported here has demonstrated that the number and nature of spurious kinematic modes present in macro elements of degree of approximation greater than two is the same as that for degree of approximation equal to two. This was an *a priori* prediction made by Maunder and Almeida. However, despite this work and despite this prediction no satisfactory proof exists or has been found to determine the number and nature of skm's present in an arbitrary arrangement of primitive elements. This then

remains an unanswered yet important question for which further research should be dedicated.

The formulation for the robust equilibrium element presented in chapter 2 of this report was written as a *FORTRAN* program capable of analysing arbitrary meshes of macro elements. The results shown in chapter 3 demonstrates some of the capabilities of this program. This work represents the authors first departure into the realm of p-type elements and the ability to model problems of high complexity with small numbers of high degree elements was found to be impressive. Whilst smooth polynomial functions are used the accurate prediction of behaviour at and near to singularities remains a problem.

The comparison between equilibrium and displacement elements which was made in chapter 4 of this report was rather revealing. Whilst the results presented were somewhat limited it was seen that the standard 8-noded displacement element performed better than the corresponding linear equilibrium element. The oft stated belief that equilibrium elements provide 'better stresses' than displacement elements was not substantiated by this study. Rather, it was seen that the 8-noded displacement element provided smoother and more realistic, albeit statically inadmissible, stresses than did the linear equilibrium element. This rather subjective view of the stress fields was confirmed by the values of the strain energy of the error which showed that the stress field for the 8-noded displacement element was nearer to the truth than the linear equilibrium element. Conversely, it was also observed that the displacements provided by the linear equilibrium element whilst being discontinuous were not unreasonable when compared with those given by the displacement element. Amongst advocates of equilibrium elements, the traditional displacement element gets something of a bad press. This study shows that this bad press is totally unfounded and more than a little misleading.

Chapter 5 of this report investigated how p-type refinement improved the estimated stress field recovered by the Ladevèze/Maunders technique. It was seen that a significant improvement in the effectivity of the error estimator could be achieved by such refinement. However, in its present state of development this error estimator is not asymptotically exact and whilst p-type refinement improved the absolute values of the effectivity ratio it did not do so sufficiently to cure the divergent behaviour of this error estimator. This error estimator possesses the unique and highly desirable property amongst existent error estimators that it provides a strict upper bound on the error. Further work is required to improve this error estimator and it would appear that here, p-type refinement has a useful role to play.

Finally, the finite element model shown in the introduction of this report which was seen to be unsolvable with primitive-type equilibrium elements will be solved with macro-elements.

A symmetric quarter of the model shown in figure 1.1 will be analysed using two quadrilateral macro elements. The dimensions of the plate are 20m by 20m and the central hole has a radius of 2m. The solution for a degree of approximation $p=5$ is shown in figure 6.1.

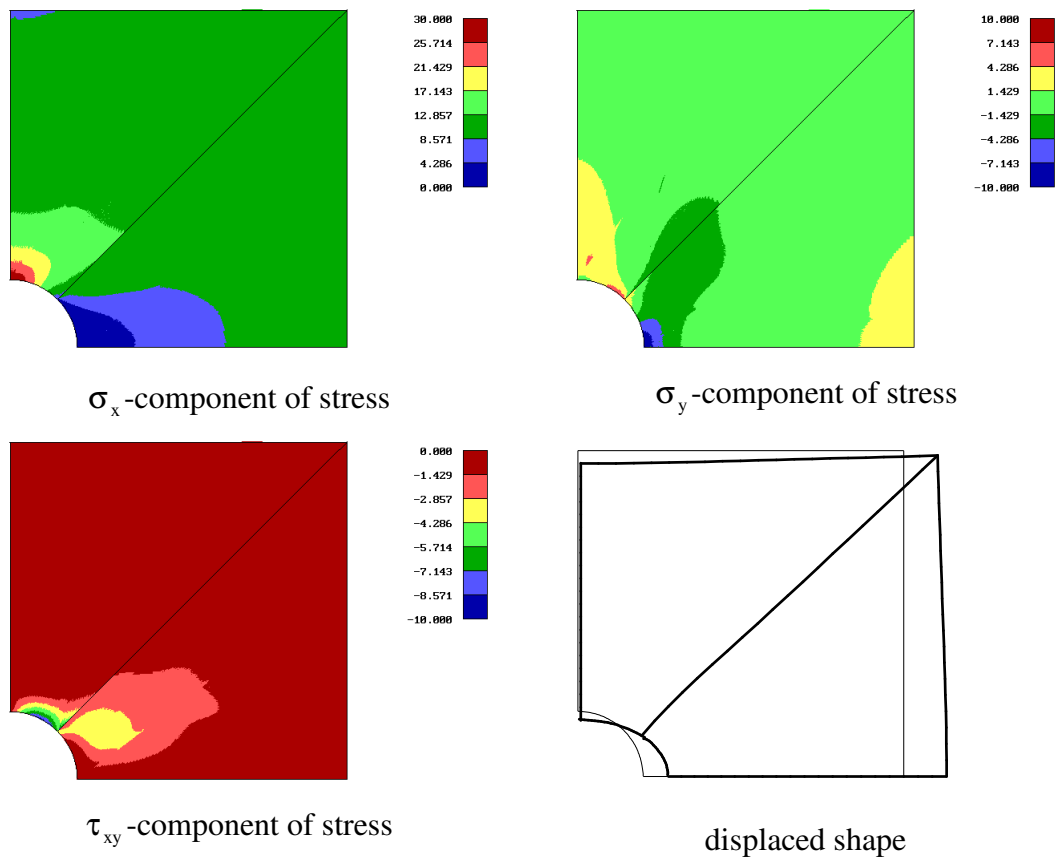


Figure 6.1 Equilibrium element solution for problem of figure 1.1 ($p=5$)

The problem admits a stress concentration in the σ_x -component of stress at the points $x=0, y = \pm 2m$ and the distribution of this component of the stress along the line $x=0m$ is shown in figure 6.2.

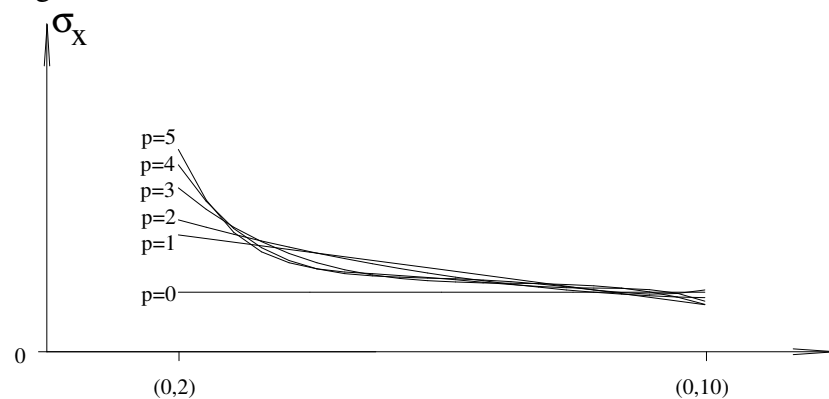


Figure 6.2 Distribution of σ_x -component of stress along line $x=0m$

APPENDICES

APPENDIX 1: Robust Equilibrium Elements: A Proposal

ROBUST EQUILIBRIUM ELEMENT
A Proposal for the Human, Capital and Mobility Project
'Advanced Finite Element Solution Techniques and Innovative Computer Architecture'
(May 1994 - May 1995)
by A.C.A. Ramsay

Background:

If equilibrium elements are to gain acceptance in the wider engineering environment then it is considered essential that they be free from spurious kinematic modes i.e. that all possible load-cases be admissible. Such equilibrium element could be described as *robust*. In addition to the traditional concept of dual analysis [1], equilibrium elements may also be used at the local, element level, in error analysis for the traditional displacement finite elements. The Ladevèze/Maunders technique [2] is an example of such local error analysis.

One path for the development of such robust equilibrium elements is available through the macro-element approach discussed in [3] for example. In this method equilibrium elements, each of which possess spurious kinematic modes, are assembled into a macro-element which is free from spurious kinematic modes.

A part of the research at I.S.T. has concentrated on general techniques for generating families of equilibrium elements [4]. This has been done without undue consideration of the elimination of spurious kinematic modes. At Exeter, the body of research into macro-elements is limited to linear and quadratic (stress field) quadrilateral membrane elements, and to linear and quadratic (moment field) quadrilateral plate bending elements. There is, therefore, a need to bring these two bodies of research together through the development of more general macro-type elements.

Proposal:

a) It is proposed to develop and implement a range of robust equilibrium macro-elements with the following characteristics:

1. to be of variable degree stress field,
2. to include both triangular and quadrilateral formats.

In conjunction with the work being undertaken at Exeter and Liege the performance of these robust elements in the field of local error estimation can then be studied.

Although initially the study will be conducted on the problem of plane, linear-elasticity, the work may be extended to include plate-bending elements and three-dimensional linear-elasticity. The performance of equilibrium elements in other fields such as that of structural dynamics and heat conduction are also of interest and, time permitting, some studies in these areas will be performed.

b) It is further proposed that a study into the relative performance of the elements that have been developed at I.S.T. be conducted. The performance of the elements on a set of benchmark tests (those laid down in [5] can form a basis for these tests) will be collated and reported.

References:

- 1) F.J. de Veubeke, 'Displacement and Equilibrium Models in the Finite Element Method', in O.C. Zienkiewicz and G.S. Hollister, 'Stress Analysis', Wiley, New York. (1965).
- 2) E.A.W. Maunders & W.G. Hill, 'Complimentary use of Displacement and Equilibrium Models in Analysis and Design', Proceedings of the sixth World Congress on Finite Element Methods, Banff, (1990).
- 3) E.A.W. Maunders & A.C.A. Ramsay, 'Quadratic Equilibrium Elements', Proceedings of the seventh World Congress on Finite Element Methods, Monte-Carlo, (1993).
- 4) J.P.B. Moitinho de Almeida & J.A. Teixeira de Freitas, 'Continuity Conditions for Finite Element Analysis of Solids', Int. J. Num. Meth. in Eng. Vol. 33, 845-853 (1992).
- 5) A.C.A. Ramsay, 'Finite Element Shape Sensitivity and Error Measures', Ph.D. Thesis, University of Exeter (1994).

APPENDIX 2: Curious Convergence Characteristics

It was demonstrated in section 2.2 of chapter 2 that ssm's and skm's could co-exist in equilibrium models if the matrix **D** was rank deficient i.e. if $s \neq 0$. In this appendix a problem demonstrating a curious type of convergence behaviour is given where the behaviour is directly attributable to the rank deficiency of **D**. Table A2.1 lists the number of skm's and ssm's for a quadrilateral primitive element.

p	0	1	2	3	4	5	6	7	8	9	10
m α	3	7	12	18	25	33	42	52	63	75	88
n γ	8	16	24	32	40	48	56	64	72	80	88
s	0	0	0	0	0	0	1	3	6	10	15
n _{skm}	2	6	9	11	12	12	12	12	12	12	12
n _{ssm}	0	0	0	0	0	0	1	3	6	10	15

Table A2.1 Quadrilateral primitive element characteristics

From table A2.1 it is seen that $s=0$ for degree of approximation $p < 6$. For $p \geq 6$ the value of s is non-zero and increases with increasing p . For this range of degree of approximation ssm's co-exist with skm's as highlighted in the table. The problem chosen in one for which the applied tractions are admissible and is shown in figure A2.1.

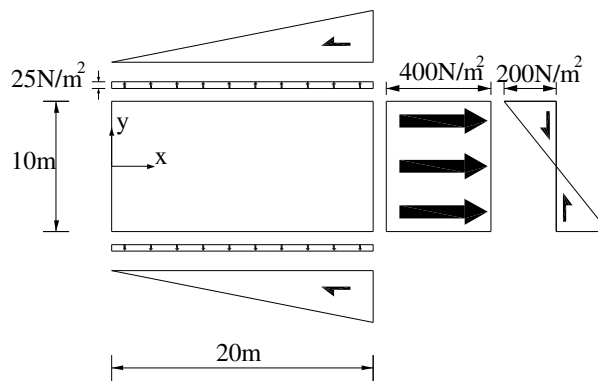


Figure A2.1 Plane elasticity problem

The static boundary conditions are determined from the following stress field

$$\begin{aligned}
 \sigma_x &= x^2 \\
 \sigma_y &= y^2 \\
 \tau_{xy} &= -2xy
 \end{aligned}
 \tag{A2.1}$$

Although statically admissible, this stress field is not kinematically admissible and is, therefore, invalid as the solution to this problem. The strain energy for the stress field of equation (A2.1) is $387125 / 189 \approx 2048.2804$.

For the analysis of this problem a plane stress constitutive relationship is used with a Young's modulus of $E = 210\text{N} / \text{m}^2$ a Poisson's ratio of $\nu = 0.3$ and a material thickness of $t=0.1\text{m}$. The following finite element strain energies were calculated.

p	2	3	4	5	6	7	8	9	10
U_h	2048.2804	2048.2804	2048.2804	2048.2804	2042.1350	2042.1350	2041.6208	2041.6208	2041.6028

Table A2.2 Finite element strain energy for quadrilateral primitive

In figure A2.2 the strain energy has been plotted against the degree of approximation. A rather curious 'stepped' type of convergence is noted. The reason for the lack of convergence in the range $2 \leq p \leq 5$ is clearly due to the fact that for this range of the degree of approximation $n_{ssm} = 0$. In fact the stress field for this range is the statically admissible one given in equation(A2.1). At $p=6$ a self-stressing mode is made available and is used to reduce the model strain energy. For the range $6 \leq p \leq 7$ no convergence is observed even though three more self-stressing modes have become available. This is reasonable since although ssm's may be available they will only be used if they can reduce the model strain energy. Clearly in this case they cannot and the strain energy remains unchanged. For $p=8$ convergence is again observed whilst for the range $8 \leq p \leq 9$ the strain energy again remains constant. Finally, for $p=10$ convergence is again noted and leads to a solution which has an error in energy of less than 0.00003%. The 'exact' strain energy for this problem is taken as $U=2041.602291$ and was determined by finite element analysis with a highly refined equilibrium model.

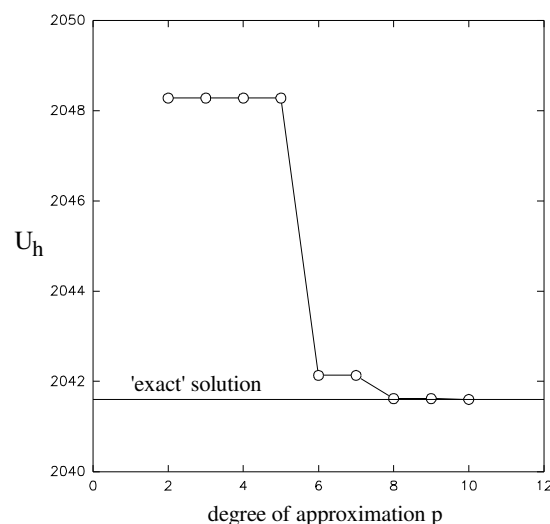


Figure A2.2 Convergence of finite element strain energy

The characteristics of a self-stressing mode are illustrated in figure A2.3 which shows the ssm made available when $p=6$ i.e. it is a plot of the stress field for equation (A2.1) subtracted from the finite element stress field for $p=6$.

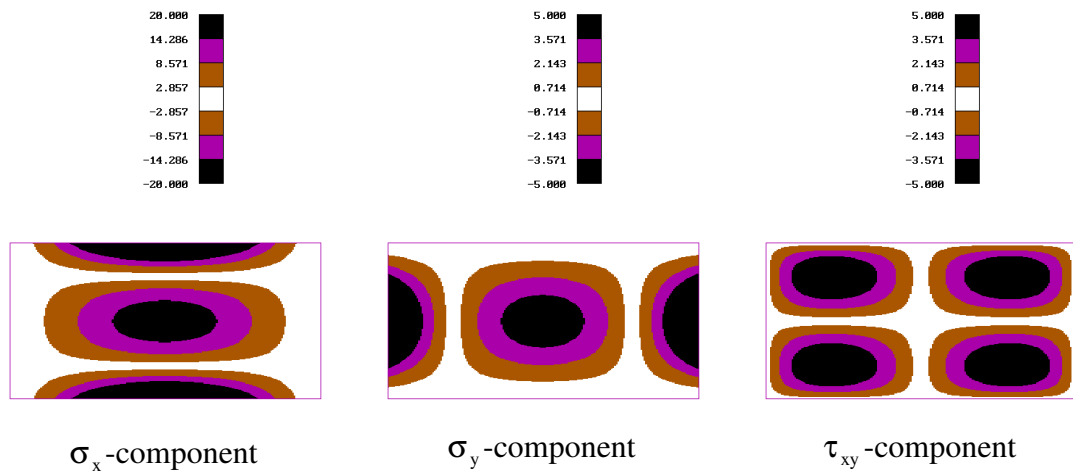


Figure A2.3 A self-stressing mode

Thus the curious convergence characteristics are explained through the existence of ssm's. This type of convergence, although not restricted to single primitive elements, is less likely to occur in meshes of elements (be they primitive or macro) where the number of ssm's even for low degrees of approximation is large.

APPENDIX 3: The Pseudo-Inverse: An Example

The pseudo-inverse for the structural stiffness matrix of an assembly of pin jointed trusses containing a mechanism will be used to obtain solutions when the load vector is admissible. Consider the four-bar linkage shown in figure A3.1. This linkage is clearly capable of motion if one rotates either of the links that have been restrained. However, it is also capable of supporting loads provided that the loads are such that they act along the axis of the restrained links i.e. forces q_2 and q_4 can be supported whilst q_1 and q_3 (individually) will induce motion of the linkage.

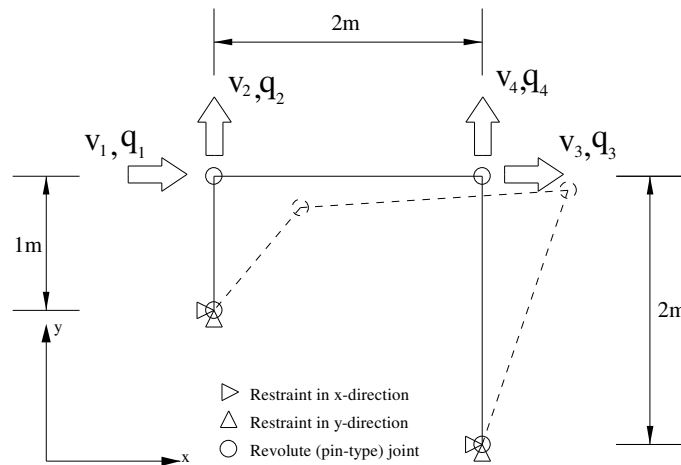


Figure A3.1 Four-bar linkage

The kinematic mode for the four-bar linkage is easily detected by visual inspection. For more complicated assemblies of truss elements kinematic modes are less easily detected and in these cases a mathematical approach is to be preferred.

One such approach which is to construct the structural stiffness equations for the assembly of truss elements and perform an eigen-analysis on these equations. Kinematic modes present in the structure will be revealed as those eigenvectors for which the corresponding eigenvalue is zero.

Assuming a Young's Modulus of $E = 1\text{N/m}^2$, and an area of $A = 2\text{m}^2$ for all the links leads to the following stiffness equations $\mathbf{Kv}=\mathbf{q}$:

$$\begin{bmatrix} 1 & 0 & -1 & 0 \\ 0 & 1 & 0 & 0 \\ -1 & 0 & 1 & 0 \\ 0 & 0 & 0 & 1 \end{bmatrix} \begin{Bmatrix} v_1 \\ v_2 \\ v_3 \\ v_4 \end{Bmatrix} = \begin{Bmatrix} q_1 \\ q_2 \\ q_3 \\ q_4 \end{Bmatrix} \tag{A3.1}$$

The four eigenvectors for this model are shown in figure A3.2.

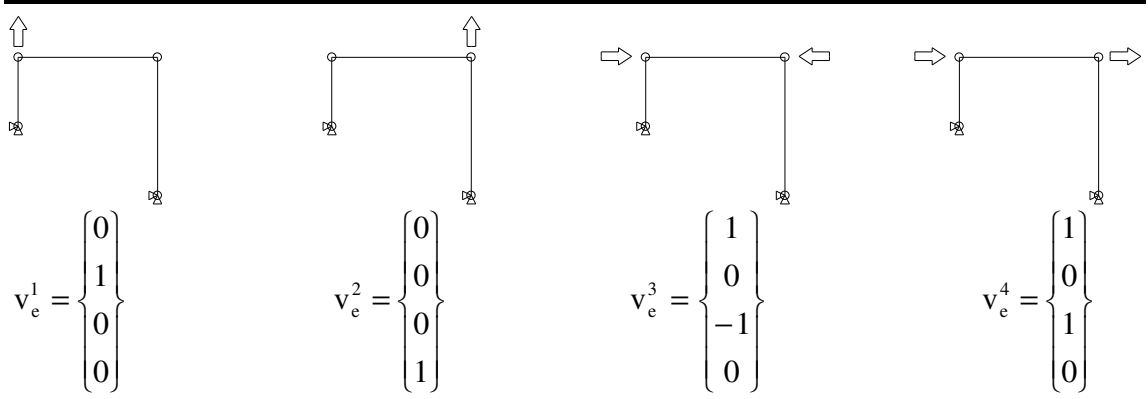


Figure A3.2 Eigenvectors for the four-bar linkage

The fourth eigenvector v_e^4 has a corresponding eigenvalue that is zero and, therefore, represents the single kinematic mode present in this model.

Singular value decomposition of the stiffness matrix \mathbf{K} of equation (A3.2) leads to:

$$\mathbf{K} = \mathbf{U}\mathbf{W}\mathbf{V}^T = \begin{bmatrix} -\frac{1}{\sqrt{2}} & -\frac{1}{\sqrt{2}} & 0 & 0 \\ 0 & 0 & 1 & 0 \\ \frac{1}{\sqrt{2}} & -\frac{1}{\sqrt{2}} & 0 & 0 \\ 0 & 0 & 0 & -1 \end{bmatrix} \cdot \begin{bmatrix} 2 & 0 & 0 & 0 \\ 0 & 0 & 0 & 0 \\ 0 & 0 & 2 & 0 \\ 0 & 0 & 0 & 1 \end{bmatrix} \cdot \begin{bmatrix} -\frac{1}{\sqrt{2}} & 0 & \frac{1}{\sqrt{2}} & 0 \\ \frac{1}{\sqrt{2}} & 0 & \frac{1}{\sqrt{2}} & 0 \\ 0 & 1 & 0 & 0 \\ 0 & 0 & 0 & -1 \end{bmatrix} \quad (\text{A3.2})$$

Partitioning into the form shown in section 2.7 of chapter 2 (equation 2.55) gives us:

$$\mathbf{K} = \mathbf{U}_1\mathbf{W}_1\mathbf{V}_1^T = \begin{bmatrix} -\frac{1}{\sqrt{2}} & 0 & 0 \\ 0 & 1 & 0 \\ \frac{1}{\sqrt{2}} & 0 & 0 \\ 0 & 0 & -1 \end{bmatrix} \cdot \begin{bmatrix} 2 & 0 & 0 \\ 0 & 2 & 0 \\ 0 & 0 & 1 \end{bmatrix} \cdot \begin{bmatrix} -\frac{1}{\sqrt{2}} & 0 & \frac{1}{\sqrt{2}} & 0 \\ 0 & 1 & 0 & 0 \\ 0 & 0 & 0 & -1 \end{bmatrix} \quad (\text{A3.3})$$

The pseudo-inverse of the stiffness matrix is now written as:

$$\mathbf{K} = \mathbf{V}_1 \mathbf{W}_1^{-1} \mathbf{U}^T = \begin{bmatrix} -\frac{1}{\sqrt{2}} & 0 & 0 \\ 0 & 1 & 0 \\ \frac{1}{\sqrt{2}} & 0 & 0 \\ 0 & 0 & -1 \end{bmatrix} \cdot \begin{bmatrix} \frac{1}{2} & 0 & 0 \\ 0 & \frac{1}{2} & 0 \\ 0 & 0 & 1 \end{bmatrix} \cdot \begin{bmatrix} -\frac{1}{\sqrt{2}} & 0 & \frac{1}{\sqrt{2}} & 0 \\ 0 & 1 & 0 & 0 \\ 0 & 0 & 0 & -1 \end{bmatrix} \quad (\text{A3.4})$$

which leads to the following expression for the pseudo-inverse of the stiffness matrix \mathbf{K} :

$$\mathbf{K}^* = \begin{bmatrix} \frac{1}{4} & 0 & -\frac{1}{4} & 0 \\ 0 & \frac{1}{2} & 0 & 0 \\ -\frac{1}{4} & 0 & \frac{1}{4} & 0 \\ 0 & 0 & 0 & 1 \end{bmatrix} \quad (\text{A3.5})$$

Note that the pseudo-inverse does not satisfy the condition $\mathbf{K}\mathbf{K}^* = \mathbf{I}$.

The non-unique solution to the stiffness equations can now be written in terms of the pseudo-inverse and the kinematic modes:

$$\mathbf{v} = \mathbf{K}^* \mathbf{q} + \varphi \mathbf{v}_e^4 \quad (\text{A3.6})$$

where \mathbf{v}_e^4 is the kinematic mode and φ is its amplitude.

For an *admissible applied load* say $\mathbf{q} = [0, 1, 0, 0]^T$ from equation (A3.6) we have:

$$\mathbf{v} = \mathbf{K}^* \begin{Bmatrix} 0 \\ 1 \\ 0 \\ 0 \end{Bmatrix} + \varphi \begin{Bmatrix} 1 \\ 0 \\ 1 \\ 0 \end{Bmatrix} = \begin{Bmatrix} 0 \\ 1 \\ 0 \\ 0 \end{Bmatrix} + \varphi \begin{Bmatrix} 1 \\ 0 \\ 1 \\ 0 \end{Bmatrix} \quad (\text{A3.7})$$

where φ is an arbitrary multiplier.

For an *inadmissible applied load* $\mathbf{q} = [1, 0, 1, 0]^T$ it is seen that the solution is:

$$\mathbf{v} = \mathbf{K}^* \begin{Bmatrix} 1 \\ 0 \\ 1 \\ 0 \end{Bmatrix} + \varphi \begin{Bmatrix} 1 \\ 0 \\ 1 \\ 0 \end{Bmatrix} = \begin{Bmatrix} 0 \\ 0 \\ 0 \\ 0 \end{Bmatrix} + \varphi \begin{Bmatrix} 1 \\ 0 \\ 1 \\ 0 \end{Bmatrix} \quad (\text{A3.8})$$

i.e. the pseudo-inverse maps the inadmissible load vector into the null vector leaving the solution as the kinematic mode. For each kinematic mode there is a corresponding mode of applied loads that is inadmissible.

APPENDIX 4: The Computer Program: A User Guide

The variable degree macro elements for which the theory was propounded in chapter 2 have been coded up into a *FORTRAN* computer program. This program, and a number of associated programs written to aid the user in the generation of meshes, application of boundary conditions and visualisation of the results, are discussed in this appendix.

A4.1 The Analysis Program

The analysis program EQUIL.FOR written for the analysis of arbitrary meshes of macro-type equilibrium elements offers the following features:

- both quadrilateral and triangular macro elements may be used in the same mesh,
- the degree of approximation can vary in the range $0 \leq p \leq 10$,
- constant body forces are available,
- isotropic thermal strains are available,
- element edges may be linear or quadratic curves,
- internal geometry of macro elements is variable through positioning of a central node,
- both plane stress and plane strain constitutive relations are available.

The program takes as input a data deck containing the complete information for the model. The format of this data deck is discussed later but first a brief description of what are considered the important aspects of the analysis program will be given.

The flow of information through the program is as follows. The data deck is read in to the program. The half-bandwidth and number of degrees of freedom are then determined. At this stage of the analysis the user is presented with the pre-analysis problem statistics an example of which is shown in figure A4.1.

The purpose of these statistics is to inform the user of the actual and the maximum possible values of certain important parameters. The actual number of nodes, edges, elements, edges to which kinematic boundary conditions are applied, edges to which static boundary conditions are applied, and property definitions are compared with the maximum possible value for these parameters. The maximum possible values for the various parameters listed is a program variable that can be changed in the *FORTRAN INCLUDE* file MAX.VAL. For any changes to take affect EQUIL.FOR must be re-compiled subsequent to any modifications that are made to these parameters. The vector {A} referred to in these statistics is the vector in which the final assembled equations will be stored within the program and constitutes the prime user of system memory.

PROBLEM STATISTICS FOR EXAMPLE.DAT			
	MAX POS VAL	ACTUAL VALUE	
NODES	5000	9	
EDGES	5000	15	
ELEMENTS	5000	6	
KIN. BOUN	100	3	
STA. BOUN	100	2	
PROPERTIES	20	2	
DIMENSION OF {A}	1000000	52932	
TOTAL NUMBER OF STRESS DOF IS			1760
TOTAL NUMBER OF DISP. DOF IS			858
REDUCED NUMBER OF DISP. DOF IS			330
HALF BANDWIDTH FOR REDUCED PROBLEM IS			264

Figure A4.1 Pre-analysis problem statistics

A loop over all macro-elements is then performed. Within this loop the stiffness matrix for each macro-element is formed. These matrices are then assembled into the structural stiffness matrix.

Because of the symmetric, banded nature of the structural stiffness matrix, only those coefficients appearing in the upper half-bandwidth are stored. These coefficients are stored in the vector {A} which also holds the amplitudes of the edge displacements and edge tractions.

Following assembly of the system equations, the static and kinematic boundary conditions are applied. The equations are then solved using a Gauss elimination method in a form suitable for taking advantage of the symmetric and banded properties of the equations.

The solution is then used to recover the amplitudes of the degrees of freedom that were condensed out during the formulation of the stiffness matrix for the macro-element i.e. the internal degrees of freedom for each macro-element. The amplitudes of the stress fields s are recovered and the strain energy for the model evaluated.

The post-analysis problem statistics are now listed and an example of these statistics is given in figure A4.2.

```

SYSTEM EQUATIONS FORMED
STATIC BOUNDARY CONDITIONS APPLIED
KINEMATIC BOUNDARY CONDITIONS APPLIED
STIFFNESS MATRIX DECOMPOSED
GLOBAL FORCE VECTOR DECOMPOSED
SOLUTION FINISHED
TIME TAKEN TO GENERATE AND REDUCE EQUATIONS = 556.31868130
TIME TAKEN TO SOLVE REDUCED EQUATIONS = 63.02197802
MODEL STRAIN ENERGY = 168516.455572
POTENTIAL ENERGY OF LOADS= 5268.72238317
TOTAL POTENTIAL ENERGY = 163247.733189
COMPLIMENTARY STRAIN ENERGY = 168660.790689

```

Figure A4.2 Post-analysis problem statistics

The first six lines of these statistics appear on the screen after the pertinent operation has been completed by the program. Useful measures of the efficiency of a program are the CPU times required to generate and to solve the system of equations. These are given and the model strain energy reported. Both pre- and post-analysis problem statistics are also written to a data file called MESSAGE.DAT.

A4.2 The Data Deck

The data deck is the method by which the user inputs data to the analysis program. The format of this data is important and is discussed in this section. In order to aid this discussion a sample data deck is shown in figure A4.4. This sample data deck relates to the example problem shown in figure A4.3.

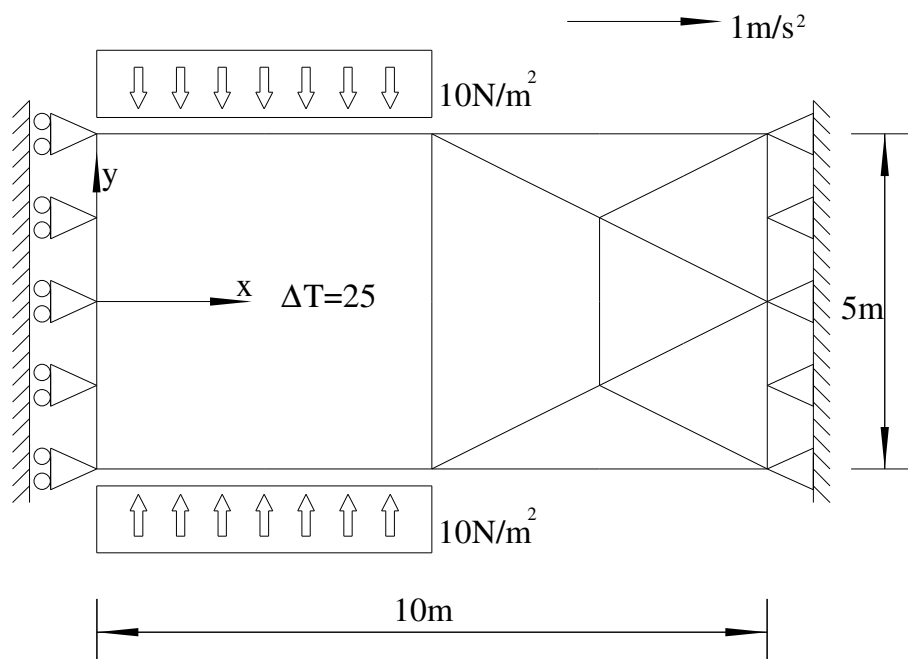


Figure A4.3 Example problem

The topology for the example problem is shown in figure A4.5.

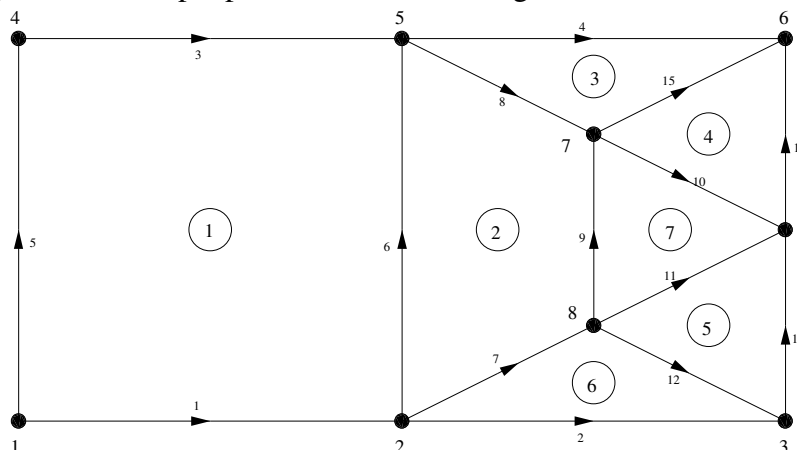


Figure A4.5 Topology for example problem

The model consists of two material regions. The first region is modelled by element number 1 and the second region by the remaining elements. Both regions have the same material properties of Young's modulus of $E = 1\text{N} / \text{m}^2$, Poisson's ratio of $\nu = 0.3$, a mass density of $\rho = 11\text{Kg} / \text{m}^3$ and a coefficient of linear thermal expansion of $\mu = 0.01 / ^\circ \text{C}$. For the first region the thickness is $t=1\text{m}$ and a plane stress constitutive relationship is used whilst the second region is 10m thick and uses a plane strain constitutive relationship.

Figure A4.6 shows the internal geometry of the macro-elements. The internal edges are shown as dotted lines. In figure A4.6(a) the geometry for the case of linear degree of approximation is shown. For this degree of approximation the assembly point for the quadrilateral macro-element must lie at the intersection of the diagonals so as to avoid problems with spurious kinematic modes. Although the program allows the user to define the internal geometry of macros through the positioning of the central node (i.e. the node corresponding to the assembly point) for the case of $p=1$ the program overrides this facility for the quadrilateral macro-element. For any other degree of approximation the position of the assembly point is arbitrary. If the user does not state a preference then the program defaults the position of the assembly point to the centre of mass of four unit masses placed at the vertices of the macro. The default internal geometry for $p \geq 2$ is shown in figure A4.6(b). Because element number 1 is square no difference is observed between figures A4.6(a) and A4.6(b). For element number 2 which is distorted the difference is clearly visible. For the triangular macro-elements the position of the assembly point is arbitrary and the program defaults it to the centre of mass of three unit masses placed at the vertices of the macro.

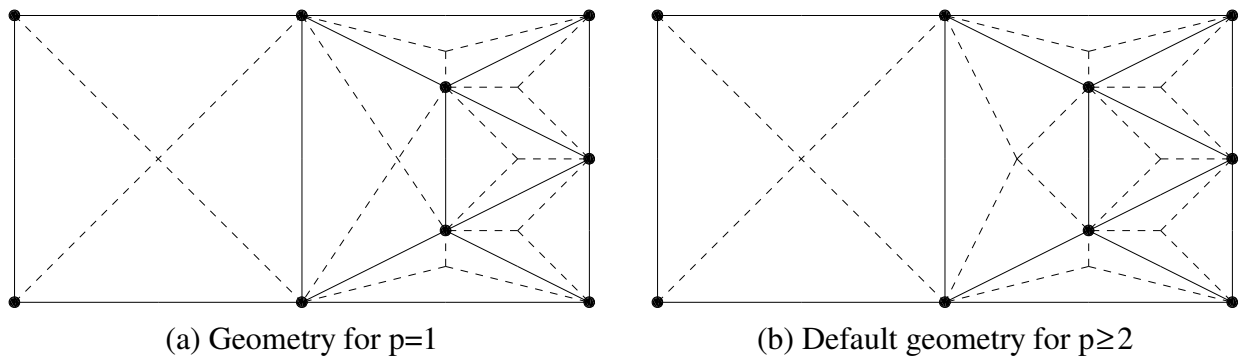


Figure A4.6 Internal geometry for example problem

The loading applied to the example problem is shown in figure A4.3. The model edge $x=10\text{m}$ is fully restrained whilst the model edge $x=0$ is restrained in the x -direction only. The first region is subjected to a thermal loading induced by a temperature increase of 25 degrees. This region is also subjected to a distributed pinching load of $10\text{N} / \text{m}^2$ as shown. Both regions are subjected to body forces due to uniform acceleration of $1\text{m} / \text{s}^2$ in the x -direction. Having briefly described the example problem we shall now consider the general format of the data deck.

The data deck consists of a number of lines, called headers, that are essential. These headers begin with an asterisk (*) and are shown in bold type face in figure A4.4. The headers tell the program where to look for specific types of information. Even if there are no entries following a header - such a case could be envisaged when no static boundary conditions are applied to a model - the header must exist. The remaining (normal type face) lines are the data that defines one's model.

The meaning and format of the data associated with each header is now discussed.

***TITLE:** The line following this header can be used to put an identifying title to the data deck.

***PARAMETER:** The number on the line following this header tells the analysis program what degree of approximation to use and can range from 0 to 10. There is no facility for having different degrees of approximation for different elements in the same mesh since this would lead to a non-equilibrium solution.

***NODES:** The nodes used to define the edges and centre nodes of the elements used in the model are defined below this header. Nodes should be numbered consecutively and continuously. For each node, the nodes number, x -coordinate and y -coordinate must be given.

*EDGES: The edges used to define the elements used in the model are defined below this header. Edges should be numbered consecutively and continuously. For each edge, the edge number, the first specifying node, the second specifying node and the third specifying node must be given. The edge is defined to run from the first specifying node to the second specifying node and to go through the third specifying node. If the third specifying node lies at the mid-point of the line between the first and second specifying nodes then it is permissible, if one so desires, to put a zero for the third specifying node.

*ELEMENTS: The macro-type elements used to define the model are defined below this header. Elements should be numbered consecutively and continuously. For each element, the element number, is followed by nine specifying numbers. The first four of these numbers specify the edges that define the element. If the element is a triangular macro-element then the fourth of these numbers should be zero. The edges that define an element should be numbered consecutively in an anti-clockwise direction and the direction of each edge (as defined by the edges specifying nodes - see *EDGES above) should also follow this anti-clockwise rule. Thus, if an edge, as defined under *EDGE is oriented in the wrong direction for a particular element the edge number should be prefaced with a minus sign.

The fifth specifying number is the node number of the centre of the macro-type element. The configuration for the internal geometry of the macro-type elements is as follows. The triangular macro-element is divided into three triangular primitive-elements such that each of the triangular primitive-elements consists of one edge of the macro-element with the remaining two edges specified as (straight) lines running between the end points of the macro-element edge and the centre node. The default position of this centre node is the centre of mass of three unit masses placed at the vertices of the triangular macro. For the quadrilateral macro-element a similar procedure is adopted with the centre node being positioned at the centre of mass of four unit masses placed at the vertices of the quadrilateral macro. The default internal geometry of the macro-type elements is obtained by specifying zero for the centre node. Alternative internal geometries may be obtained by specifying a non-zero node number for the centre node.

The sixth specifying number is a pointer to the property card that will be used for the element.

The remaining three specifying numbers are, respectively, the temperature of the element above some arbitrary datum temperature, and the values of the (constant) acceleration of the element in the x- and y-directions.

***KBC:** The kinematic boundary conditions to be applied to the model are defined under this header. For each edge to which a kinematic boundary condition is to be applied the edge number is specified followed by a set of values representing the amplitudes of the modes of edge displacement the number of which need to be consistent with the degree of approximation defined under the ***PARAMETER** card. For constant stress fields there are two numbers corresponding to the constant normal and tangential displacements of the edge. For each further unit increase in degree of approximation two more numbers need to be added corresponding to the amplitudes of the linear, quadratic etc. normal and tangential modes of edge displacement. Even though for an edge to which a kinematic boundary condition is applied all possible modes of edge displacement must be specified, a particular mode can be specified as being free. This is done by inserting the number 999 for the amplitude of the free mode. The program will then understand that this mode of edge displacement is to remain free.

***SBC:** The static boundary conditions to be applied to the model are defined under this header. For each edge to which a static boundary condition is to be applied the edge number is specified followed by a set of values representing the amplitudes of the modes of edge traction the number of which needs to be consistent with the degree of polynomial approximation defined under the ***PARAMETER** card. For constant stress fields there are two numbers corresponding to the constant normal and tangential edge tractions. For each further unit increase in degree of approximation two more numbers need to be added corresponding to the amplitudes of the linear, quadratic etc. normal and tangential modes of edge traction.

***PROPERTIES:** The material properties, the material thickness and the type of constitutive relationship to be used are defined under this header. For each different property definition, the first number specifies the property number and is the number to which the sixth specifying number of an element definition points to. The next three numbers define, respectively Young's Modulus, Poisson's Ratio and the material thickness. The following two numbers in each property card are the values of the coefficient of linear expansion and the material density respectively. The final number, which can be either 0 or 1 defines the type of constitutive relation to be used. If it is 0 then a plane stress constitutive relationship is used. If this number is 1 then a plane strain constitutive relationship is used.

***END OF DATA:** This header simply indicates the end of the data deck.

A4.3 Mesh generation

Automatic generation of finite element meshes for both triangular and quadrilateral macro-elements on arbitrary quadrilateral regions with parabolic edges is available. The program MGQQM.FOR generates quadrilateral macro-elements whilst the program MGQTM.FOR generates triangular macro-elements. The input to the program is the number of element divisions along the first two edges and the co-ordinates for eight points that define the region. Figure A4.7 shows the ordering of the eight points for a sample region and for a mesh of (a) quadrilaterals and (b) triangles.

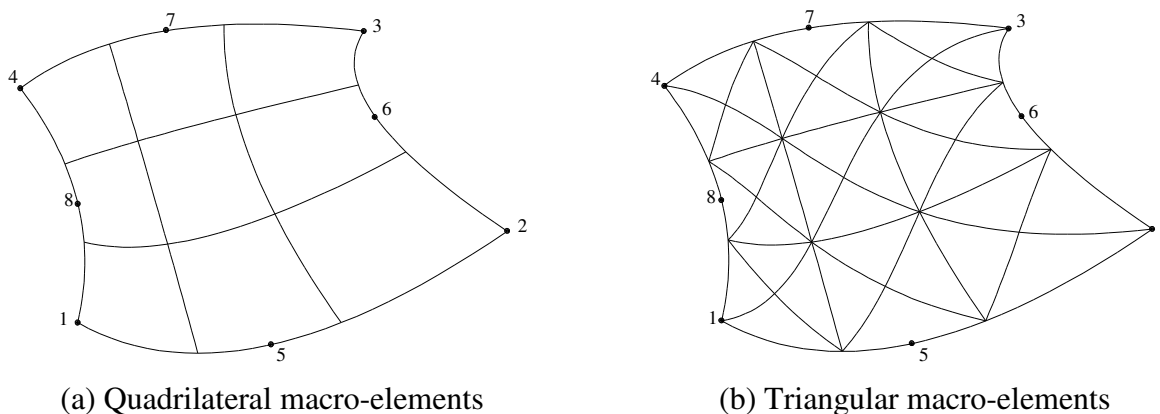


Figure A4.7 Samples of automatically generated meshes

The output of these programs is a data deck titled MMMM.MSH.

A4.4 Application of Static Boundary Conditions

Application of static boundary conditions for anything but the simplest problems is a time consuming and error prone process. As such, a program for the application of static boundary conditions to a mesh has been written. The program SBC.FOR may be used to generate static boundary conditions for an arbitrary mesh of elements. For the purpose of the work conducted in this report it has been written such that the user must edit the *FORTRAN* code to change the stress field for which the corresponding static boundary conditions are evaluated. The output to this program is a file called SBC.DAT which contains the static boundary conditions for all boundary edges of the model. Some of these static boundary condition cards may be full of zeros (or computer zeros!) and can be discarded by the user should he so desire.

A4.5 Application of Kinematic Boundary Conditions

In order to assist the user in the application of typical forms of homogeneous kinematic boundary conditions table A4.1 has been produced.

Type of KBC	n0	t0	n1	t1	n2	t2	n3	t3	n4	t4	n5	t5
Rigid body	0	0	0	999	999	999	999	999	999	999	999	999
Encastre	0	0	0	0	0	0	0	0	0	0	0	0
Symmetry	0	999	0	999	0	999	0	999	0	999	0	999
Anti-symmetry	999	0	999	0	999	0	999	0	999	0	999	0

(i) n_i and t_i represent the amplitudes of the normal and tangential modes of edge displacement respectively for degree of approximation i .

(ii) amplitudes with the value 999 indicates a free mode of edge displacement.

Table A4.1 Amplitudes of the modes of displacement for common homogeneous KBC

A4.6 Displaced shape

Following any analysis perhaps the first results to inspect are the displacements. A program that displays the displaced shape of the model is provided. This program PDISP.FOR plots the displaced shape of the edges of each macro-element - the internal edges (which may still be affected by SKM's) are not displayed.

The output of this program is a file called PDXF.DAT and containing the co-ordinates of the end points of the lines that define the edges of the model. This file may be converted into a DXF format (PDXF.DXF) using the supplementary program DXF.FOR. This file is suitable for use with drawing programs such as AutoSketch and AutoCad and can then be read into standard word-processors.

A4.7 Stress Distributions

The stress distributions for a model may be viewed with the program PSTRS.FOR. This program plots the exact finite element stress distribution - there is no interpretation or smoothing of this stress field. The user is able to specify the component of stress that he wishes to plot either in the global Cartesian co-ordinate system or in a polar co-ordinate system. The polar co-ordinate system is defined such that its origin coincides with the origin of the global Cartesian co-ordinate system, and the angle θ is measured from the global x-axis and is positive according to the right hand screw convention. The user is prompted for the level of refinement that he requires. In order to explain the meaning of this number it is necessary to describe the manner in which the stresses are actually plotted. Each primitive-element is divided into four triangles by intersection of the mid-sides of the primitive-type element as shown in figure A4.8. Each of these four new triangles is further divided into three quadrilateral regions as shown for the bottom left triangle in the figure. Further uniform sub-division of each quadrilateral into smaller quadrilaterals then take place such that the level of refinement given by the user specifies the number of sub-divisions along each side of the original quadrilateral.

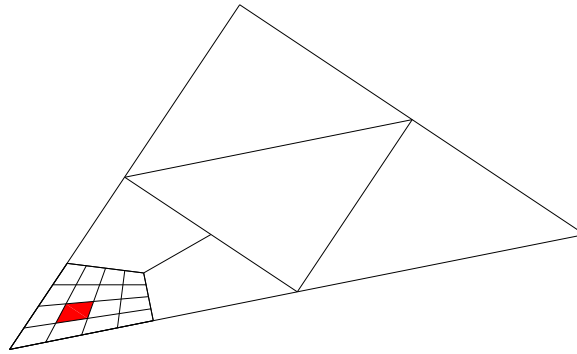


Figure A4.8 Stress plotting on a primitive-type element

The stress is evaluated at the centre of each of these new quadrilaterals and the quadrilateral is filled with colour (or shade of grey if using a mono-chrome screen) according to this value of stress.

The output to this program is a PCX format file with the title indicating the stress component that was plotted. Thus, if the σ_x -component of the stress was plotted then the output file will be called SXX.PCX and similarly for the other components of stress the output will be SYY.PCX and SXY.PCX.

A4.8 Point Values of Stress

Point values of stress are obtained from the program PVAL.FOR. The user is requested for the co-ordinates of the point for which the stresses are required. Since the point may lie on the boundary between two or more elements the user is presented with a diagram of the mesh showing the macro-elements and the primitive elements that constitute the macro-elements. The element numbers of these primitive elements are given and the user is requested to select the element for which he desires the stress to be evaluated. This program can be used to view the internal geometry of the macro-elements.

A4.9 Closure

In writing this appendix the author would not wish to give the impression that the programs that he has written and produced are anything other than research tools. They have been written for his use and were not designed for use by a third party. As such, the codes are fairly sparsely commented and by no means optimally written. The author will not be held responsible for any damages arising from the use (or misuse) of the programs that he is making available with this report.

APPENDIX 5: PAPER I (Submitted to *Computers & Structures* March 1995)EFFECTIVE ERROR ESTIMATION FROM CONTINUOUS, BOUNDARY
ADMISSIBLE ESTIMATED STRESS FIELDSA.C.A. Ramsay[†] and E.A.W. Maunder[‡][†] Departamento de Engenharia Civil, Instituto Superior Técnico, Universidade Técnica de Lisboa, Avenida
Rovisco Pais, 1096 Lisboa CODEX, Portugal.[‡] School of Engineering, University of Exeter, North Park Road, Exeter, Devon, EX4 4QF, England.

Abstract - Effective error estimation in plane stress linear-elastic problems using continuous, boundary admissible estimated stress fields is discussed. An error estimator based on continuous estimated stress fields achieved by interpolating from unique nodal stresses over the element with the element shape functions and in which the static boundary conditions are applied is introduced. The unique nodal stresses are achieved by the computationally cheap approach of simple nodal averaging of the finite element stresses at a common node. Results for this error estimator on a number of familiar benchmark problems are presented for the standard four-noded Lagrangian displacement element, and compared with those of other error estimators currently under research.

INTRODUCTION

Application of the standard displacement finite element method to problems in stress analysis results in a solution which, whilst satisfying compatibility¹ and the constitutive relations for the material(s), generally violates equilibrium. This lack of equilibrium manifests itself in:

1. a lack of internal equilibrium,
2. a lack of interface equilibrium, and
3. a lack of equilibrium on the static boundary.

Of these three *error indicators* the lack of interface equilibrium may be considered the most readily observed through consideration of the continuity, or otherwise, of the direct stress normal to, and the shear stress tangential to an element interface. Traditionally this error indicator has served the engineer in highlighting areas of the mesh for which the finite element approximation is insufficient.

Error indicators such as this, although indicating the presence of error, do little to help the

engineer actually to quantify the error. More recently, however, *error estimators* which can quantify the error in the form of a single number known as an *error measure* have become popular areas of research. The error measure represents the total error in a single element and thus can be used to indicate the distribution of error within a mesh. Alternatively, the elemental error measures may be summed to give an error measure for the entire mesh. The motivation behind such research lies in the need for effective error estimation in the *self-adaptive procedures* which are, increasingly, being implemented in commercial finite element software codes.

Error estimators currently under research can be divided into the following three categories:

1. those that quantify the error directly in terms of residual quantities [1,2,3,4],
2. those that quantify the error indirectly through the construct of a stress field that is continuous [4,5,6,7], and a better estimate of the true stress field, and

¹Note: this assumes that the kinematic boundary conditions are satisfied exactly.

3. those that quantify the error indirectly through the construct of stress field that is statically admissible [8,9,10,11], and a better estimate of the true stress field.

Recent research [16,17,20] has demonstrated that the effectivity of error estimators based on estimated stress fields that are continuous can be significantly enhanced through the simple expedient of 'applying the static boundary conditions' to the estimated stress field. Such estimated stress fields could then be termed *boundary admissible*. In this paper a simple error estimator utilising an estimated stress field which is both continuous and boundary admissible is considered.

The research detailed in this paper considers the problem of plane linear elasticity. In particular, the performance of error estimators for the standard four-noded Lagrangian displacement element are examined.

ERROR MEASURES

The philosophy of error estimation given here is presented in terms of familiar strain energy quantities rather than the, perhaps, less familiar energy norm quantities generally used in the literature. This approach was developed in [15] with the aim of making the subject of error estimation more approachable to the practising engineer - the people who will ultimately use such concepts.

The finite element method results in a finite element stress field $\{\sigma_h\}$ as an approximation to the true stress field $\{\sigma\}$. The difference between the true stress field and the finite element stress field defines an *error stress field*:

$$\{\sigma_e\} = \{\sigma\} - \{\sigma_h\} \quad (1)$$

This error stress field may be integrated over the model to form the *strain energy of the error*:

$$U_e = \frac{1}{2} \int_V \{\sigma_e\}^T \{\epsilon_e\} dV \quad (2)$$

where $\{\epsilon_e\}$ are the elastic strains corresponding to $\{\sigma_e\}$ and V is the volume of the model.

In practice this integral is performed at the element level and the strain energy of the error (for the model) formed as the summation of elemental contributions. It is noted that for models for which the static boundary conditions are represented by consistent node forces, and for which the kinematic boundary conditions are homogeneous, the strain energy of the error is given directly as the difference between the true strain energy and the finite element strain energy:

$$U_e = U - U_h \quad (3)$$

Equation (3) states that the strain energy of the error is equal to the error of the strain energy.

The significance of the strain energy of the error can be determined by forming the *percentage error* with the true strain energy:

$$\alpha = \frac{U_e}{U} \times 100\% \quad (4)$$

The larger the value of α the more significant is the error in the model.

The development thus far has assumed that the true stress field $\{\sigma\}$ is known. Of course, in any practical situation the true solution will not be known and in order to proceed an estimate of the true stress field is required. The details of

precisely how this is to be done will be discussed in the following section, however, assuming for the moment that an *estimated (true) stress field* $\{\tilde{\sigma}\}$ ² has been obtained, then an *estimated error stress field* can be defined as:

$$\{\tilde{\sigma}_e\} = \{\tilde{\sigma}\} - \{\sigma_h\} \quad (5)$$

The *strain energy of the estimated error* is formed in a similar way to the strain energy of the (true) error as:

$$\tilde{U}_e = \frac{1}{2} \int_V \{\tilde{\sigma}_e\}^T \{\tilde{\epsilon}_e\} dV \quad (6)$$

where $\{\tilde{\epsilon}_e\}$ are the elastic strains corresponding to $\{\tilde{\sigma}_e\}$.

The *estimated percentage error* is given as:

$$\tilde{\alpha} = \frac{\tilde{U}_e}{\tilde{U}} \times 100\% \quad (7)$$

where $\tilde{U} = U_h + \tilde{U}_e$.

The parameter $\tilde{\alpha}$ is the error measure that can be used in a practical analysis to inform the engineer of the accuracy of the finite element solution. Elementwise distributions of $\tilde{\alpha}$ could be used in self-adaptive procedures to indicate areas of the model that required more (or indeed less) refinement for a specified level of accuracy.

The quality of the error measure is clearly dependent on the quality of the estimated stress field. Before one can confidently use any error estimator it must be tested on *benchmark problems* for which the (true) solution is known. The effectivity of an error estimator is formally quantified in terms of the *effectivity ratio*:

$$\beta = \frac{\tilde{U}_e}{U_e} \quad (8)$$

The closer the effectivity ratio is to unity the more effective the error estimation. A desirable property of any error estimator is that as the mesh is refined the effectivity ratio tends to unity. Such a property is called asymptotic exactness. A good effectivity ratio (i.e. one that is close to unity) whilst indicating good error estimation in the sense of the definition of the effectivity ratio does not necessarily imply that the estimated stress field is a good approximation to the true one. Another integral quantity which measures the proximity of the estimated stress field to the true one is therefore defined. The *error in the estimated stress field* is defined as the difference between the true stress field and the estimated stress field:

$$\{\hat{\sigma}\} = \{\sigma\} - \{\tilde{\sigma}\} \quad (9)$$

The *strain energy of the error in the estimated stress field* is then given as:

$$\hat{U} = \frac{1}{2} \int_V \{\hat{\sigma}\}^T \{\hat{\epsilon}\} dV \quad (10)$$

where $\{\hat{\epsilon}\}$ are the elastic strains corresponding to $\{\hat{\sigma}\}$.

The smaller the value of this quantity, the closer the estimated stress field is to the true one.

²Note: the tilde will be used throughout to indicate estimated quantities.

CONTINUOUS ESTIMATED STRESS
FIELDS

Before discussing estimated stress fields that are both continuous and boundary admissible, let us first review a number of available methods for obtaining estimated stress fields that are continuous. Procedures for achieving boundary admissibility will be discussed in the following section.

A standard method for achieving continuous stress fields is to interpolate from unique nodal stresses over each element with the element shape functions. The process of transforming a discontinuous finite element stress field into an estimated stress field that is continuous is shown diagrammatically for a single component of stress and a patch of four elements in Fig. 1.

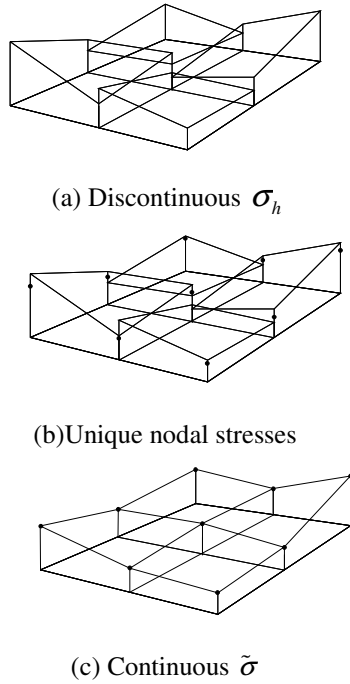


Fig. 1. Continuous $\tilde{\sigma}$ from discontinuous σ_h

The continuous estimated stress field $\{\tilde{\sigma}\}$ is defined, for each element, in terms of the shape functions for the element and a vector of unique nodal stresses $\{s\}$:

$$\{\tilde{\sigma}\} = [\bar{N}]\{s\} \quad (11)$$

where $[\bar{N}]$ is a matrix containing the shape functions for the element.

The vector $\{s\} = \left[\left[s \right]_1^T, \left[s \right]_2^T, \left[s \right]_3^T, \left[s \right]_4^T \right]^T$ where $\{s\}_i = \left[s_x, s_y, s_{xy} \right]^T$ is the vector of unique nodal stresses for node i .

Over recent years many methods for determining unique nodal stresses have been proposed. One might say that the method for obtaining unique nodal stresses is not in itself unique. Perhaps the simplest of all these methods is that of nodal averaging of the finite element stresses at a common node:

$$\{s\}_i = \frac{1}{n} \sum_{j=1}^n \{\sigma_h\}_i^j \quad (12)$$

where the summation is taken over the nodes of all elements j connected to node i .

Simple nodal averaging, as this technique is generally known, is commonly used in commercial finite element codes as a method for making the discontinuous finite element stresses more palatable to the engineer. The ANSYS suite of finite element software has included an error estimator based on a continuous estimated stress field derived from unique nodal stresses achieved through simple nodal averaging in its recent versions. The ANSYS error estimator, however, uses an inexact integration scheme known as nodal quadrature to perform the integration of the strain energy of the estimated error (equation (6)) and, although being commendably cheap in computational terms, this additional approximation results in an error estimator which is not asymptotically exact. Results demonstrating this point will be presented later in this paper (see Problem 3). Recent studies [15] have demonstrated that by using a slightly more costly, but exact, (at least

for parallelogram shaped elements) integration scheme the property of asymptotic exactness can be recovered for the ANSYS error estimator.

Other methods of achieving sets of unique nodal stresses have concentrated on obtaining them through a least squares fit between the continuous estimated stress field and the finite element stress field [5,12]. However, although mathematically elegant, in addition to the high cost of obtaining the unique nodal stresses through global computations (c.f. simple nodal averaging where calculations are performed at a local, nodal level), the resulting error estimation has been demonstrated to be less effective than some that use simple nodal averaging [17].

More recently, the superconvergent patch recovery scheme of Zienkiewicz and Zhu [6] has received much attention. In this method the unique nodal stresses are obtained by interpolating from a stress surface fitted to the superconvergent stress points surrounding the node of interest. The fit is performed in a least squares manner individually for each component of stress. It has been claimed that this method results in high accuracy error estimation and that the nodal stresses thereby recovered are superconvergent. These claims have been investigated in [17] and the results are the subject of a paper shortly to be published [18].

The concept of a patch recovery scheme has been adopted by other researchers. For example Wiberg et al [7,20] employ a patch recovery scheme but, rather than perform the recovery individually for each component of stress as is done in the Zienkiewicz and Zhu approach, they do so for all components simultaneously. The

coupling of the stress components is made through the equations of equilibrium.

Beckers, Zhong and Maunder have proposed a method of averaging and extrapolation for obtaining unique nodal stresses in a local manner [4]. This method bears strong similarities with the patch recovery scheme of Zienkiewicz and Zhu.

BOUNDARY ADMISSIBILITY

From a purely intuitive standpoint one might suggest that since the true stress field generally exhibits continuity then so an estimated stress field constructed from the finite element stress field such as to be continuous is likely to be a good candidate for the true stress field. One can reinforce this intuitive argument by considering that a continuous estimated stress field is also better than the original finite element stress field in that interface equilibrium is recovered i.e. some attempt is being made to recover the lost equilibrium. One can extend this idea further by requiring the estimated stress field to, in addition, satisfy the static boundary conditions. The idea of applying the static boundary conditions to an already continuous estimated stress field and thereby achieving a *continuous, boundary admissible estimated stress field* is discussed in this section.

The concept of modifying the *finite element stress field* with the known static boundary conditions is not new. Indeed, common sense tells us that where static boundary conditions are applied and, therefore, the direct stress normal to and the shear stress tangential to the surface are known we should disregard the finite element values and use values that are known to be true. Unfortunately, however, it is usually

the third component of stress, the direct stress tangential to the surface, that is of interest to the engineer in any analysis. In an analogous fashion it makes sense to modify the *estimated stress field* with known values of stress. This idea has been used before in the improvement of the original finite element stress field $\{\sigma_h\}$ [13].

In [14] the importance of the static boundary conditions in achieving an asymptotically exact error estimator is discussed. Ways in which these boundary conditions can be applied to modify the continuous estimated stress field are now considered. All the ways aim to estimate the state of stress at nodes on the static boundary using original finite element stresses, and the specified boundary tractions, for patches of elements connected to the boundary nodes. Such a patch is illustrated in Fig. 2 for three methods: (a) a simple direct method as proposed in this paper [17], (b) that proposed by Mashaie [16] and (c) that proposed by Wiberg [20].

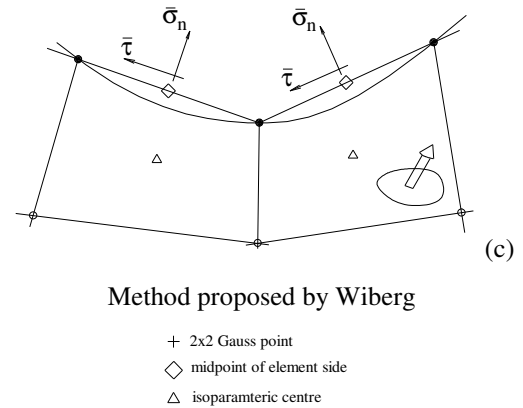
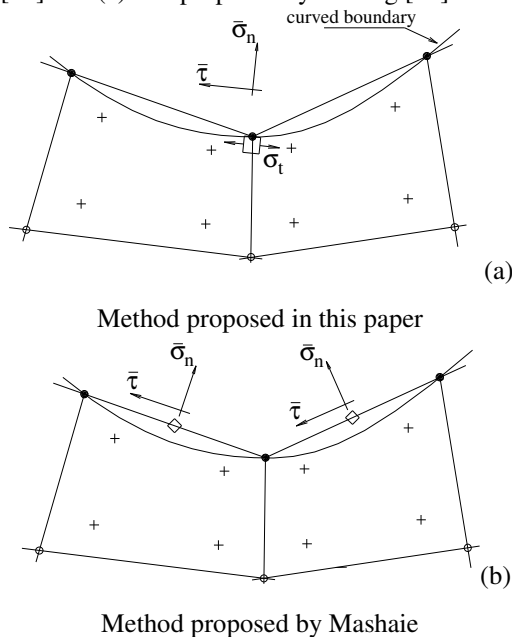


Fig. 2. Application of static boundary conditions on a smooth boundary

In the proposed method (a) the stress components σ_n and τ , which are normal and tangential to the boundary surface at the node, are equated to the specified tractions; the third component σ_t is determined by averaging nodal values in adjacent elements. As with internal nodes, the nodal values for an element are extrapolated from the four Gauss integration points using bilinear extrapolation functions. In method (b) three stages of stress averaging are involved. Nodal stresses are first determined as the average of the nearest Gauss point stresses. Stresses at the midpoints of the sides of elements which represent the boundary surface are then determined by averaging adjacent nodal stresses. These midpoint stresses are modified so that components σ_n and τ are equated to local values of the specified traction, and finally the nodal stresses are modified to be the average of adjacent midpoint stresses. Method (c) involves significantly more computation. The Superconvergent Patch Recovery concept [7] is extended to impose, in a weak sense, both internal equilibrium throughout the patch and boundary equilibrium at the two midpoints. The weak form of equilibrium is achieved by fitting a continuous stress field in a least squares sense

to minimise weighted residuals in stress and body forces.

The examples considered in references [16,20] demonstrate that improvements can be achieved in error estimators through applying the static boundary conditions. The results presented in this paper using the simplified method of application, confirm the trends in improvements in comparison with the results of other error estimators currently under research. The details for the implementation of method (a) are now given with reference to Mesh 1 of Problem 2. This mesh is shown in detail in Fig.3.

For all nodes the first step in recovering the unique nodal stresses is to perform simple nodal averaging at each node. For internal nodes, such as node number 9, this is all the processing that is required. For boundary nodes, however, additional processing is necessary. For nodes that lie on a smooth boundary the direct stress normal to the surface σ_n and the shear stress tangential to the surface τ are defined. The remaining component of stress, the direct stress tangential to the surface σ_t , is generally unknown.

The unit vectors for node number 8 are shown in Fig. 3 normal (n) and tangential (t) to the actual boundary. The first step in the procedure for applying the static boundary conditions is to transform the nodal averaged stresses at the node of interest $\{s\}_i$ into the local, boundary co-ordinate system shown in Fig. 3. This requires a rotation of the stress components through an angle ϕ :

$$\{b\}_i = [R]\{s\}_i \quad (13)$$

$$\text{where } [R] = \begin{bmatrix} \cos^2 \phi & \sin^2 \phi & \sin 2\phi \\ \sin^2 \phi & \cos^2 \phi & -\sin 2\phi \\ -\frac{1}{2} \sin 2\phi & \frac{1}{2} \sin 2\phi & \cos 2\phi \end{bmatrix}$$

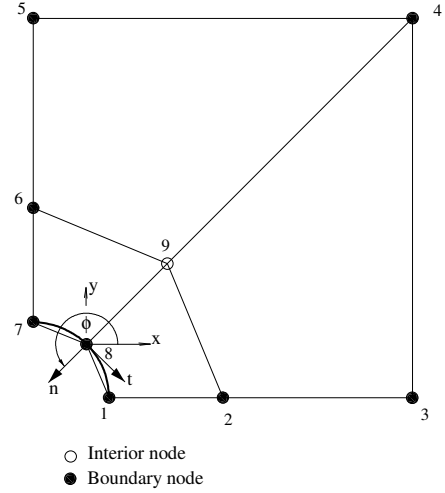


Fig. 3. Mesh 1 of Problem 2

The nodal averaged stresses in the local, boundary co-ordinate system $\{b\}_i$ are now modified with the static boundary conditions:

$$\{\hat{b}\}_i = \begin{bmatrix} 0 & 0 & 0 \\ 0 & 1 & 0 \\ 0 & 0 & 0 \end{bmatrix} \{b\}_i + \begin{bmatrix} 1 & 0 & 0 \\ 0 & 0 & 0 \\ 0 & 0 & 1 \end{bmatrix} \begin{Bmatrix} \sigma_n \\ \sigma_t \\ \tau \end{Bmatrix} \quad (14)$$

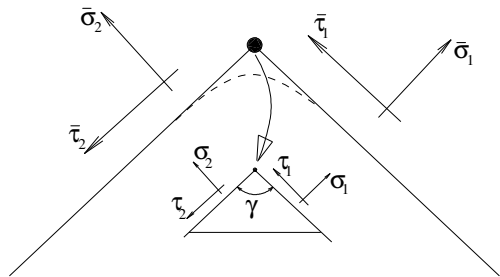
Finally, the modified nodal averaged stresses $\{\hat{b}\}_i$ are transformed back into the global co-ordinate system:

$$\{\hat{s}\}_i = [R]^{-1} \{\hat{b}\}_i \quad (15)$$

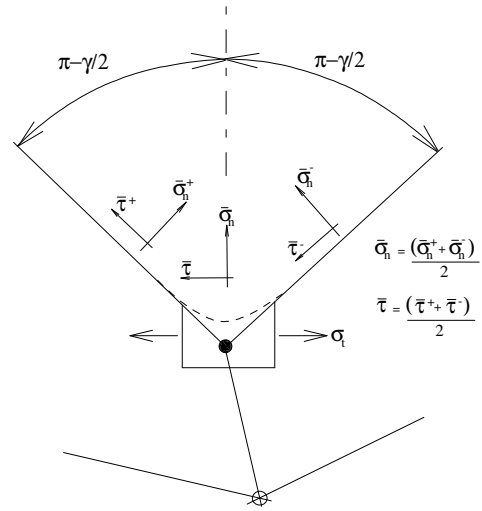
For nodes that lie at the intersection of two orthogonal static boundaries e.g. node number 4 of Fig. 3, application of the static boundary conditions results in all three components of stress being modified to known true values. For nodes that lie completely on symmetry boundaries e.g. node numbers 2 & 6 of Fig. 3, the only known condition on the stresses is that

the shear stress tangential to the surface is zero i.e. $\tau=0$. Node numbers 1,3,5 & 7 lie at the intersection of static and symmetric boundaries. For these nodes the symmetry condition is automatically satisfied by modifying according to the static boundary conditions on the static boundary.

This method can easily be extended to cover the more general case of a boundary surface with convex or concave corners, where normal and tangential directions are not uniquely defined. These cases are illustrated in Fig. 4. In reality such corners will have radii, albeit with small values. However, finite element models composed of four-noded straight sided elements cannot represent exactly general curved boundaries, let alone corner radii with possibly uncertain values. This is only really of concern if stress distributions are sought in the neighbourhood of corners. Otherwise it is common to represent a corner by the node at the intersection of two sides.



(a) Convex corner



(b) Concave corner

Fig. 4. Application of static boundary conditions on a polygonal boundary

Fig. 4(a) shows a convex corner with four specified components of traction adjacent to the corner node. If the components are consistent with a unique state of stress within the corner, then this stress is imposed at the node. If the components are inconsistent, then a unique nodal stress can be defined from consistent components $\sigma_1, \tau_1, \sigma_2, \tau_2$ defined so that:

$$(\sigma_1 - \bar{\sigma}_1)^2 + (\tau_1 - \bar{\tau}_1)^2 + (\sigma_2 - \bar{\sigma}_2)^2 + (\tau_2 - \bar{\tau}_2)^2 \quad (16)$$

is minimised subject to:

$$(\tau_1 + \tau_2) = (\sigma_1 - \sigma_2) \cot \gamma \quad (17)$$

which is the consistency condition for a unique state of stress.

In this case:

$$\begin{Bmatrix} \sigma_1 \\ \tau_1 \\ \sigma_2 \\ \tau_2 \end{Bmatrix} = \begin{Bmatrix} \bar{\sigma}_1 \\ \bar{\tau}_1 \\ \bar{\sigma}_2 \\ \bar{\tau}_2 \end{Bmatrix} - e \frac{\sin \gamma}{2} \begin{Bmatrix} -\cos \gamma \\ \sin \gamma \\ \cos \gamma \\ \sin \gamma \end{Bmatrix} \quad (18)$$

$$\text{where } e = [\bar{\tau}_1 + \bar{\tau}_2 - (\bar{\sigma}_1 - \bar{\sigma}_2) \cot \gamma] \neq 0.$$

Fig. 4(b) shows a concave (re-entrant) corner with normal and tangential tractions which may be specified with discontinuities at the corner node. In this case average values are assumed in the directions of the bisector of the corner angle, and perpendicular to this bisector. The stress components at the corner node are taken as the average traction values $\bar{\sigma}_n$ and $\bar{\tau}$, and σ_i is averaged as in the case of a smooth boundary surface as illustrated in Fig. 2(a).

ERROR ESTIMATORS INVESTIGATED

In the following sections the performance of a number of error estimators using continuous and continuous, boundary admissible estimated stress fields will be investigated. However, before doing this it is necessary to formally define the error estimators that will be examined.

Two error estimators will be examined. Both use continuous estimated stress fields as defined by equation (11). The first error estimator EE_2 (the subscript 2 is used in order to retain a consistency with previously published work e.g. [15]) uses unique nodal stresses obtained by a process of simple nodal averaging. The second error estimator EE_2^b is identical to EE_2 in all respects except that the estimated stress field in addition to being continuous is also boundary admissible. Boundary admissibility is achieved by modifying all values of nodal stress affected by the static boundary conditions to the known, true values using the simple direct method detailed in this paper. Comparison of the two error estimators (EE_2 and EE_2^b) will be made on the basis of the effectivity ratio of equation (8) (β_2 and β_2^b respectively for the two error estimators) and on the strain energy of the error of the estimated stress field of equation (10) (\hat{U}_2

and \hat{U}_2^b respectively for the two error estimators).

In addition to the two error estimators EE_2 and EE_2^b , for the third problem presented in this paper the effectivity ratios of a number of other error estimators using continuous estimated stress fields will also be reported. These error estimators are:

EE_p : This error estimator uses unique nodal stresses recovered from a patch recovery scheme. The parent patch recovery scheme of reference [19] is used here.

EE_{zz} : This error estimator is the original Zienkiewicz and Zhu error estimator proposed in [5] and uses unique nodal stresses recovered from a global least squares fit between the continuous estimated stress field and the finite element stress field³.

EE_4 : This error estimator is the one used in the ANSYS suite of finite element software and has been discussed in detail in reference [15].

NUMERICAL EXAMPLES

In order to demonstrate the improved effectivity of error estimators using continuous, boundary admissible estimated stress fields over those that simply use a continuous estimated stress field, four numerical examples will be presented. The problems investigated, although perhaps chosen in an arbitrary fashion, are realistic problems exhibiting characteristics with which a practising engineer is likely to be familiar. All problems are force driven with a plane stress constitutive relationship. The only conditions

³The results for this error estimator have been taken from reference [4].

placed on the displacements are those necessary to eliminate rigid body motions.

Problem 1. This problem involves a rectangular membrane loaded with static boundary conditions consistent with the linear statically and kinematically admissible stress field generally associated with a beam under pure (engineer's) bending. The true stress field for this problem is:

$$\begin{aligned} \sigma_x &= 30y \\ \sigma_y &= 0 \\ \tau_{xy} &= 0 \end{aligned} \quad (19)$$

and has been plotted in Fig. 8(a).

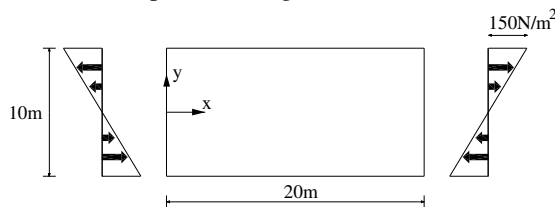


Fig. 5. Geometry of Problem 1

For a Young's Modulus of $E = 210 \text{ N/m}^2$, a Poisson's Ratio of $\nu = 0.3$ and a material thickness of $t = 0.1 \text{ m}$, the strain energy for the problem is:

$$U = \frac{2500}{7} \approx 357.14 \text{ Nm} \quad (20)$$

This problem has also been reported in [15,17,19]. The geometry and static boundary conditions are shown in Fig. 5.

The way in which an error estimator performs with coarse and, possibly, distorted meshes is of interest to an engineer. This problem investigates the performance of the error estimators as a coarse, but regular mesh is progressively distorted. The meshes that will be used in the problem are shown in Fig. 6.

Table 1. Results for Problem 1

Mesh	β_2	β_2^b	\hat{U}_2	\hat{U}_2^b
1	0.71	0.82	103.7	7.7
2	0.60	0.81	114.7	20.3
3	0.37	0.81	146.6	54.3
4	0.20	0.82	196.7	100.5
5	0.13	0.81	272.1	147.3

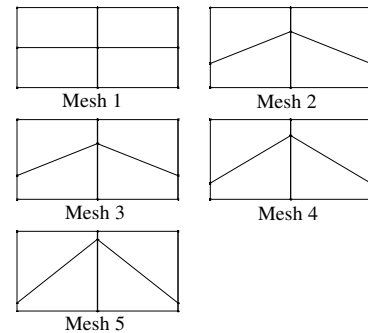


Fig. 6. Meshes for Problem 1

The effectivity ratio and the strain energy of the error of the estimated stress are tabulated in Table 1 and the variation of effectivity ratio with distortion is shown in Fig. 7. The stress fields for Mesh 1 are illustrated in Figure 8.

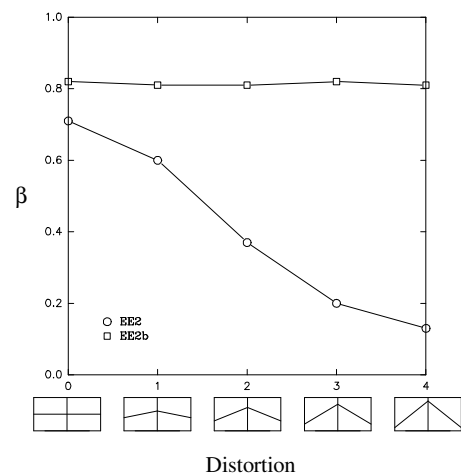


Fig. 7. β versus distortion for Problem 1

Problem 2. This problem involves a square membrane with a central circular hole of radius a and is the classical problem of a stress concentration in an infinite membrane. The true stress field for this problem is:

$$\begin{aligned} \sigma_x &= \sigma_\infty \left\{ 1 - \frac{a^2}{r^2} \left(\frac{3}{2} \cos 2\theta + \cos 4\theta \right) + \frac{3}{2} \frac{a^4}{r^4} \cos 4\theta \right\} \\ \sigma_y &= \sigma_\infty \left\{ 0 - \frac{a^2}{r^2} \left(\frac{1}{2} \cos 2\theta - \cos 4\theta \right) - \frac{3}{2} \frac{a^4}{r^4} \cos 4\theta \right\} \\ \tau_{xy} &= \sigma_\infty \left\{ 0 - \frac{a^2}{r^2} \left(\frac{1}{2} \sin 2\theta + \sin 4\theta \right) + \frac{3}{2} \frac{a^4}{r^4} \sin 4\theta \right\} \end{aligned} \quad (21)$$

where σ_∞ is the value of σ_x at $x = \pm\infty$ and is chosen as $10,000 \text{ N/m}^2$ for this problem. This stress field has been taken from reference [3].

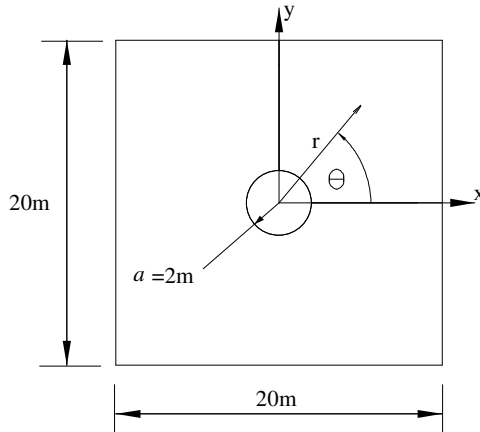


Fig. 9. Geometry of Problem 2

The finite portion of this infinite membrane shown in Fig. 9 will be modelled. Static boundary conditions are determined from the stress field given above. Through the symmetry present in this problem only one quarter of the membrane need be modelled and the four meshes, of increasing refinement, that will be used are shown in Fig. 10.

For a Young's Modulus of $E = 10 \times 10^6 \text{ N/m}^2$, a Poisson's Ratio of $\nu = 0.25$ and a material thickness of $t = 0.01 \text{ m}$ the strain energy for this problem is:

$$U = 5.188448459 \text{ Nm} \quad (22)$$

and is accurate to the number of digits quoted [17].

This problem has also been reported in [17,18].

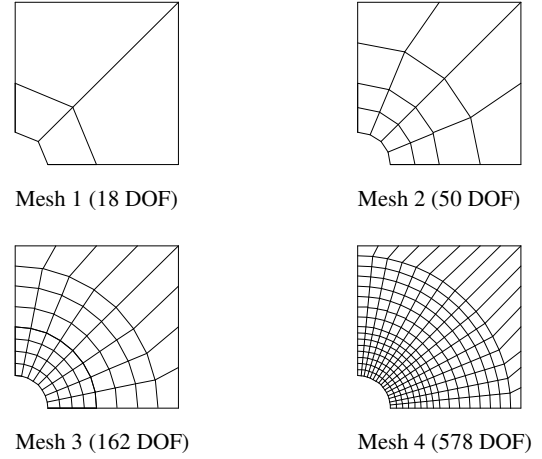


Fig. 10. Meshes for Problem 2

The results for Problem 2 are tabulated in Table 2 and the convergence of the effectivity ratios with number of degrees of freedom are plotted in Fig. 11.

Table 2. Results for Problem 2

Mesh	β_2	β_2^b	\tilde{U}_2	\tilde{U}_2^b
1	0.2768	0.8766	0.1498	0.1590
2	0.4456	1.1349	0.0469	0.0459
3	0.5855	1.0429	0.0115	0.0078
4	0.7054	0.9309	0.0023	0.0009

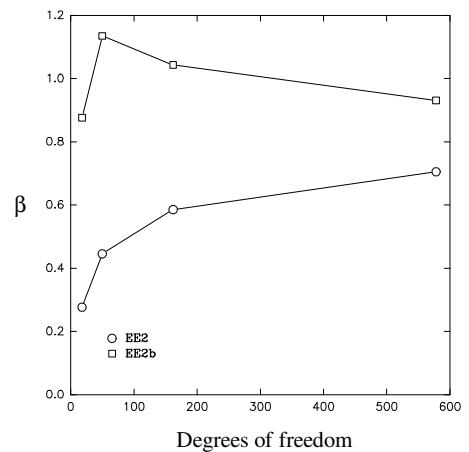


Fig. 11. β versus DOF for Problem 2

Problem 3. This problem involves a rectangular membrane loaded with static boundary conditions consistent with the quadratic statically and kinematically admissible stress field typically associated with a simply supported beam under the action of a transverse shear force. The true stress field for this problem is:

$$\begin{aligned} \sigma_x &= 46.875xy \\ \sigma_y &= 0 \\ \tau_{xy} &= 93.75 - 23.4375y^2 \end{aligned} \quad (23)$$

For a Young's Modulus of $E = 3 \times 10^7 \text{ N/m}^2$, a Poisson's Ratio of $\nu = 0.3$ and a material thickness of $t = 1\text{m}$, the strain energy for the problem is:

$$U = \frac{239}{6000} \approx 0.03983 \text{ Nm} \quad (24)$$

This problem has also been reported in [4,17].

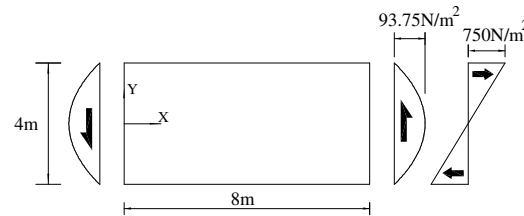


Fig. 12. Geometry of Problem 3

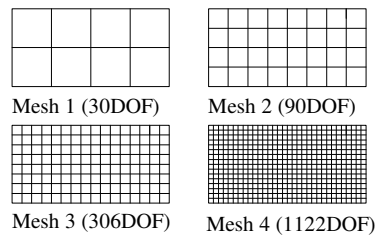


Fig. 13. Meshes for Problem 3

Whereas Problem 1 dealt with the performance of error estimators with coarse and distorted meshes, this problem looks at how the error estimators perform as a mesh is refined. The geometry and static boundary conditions for

Problem 3 are shown in Fig. 12 and the meshes that are used are shown in Fig. 13. The convergence of the effectivity ratios with number of degrees of freedom are plotted in Fig. 14.

Table 3. Results for Problem 3

Mesh	1	2	3	4
β_2	0.7120	0.9270	0.9804	0.9947
β_2^b	1.0887	1.0518	1.0188	1.0062
\tilde{U}_2	375e-5	66e-5	9.43e-5	1.25e-5
\tilde{U}_2^b	171e-5	20e-5	1.68e-5	0.13e-5
β_p	0.7450	0.9442	0.9853	0.9960
β_{zz}	(i)	0.81	0.90	0.96
β_4	1.76	2.28	2.60	2.79

(i) The result for this error estimators and this mesh was not available in [4].

(ii) The effectivity ratios β_p , β_{zz} and β_4 correspond to the error estimators EE_p , EE_{zz} and EE_4 defined in the section 'Error Estimators Investigated'.

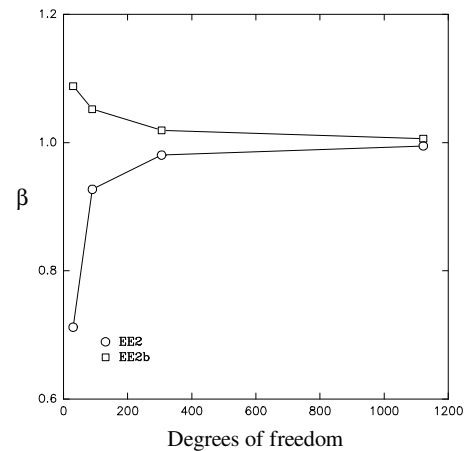


Fig. 14. β versus DOF for Problem 3

Problem 4. This problem involves a rectangular membrane with an infinitesimally thin crack of length $5m$ as shown in Fig. 15. The true stress field for this problem is:

$$\begin{aligned} \sigma_x &= \frac{100}{\sqrt{r}} \cos \frac{\theta}{2} \left\{ 1 - \sin \frac{\theta}{2} \sin \frac{3\theta}{2} \right\} \\ \sigma_y &= \frac{100}{\sqrt{r}} \cos \frac{\theta}{2} \left\{ 1 + \sin \frac{\theta}{2} \sin \frac{3\theta}{2} \right\} \\ \tau_{xy} &= \frac{100}{\sqrt{r}} \sin \frac{\theta}{2} \cos \frac{\theta}{2} \cos \frac{3\theta}{2} \end{aligned} \quad (25)$$

and is taken from reference [3].

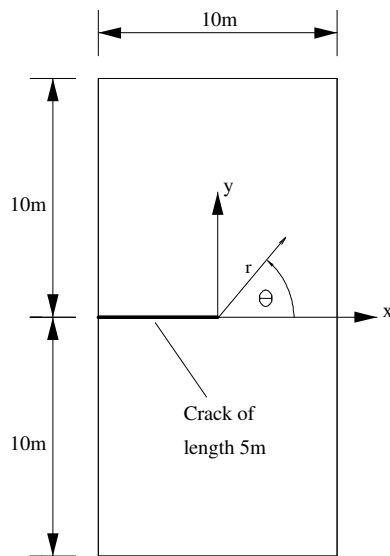


Fig. 15. Geometry of Problem 4

For a Young's Modulus of $E = 210 N/m^2$, a Poisson's Ratio of $\nu = 0.3$ and a material thickness of $t = 0.1m$ the strain energy for this problem is:

$$U = 124.885926020 Nm \quad (26)$$

and is accurate to the number of figures quoted [17].

Static boundary conditions are determined from the stress field given in equation (25) and are applied to the four meshes shown in Fig. 16.

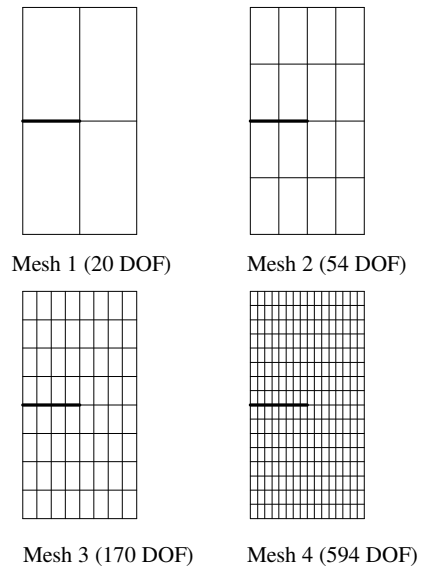


Fig. 16. Meshes for Problem 4

The results for Problem 4 are tabulated in Table 4 and the convergence of the effectivity ratios with number of degrees of freedom are plotted in Fig. 17.

Table 4. Results for Problem 4

Mesh	β_2	β_2^b	\hat{U}_2	\hat{U}_2^b
1	0.23	0.53	32.38	28.56
2	0.45	0.64	19.01	17.99
3	0.51	0.73	10.36	9.95
4	0.57	0.81	5.33	5.04

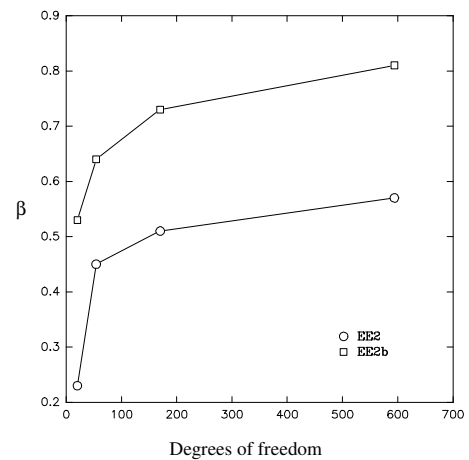


Fig. 17. β versus DOF for Problem 4

DISCUSSION AND CONCLUSIONS

This paper has presented a simple error estimator (EE_2^b) for the four-noded Lagrangian quadrilateral element in which a continuous, boundary admissible estimated stress field is used. Unique nodal stresses achieved by simple nodal averaging for which the components defined by the static boundary conditions have been corrected to the true values are interpolated over each element with the finite element shape functions. The effectivity of this error estimator is then compared with that of one which does not take account of the static boundary conditions (EE_2). The basis for comparison is made on the effectivity ratio β , and the strain energy of the error in the estimated stress field \hat{U} . The effectivity ratio measures the proximity of the strain energy of the estimated error with that of the true error in the form of a ratio whilst \hat{U} measures the proximity of the estimated stress field to the true one. For effective error estimation one requires an effectivity ratio that is close to unity and, further, it is desirable that the effectivity ratio tends to unity as the mesh is refined i.e. that it is asymptotically exact. Recognising that the effectivity ratio says little about the pointwise quality of the estimated stress field leads to the introduction of the quantity \hat{U} . This quantity is an absolute value; small values indicating good pointwise quality of the estimated stress field.

The two error estimators, EE_2 and EE_2^b , have been tested on four problems that should be familiar to practising engineers. Problem 1 looks at how the error estimators are affected by element distortion for a fairly coarse mesh. This is important because it is in precisely these types of situation that one would like to achieve good error estimation. Problem 2 looks at how the

error estimators perform with mesh refinement for a problem involving a stress concentration. Problem 3 looks at how the error estimators perform with mesh refinement for a problem involving a smooth solution but one which is one degree higher than the element is capable of modelling. For this problem the effectivities of a number of other error estimators are reported for comparison. Finally, Problem 4 shows how the error estimators perform in the presence of a singularity in stress.

For all four problems it is clearly seen that the simple expedient of applying the static boundary conditions to the estimated stress field results in higher quality error estimation. This is evidenced by the fact that β_2^b is closer to unity than β_2 and that \hat{U}_2^b is always close to and is generally less than \hat{U}_2 .

For Problem 1, where the effectivity of EE_2 is strongly affected by the level of distortion (see Fig. 7), it is seen that application of the static boundary conditions leads to an error estimator EE_2^b that is virtually unaffected by the level of distortion present in the mesh. The process of transforming the finite element stress field into one which is continuous and then into one which is continuous and boundary admissible is shown for Problem 1 in Fig 8(b,c and d). The improvement in the pointwise quality of the estimated stress field through application of the static boundary conditions is clearly seen in this figure and is reflected in the value of \hat{U}_2^b when compared with that of \hat{U}_2 .

For Problem 2 similar improvements are also noted with EE_2^b providing significantly more effective error estimation than EE_2 . Note, with respect to this problem, that β_2^b appears to be

converging but not monotonically. The reason for this is felt to lie in the coarseness of the approximation of Mesh 1 both in terms of the mesh discretisation and in terms of the geometry; the circular arc is being approximated by two lines. This mesh also produces a situation where, whilst being close to each other, \widehat{U}_2^b is greater than \widehat{U}_2 .

For Problem 3 similar improvements in the quality of the error estimation observed for the previous two problems are also noted. It is interesting to observe, for this problem, that β_2^b is always greater than unity. This, in turn, implies that the strain energy of the estimated error is greater than that of the true error. This 'upper bound' type of behaviour is typical for error estimators that use statically admissible estimated stress fields (see reference [10] for example). However, although the estimated stress field of EE_2^b does satisfy equilibrium on element interfaces and at the static boundary of the model, nothing has been done to enforce internal equilibrium and, as such, in general one cannot expect this upper bound type of behaviour. Indeed, for Problem 1 and for Mesh 1 of Problem 2, β_2^b is less than unity.

For Problem 3 the effectivity ratios for a number of other error estimators are presented. These are discussed in order of appearance in Table 3. Error estimator EE_p is a modified version of the error estimator proposed by Zienkiewicz and Zhu in which the unique nodal stresses are recovered using a patch recovery scheme [6]. The modification that has been applied takes the form of a re-definition of the co-ordinate system in which the patch is defined (see reference [19]) and has been made to overcome the problem of ill-conditioning (and possible

singularity) of the equations used to recover the unique nodal stress whilst using the bi-linear form of the stress surface recommended in [6]. The performance of this error estimator is comparable, and slightly better than that of EE_2 . It is, however, significantly less effective than EE_2^b . Recent studies [17] have demonstrated that similar improvements in effectivity by applying the static boundary conditions, here demonstrated for an error estimator using simple nodal averaging as a means for determining unique nodal stresses, can also be achieved when using a patch recovery scheme for achieving unique nodal stresses.

Error estimator EE_{zz} is the original error estimator proposed by Zienkiewicz and Zhu in their 1987 paper [5] and uses a global least squares fit between the continuous estimated stress field and the finite element stress field as a means of obtaining unique nodal stresses. This error estimator is significantly more costly than the other ones detailed in this paper due to the fact that the computations required to recover the unique nodal stresses are performed at the global level (i.e. for the whole model simultaneously) rather than at the element or nodal level. The performance of this error estimator can be seen (c.f. Table 3) to be not as good as those that use the cheaper, local computations i.e. EE_2 , EE_2^b and EE_p .

Finally, results for the error estimator EE_4 have also been reported. This error estimator is similar to EE_2 in that it uses simple nodal averaging to achieve the unique nodal stresses. However, it differs in two significant ways. Firstly, for elements involving nodes that are attached to only a single element, a modification factor is applied to take account of the fact that

no error is detected at such nodes (the nodal averaged values of stress are identical to the finite element values). Details of this correction factor can be found in reference [15]. Secondly, and more significantly the way in which the integration of the strain energy of the estimated error is performed is different. Whereas in all other error estimators detailed in this paper this quantity is integrated using the appropriate Gauss quadrature scheme i.e. using a 2x2 scheme yields exact integration for undistorted (parallelogram shaped) elements, EE_4 uses a method of integration, termed nodal quadrature, which is approximate even for undistorted elements. It has been shown [15] that the nature of this approximation is such that the strain energy of the estimated error achieved in this manner is always greater than that which would have been achieved using an appropriate Gauss quadrature scheme. This leads to the very high effectivity ratios detailed in Table 3 and gives an explanation for the lack of asymptotic exactness exhibited by this error estimator.

The singularity in stress makes Problem 4 a challenging one for the element under consideration. However, even with such poor finite element approximation the enhancement in quality of error estimation obtained by applying the static boundary conditions is dramatic c.f. Fig. 17.

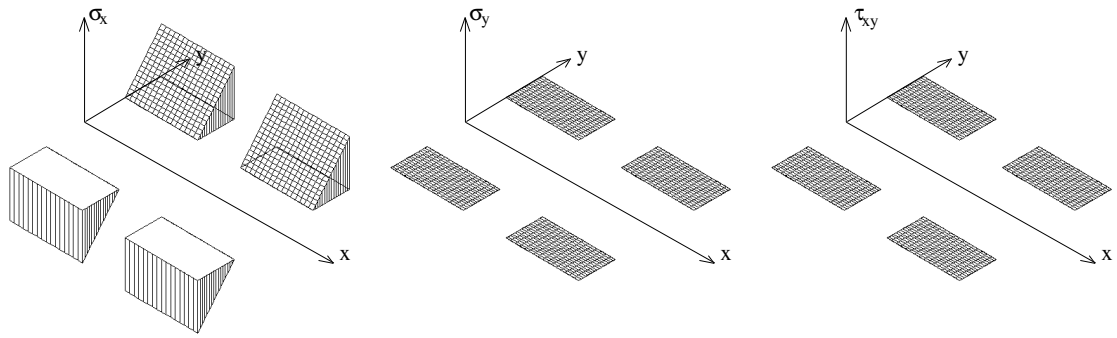
In conclusion, this paper has attempted to demonstrate the increased effectivity of error estimators that can be achieved by the simple expedient of applying the static boundary conditions to the estimated stress field. This increase in effectivity is significant especially for coarse and distorted meshes where effective error estimation is most called for. With the

current trend in pre- and post-processors being such that geometrical and boundary condition information is available after completion of the analysis stage, it is a relatively simple task to code this facility into existing finite element software. However, it should be noted that the studies presented in this paper pertain to a particular element type, namely, to the standard four-noded Lagrangian displacement element. The extension to higher order elements such as the eight-noded serendipity element is not (as has often been surmised) straight forward for it is well known, and has been widely reported [4] that for the eight-noded element consideration of lack of interface equilibrium alone is insufficient to provide effective error estimation.

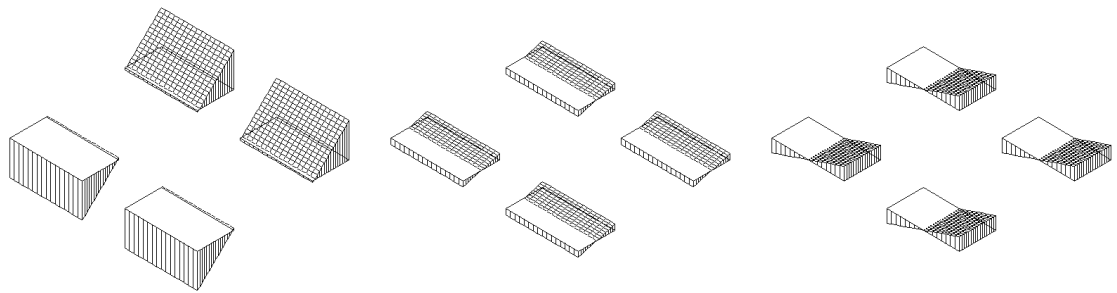
REFERENCES

1. I. Babuska and W. C. Rheinbolt, *A posteriori* error estimates for the finite element method, *Int. J. Numer. Meth. Engng.* **12**, 1597-1615, (1978).
2. D. W. Kelly, J. P. Gago, O. C. Zienkiewicz and I. Babuška, *A posteriori* error analysis and adaptive processes in the finite element method: Part I-Error analysis, *Int. J. Numer. Meth. Engng.* **19**, 1593-1619 (1983).
3. B. Szabó and I. Babuška, *Finite element analysis*, John Wiley & Sons, (1991).
4. P. Beckers, H. G. Zhong and E. A. W. Maunder, Numerical comparison of several *a posteriori* error estimators for 2D stress analysis, *Revue Européene des Éléments Finis*, 2(2), 155-178, (1993).
5. O. C. Zienkiewicz and J. Z. Zhu, A simple error estimator and adaptive procedure for practical engineering analysis, *Int. J. Numer. Meth. Engng.* **24**, 337-357, (1987).
6. O. C. Zienkiewicz and J. Z. Zhu Superconvergent derivative recovery techniques and *a posteriori* error estimation in the finite element method Part I: A general superconvergent recovery technique, *Int. J. Numer. Meth. Engng.* **33**, 1331-1364 (1992).

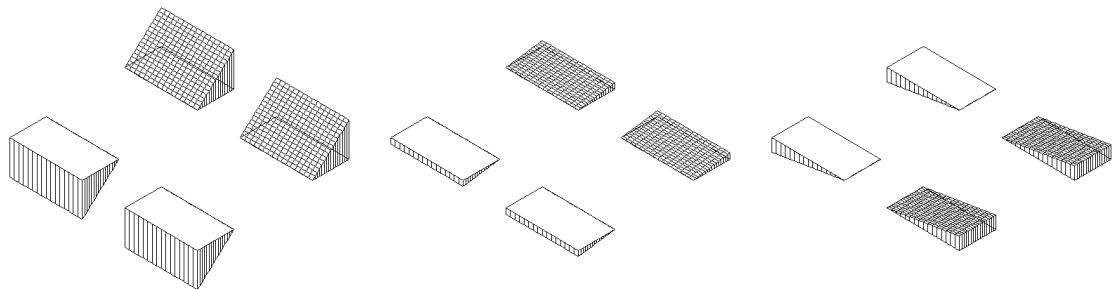
7. N. E. Wiberg and F. Abdulwahab Patch recovery based on superconvergent derivatives and equilibrium, *Int. J. Numer. Meth. Engng.* **36**, 2703-2724 (1993).
8. P. Ladevèze and D. Leguillon, Error estimate procedure in the finite element method and applications', *SIAM J. Numer. Anal.* **20** (No. 3), 483-509 (1983).
9. H. Ohtsubo and M. Kitamura, Element by element *a posteriori* error estimation and improvement of stress solutions for two-dimensional elastic problems, *Int. J. Numer. Meth. Engng.* **29**, 233-244, (1990).
10. E. A. W. Maunder and W. G. Hill, Complementary use of displacement and equilibrium models in analysis and design, *Proceedings of the sixth World Congress on Finite Element Methods, Banff*, (1990).
11. J. D. Yang, D. W. Kelly and J. D. Isles, *A posteriori* pointwise upper bound error estimates in the finite element method, *Int. J. Numer. Meth. Engng.* **36**, 1279-1298 (1993).
12. E. Hinton and J. S. Campbell, Local and global smoothing of discontinuous finite element functions using a least squares method, *Int. J. Numer. Meth. Engng.* **8**, 461-480, (1974).
13. G. Cantin, G. Lobignac and G. Touzot, An iterative algorithm to build continuous stress and displacement solutions, *Int. J. Numer. Meth. Engng.* **12**, 1439-1506, (1978).
14. M. Ainsworth, J. Z. Zhu, A. W. Craig and O. C. Zienkiewicz, Analysis of the Zienkiewicz-Zhu *a posteriori* error estimator in the finite element method, *Int. J. Numer. Meth. Engng.* **28**, 2161-2174 (1989).
15. J. Robinson, E. A. W. Maunder and A. C. A. Ramsay, Some studies of simple error estimators, *FEN, Issues 4, 5 and 6*, (1992) and *Issues 1, 2 and 3*, (1993).
16. A. Mashaie, E. Hughes and J. Goldak, Error estimates for finite element solutions of elliptic boundary value problems, *Comput. Struct.* **49**(1), 187-198, (1993).
17. A. C. A. Ramsay, Finite element shape sensitivity and error measures, Ph. D. Thesis, University of Exeter (1994).
18. A. C. A. Ramsay and H. Sbresny, Evaluation of some error estimators for the four-noded Lagrangian quadrilateral, Accepted for publication in *Comm. Numer. Meth. Engng.*, (1995).
19. A. C. A. Ramsay and H. Sbresny, Some studies of an error estimator based on a patch recovery scheme, *FEN, Issues 2 and 4* (1994).
20. N. E. Wiberg, F. Abdulwahab and S. Ziukas, Enhanced superconvergent patch recovery incorporating equilibrium and boundary conditions, *Int. J. Numer. Meth. Engng.* **37**, 3417-3440, (1994).



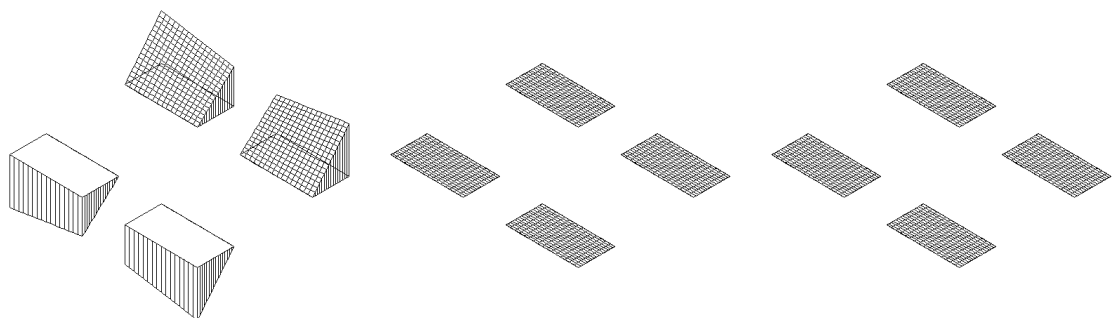
(a) True stress field $\{\sigma\}$



(b) Finite element stress field $\{\sigma_h\}$



(c) Continuous estimated stress field of EE_2 ($\beta_2 = 0.71$, $\hat{U}_2 = 103.7$)



(d) Continuous, boundary admissible estimated stress field of EE_2^b ($\beta_2^b = 0.82$, $\hat{U}_2^b = 7.7$)

Fig. 8. Stress fields for Problem 1

APPENDIX 6: PAPER II (Submitted to the *International Journal of Numerical Methods in Engineering*, May 1995)

A General Formulation of Equilibrium Macro-Elements with Control of Spurious Kinematic Modes.

The exorcism of an old curse.

E.A.W. Maunder, School of Engineering, University of Exeter, UK.

J.P. Moitinho de Almeida, A.C.A. Ramsay, Department of Civil Engineering, IST, Technical University of Lisbon, Portugal.

Abstract

This paper illustrates a method whereby a family of robust equilibrium elements can be formulated in a general manner. The effects of spurious kinematic modes, present to some extent in all primitive equilibrium elements, are eliminated by judicious assembly into macro-equilibrium elements. These macro-elements are formulated with sufficient generality so as to retain the polynomial degree of the stress field as a variable. Such a family of macro elements is a new development, and results for polynomials of degree greater than two have not been seen before. The quality of results for macro equilibrium elements with varying degrees of polynomial is demonstrated by numerical examples.

1. Introduction

The concepts of equilibrium elements and spurious kinematic modes are here introduced. Equilibrium elements offer possibilities of providing alternative solutions which give considerable scope for taking advantage of their results: e.g. dual analyses become possible which can provide bounds on quantities of interest such as the discretisation errors, "safe" designs of structures can be achieved when the lower bound theorem of plasticity is applicable. They have not however gained widespread popularity due to their relative complexity, the difficulties of incorporating into conventional software, and the more general problem with spurious kinematic modes.

The main tasks in formulating equilibrium elements are those of defining stress fields in elements, and assembling the elements. One approach [1,2,3] has been to utilise stress functions (such as Airy stress functions) interpolated from nodal values in a similar way to displacement fields. The principle of minimum complementary energy is then appropriate

in formulating equations for a system of elements. However, the imposition of boundary conditions is not so straightforward. An alternative approach defines stress fields directly within elements (e.g. as polynomial functions), and also introduces "secondary" quantities in the form of displacement connection variables associated with element boundaries [1,2,4,5,6,]. Elements defined in this way are generally termed "hybrid" elements. The displacement variables allow assembly to proceed, for example, with a stiffness method. Alternatively a force method is feasible [7,8] if dual force connection variables are defined.

Displacement variables can be associated with displacements of discrete points, e.g. conventional nodes, or nodes associated only with the sides of elements, or modes of displacement of the sides of elements. A strong form of element interface equilibrium is not generally achieved when corner node displacements are included. This is due to the fact that the corresponding nodal forces are not directly associated with interfaces. However diffusion of tractions and complete equilibrium may be locally enforced by using appropriate side displacement modes. The side displacement modes and internal stress fields defined for an element may give rise to spurious kinematic modes. These are modes of relative displacements of the sides of an element which can occur without the presence of side tractions. These spurious modes are also referred to as zero energy modes, and they produce an element stiffness matrix which is rank deficient. This situation is similar to that which can occur with conventional displacement elements due to the use of reduced integration. For example the 8-noded isoparametric serendipity element with 2×2 Gauss quadrature has the spurious kinematic mode in the form of an hourglass [9]. However, unlike the case with displacement elements where such modes rarely propagate through a finite element mesh, the spurious modes with equilibrium elements are more common and they are more likely to propagate.

The main challenge with equilibrium elements is to be able to achieve complete equilibrium without hindrance from spurious kinematic modes. Most elements based on polynomial fields are bedevilled by these modes! In this paper it is intended to present an approach based on decomposing each element into an assembly of primitive elements to form a macro-element. For the primitive elements the internal stress fields and the modes of side displacements are considered in polynomial forms. Using these stress fields complete equilibrium may be achieved with specified boundary tractions. The concept of macro-elements :

- 1) ensures that the effect of spurious kinematic modes can be eliminated from an arbitrary finite element mesh, and

2) enables elements of any degree to be formulated in a simple and efficient way.

Whilst the basic idea of using macro-elements is not new [1], the proposed approach is more general, and should allow for a rethinking on the usual concepts for the use of equilibrium elements.

2. Formulation of a primitive equilibrium element.

The formulation summarised here is based on that presented in references [4,10]. In each element the stress field is approximated by a linear combination of independent continuous functions which satisfy the equilibrium equations with zero body forces. A stress field $\boldsymbol{\sigma}$ is expressed as :

$$\boldsymbol{\sigma} = \mathbf{S} \mathbf{s} \quad (1)$$

where the columns of \mathbf{S} represent n_s independent stress fields, and the vector \mathbf{s} contains n_s stress field parameters.

The boundary displacements of each element are approximated by a linear combination of independent functions. These functions describe the modes of displacement of each side \mathbf{i} as a separate entity, so that compatibility of displacements of the different sides of an element is not an a priori assumption. The displacement field \mathbf{u}_i for side \mathbf{i} is expressed as :

$$\mathbf{u}_i = \mathbf{V}_i \mathbf{v}_i \quad (2)$$

where the columns of \mathbf{V}_i represent the independent modes of displacement of side \mathbf{i} . The displacement \mathbf{u} of an arbitrary point on a side of an element can then be expressed as :

$$\mathbf{u} = \sum_i \mathbf{V}_i \mathbf{v}_i = \mathbf{V} \mathbf{v} \quad (3)$$

by extending the functions in \mathbf{V}_i to cover all sides of an element. Thus \mathbf{V}_i has zero value on side \mathbf{j} when $\mathbf{j} \neq \mathbf{i}$. The columns of \mathbf{V} now represent n_v independent displacement modes for all sides of an element.

The hybrid fields of internal stress and boundary displacement are used to impose weak integral forms of boundary equilibrium and internal compatibility. Equilibrium on the boundary of an element e is imposed by :

$$\left\{ \int_{\partial e} \mathbf{V}^T \mathbf{N} \mathbf{S} ds \right\} \{s\} = [\mathbf{D}] \{s\} = \{g\} = \left\{ \int_{\partial e} \mathbf{V}^T \mathbf{t} ds \right\} \quad (4)$$

where the 2x3 transformation matrix \mathbf{N} resolves stress at a boundary point into traction components, and \mathbf{t} represents applied boundary tractions.

A weak integral form of compatibility within an element is imposed by :

$$\left[\int_{\partial e} \mathbf{S}^T \mathbf{N}^T \mathbf{V} ds \right] \{\mathbf{v}\} = [\mathbf{D}^T] \{\mathbf{v}\} = \{\boldsymbol{\delta}\} = \left[\int_e \mathbf{S}^T \mathbf{f} \mathbf{S} de \right] \{\mathbf{s}\} = [\mathbf{F}] \{\mathbf{s}\} \quad (5)$$

where \mathbf{f} represents the constitutive relations :

$$\mathbf{f} \boldsymbol{\sigma} = \boldsymbol{\varepsilon} \quad (6)$$

The vectors \mathbf{g} and $\boldsymbol{\delta}$ represent generalised tractions and deformations corresponding to stress parameters \mathbf{s} and displacement parameters \mathbf{v} respectively. Equations (4) and (5) can be written together for the primitive element \mathbf{e} as :

$$\begin{bmatrix} -\mathbf{F}^e & \mathbf{D}^{eT} \\ \mathbf{D}^e & 0 \end{bmatrix} \begin{Bmatrix} \mathbf{s}^e \\ \mathbf{v}^e \end{Bmatrix} = \begin{Bmatrix} 0 \\ \mathbf{g}^e \end{Bmatrix} \quad (7)$$

where matrices \mathbf{D}^e and \mathbf{F}^e are defined in Equations (4) and (5) respectively. \mathbf{F}^e is termed the natural flexibility matrix, and the superscript \mathbf{e} now identifies the element.

It should be emphasized that the weak form of equilibrium expressed by Equation (4) may become a strong form of equilibrium for arbitrary applied boundary tractions \mathbf{t} when in polynomial form of degree p . This may occur when the columns of \mathbf{V} and \mathbf{S} generate complete polynomial displacements and equilibrating stress fields respectively of degree $\geq p$.

3. Spurious kinematic modes.

The origins and the consequences of spurious kinematic modes for equilibrium elements are reviewed in this section. The effects of these modes, which originate at the level of a single primitive element, can be demonstrated by means of the generalised tractions and deformations \mathbf{g}^e and $\boldsymbol{\delta}^e$ which are related to \mathbf{s}^e and \mathbf{v}^e by the contragredient transformations in Equations (4) and (5). These transformations involve the $n_v \times n_s$ matrix \mathbf{D}^e . The work done by displacements \mathbf{v}^e with tractions equilibrating with stresses \mathbf{s}^e is thus given by :

$$\mathbf{s}^{eT} \mathbf{D}^{eT} \mathbf{v}^e = \mathbf{g}^{eT} \mathbf{v}^e = \mathbf{s}^{eT} \boldsymbol{\delta}^e \quad (8)$$

Clearly for all displacements $\mathbf{v}^e_{\mathbf{r}}$ conforming with the n_r rigid body modes of an element

$$\mathbf{D}^{eT} \mathbf{v}_r^e = \mathbf{0} \quad (9)$$

Although not strictly necessary, it is here assumed that all the rigid body modes for each side of an element are permitted within \mathbf{v}^e .

Spurious kinematic modes \mathbf{v}_{skm}^e are defined as all other non trivial solutions to :

$$\mathbf{D}^{eT} \mathbf{v}_{skm}^e = \mathbf{0} \quad (10)$$

Displacements satisfying Equations (9) and (10) form the nullspace of \mathbf{D}^{eT} , represented by the matrix \mathbf{C}^e which has dimensions $n_v \times (n_v - \text{rank } \mathbf{D}^e)$ and satisfies :

$$\mathbf{D}^{eT} \mathbf{C}^e = \mathbf{0} \quad (11)$$

For these displacements no work is done with any of the internal stress fields. The number of independent spurious kinematic modes, n_{skm} , is thus given by :

$$n_{skm} = (n_v - n_r - \text{rank } \mathbf{D}^e), \quad (12)$$

and a necessary, but not sufficient, condition for an element to be free of spurious kinematic modes is that :

$$n_s \geq n_v - n_r \quad (13)$$

Boundary tractions \mathbf{t} applied to an element are admissible only if :

(a) they are in overall equilibrium i.e. they do no work with the rigid body modes, and

(b) they do not excite any spurious kinematic mode i.e. they do no work with any such mode.

\mathbf{t} is represented by \mathbf{g}^e as defined in Equation (4). It follows that for \mathbf{t} to be admissible, \mathbf{g}^e must satisfy :

$$\begin{aligned} \mathbf{g}^{eT} \mathbf{v}^e &= \mathbf{0} \text{ for all } \mathbf{v}^e \text{ such that } \mathbf{D}^{eT} \mathbf{v}^e = \mathbf{0} \\ \text{or } \mathbf{C}^{eT} \mathbf{g}^e &= \mathbf{0} \end{aligned} \quad (14)$$

It is now possible to stipulate the conditions for strong equilibrium on the boundary of an element: the applied traction must be admissible and in polynomial form of degree $\leq p$, where p is the degree of the element. The degree p refers to the degree of the polynomial approximations assumed within, and on the boundary of, the element. On the other hand,

tractions are inadmissible if they do not satisfy the homogeneous Equation (14), and hence they would excite spurious kinematic modes which in effect deny the means for load transmission.

By analogy with skeletal structures, spurious kinematic modes can be considered like "mechanisms", and consequently they also act like "releases" which prohibit the transmission of certain generalised forces or "stress resultants". These two aspects of spurious modes are illustrated in the case of a primitive triangular element with degree $p = 1$ in Figure 1. For this element, $n_s = 7$, $n_v = 12$, and $n_r = 3$. The rank of $\mathbf{D}^e = 7$, which implies the existence of 2 spurious kinematic modes.

A typical spurious mode is shown in Figure 1 with relative values of side displacement modes for an equilateral element. Two other similar modes exist by reason of cyclic symmetry, however only two of the three are independent. Admissible side loads must do no work with any of the spurious kinematic modes, hence the normal tractions shown, which are statically equivalent to three couples, are inadmissible. It should be noted that when the degree p is increased for the primitive, to a value of 5 say, then in this case $n_s = 33$, $n_v = 36$, $n_r = 3$, and hence $n_s = n_v - n_r$. Thus the necessary condition of Equation (13) for no spurious kinematic modes is satisfied. However, it is found that \mathbf{D}^e is rank deficient with a rank of only 30 [11]. In this case, from Equation (12), $n_{skm} = 3$.

Although spurious kinematic modes originate at the element level, the main problem with such modes is that they may propagate throughout a finite element mesh thereby leading to a rank deficient structural stiffness matrix for the system, and the possibility of load vectors being inadmissible. Such propagation is illustrated for patches of primitive triangular elements in Figure 2 for $p = 1$ and 2.

In each patch there exists just the one spurious kinematic mode for the system of elements. If these modes, or mechanisms, are excited by the applied loads, then a solution to the given problem is not feasible since the behaviour of the finite element model is described by an inconsistent system of equations. When mechanisms are not excited by the loads, the solution of the problem is unique in terms of stress distributions, but multiple in terms of displacements. This is indicated by a consistent, but singular, system of equations whose solution is not obtainable using solution algorithms designed for positive definite matrices.

As with the single element, the existence of spurious kinematic modes for an assembly of elements can be determined *a priori* to the formation of the stiffness equations, but this may involve significant computational effort. If \mathbf{d} represents the modes of displacement of the

sides or interfaces of an assembly of elements, the compatibility condition can be expressed by :

$$\mathbf{A} \mathbf{d} = \mathbf{v} \quad (15)$$

where \mathbf{v} now represents the side displacements of the set of all elements, and \mathbf{A} is a Boolean type of assembly matrix. Let \mathbf{D} now denote the block diagonal matrix :

$$\mathbf{D} = \begin{bmatrix} \mathbf{D}^1 & & & \\ & \mathbf{D}^2 & & \\ & & \bullet & \\ & & & \bullet \end{bmatrix} \quad (16)$$

where \mathbf{D}^e represents the matrix defined by Equation (4) for element e . Then compatible spurious kinematic modes \mathbf{d}_{skm} for the assembly must satisfy :

$$[\mathbf{D}^T \mathbf{A}] \mathbf{d}_{\text{skm}} = \mathbf{0} \quad (17)$$

Thus the determination of these modes requires the computation of the rank and nullspace of $[\mathbf{D}^T \mathbf{A}]$.

4. A General Approach to Analysis with Primitive Equilibrium Elements.

One possible way to treat the problems associated with spurious kinematic modes in a mesh has been proposed in [4,10]. A general formulation for equilibrium elements is there presented, and the possible spurious kinematic modes in a mesh are controlled by an equation solver which is capable of accounting for a matrix of reduced rank, but in a consistent system of equations.

As this solver encounters a dependent equation it zeroes the relevant variable, thus "freezing" the spurious kinematic mode in an arbitrary position, and presents to the user a solution which is unique and of good quality in terms of the static variables, but whose quality may be doubtful in terms of kinematic variables. In cases where the system of equations is ill-conditioned, the definition by numerical techniques of those equations that are to be considered as dependent can be problematic. Also the *a priori* recognition of spurious kinematic modes and inadmissible loads for a mesh is not possible without significant additional analysis when this approach is used.

This approach allows for a very simple formulation of elements of any degree, but although the numerical problems associated with spurious kinematic modes may be controlled, the influence of these modes remains difficult to predict.

5. A Robust Approach based on Macro-Elements.

Other authors have used assemblies of triangular equilibrium elements to form macro-elements, in such a way that the spurious kinematic modes are either totally eliminated, or remain internal to the macro-element. These macro-elements are either triangular or quadrilateral, as presented in Figure 3.

In the definition of macro-elements initially developed at Liège [1,2,12,13,14], the position of the internal node P of the triangular macro-element is not constrained, and as was noted [1], this macro-element is free of spurious kinematic modes. The position of P in the quadrilateral however, was constrained to be positioned at the intersection of the diagonals. This macro-element was studied for polynomial approximations of the stress field up to the second degree and it was found that a single spurious mode was always present. This mode was explained with reference to a skeletal model formed from pin-jointed subtriangles. The stiffness matrix for the macro-element was formed by assembling the stiffness matrices of its four constituent elements, and then condensing out the internal degrees of freedom. However some of these freedoms were indeterminate due to the spurious mode. The mode was blocked by the device of adding a fictitious bar which effectively coupled certain internal freedoms. The number of internal degrees of freedom to be eliminated was thus reduced by one. The stiffness matrix of the macro-element is correct as long as the spurious kinematic mode is not excited, and the fictitious bar remains unstressed. Figure 2(b) illustrates the important property of the spurious mode : it only involves relative displacements of the internal sides, and consequently all tractions applied to the external sides are admissible.

An alternative procedure [1,12,13] based on direct construction of stress fields was however found to be a more convenient way to obtain a stiffness matrix for a macro-element. By taking advantage of the oblique axes formed by the diagonals of the quadrilateral, statically admissible stress fields were formed directly so as to satisfy traction continuity between the elements. From these independent stress fields in the macro-element it is a straightforward matter to form a natural flexibility matrix and then a stiffness matrix. In the case of a hyperstatic element the principle of minimum complementary energy is invoked. The spurious kinematic mode thus does not explicitly appear in this procedure. More recently, other procedures based on directly satisfying internal traction continuity in triangular and

quadrilateral macro-elements have been proposed [15-18]. Other authors have studied these macro elements in the context of elastic and elastoplastic analyses, and error estimation [19-24].

The idea behind the macro-element is thus a simple one. For a macro-element to be effective, it should consist of an assembly of primitive elements for which any spurious kinematic modes which may exist only involve displacements of the internal sides, and consequently all tractions applied to the external sides are admissible. A mesh of such macro-elements will always be free of spurious mode problems provided the load is applied to the sides of the macro-elements. For the triangular macro-element there are no spurious kinematic modes irrespective of the degree of the stress field or the form of the internal geometry. In contrast, for the quadrilateral macro-element, the number and nature of the spurious kinematic modes are dependent on both the degree of the stress field and the form of the internal geometry. With reference to Figure 3, when P lies at the intersection of the diagonals, there is always one internal spurious kinematic mode for degree $p \geq 1$ (the "benign" case). When P is in an arbitrary position and does not lie at the intersection of the diagonals, the kinematics depend on the degree p. In this case, when $p = 1$, there is one spurious kinematic mode, but now it involves relative movements of the external sides (the "malignant" case). However when $p \geq 2$ there is no spurious kinematic mode. These properties of the quadrilateral macro-element are summarised in Table 1, and illustrated in Figure 2, where the patches of primitive elements are now considered as macro-elements. **Thus for the more general case, the spurious mode is eliminated from the macro-element, and it is only in particular cases that the mode exists.** These findings are based on recent numerical studies reported by Maunder [18,25], and Ramsay [11], and not on formal proofs. More comprehensive results and explanations for these findings are in preparation.

Degree of Stress field	Position of point P	
	Intersection of diagonals	Arbitrary
$p = 1$	$n_{skm} = 1$ (benign)	$n_{skm} = 1$ (malignant)
$p \geq 2$	$n_{skm} = 1$ (benign)	$n_{skm} = 0$

Table 1 Number and nature of spurious kinematic modes for a quadrilateral macro-element

The different characteristics of the quadrilateral macro-elements when under load are illustrated in Figure 4. This Figure illustrates the deformed shapes of four rectangular macro-elements when loaded with a uniform compressive stress, which is an admissible form of loading for all four elements. When spurious kinematic modes are present, their amplitudes, which are arbitrary, have been chosen so as to produce displacements of the same order of magnitude as for the other modes of displacement.

6. Proposed approach

Based on the observations made in Sections 4 and 5, an efficient approach which combines generality with robustness is proposed. In this approach macro-elements are first defined as composed from primitive elements of general degree. Then the internal displacement variables are eliminated (condensed out) from the macro-element equations so as to obtain a stiffness matrix in terms of external variables. This approach requires that the composition of the macro-element either excludes spurious kinematic modes altogether, or if such modes are present they only involve the internal degrees of freedom. In the latter case the elimination procedure, as in Section 4, must recognize and account for dependent equations. The resulting stiffness matrix for the macro-element is then free of the singularities associated with spurious kinematic modes, and the assembly of all the macro-element matrices into a global set of equations follows the conventional procedure for a stiffness method [9].

This approach is illustrated for the macro-element in Figure 5 composed of four primitive triangles. The triangles are numbered 1 to 4, the "internal sides" or interfaces are numbered

Due to the possible presence of one spurious kinematic mode the solution for the \mathbf{v}_i 's from these equations may not be unique. Nevertheless, since these equations are always consistent, a solution can be obtained either by using an appropriate form of Gauss elimination, or by using the pseudoinverse \mathbf{K}_{ii}^+ as determined by singular value decomposition [26].

When \mathbf{s} is replaced by \mathbf{v}_e in the third set of Equations (18), the macro-element stiffness matrix is obtained which transforms the external displacements to external tractions :

$$\bar{\mathbf{K}} \mathbf{v}_e = \mathbf{g}_e$$

where the general form of $\bar{\mathbf{K}}$ can be expressed as :

$$\bar{\mathbf{K}} = \left[\mathbf{K}_{ee} - \mathbf{K}_{ie}^T \mathbf{K}_{ii}^+ \mathbf{K}_{ie} \right], \text{ where } \mathbf{K}_{ee} = \mathbf{D}_e \mathbf{F}^{-1} \mathbf{D}_e^T \quad (21)$$

7. Processing of the results

Once the global stiffness matrix is obtained the resulting system of equations can be solved using an algorithm appropriate for its structure: band, profile or sparse matrix [9]. The solution consists of the values of the displacement modes of the external sides of the macro-elements.

From these values the displacement modes of the internal sides of the macro-elements can be obtained from Equation (20). However, these displacements should in general be disregarded when \mathbf{K}_{ii} is singular, as then they only indicate one of the feasible solutions. Only the internal displacements, and not the stresses, are dependent on the spurious kinematic modes. The unique stress parameters are recovered from Equation (19) after using Equation (20) :

$$\mathbf{s} = \mathbf{F}^{-1} \left[\mathbf{D}_e^T - \mathbf{D}_i^T \mathbf{K}_{ii}^+ \mathbf{K}_{ie} \right] \mathbf{v}_e \quad (22)$$

8. Numerical examples.

The behaviour and performance of the macro-elements discussed in this paper will be demonstrated through three numerical examples. In all the examples the macro-elements are rectangular, use diagonal subdivision, and the degrees of the stress fields are considered in the range 1 to 10. These properties of the macro-elements are chosen to simplify the examples, and are not constraints of the formulation. In Problem 1 equilibrium elements will be compared with conventional conforming displacement elements in order to compare the characteristics of the two different types of solution. Problem 2 illustrates the

performance of equilibrium elements for a case with discontinuous material properties, whilst in Problem 3 a case involving a stress singularity due to geometry is investigated.

The stress plots that appear for the examples in the Figures show unprocessed finite element stresses i.e. no averaging or smoothing has been performed. For all the problems, the numbers of degrees of freedom (dof) tabulated for the equilibrium models refer to those associated with the displacements of the external sides of the macro-elements. Other measures of the dofs of the equilibrium models are possible which depend on considering the models as composed of primitive elements, rather than macro-elements, namely :

dof_d - the total number of displacement degrees of freedom ;

dof_σ - the number of stress degrees of freedom.

dof_t - the total number of degrees of freedom (displacements and stresses) as used in [10];

These quantities are compared in Table 2 for the meshes considered in Figure 6, when $p = 2$.

Mesh	dof (macro)	dof_d	dof_t	dof_σ
1	72	168	360	192
2	240	624	1392	768
3	864	2400	5472	3072
4	3264	9408	21696	12288

Table 2 : Degrees of freedom for the meshes in Figure 6 when $p = 2$.

Problem 1

The geometry, boundary conditions and meshes are shown in Figure 6. The boundary tractions are linear and are defined to be in equilibrium with the stress field given in Equation (23). It should be noted that whilst this stress field is statically admissible with zero body forces, it is not kinematically admissible and is, therefore, invalid as the solution to the problem.

$$\begin{aligned}\sigma_x &= x^2 \\ \sigma_y &= y^2 \\ \tau_{xy} &= -2xy\end{aligned}\tag{23}$$

Finite element analyses were performed using both conforming displacement elements (the standard 4-noded Lagrangian element and the 8-noded serendipity element) and the macro-equilibrium elements. Full integration was used in the analyses with both types of elements. The finite element strain energies U_h are shown in Table 3 and were calculated using Young's Modulus $E = 210\text{N/m}^2$, Poisson's Ratio $\nu = 0.3$, and a material thickness $t = 0.1\text{m}$ with the assumption of plane stress. The right superscripts C and E refer, respectively, to the conforming and equilibrium models whilst the left superscripts refer to the number of nodes per conforming element, and to the degree of the stress field in the case of the equilibrium element.

Mesh	conforming element				equilibrium element			
	$^4U_h^C$	dof	$^8U_h^C$	dof	$^1U_h^E$	dof	$^2U_h^E$	dof
1	1702.598	18	2036.765	42	2050.422	48	2041.809	72
2	1953.359	50	2041.174	130	2042.310	160	2041.615	240
3	2019.156	162	2041.570	450	2041.655	576	2041.602	864
4	2035.951	578	2041.600	1666	2041.604	2176	2041.602	3264

Table 3: Finite element results for Problem 1

The convergence of strain energies for the four types of element are shown in the graph of Figure 7. These results demonstrate the upper bounded nature of the strain energy for equilibrium models in contrast to the lower bound values achieved by conforming models. From the results given in Table 3 it is possible to state that the true value of the model strain energy U is such that $2041.60015 \leq U \leq 2041.60229$ (two additional decimal places are given).

The displaced shapes for Mesh 1 for the 4-noded displacement element and the linear equilibrium element are shown in Figure 8. The non-conforming edges of the equilibrium model are clearly seen.

Figure 9 demonstrates, qualitatively, the way in which equilibrium is violated when using conforming displacement elements. The discontinuities in the τ_{xy} -component of the stress across the element interfaces can be readily observed.

Problem 2

This problem compares the quality of results obtained by p and h refinement schemes with equilibrium elements. A rectangular membrane is formed from two square regions of different materials. Each material has a different Young's Modulus but the same Poisson's Ratio. The membrane is loaded with uniform tension as shown in Figure 10.

Region 1 has a Young's modulus of $E_1 = 100\text{N/m}^2$ and for Region 2 $E_2 = 10\text{N/m}^2$. Both regions have a Poisson's ratio of $\nu = 0.3$ and a material thickness $t = 10\text{m}$. An assumption of plane stress has been made for the purpose of this analysis. The coarsest mesh that can be used for this problem is the two element mesh shown as Mesh 1 in Figure 10(b). In addition to this mesh two uniform (h) refinements are also investigated (Meshes 2 and 3). In terms of p refinement, results for polynomial stress fields of degree one (linear) to degree five (quintic) are presented. The finite element strain energies U_h^E are shown in Table 4, and their convergence characteristics are shown graphically in Figure 11.

	Mesh 1		Mesh 2		Mesh 3	
Degree (p)	U_h^E	dof	U_h^E	dof	U_h^E	dof
1	0.5477909	28	0.5467302	88	0.5462864	304
2	0.5464224	42	0.5462343	132	0.5461185	456
3	0.5463319	56	0.5461381	176	0.5460849	608
4	0.5461697	70	0.5461002	220	0.5460724	760
5	0.5461382	84	0.5460829	264	0.5460669	912

Table 4: Finite element strain energy for Problem 2

An idea of the different characteristics of the two types of refinement (p and h) can be obtained by studying the stress fields, and the distribution of normal traction along the material interface. For this purpose, contour plots of the σ_{xx} -component of stress are shown in Figure 12.

For Mesh 1 ($p=1$) the discontinuities in stress that may occur across interfaces of equilibrium elements are clearly visible between the primitive elements. The discontinuities reveal the fact that each of the two square macro-elements is actually composed of four triangular primitive elements. Even though such stress discontinuities may occur, pointwise equilibrium across interfaces is strictly maintained. This is confirmed, for example, by the continuity in the x-direction of the σ_{xx} -component of stress at the interface between the two regions.

Figure 13 gives a more quantitative view of the stress distribution at the interface of the two regions by showing the σ_{xx} -component of stress plotted along this interface for a number of selected models. Discontinuities in the y-direction of the stress σ_{xx} are observed for Mesh 3 ($p=1$), which violate the true solution, but do not violate equilibrium.

Problem 3

This problem involves a stress concentration due to a crack of infinitesimal width, and of length 5m as shown for the symmetric half in Figure 14. The extent of the crack is illustrated by the thick line. The boundary tractions are evaluated from the following stress field which is both statically and kinematically admissible [27] :

$$\begin{aligned}\sigma_x &= \frac{100}{\sqrt{r}} \cos \frac{\theta}{2} \left\{ 1 - \sin \frac{\theta}{2} \sin \frac{3\theta}{2} \right\} \\ \sigma_y &= \frac{100}{\sqrt{r}} \cos \frac{\theta}{2} \left\{ 1 + \sin \frac{\theta}{2} \sin \frac{3\theta}{2} \right\} \\ \tau_{xy} &= \frac{100}{\sqrt{r}} \sin \frac{\theta}{2} \cos \frac{\theta}{2} \cos \frac{3\theta}{2}\end{aligned}\tag{24}$$

Symmetric boundary conditions are applied on the line of symmetry. For Young's Modulus $E = 210\text{N/m}^2$, Poisson's Ratio $\nu = 0.3$, and a material thickness $t = 0.1\text{m}$ with a plane stress assumption, the strain energy U for the symmetric half shown is 62.442963Nm [28].

The strain energy results from the finite element analyses performed on the four meshes shown in Figure 14(b) are given in Table 5.

p	Mesh 1		Mesh 2		Mesh 3		Mesh 4	
	U_h^E	dof	U_h^E	dof	U_h^E	dof	U_h^E	dof
1	73.313361	28	67.107610	88	64.577097	304	63.470253	1120
2	66.731729	42	64.333771	132	63.356702	456	62.892746	1680
3	64.713918	56	63.525367	176	62.974219	608	62.706200	2240
4	63.909238	70	63.153881	220	62.794140	760	62.617507	2800
5	63.471788	84	62.946635	264	62.692650	912	62.567278	3360
6	63.207607	98	62.819312	308	62.629937	1064	62.536154	3920
7	63.034270	112	62.735024	352	62.588271	1216	62.515438	4480
8	62.914096	126	62.676244	396	62.559142	1368	62.500936	5040
9	62.827305	140	62.633612	440	62.537979	1520	62.490399	5600
10	62.762547	154	62.601702	484	62.522117	1672	62.482472	6160

Table 5 : Finite element results for Problem 3

Figure 15 shows the convergence characteristics of the finite element strain energies. Note the significantly increased rate of convergence obtained with p -refinement compared with h -refinement. For Mesh 4, the 8-noded displacement element gives a finite element strain energy of ${}^8U_h^C = 61.056022\text{Nm}$ (866 dof) thereby confirming the bounded nature of the two types of solution.

The convergence of the stresses is demonstrated for the τ_{xy} -component of the stress in Figure 16, whilst that of the displacements is shown in Figure 17.

Although p -refinement has the faster convergence rate, it is of interest to consider qualitatively the stress fields obtained in the four meshes for the same energy of the error. For example, Figure 18 shows τ_{xy} for the four meshes when the error is approximately 1.6% in energy terms. This corresponds to $\log(U_h^E - U) \approx 0$ in Figure 15. It appears that the continuity and quality of τ_{xy} does improve with the number of degrees of freedom achieved with h -refinement.

9. Conclusions

1. By recognizing the general properties of macro-elements, a p-type equilibrium element has been formulated which effectively removes the usual problems associated with spurious kinematic modes.

2. Numerical examples with rectangular macro-elements with p in the range 1 to 10 confirms the feasibility of the proposed formulation, and indicates that solutions of good quality are obtainable for both statically admissible stress fields **and** side displacements.

3. Numerical examples indicate that, in energy terms, p-refinement produces much faster convergence than h-refinement. However, for the same overall error, it appears that the stress fields from p-refinement of a coarse mesh, although incurring less degrees of freedom, are inferior to those obtained with some h-refinement.

4. Further work is required to:

(a) formally prove the observed properties of the macro-elements as regards spurious kinematic modes,

(b) investigate alternative numerical procedures for the formulation of macro-elements, and their assembly into finite element equations, with a view to minimising computational effort,

(c) extend numerical studies to include triangular and general distorted quadrilateral macro-elements. These studies should also address such questions as: what are the optimum positions of the internal points P?

(d) make a detailed comparison between equilibrium and displacement elements, both from the computational and the engineering points of view.

5. The p-refinement capability of the macro-element also makes it suitable for use in dual type error estimation of finite element models with hierarchical p-type displacement elements. This is in contrast to existing methods which approximate equilibrium solutions by using higher order displacement elements [29,30].

References

1. Sander G. *Application of the dual analysis principle*, High Speed Computing of Elastic Structures, Ed by B. Fraeijs de Veubeke, Les Congres et Colloques de l'Universite de Liege, Vol 61, 167-207, 1971.
2. Fraeijs de Veubeke B., Sander G., Beckers P. *Dual analysis by finite elements: linear and non linear applications*, Technical Report AFFDL-TR-72-93, Ohio, 1972.
3. Gallagher R.H., Heinrich J.C., Sarigul N. *Complementary energy revisited*, in Hybrid and Mixed Finite Element Methods, Ed by S.N.Atluri, R.H.Gallagher, O.C.Zienkiewicz, Chapter 23, 453-465, Wiley, 1983.
4. Moitinho de Almeida J.P.B. *Modelos de elementos finitos para a analise elastoplastica*, Ph.D. thesis, Technical University of Lisbon, 1989.
5. Pian T.H.H. *Evolution of assumed stress hybrid finite elements*, in ART in FEM Technology, Ed by J. Robinson, Robinson and Associates, 602-619, 1984.
6. Robinson J. *The mode-amplitude technique and hierarchical stress elements - a simplified and natural approach*, Int.J.Num.Meth.in Eng. Vol 21, 487-507, 1985.
7. Robinson J. *Integrated theory of finite element methods*, Wiley, 1973.
8. Maunder E.A.W., Savage G.J. *A graph-theoretic model for finite elements with side variables*, Civil Eng. Syst. Vol 11, 111-141, 1994.
9. Zienkiewicz O.C., Taylor R. *The Finite Element Method*, 4th Ed, McGraw-Hill, 1989.
10. Moitinho de Almeida J.P.B., Teixeira de Freitas J.A. *Alternative approach to the formulation of hybrid equilibrium finite elements*, Computers and Structures, Vol 40, No 4, 1043-1047, 1991.
11. Ramsay A.C.A. *Robust Variable Degree Equilibrium Elements: their formulation and application*, Report for Human, Capital and Mobility Network, ERB4050p1930382, 1995.
12. Kieffer M. *Element de quadrilatere, statiquement admissible et co-diffusif, a champ de tensions du premier degre*, LTAS Report SF-5, Universite de Liege, 1969.
13. Kieffer M. *Element quadrilateral de membrane, statiquement admissible et co-diffusif a champ des tensions du second degre*, LTAS Report SF-7, Universite de Liege, 1970.

14. Fraeijns de Veubeke B. *Diffusive equilibrium models*, in B.M.Fraeijns de Veubeke Memorial Volume of Selected Papers, Ed by M.Geradin, Sijthoff and Noordhoff/Waterloo University, 569-628, 1980.
15. Maunder E.A.W. *A direct approach to a flexibility matrix for a triangular equilibrium membrane element*, in Accuracy, Reliability and Training in FEM Technology, Ed by J.Robinson, Robinson and Associates, 119-128, 1984.
16. Allman D.J. *The linear stress triangular equilibrium model in plane elasticity*, Computers and Structures, Vol 31, No 5, 673-680, 1989.
17. Maunder E.A.W., Hill W.G. *Complementary use of displacement and equilibrium models in analysis and design*, in FEM in the Design Process, Ed by J.Robinson, Robinson and Associates, 493-501, 1990.
18. Maunder E.A.W., Ramsay A.C.A. *Quadratic equilibrium elements*, in FEM Today and the Future, Ed by J.Robinson, Robinson and Associates, 401-407, 1993.
19. Watwood V.B., Hartz B.V. *An equilibrium stress field model for finite element solutions of two-dimensional elastostatic problems*, Int.J.Solids and Structures, Vol 4, 857-873, 1968.
20. Johnson C., Mercier B. *Some equilibrium finite element methods for two-dimensional problems in continuum mechanics*, in Energy Methods in Finite Element Analysis, Ed by R.Glowinski, E.Y.Rodin, O.C.Zienkiewicz, Chapter 11, 213-224, Wiley, 1979.
21. Zavelani-Rossi A. *Collapse load analysis by finite elements*, in Engineering Plasticity by Mathematical Programming, Ed by M.Z.Cohn, G.Maier, Chapter 11, 257-269, Pergamon, 1979.
22. Ladeveze P., Coffignal G., Pelle J.P. *Accuracy of elastoplastic and dynamic analysis*, in Accuracy Estimates and Adaptive Refinements in Finite Element Computations, Ed by I.Babuska, O.C.Zienkiewicz, J.Gago, E.R.deA.Oliveira, Chapter 11, 181-203, Wiley, 1986.
23. Rougeot P. *Sur le controle de la qualite des maillages elements finis*, Ph.D. thesis, Universite Paris 6, 1989.
24. Temin-Gendron P., Laurent-Gengoux P. *Calculation of limit loads for composite materials via equilibrium finite elements*, Computers and Structures, Vol 45, Nos 5/6, 947-957, 1992.

25. Maunder E.A.W. *A reappraisal of compound equilibrium elements*, Proceedings 12th Canadian Congress of Applied Mechanics, Carleton University, Ed by M.A. Erki, J.Kirkhope, 796-797, 1989.
26. Strang G. *Linear algebra and its applications*, 3rd Ed, Harcourt Brace Jovanovich, 1988.
27. Szabo B., Babuska I. *Finite Element Analysis*, Wiley, 1991.
28. Ramsay A.C.A. *Finite element shape sensitivity and error measures*, Ph.D. thesis, University of Exeter, 1994.
29. Ohtsubo H., Kitamura M. *Element by element a posteriori estimation and improvement of stress solutions for two-dimensional elastic problems*, Int.J.Num.Meth.in Eng. Vol 29, 223-244, 1990.
30. Ainsworth M., Oden J.T., Wu W. *A posteriori error estimation for h-p approximations in elastostatics*, Applied Numerical Mathematics, Vol 14, 23-54, 1994.

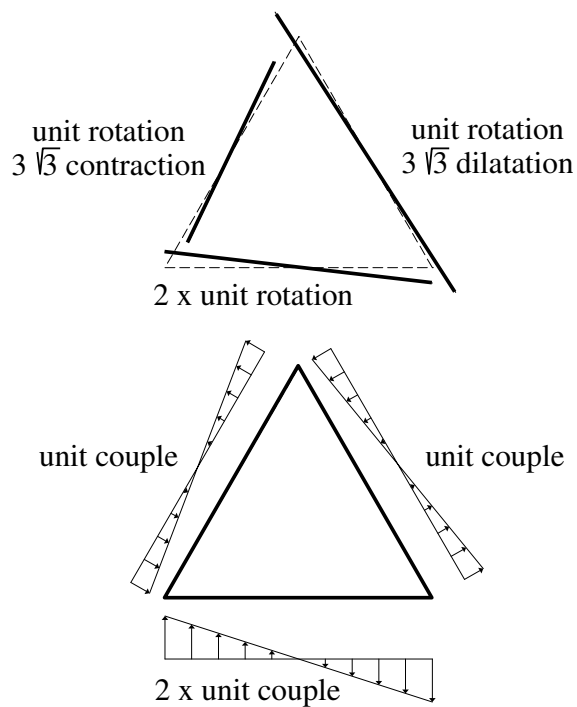


Figure 1: A typical spurious kinematic mode and an inadmissible load for an equilateral triangular primitive element with $p=1$.

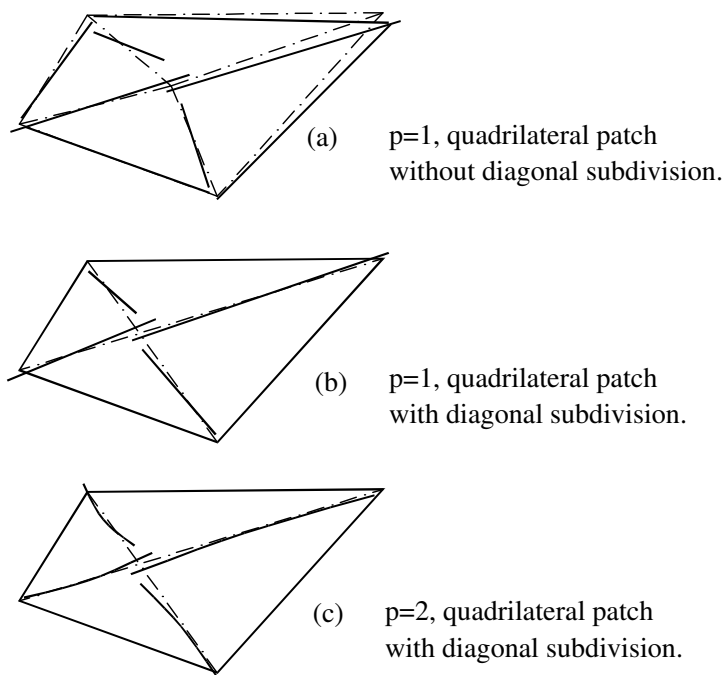


Figure 2: Spurious kinematic modes in a patch of primitive triangular elements.

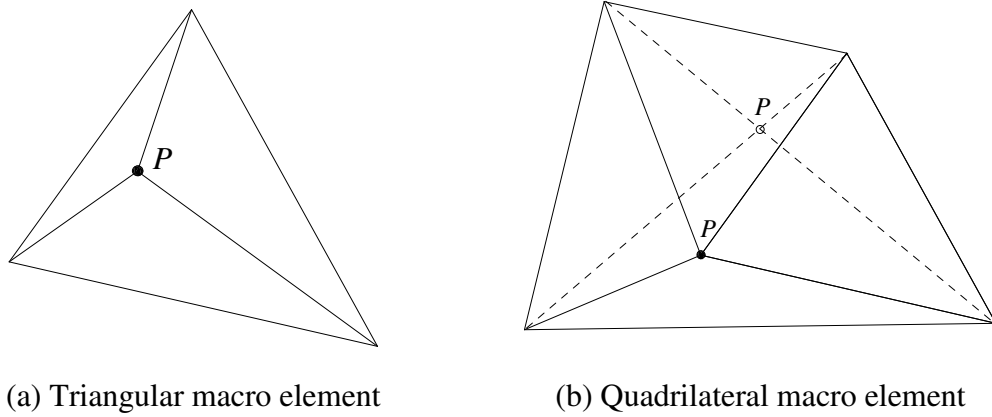
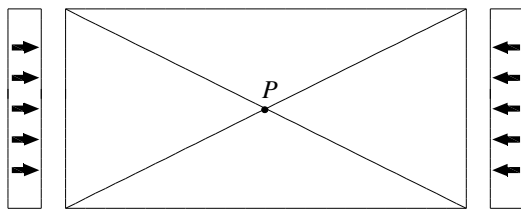
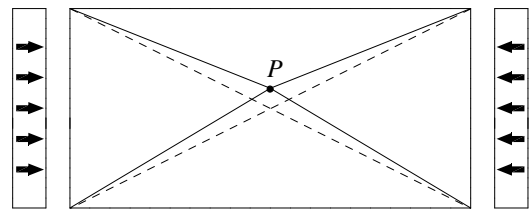


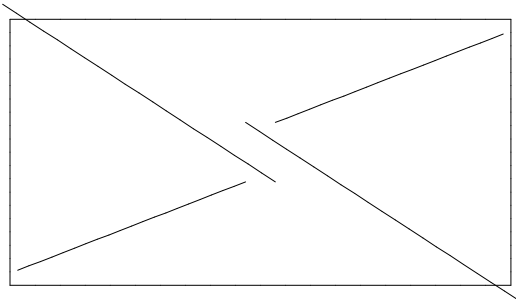
Figure 3: Macro-elements as assemblies of primitive elements.



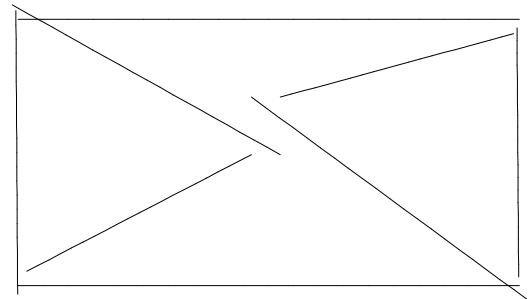
(a) Point P at intersection of diagonals



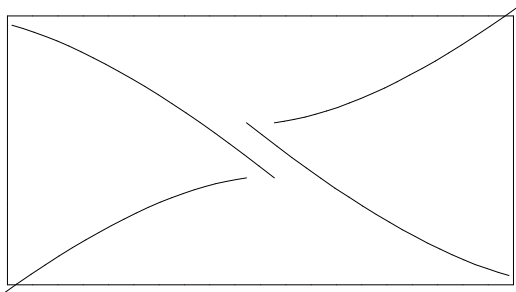
(b) Point P not at intersection of diagonals



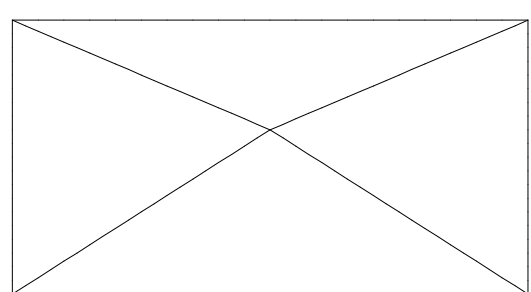
(c) Linear stress fields P at intersection



(d) Linear stress fields P not at intersection



(e) Quadratic stress fields P at intersection



(f) Quadratic stress fields P not at intersection

Figure 4: Displaced shapes for single rectangular macro-element problem.

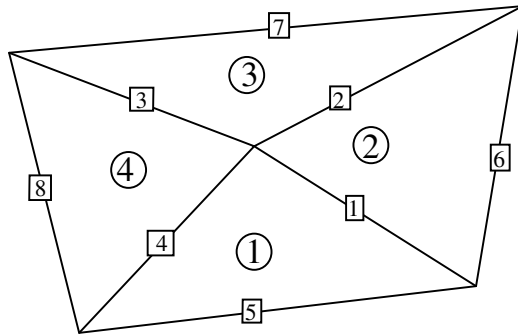
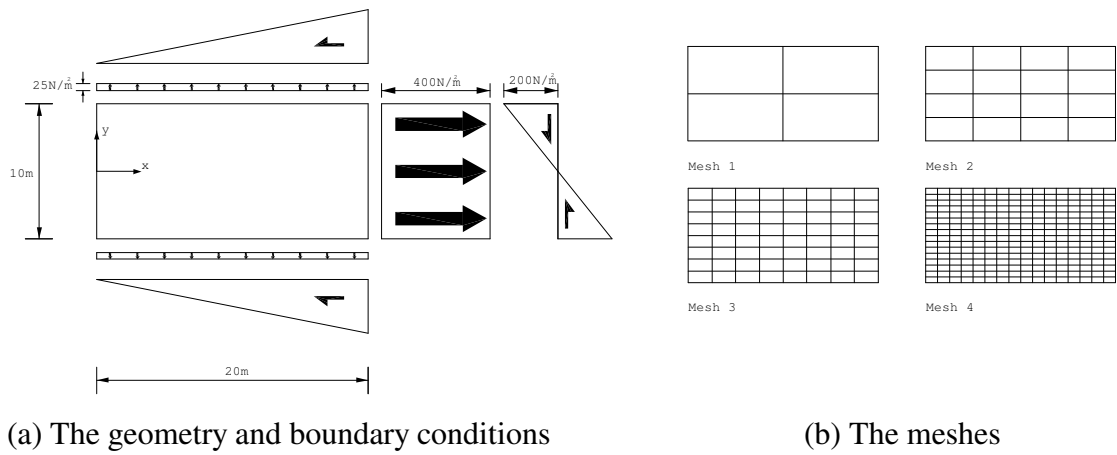


Figure 5: A general quadrilateral macro-element.



(a) The geometry and boundary conditions

(b) The meshes

Figure 6: Problem 1.

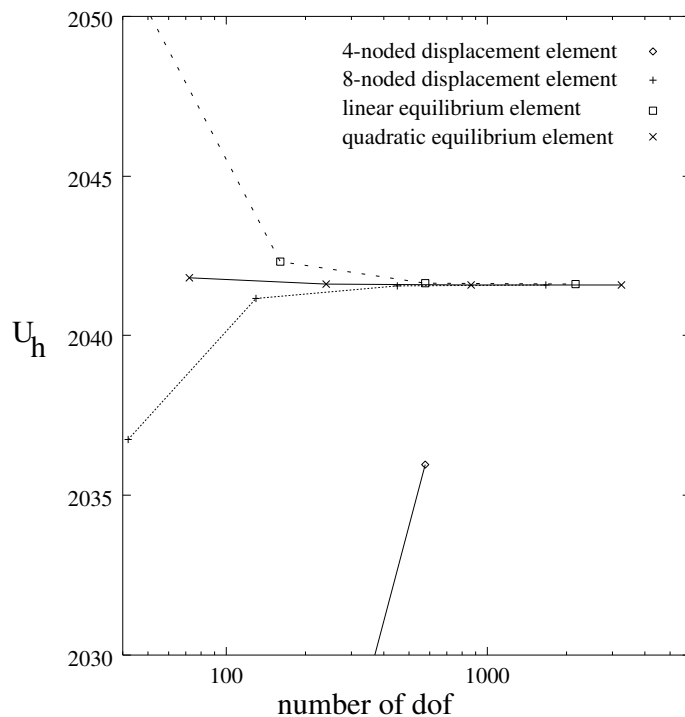
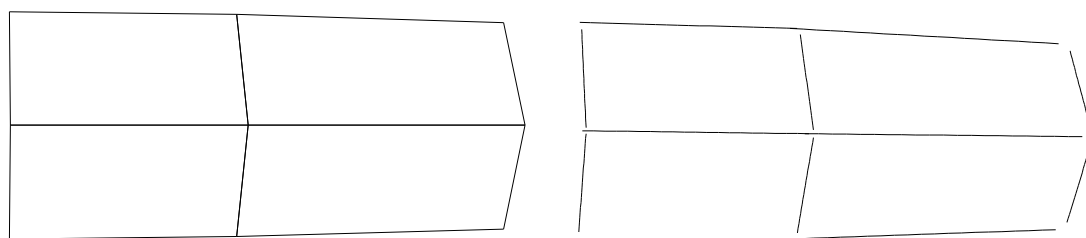


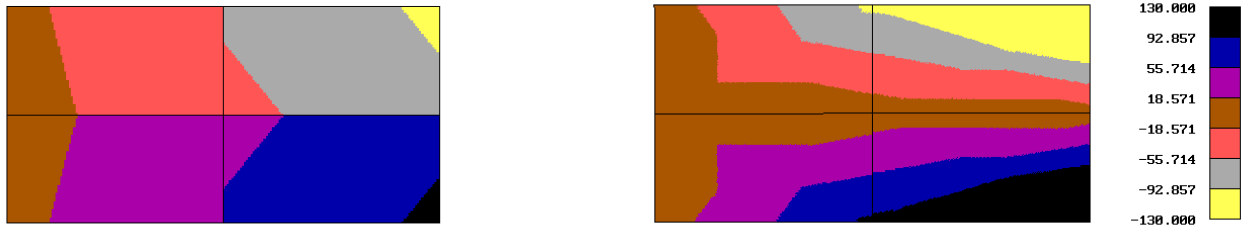
Figure 7: Convergence of the strain energy for Problem 1.



(a) Conforming (4-noded) elements

(b) Equilibrium (linear) elements

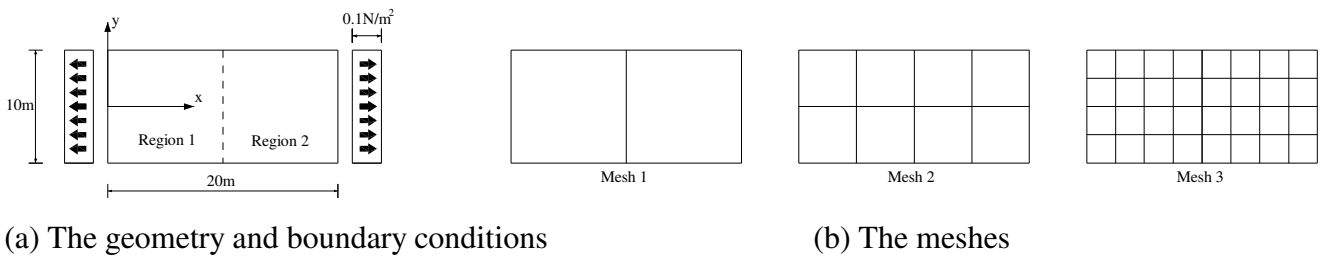
Figure 8: Displaced shapes for Mesh 1 of Problem 1.



(a) Conforming (4-noded) elements

(b) Equilibrium (linear) elements

Figure 9: Contours of the τ_{xy} -component of stress for Mesh 1 of Problem 1.



(a) The geometry and boundary conditions

(b) The meshes

Figure 10: Problem 2.

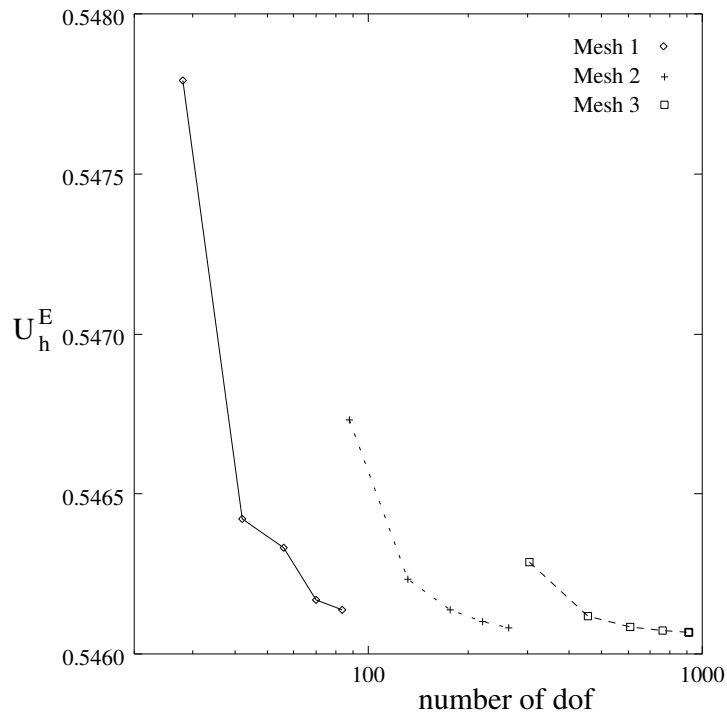
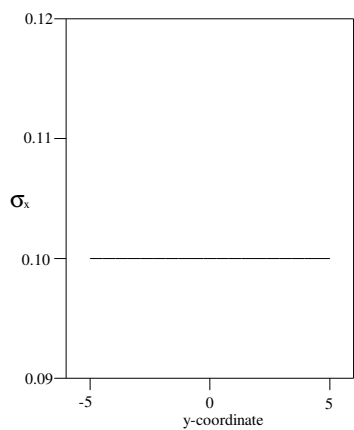
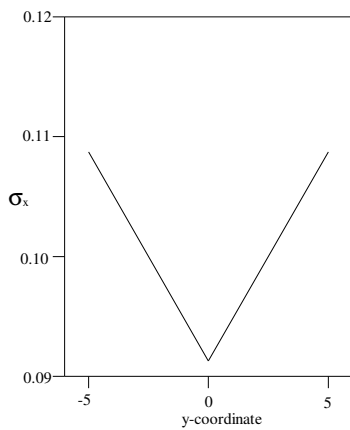


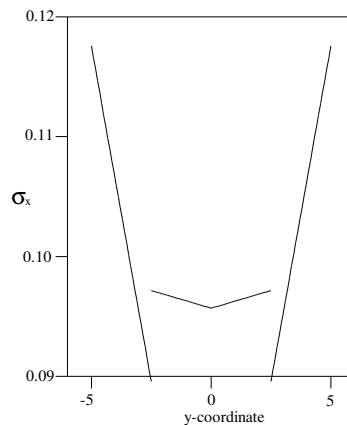
Figure 11: Convergence of the strain energy for Problem 2.



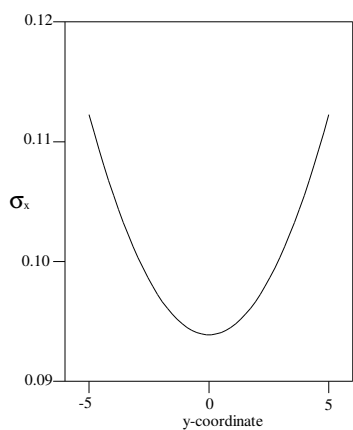
Mesh 1 ($p=1$)



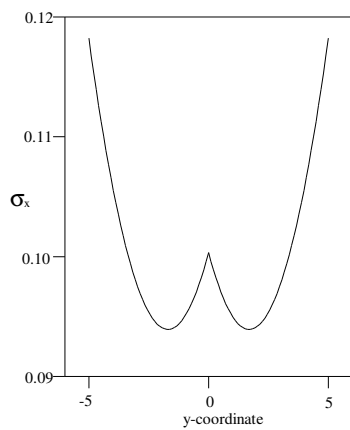
Mesh 2 ($p=1$)



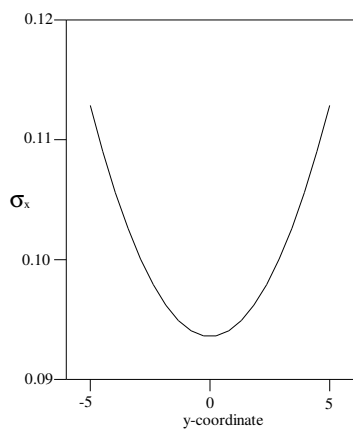
Mesh 3 ($p=1$)



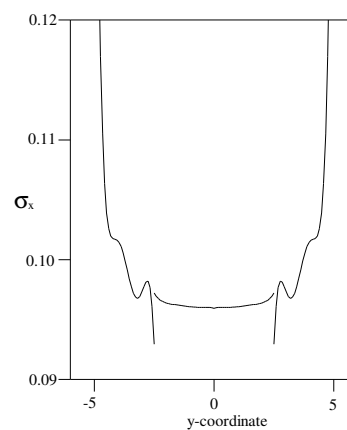
Mesh 1 ($p=2$)



Mesh 2 ($p=2$)



Mesh 1 ($p=3$)



Mesh 3 ($p=5$)

Figure 13: Plot of σ_{xx} -component of stress along the line $x = 10m$ for Problem 2.

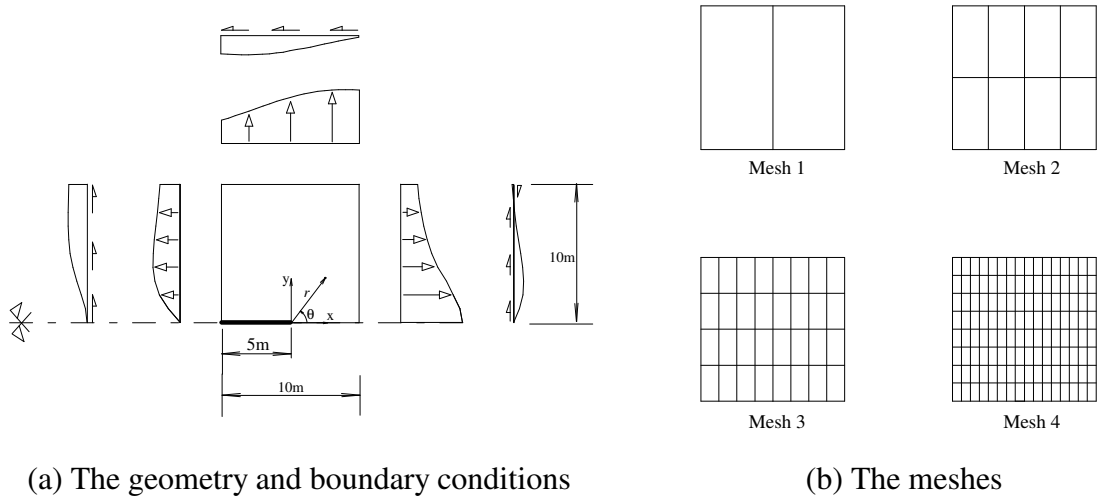


Figure 14: Problem 3.

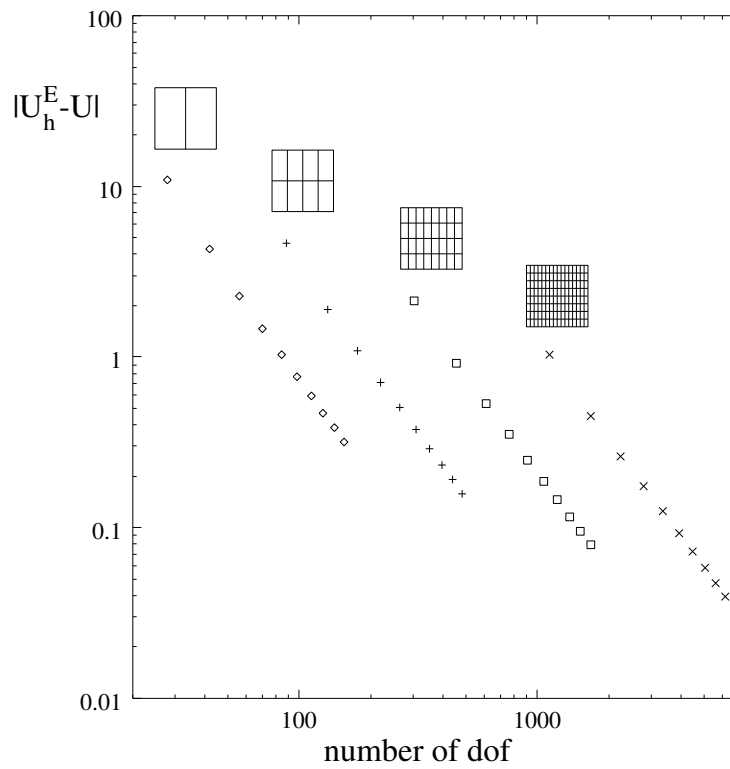


Figure 15: Convergence characteristics of the equilibrium models for Problem 3.

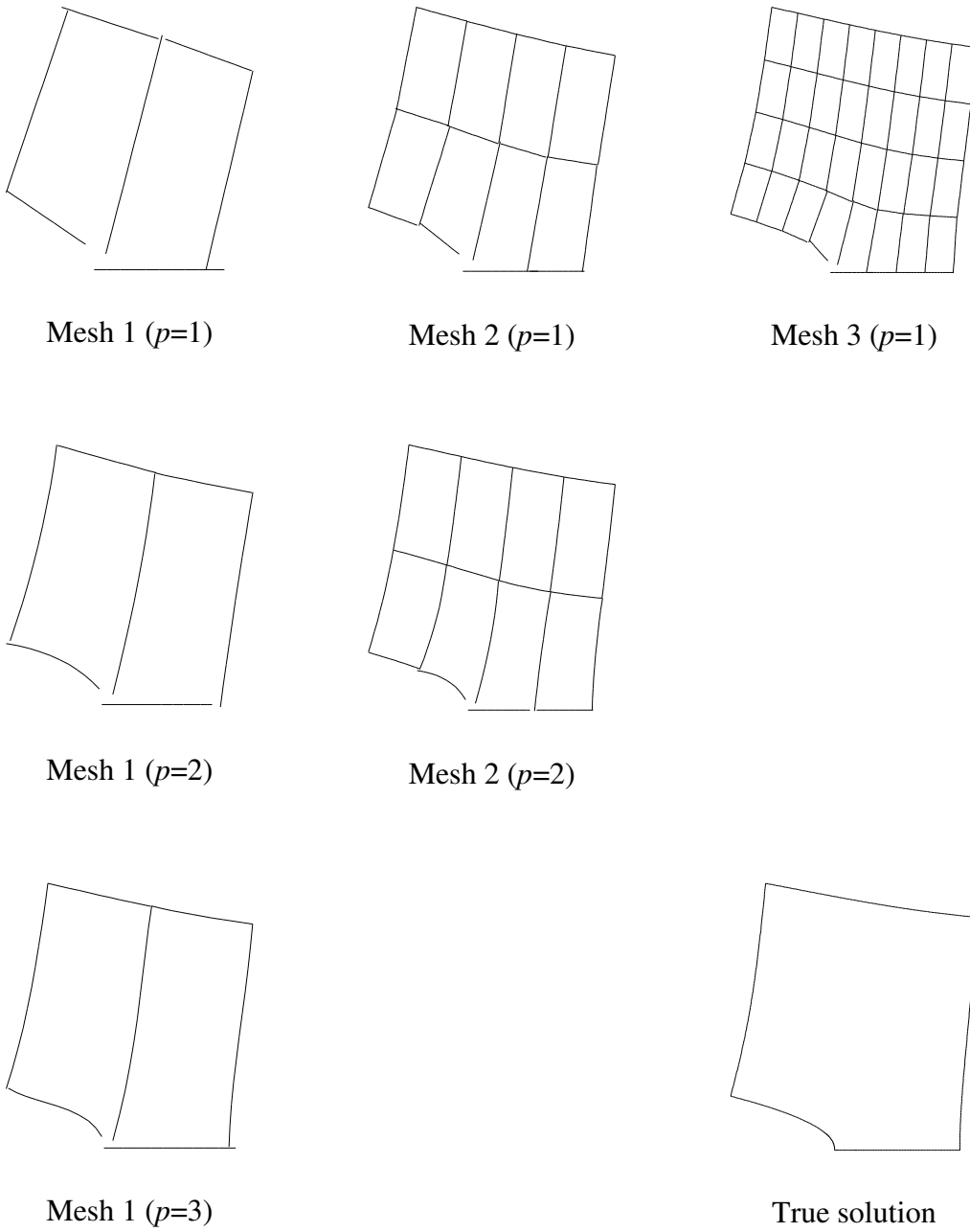


Figure 17: Convergence of the displaced shape for Problem 3.

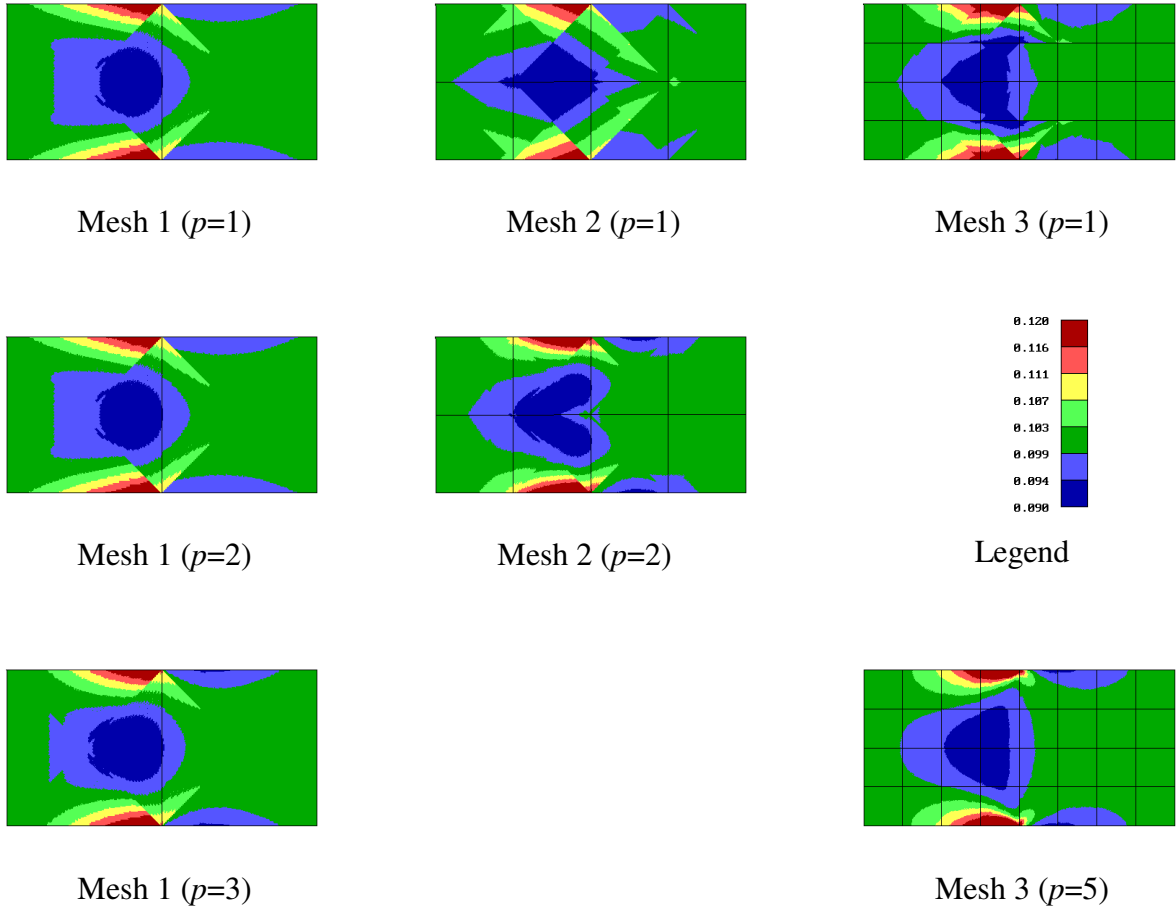


Figure 12: Contours of the σ_{xx} -component of stress for selected p/h combinations.

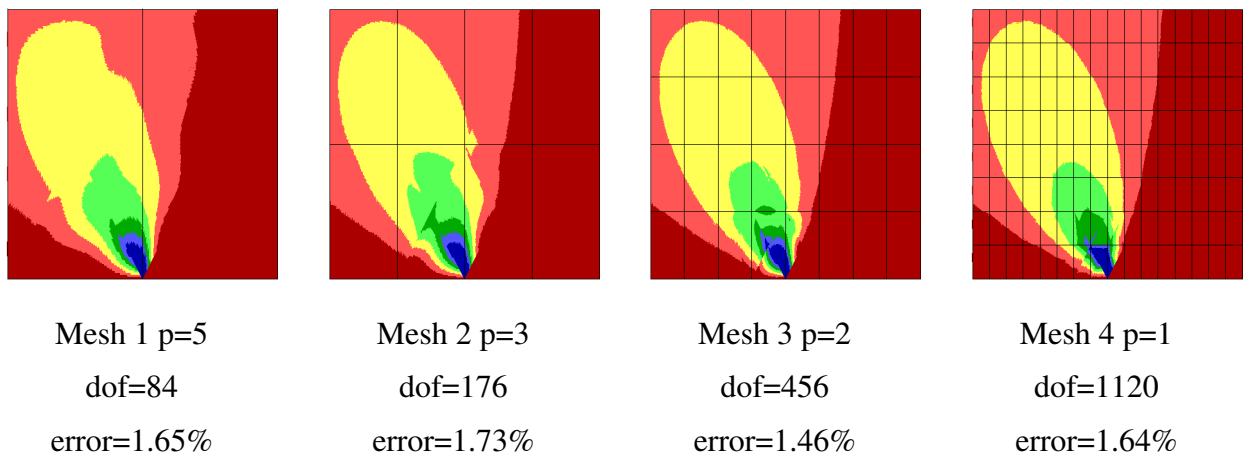


Figure 18: Contours of τ_{xy} for similar errors in strain energy.

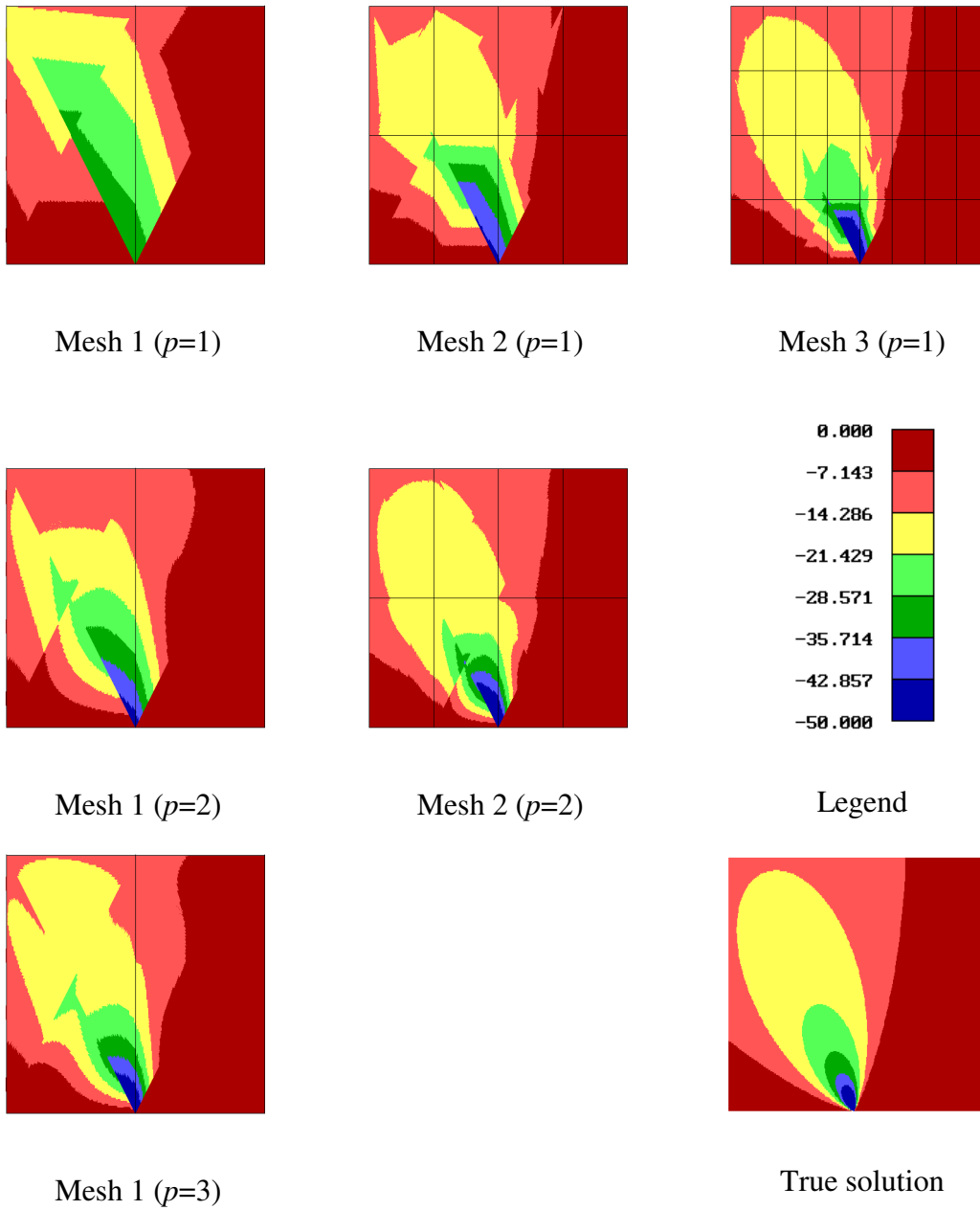


Figure 16: Convergence of τ_{xy} -component of the stress for Problem 3.

REFERENCES

- [1]. Moitinho de Almeida J.P.B. *Modelos de elementos finitos para a analise elastoplastica*, Ph.D. thesis, Technical University of Lisbon, 1989.
- [2]. Moitinho de Almeida J.P.B., Teixeira de Freitas J.A. *Alternative approach to the formulation of hybrid equilibrium finite elements*, Computers and Structures, Vol 40, No 4, 1043-1047, 1991.
- [3]. Zienkiewicz O.C., Taylor R. *The Finite Element Method*, 4th Ed, McGraw-Hill, 1989.
- [4]. Sander G. *Application of the dual analysis principle*, High Speed Computing of Elastic Structures, Ed by B. Fraeijs de Veubeke, Les Congres et Colloques de l'Universite de Liege, Vol 61, 167-207, 1971.
- [5]. Fraeijs de Veubeke B., Sander G., Beckers P. *Dual analysis by finite elements: linear and non linear applications*, Technical Report AFFDL-TR-72-93, Ohio, 1972.
- [6]. Maunder E.A.W. *A direct approach to a flexibility matrix for a triangular equilibrium membrane element*, in Accuracy, Reliability and Training in FEM Technology, Ed by J.Robinson, Robinson and Associates, 119-128, 1984.
- [7]. Maunder E.A.W. & Hill W.G. *Complementary use of displacement and equilibrium models in analysis and design*, in FEM in the Design Process, Ed by J.Robinson, Robinson and Associates, 493-501, 1990.
- [8]. Maunder E.A.W. & Ramsay A.C.A. *Quadratic Equilibrium Elements*, in FEM Today and the Future, Ed by J.Robinson, Robinson and Associates, 401-407, 1993.
- [9]. Love A.E.H. *A Treatise on the Mathematical Theory of Elasticity*, Dover, 1927.
- [10]. Davies G.A.O. *Virtual Work in Structural Analysis*, Wiley, 1982.
- [11]. Barnett S. *Matrices: Methods and Applications*, Clarendon Press, 1990.

- [12]. Maunder E.A.W. *A Direct Approach to a Flexibility Matrix for a Triangular Equilibrium Membrane Element*, in Accuracy, Reliability and Training in FEM Technology, Ed. by J. Robinson and Associates, 119-128, 1984.
- [13]. Ramsay A.C.A. *Finite Element Shape Sensitivity and Error Measures*, Ph.D. thesis, University of Exeter, 1994.
- [14]. Maunder E.A.W. *Some Structural Studies of Exeter Cathedral*, Internal Report, Exeter University, 1994.
- [15]. Ladevèze P. & Leguillon D. *Error estimate procedure in the finite element method and applications*, SIAM J. Numer. Anal., Vol.20, No.3, 485-509, 1983
- [16]. Maunder E.A.W., Beckers P. & Zhong H.G. *Reliability of some a posteriori error estimators related to the equilibrium defaults of finite element solutions*. Report SA-167, LTAS University de Liege, 1993.
- [17]. Beckers P, Zhong H.G. & Maunder E.A.W. *Numerical Comparison of Several a posteriori Error Estimators for 2D Stress Analysis*, Revue Européenne des Éléments Finis. Vol. 2 pp155-178, 1993.
- [18]. Robinson J., Maunder E.A.W. & Ramsay A.C.A. *Some Studeis of Simple Error Estimators*, Finite Element News, Issues 4,5 & 6, 1992 and Issues 1,2 & 3, 1993.
- [19] Ramsay A.C.A. & Maunder E.A.W. *Effective Error Estimation from Continuous Boundary Admissible Estimated Stress Fields*, Submitted to Computers and Structures, March 1995.